université PARIS-SACLAY

Simulation of interfaces to improve the stability and performance of perovskite solar cells

Simulation des interfaces pour améliorer la stabilité et les performances de cellules solaires pérovskites

Thèse de doctorat de l'université Paris-Saclay

École doctorale n° 564 Physique en Ile-de-France (PIF)
Spécialité de doctorat: Physique
Graduate School : Physique
Référent : Faculté des sciences d'Orsay

Thèse préparée dans le **Service de recherche en Corrosion et Comportement des Matériaux** (Université Paris-Saclay, CEA), sous la direction de **Guido ROMA**, Directeur de recherche (CEA Paris-Saclay - SRMP) et le co-encadrement de **Jacky EVEN**, Professeur à l'INSA Rennes (Univ Rennes, CNRS, Institut FOTON - UMR 6082).

Thèse soutenue à Paris-Saclay le 13 octobre 2026 par

Jasurbek GULOMOV

Composition du jury

Membres du jury avec voix délibérative

Thomas NIEHAUS Professeur, Institut Lumière Matière, Université Claude Bernard Lyon 1	Président & Rapporteur
Giorgia FUGALLO Chargée de recherche (HDR), Laboratoire de Physique de l'ENS (LPENS), ENS–PSL, Sorbonne Université, Université Paris Cité	Rapporteure & Examinatrice
Shuxia TAO Professeure, Department of Applied Physics and Science Education, Eindhoven University of Technology	Examinatrice
Zhuoying CHEN Chargée de recherche (HDR), ESPCI Paris-PSL, Sorbonne Université	Examinatrice

THÈSE DE DOCTORAT

NNT : 2026UPASP108

université PARIS-SACLAY | ÉCOLE DOCTORALE Physique en Île-de-France (PIF)

Titre: Simulation des interfaces pour améliorer la stabilité et les performances de cellules solaires pérovskites

Mots clés: Pérovskite, surfaces, désordre local, ab initio, interfaces

Résumé:

Les pérovskites halogénées sont des matériaux prometteurs en raison de leurs excellentes propriétés optoélectroniques. Bien que les cellules solaires à pérovskite à simple jonction aient atteint des rendements supérieurs à 27 %, leur stabilité opérationnelle et environnementale limitée demeure un obstacle majeur à leur commercialisation. Les pérovskites lamellaires (2D) sont généralement plus stables que leurs homologues 3D, mais les phases à faible n possèdent des bandes interdites plus larges et un confinement quantique plus marqué, ce qui limite leurs performances comme absorbeurs. La combinaison de pérovskites lamellaires et 3D pourrait donc permettre d'obtenir des matériaux et des interfaces associant haut rendement et stabilité accrue.

Les mesures de diffusion diffuse sur les pérovskites ont révélé des motifs localement désordonnés (polymorphes) qui s'écartent de la structure moyenne de haute symétrie (monomorphe) déterminée par diffraction des rayons X. Les études antérieures ont examiné l'influence du désordre local uniquement sur les propriétés volumiques des pérovskites halogénées, mais son effet sur les propriétés de surface demeure inexploré. Dans la première partie de cette thèse, l'effet du désordre local sur les propriétés de surface des pérovskites cubiques $CsBX_3$ (B = Sn, Pb ; X = I, Br, Cl) a été étudié à l'aide de modèles de surface monomorphes et polymorphes. Pour les deux descriptions structurales, les calculs dans l'approximation du gradient généralisé ont prédit, lors de la substitution de l'halogène, une évolution des positions absolues des bandes opposée à celle observée expérimentalement, tandis que la correction DFT-1/2 a permis de retrouver la tendance expérimentale. La prise en compte du désordre local dans les modèles de surface a amélioré la description des propriétés électronique de surface en modifiant le sommet de la bande de valence du matériau massif et le dipôle de surface. Les énergies de surface plus faibles des modèles polymorphes par rapport aux monomorphes ont en outre indiqué que le désordre local contribue à stabiliser les surfaces.

Dans la seconde moitié de cette thèse, nous avons étudié les pérovskites $Cs_{n+1}Pb_nI_{n+1}Cl_{2n}$ pour des épaisseurs de couches d'octaèdres $n = 1 - 5$. Les calculs de phonons ont montré que la structure de haute symétrie pour $n = 1$ est dynamiquement stable, tandis que celles avec $n > 1$ sont instables. Nous avons donc généré des structures polymorphes pour $n > 1$. Les distorsions de l'angle Pb–X–Pb et le gain énergétique induits par le désordre local augmentent tous deux avec n. Les énergies de décomposition ont montré que les composés monomorphes avec $n > 4$ sont thermodynamiquement défavorables, tandis que les structures polymorphes restent favorables, avec des valeurs se rapprochant de celle de la référence 3D. La prise en compte du désordre local élargit la bande interdite et ralentit sa diminution avec avec n, rapprochant ainsi la tendance calculée de l'expérience. En outre, le désordre local augmente la masse effective et inverse son évolution avec n.

Pour les pérovskites lamellaires, CsI est la terminaison de surface la plus favorable et le potentiel d'ionisation diminue lorsque n augmente. De plus, le désordre local améliore également la stabilité de surface. Pour l'interface $Cs_2PbI_2Cl_2/CsPbBr_3$, les énergies d'adhésion montrent que $CsI/PbBr_2$ et $PbCl_2/CsBr$ sont les terminaisons les plus favorables, et ces mêmes terminaisons sont celles pour lesquelles nous avons calculé les décalages de bande de valence les plus proches des valeurs expérimentales.

université PARIS-SACLAY | ÉCOLE DOCTORALE Physique en Île-de-France (PIF)

Title: Simulation of interfaces to improve the stability and performance of perovskite solar cells
Keywords: perovskite, surfaces, local disorder, ab initio, interfaces

Abstract: Halide perovskites are promising materials because of their excellent optoelectronic properties. Although single-junction perovskite solar cells have achieved efficiencies above 27%, limited operational and environmental stability remains a major barrier to commercialization. Layered (2D) perovskites are generally more stable than their 3D counterparts, but low-(n) phases have wider band gaps and stronger quantum confinement, limiting their performance as absorbers. Combining layered and 3D perovskites may therefore enable materials and interfaces with both high efficiency and improved stability.

Diffuse scattering measurements of perovskites have revealed locally disordered motifs (polymorphous) that deviate from the average high-symmetry (monomorphous) structure determined by X-ray diffraction. Previous studies have investigated the influence of local disorder only on the bulk properties of halide perovskites and its impact on surface properties remain unexplored. In the first part of this thesis, the effect of local disorder on the surface properties of cubic $CsBX_3$ (B = Sn, Pb; X = I, Br, Cl) was investigated using monomorphous and polymorphous surface slabs. For both structural descriptions, semilocal generalized-gradient-approximation calculations predicted a trend in absolute band positions with halogen substitution opposite to experiment, whereas the DFT-1/2 correction recovered the experimental trend. Incorporating local disorder into the surface-slab models improved the description of surface electronic properties by modifying the bulk valence-band maximum and surface dipole. The lower surface energies of polymorphous slabs relative to monomorphous slabs further indicated that local disorder contributes to stabilizing surfaces.

In the second half of this thesis, we investigated $Cs_{n+1}Pb_nI_{n+1}Cl_{2n}$ perovskites with octahedral-layer thicknesses $n = 1 - 5$. Lattice-dynamics calculations showed that the high-symmetry structure with $n = 1$ is dynamically stable, whereas those with $n > 1$ are unstable. We therefore generated polymorphous structures for $n > 1$. The Pb–X–Pb angle changes and energy gain induced by local disorder both increased with n. Decomposition energies showed that monomorphous compounds with $n > 4$ are thermodynamically unfavorable, whereas polymorphous structures remain favorable, with values approaching that of the 3D reference. The inclusion of local disorder opens the band gap and reduces the slope of its variation with octahedral thickness n, bringing the calculated trend into closer agreement with experiment. In addition, local disorder enhances the effective mass and reverses its trend with n.

For layered perovskites, CsI was the most favorable surface termination and the ionization potential decreased with increasing n. Moreover, local disorder also improves surface stability. For the $Cs_2PbI_2Cl_2/CsPbBr_3$ interface, adhesion energies showed $CsI/PbBr_2$ and $PbCl_2/CsBr$ as the most favorable terminations, and these same terminations yielded valence-band offsets in the closest agreement with experiment.

Résumé étendu en français

Les pérovskites halogénées sont des matériaux prometteurs pour les applications optoélectroniques, en particulier pour les cellules solaires. Parmi les propriétés remarquables de ces matériaux on note des largeurs de bande interdite ajustables, de grandes longueurs de diffusion des porteurs de charge, une forte absorption optique ainsi qu'une tolérance élevée aux défauts, dont beaucoup n'introduisent que des états électroniques peu profonds. Les cellules solaires à pérovskite à simple jonction ont atteint des rendements de conversion énergétique certifiés supérieurs à 27%. Cependant, leur stabilité limitée en conditions de fonctionnement et vis-à-vis de l'environnement demeure un obstacle majeur à leur commercialisation.

Les pérovskites bidimensionnelles (2D) en couches peuvent présenter une meilleure stabilité que leurs homologues tridimensionnelles (3D). Néanmoins, les pérovskites en couches à faible valeur de n possèdent généralement des bandes interdites plus larges et un confinement quantique plus prononcé, ce qui peut limiter leurs performances lorsqu'elles sont utilisées seules comme matériaux absorbeurs dans des cellules solaires. La combinaison de pérovskites en couches et de pérovskites 3D pourrait donc permettre d'obtenir des matériaux et des interfaces offrant à la fois des performances élevées et une stabilité améliorée.

Les propriétés des surfaces et des interfaces jouent un rôle central dans les performances et la stabilité des cellules solaires. Cette thèse étudie donc les propriétés de surface et d'interface de pérovskites halogénées entièrement inorganiques, en couches et tridimensionnelles. Des mesures de diffusion diffuse ont montré que les structures locales des pérovskites halogénées sont souvent distordues et diffèrent des structures moyennes de haute symétrie déterminées par diffraction des rayons X. Les effets de ce désordre positionnel local sur les propriétés volumiques des pérovskites 3D ont été largement étudiés. Cependant, son influence sur les propriétés volumiques et de surface des pérovskites en couches reste encore mal comprise.

En outre, les études numériques portant sur les surfaces des pérovskites 3D utilisent souvent des structures idéalisées de haute symétrie et négligent ainsi les distorsions structurales locales. Afin de combler ces lacunes, cette thèse examine les effets du désordre positionnel local sur les propriétés volumiques et de surface des pérovskites en couches, après avoir étudié par la même approche des modèles de surface de pérovskites halogénées 3D.

Les calculs présentés dans cette thèse ont été réalisés à l'aide de méthodes ab initio fondées sur la théorie de la fonctionnelle de la densité (DFT), telles qu'elles sont implémentées dans le logiciel Quantum ESPRESSO. Le chapitre 2 présente les détails des calculs ainsi que les fondements théoriques des méthodes utilisées dans l'ensemble de la thèse. Celles-ci comprennent des méthodes permettant de générer des structures polymorphes, de calculer les positions absolues des bords de bande et les én-

ergies de surface, ainsi que plusieurs approches permettant de déterminer les décalages de bandes aux interfaces. Étant donné que l'approximation du gradient généralisé (GGA) sous-estime souvent les largeurs de bande interdite et les potentiels d'ionisation, la méthode DFT-1/2 a été employée afin d'améliorer les propriétés électroniques calculées.

Les structures présentant un désordre local ont été générées à l'aide de l'ASDM développée par Zacharias *et al.* [1]. Les modèles de surface polymorphes ont été construits en répétant la structure polymorphe du matériau massif, tandis que les modèles de surface monomorphes ont été obtenus en répétant la structure monomorphe suivant la direction [001]. Des modèles de surface symétriques ont été utilisées afin d'éviter les interactions dipôle–dipôle parasites. Dans l'ensemble de cette thèse, les structures idéales de haute symétrie sont désignées comme des structures monomorphes, tandis que les structures présentant un désordre positionnel local sont appelées structures polymorphes.

Le chapitre 3 est consacré à l'effet du désordre positionnel local sur les propriétés volumiques et de surface des composés cubiques $CsBX_3$ (B=Pb, Sn ; X=I, Br, Cl). L'introduction d'un désordre local entraîne un gain d'énergie totale de tous les composés étudiés. Cet gain d'énergie est corrélé aux modifications des angles de liaison B–X–B induites par le désordre, en accord avec les travaux antérieurs [2]. Les variations des angles de liaison présentent également une relation linéaire avec le facteur de tolérance de Goldschmidt, aussi bien pour les composés à base de Pb que pour ceux à base de Sn. Les structures possédant les facteurs de tolérance les plus faibles présentent les écarts les plus importants entre les angles B–X–B et l'angle idéal de 180°.

Le désordre positionnel local augmente la largeur de la bande interdite par l'intermédiaire de deux effets structuraux principaux : l'inclinaison des octaèdres et l'allongement des liaisons B–X. Nous avons évalué séparément ces deux effets. Dans les composés à base de Pb, l'inclinaison des octaèdres constitue la contribution principale à l'augmentation de la largeur de bande interdite. Sa contribution diminue en passant des composés iodés aux composés bromés puis chlorés, tandis que la contribution de l'allongement des liaisons B–X reste pratiquement inchangée. Dans les composés à base de Sn, l'inclinaison des octaèdres et l'allongement des liaisons apportent des contributions similaires. Les calculs DFT-1/2 pour les structures monomorphes donnent des bandes interdites encore inférieures à l'expérience mais pour les structures polymorphes l'accord avec les résultats expérimentaux lest bon. Ainsi, la combinaison de la méthode DFT-1/2 et de modèles structuraux polymorphes fournit une description précise des largeurs de bande interdite de ces pérovskites halogénées.

Les surfaces de faible indice [001] peuvent présenter deux terminaisons : BX_2 et CsX. Les calculs d'énergie de surface montrent que la terminaison CsX est la plus stable dans l'ensemble du domaine des conditions de croissance autorisées pour tous les composés, à l'exception de $CsSnCl_3$. Dans le cas de $CsSnCl_3$, la terminaison $SnCl_2$ est plus stable que la terminaison CsCl. Pour chaque composé et chaque terminaison, les modèles polymorphes possèdent des énergies de surface inférieures à celles des modèles monomorphes correspondantes, ce qui indique que le désordre positionnel local stabilise les surfaces. La diminution de l'énergie de surface est également corrélée aux modifications des angles B–X–B à la surface.

Dans les modèles monomorphes, les contraintes de symétrie empêchent les angles B–X–B hors du plan de se modifier à la surface. Afin d'examiner l'effet de la reconstruction de surface, des modèles de surfaces monomorphes reconstruites ont donc été générées en déplaçant les atomes dans la région de surface avant la relaxation structurale. La reconstruction réduit l'énergie de surface, mais les

énergies obtenues restent supérieures à celles des modèles polymorphes. Ce résultat montre qu'une surface reconstruite sur un substrat monomorphe ne peut pas atteindre la configuration de surface de plus basse énergie. À l'inverse, les modèles polymorphes peuvent relaxer via de distorsions locales et des inclinaisons non uniformes des octaèdres. Les modèles monomorphes doivent donc être considérées principalement comme des structures de référence, tandis que les modèles polymorphes fournissent une description plus réaliste de la géométrie de surface de l'état fondamental.

Les positions absolues des bords de bande des pérovskites halogénées obtenues expérimentalement présentent une dispersion importante en raison des différences de préparation des couches minces et de la complexité intrinsèque de ces matériaux. Tao *et al.* ont appliqué une procédure expérimentale cohérente à une large gamme de pérovskites halogénées [3]. Leur jeu de données a donc été utilisé comme principale référence expérimentale dans cette thèse.

Les positions absolues des bords de bande des modèles monomorphes et polymorphes ont été calculées à l'aide de la GGA et de la méthode DFT-1/2. La GGA ne parvient pas à reproduire la tendance expérimentale [3] de la position absolue du maximum de la bande de valence (VBM) en fonction de la substitution de l'halogène, tandis que la méthode DFT-1/2 fournit une tendance conforme aux résultats expérimentaux [3]. Pour tous les composés étudiés, les positions du VBM obtenues par DFT-1/2 pour les modèles polymorphes à terminaison CsX présentent le meilleur accord avec les résultats expérimentaux de Tao *et al.* [3]. Combiné aux calculs d'énergie de surface, cet accord suggère que les surfaces mesurées expérimentalement sont probablement riches en CsX ou qu'elles contiennent un mélange de terminaisons CsX et BX_2. Le seuil expérimental associé au VBM est donc vraisemblablement principalement déterminé par les régions présentant une terminaison CsX.

Pour les surfaces à terminaison CsX comme pour celles à terminaison BX_2, les structures polymorphes présentent des VBM absolus situés à des énergies plus basses que ceux des structures monomorphes correspondantes. Ce déplacement résulte de deux contributions. Premièrement, le désordre local modifie le dipôle de surface et, par conséquent, le potentiel électrostatique par rapport au niveau du vide. Deuxièmement, l'allongement des liaisons B–X et l'inclinaison des octaèdres stabilisent le sommet de la bande de valence du matériau volumique. Bien que ce déplacement du bord de bande dans le volume soit important, la contribution du dipôle de surface le compense partiellement. Par conséquent, le déplacement total du sommet de la bande de valence par rapport au niveau de vide est inférieur à la seule contribution volumique. Les surfaces pour lesquelles la compensation venant du dipôle de surface est plus important présentent donc un bord de bande qui varie moins avec l'introduction du désordre local.

Le dernier chapitre traite de l'effet du désordre local sur les propriétés volumiques et de surface des pérovskites en couches $Cs_{n+1}Pb_nI_{n+1}Cl_{2n}$ avec $n = 1 - 5$. D'après les dispersions de phonons, la configuration monomorphe de la phase $n = 1$ de la pérovskite 2D est déjà dynamiquement stable, tandis que les phases $n > 1$ présentent des modes de phonons imaginaires, indiquant une instabilité dynamique. Des configurations polymorphes ont donc été générées pour les phases $n > 1$. Dans ces pérovskites 2D, le gain énergétique associé au désordre positionnel local présente une forte corrélation avec la variation de l'angle B–X–B moyen, de manière similaire au comportement observé dans les pérovskites 3D. Le gain énergétique et la variation de l'angle B–X–B augmentent tous deux avec l'épaisseur de la couche octaédrique, n. Dans la pérovskite 2D inorganique avec $n = 1$, la couche de CsI de structure NaCl contraint la couche octaédrique et inhibe les fluctuations structurales. Pour

$n > 1$, cette contrainte s'affaiblit à mesure que l'épaisseur de la couche octaédrique augmente. Par conséquent, les structures possédant des couches octaédriques plus épaisses présentent des variations plus importantes des angles B–X–B ainsi que des gains énergétiques plus élevés.

L'enthalpie de décomposition diminue lorsque l'épaisseur de la couche octaédrique augmente, aussi bien pour les configurations polymorphes que monomorphes. Pour ces dernières, elle devient négative pour les phases à valeurs élevées de n, ce qui indique que ces structures sont thermodynamiquement instables. En revanche, bien que l'enthalpie de décomposition diminue également lorsque n augmente pour les configurations polymorphes, elle reste positive et se rapproche de la valeur de la structure de référence 3D. Ainsi, les pérovskites en couches à valeurs élevées de n restent thermodynamiquement stables lorsque les distorsions structurales locales sont prises en compte, ce qui démontre que le désordre positionnel joue un rôle important dans la stabilisation des pérovskites en couches à halogénures mixtes.

Le désordre local augmente également les largeurs de bande interdite des pérovskites 2D. L'amplitude de l'ouverture de la bande interdite augmente avec n en raison des variations plus importantes des angles B–X–B. Par conséquent, le désordre local réduit la pente de la variation de la largeur de bande interdite en fonction de n, rapprochant ainsi la tendance calculée de la tendance expérimentale [4]. Les résultats montrent que les modifications de l'angle Pb–I–Pb ne produisent pas d'ouverture notable de la bande interdite, tandis que les modifications de l'angle Pb–Cl–Pb augmentent clairement cette dernière. Ce résultat indique que les distorsions des angles de liaison dans le plan jouent le rôle dominant dans l'ouverture de la bande interdite provoquée par le désordre local.

Le désordre positionnel local réduit la dispersion des bandes au voisinage du sommet de la bande de valence (VBM)et du minimum de la bande de conduction (CBM). Cet aplatissement augmente les masses effectives des porteurs de charge. Dans les configurations monomorphes, les masses effectives des électrons et des trous restent relativement faibles et diminuent généralement lorsque n augmente. À l'inverse, dans les configurations polymorphes, les masses effectives des électrons et des trous augmentent à mesure que la couche octaédrique devient plus épaisse. Le désordre positionnel local inverse donc la tendance des masses effectives prédite par le modèle monomorphe.

Les modèles de surface monomorphes [001] des pérovskites 2D ont été étudiés pour $n = 1$ et $n = 5$. Pour la configuration polymorphe, seule la structure avec $n = 2$ a été considérée, car l'extension de l'analyse à des valeurs de n plus élevées nécessiterait des modèles de taille beaucoup plus importante, la structure polymorphe étant quatre fois plus grande que la structure monomorphe. Parmi les terminaisons CsI, double-CsI et $PbCl_2$ considérées, la terminaison CsI possède l'énergie de surface la plus faible pour toutes les conditions de croissance comprises dans le domaine de stabilité. Ce résultat indique que la terminaison CsI est la terminaison de surface la plus stable, de manière similaire au comportement observé dans les pérovskites 3D. Le désordre local réduit ultérieurement l'énergie de surface de la phase $n = 2$, montrant qu'il stabilise également la surface.

Le potentiel d'ionisation des pérovskites 2D diminue lorsque n augmente et se rapproche du potentiel d'ionisation de la structure de référence 3D pour $n > 4$. Le désordre positionnel local augmente d'environ 0.2 eV les potentiels d'ionisation des terminaisons double-CsI et $PbCl_2$, tandis qu'il ne diminue le potentiel d'ionisation de la terminaison CsI que de 0.04 eV. L'effet relativement faible du désordre positionnel local sur les propriétés de surface de la phase $n = 2$ peut être attribué à son

degré de distorsion structurale plus faible que celui des pérovskites 2D plus épaisses.

Les pérovskites 2D en couches sont couramment utilisées sous la forme de fines couches de recouvrement déposées sur des pérovskites 3D afin de passiver leurs surfaces. L'interface [001] entre $Cs_2PbI_2Cl_2$ ($n = 1$) et $CsPbBr_3$ cubique a donc été étudiée. La pérovskite 3D possède deux terminaisons de surface possibles, tandis que la pérovskite 2D en possède trois, ce qui conduit à six combinaisons de terminaisons possibles à l'interface. D'après les énergies d'adhésion calculées, les interfaces CsBr/$PbCl_2$ et $PbBr_2$/CsI présentent les adhésions les plus fortes. L'énergie d'adhésion est corrélée à la distance interfaciale optimisée, et ces deux interfaces possèdent les distances d'équilibre les plus rapprochées. En outre, seules ces interfaces présentent une compatibilité structurale de part et d'autre de la jonction, l'ossature octaédrique PbX_6 restant continue à travers l'interface 3D/2D.

Le désaccord de paramètres de maille entre $Cs_2PbI_2Cl_2$ et $CsPbBr_3$ cubique est de 4.3%. Par conséquent, en plus de la méthode standard d'alignement à l'interface, la méthode du potentiel de déformation absolu et une approche en trois étapes ont été employées afin de corriger les effets de déformation introduits par la différence des paramètres de maille lors du calcul des décalages de bandes. La méthode du potentiel de déformation absolu et l'approche en trois étapes fournissent des décalages de bande de valence similaires pour les interfaces CsBr/$PbCl_2$ et $PbBr_2$/CsI, et les valeurs calculées sont proches des résultats expérimentaux [5]. En revanche, la méthode standard d'alignement à l'interface sous-estime les décalages de bande de valence. Selon l'approche en trois étapes, toutes les terminaisons d'interface présentent un alignement de bandes de type II. Le VBM de $Cs_2PbI_2Cl_2$ se situe au-dessus de celui de $CsPbBr_3$, ce qui favorise le transfert des trous de la pérovskite 3D vers la pérovskite 2D. Parallèlement, le CBM de $Cs_2PbI_2Cl_2$ se situe également au-dessus de celui de $CsPbBr_3$, créant une barrière énergétique qui empêche le transfert des électrons vers la couche 2D.

En résumé, cette thèse démontre que le désordre positionnel local doit être pris en compte afin d'obtenir une description réaliste des pérovskites halogénées 2D et 3D. Le désordre local affecte leur stabilité structurale, leurs énergies de surface, leurs enthalpies de décomposition, leurs largeurs de bande interdite, les positions absolues de leurs bords de bande ainsi que les masses effectives des porteurs de charge. Étant donné que ces propriétés déterminent l'absorption de la lumière, le transport des charges, l'extraction des charges aux interfaces et la stabilité des matériaux, leur description précise à partir des premiers principes est essentielle pour interpréter les observations expérimentales et concevoir de manière rationnelle des cellules solaires à pérovskites 3D/2D à la fois efficaces et stables.

References

[1] Marios Zacharias, George Volonakis, Feliciano Giustino, and Jacky Even. Anharmonic lattice dynamics via the special displacement method. *Physical Review B*, 108(3), July 2023.

[2] Marios Zacharias, George Volonakis, Feliciano Giustino, and Jacky Even. Anharmonic electron-phonon coupling in ultrasoft and locally disordered perovskites. *npj Computational Materials*, 9(1):153, August 2023.

[3] Shuxia Tao, Ines Schmidt, Geert Brocks, Junke Jiang, Ionut Tranca, Klaus Meerholz, and Selina Olthof. Absolute energy level positions in tin- and lead-based halide perovskites. *Nature Communications*, 10(1), June 2019.

[4] Xinting Shuai, Siraj Sidhik, Mingrui Xu, Xiang Zhang, Michael De Siena, Laurent Pedesseau, Hao Zhang, Guanhui Gao, Anand B. Puthirath, Wenbin Li, Ayush Agrawal, Jianan Xu, Jin Hou, Jessica H. Persaud, Jeremy Daum, Anamika Mishra, Yafei Wang, Robert Vajtai, Claudine Katan, Mercouri G. Kanatzidis, Jacky Even, Pulickel M. Ajayan, and Aditya D. Mohite. Vapor Growth of All-Inorganic 2D Ruddlesden–Popper Lead- and Tin-Based Perovskites. *ACS Applied Materials & Interfaces*, 16(35):46560–46569, August 2024.

[5] Xing Huang, Kuanxin Lv, Wenqiang Zhu, Zhenzhen Li, and Hang Zhao. Accessible New Non-Quantum Dot $Cs_2PbI_2Cl_2$-Based Photocatalysts for Efficient Hole-Driven Photocatalytic Applications. *Molecules*, 29(14):3249, July 2024.

Acknowledgement

As my PhD journey at the French Alternative Energies and Atomic Energy Commission (CEA) comes to an end, I look back on these three years with gratitude and many wonderful memories. I feel truly fortunate to have had the opportunity to pursue my PhD and work in such an excellent research environment, surrounded by inspiring scientists and kind people. This journey has not only helped me grow as a researcher but has also taught me many valuable lessons about life. I would like to take this opportunity to express my sincere gratitude to everyone who has been part of this journey.

In Uzbekistan, we have a beautiful quote: "A teacher is as great as a father." This quote reflects the deep respect we have for those who share their knowledge and guide us through life. With this in mind, I would like to express my deepest gratitude to my supervisors, Guido Roma and Jacky Even, for their guidance, patience, and continuous support throughout my PhD.

First and foremost, I am deeply grateful to Guido for giving me the opportunity to pursue this PhD and, most importantly, for believing in me. Words cannot fully express how thankful I am for everything he has done for me. Over the past three years, he has always taught me with great patience, generously sharing his knowledge and experience. No matter how many questions I had, he was always willing to take the time to answer them, explain difficult concepts, and help me understand things more clearly. His continuous guidance, thoughtful feedback, and valuable scientific discussions have played a key role in improving my research and helping me grow as a scientist. I have learned so much from him, not only about scientific methods and research, but also about how to think critically, approach problems, and find solutions. I feel truly fortunate to have had him as my supervisor.

Beyond his scientific guidance, Guido has also been a wonderful mentor in my personal life. I will especially remember our almost daily walks to the bus station after work. During these walks, we often had conversations that went beyond research. He shared valuable advice and life lessons that helped me grow not only as a scientist but also as a person. These simple moments have become some of my most precious memories of my PhD years, and I will truly miss them. Thank you, Guido, for your endless patience, kindness, encouragement, and for everything you have taught me. I could not have asked for a better supervisor and mentor.

I am also sincerely thankful to Jacky for his guidance, encouragement, and valuable scientific discussions. Our meetings were always productive, and his thoughtful comments and suggestions played an important role in improving my research and shaping this thesis. I am very grateful for the time and effort he dedicated to my work.

I would also like to express my heartfelt thanks to all the members of SRMP. From the beginning, I felt welcomed into a friendly and supportive environment. The people at SRMP are more than just colleagues; they are like a family. Everyone has always been kind, approachable, and willing to help,

especially when students needed support. It has been a pleasure to work in such a wonderful atmosphere, and I will always remember the kindness and generosity I experienced during these three years.

I would like to sincerely thank Jean-Luc Béchade from CEA and Sébastien Pillet from the University of Lorraine for being members of my PhD monitoring committee. During our meetings, they listened patiently to my presentations, showed genuine interest in my research, and provided thoughtful questions and valuable suggestions. Their feedback helped me improve my work and better understand the direction of my research. I am grateful for their time, attention, and encouragement.

I am also very thankful to Claudine Katan and Marios Zacharias, with whom I had the pleasure of collaborating during my PhD. Our scientific discussions were always interesting and helpful. Their expertise, thoughtful feedback, and valuable suggestions played an important role in our research and publication. I sincerely appreciate the time and effort they dedicated to our collaboration.

I would also like to extend my sincere gratitude to the members of my PhD defence jury, Thomas Niehaus, Giorgia Fugallo, Shuxia Tao, and Zhuoying CHEN, for kindly accepting to evaluate my work and for taking the time to read my thesis. I am truly honoured by their participation in this important moment of my academic journey.

Beyond research, these three years in France have brought wonderful people into my life and given me friendships that I will always value. I would like to thank my dear friends Roshal Perepadan, Rohit Vasav, Nicolas Houze, Camilo Salvador, and Zheng Fang Brice. We have shared many happy moments, interesting conversations, and unforgettable experiences together. They have always been positive, supportive, and ready to help whenever I needed them. Their friendship made my life in France much more enjoyable, and I will certainly miss the time we spent together.

I would like to express special thanks to Roshal, who has been one of my closest friends since my first days in France. When I first arrived, we spent a lot of time exploring Paris, travelling to new places, and discovering a new culture together. We learned many things along the way and created wonderful memories. He was always there whenever I needed help, and his friendship made my first experiences in France much easier and happier. I am truly grateful to have met him.

Moving to a new country and adapting to a different culture can sometimes be challenging. Fortunately, I was surrounded by people who made this transition much easier. I would like to sincerely thank my officemates, Maxime Malingre and Nicolas Houze. At the beginning of my PhD, I shared an office with Maxime, and later I had the pleasure of sharing an office with Nicolas for the last two years. Both of them helped me understand French culture, deal with administrative difficulties, and feel more comfortable in my new environment. I am especially grateful to Nicolas for his exceptional kindness, patience, and willingness to help. It is rare to meet someone so genuinely kind and thoughtful. Sharing an office with him was one of the most pleasant parts of my daily life at CEA. I will always remember and appreciate the support and friendship of both Maxime and Nicolas.

Finally, and most importantly, I would like to express my deepest gratitude to my family for their endless love, patience, and support throughout this journey. I am especially grateful to my mother, whose unconditional love, care, and encouragement have always been a source of strength for me, even from far away. I am also deeply thankful to my family for always believing in me and supporting me through both difficult and happy moments. Their love and encouragement have given me the strength and motivation to keep moving forward. Without their support, this journey would not have

been possible.

As I close this chapter of my life, I realize that the most valuable part of my PhD journey is not only the scientific knowledge I have gained, but also the people I have met, the friendships I have built, and the memories I will carry with me. To everyone who has been part of these three years, thank you from the bottom of my heart.

Contents

1 Introduction: Halide Perovskite Solar Cells, Theoretical Understanding, and Research Challenges **23**

1.1 Global energy challenge and motivation for photovoltaics . . . 24
1.1.1 Rising energy demand and the environmental cost of fossil fuels . . . 24
1.1.2 Need for efficient, stable, and low-cost photovoltaic materials . . . 25
1.2 Halide perovskites as promising photovoltaic materials . . . 27
1.2.1 Perovskite structure . . . 27
1.2.2 Emergence and rapid development of perovskite solar cells . . . 30
1.2.3 Optoelectronic properties that make halide perovskites attractive . . . 30
1.3 Stability challenges in halide perovskite solar cells . . . 32
1.3.1 Instability of 3D halide perovskites . . . 32
1.3.2 Role of 2D perovskites in improving stability . . . 33
1.4 Theoretical description of halide perovskites . . . 35
1.4.1 Electronic structure and optical properties of 3D halide perovskites . . . 35
1.4.2 Theoretical description of 2D halide perovskites . . . 36
1.4.3 Anharmonicity and local structural disorder . . . 37
1.5 Role of surfaces and interfaces in perovskite solar cells . . . 40
1.5.1 Surface orientation and termination . . . 40
1.5.2 Surface electronic structure and absolute band alignment . . . 42
1.5.3 Interface properties in perovskite solar cells . . . 43
1.6 Open questions addressed in this thesis . . . 44
1.6.1 Accurate prediction of surface properties of cubic halide perovskites . . . 44
1.6.2 Anharmonicity and local disorder in all-inorganic 2D and quasi-2D perovskites . . . 44
1.6.3 Interfaces between all-inorganic 2D and 3D perovskites . . . 45

2 Theoretical Framework and Electronic-Structure Calculations **65**

2.1 Computational Details and Quasiparticle Correction . . . 66
2.1.1 Computational details . . . 66
2.1.2 DFT-1/2 method . . . 67
2.2 Lattice Dynamics and Generation/Analysis of Locally Positionally Disordered Structures 70
2.2.1 Anharmonic Special Displacement Method (ASDM) . . . 70
2.2.2 Pair Distribution Function (PDF) . . . 75

2.3 Surface and Interface Property Calculations . . . 76
2.3.1 Surface and interface slab construction . . . 76
2.3.2 Planar and macroscopic averages of physical quantities for surfaces and interfaces 78
2.3.3 Absolute band positions of surfaces and band offsets of interfaces . . . 79
2.3.4 Strain correction of band offsets . . . 81
2.3.5 Surface dipoles . . . 83
2.3.6 Surface energy . . . 86
2.3.7 Adhesion energy . . . 87

3 Polymorphism in bulk and surfaces of 3D inorganic halide perovskites: stability and electronic structure 93
3.1 Structural Origin and Stabilization of Local Positional Disorder . . . 94
3.1.1 Ideal cubic perovskite structure . . . 94
3.1.2 Dynamical instability of the cubic phase . . . 94
3.1.3 Energy gain with local positional disorder . . . 98
3.2 Impact of Local Disorder on Bulk Electronic Structure . . . 99
3.2.1 Band structure modification due to disorder . . . 99
3.2.2 Role of bond-length variation and octahedral tilting . . . 101
3.2.3 Accurate Band-Gap Prediction . . . 103
3.3 Surface Structural Relaxation and Stability . . . 104
3.3.1 Surface relaxation in different structural models . . . 104
3.3.2 Surface energy and stability . . . 107
3.4 Surface Electronic Properties and Band Alignment . . . 110
3.4.1 Absolute band positions . . . 110
3.4.2 Role of surface dipoles . . . 112
3.4.3 Chemical trends in the absolute valence-band position . . . 114
3.4.4 Effect of local disorder on band alignment . . . 115
3.4.5 Surface states . . . 117

4 Bulk, Surface, and Interface Properties of All-Inorganic 2D Perovskites 124
4.1 Structures and Thermodynamic Stability of 2D perovskites . . . 125
4.1.1 Structures of 2D perovskites . . . 125
4.1.2 Single-halide 2D perovskites . . . 128
4.1.3 Different configurations of $Cs_2PbI_2Cl_2$ . . . 128
4.2 Role of Local Positional Disorder in the Dynamical and Thermodynamic Stability of 2D Perovskites . . . 130
4.2.1 Lattice dynamics of layered halide perovskites . . . 130
4.2.2 Energy gain due to positional local disorder . . . 133
4.2.3 Effect of positional local disorder on thermodynamic stability . . . 135
4.3 Bulk Electronic Properties of 2D Perovskites . . . 136
4.3.1 Electronic structure . . . 136
4.3.2 Band gap opening due to local disorder . . . 139
4.3.3 Effect of positional local disorder on effective masses . . . 140

4.4 Surface Properties of 2D Perovskites . . . 143
4.4.1 Surface terminations and slab structures . . . 143
4.4.2 Surface energy and phase stability . . . 145
4.4.3 Ionisation potential . . . 148
4.5 2D/3D Perovskite Interfaces . . . 151
4.5.1 Adhesion energy of different interface terminations . . . 151
4.5.2 Band offsets . . . 153

5 Conclusion & Perspectives **163**
5.1 General conclusion . . . 164
5.2 Perspectives . . . 165

Appendix A Effect of vdW Correction and XC Functionals on the Electronic Properties **169**
A.1 vdW correction . . . 169
A.2 Exchange–correlation functionals . . . 170

Appendix B Effect of Volume Relaxation on Polymorphous Structures **172**

Appendix C Projected Density of States of 2D Perovskites **175**

Appendix D Phonon Dispersion of $CsPbICl_2$ **176**

Appendix E Effect of biaxial strain on the electronic properties of the 2D perovskite $Cs_2PbI_2Cl_2$ **177**

List of Figures

1.1 Global electricity production by source, measured in terawatt-hours (TWh). Coal remains the largest source of electricity worldwide, followed by gas, while renewable energy sources such as wind and solar have grown rapidly in recent years. Source: Our World in Data, based on Ember (2026) and Energy Institute (2025) [2]. 24

1.2 Best research-cell efficiency chart reported by NREL [16]. 27

1.3 Structure of $CsPbI_3$. 28

1.4 Schematic illustration of the structural phases of $CsPbI_3$ (α, β, γ, and δ). Adapted from Ref. [20]. 29

1.5 Schematic structure of Ruddlesden–Popper and Dion–Jacobson 2D perovskites [70]. . . 33

1.6 Schematic structure of 2D, quasi-2D, and 3D perovskites [70]. 35

1.7 Comparison of the calculated pair distribution functions for polymorphous (a) and monomorphous (b) configurations of MAPI with experiment. Adapted from Ref. [114] . 38

1.8 Schematic representation of the potential-energy surface of halide perovskites, illustrating the high-symmetry monomorphous configuration and the lower-energy polymorphous configurations [111]. 39

2.1 Convergence of the total energy of high-symmetry cubic $CsPbI_3$ with respect to the plane-wave cutoff energy (a) and the k-point grid (b). In panel (b), only one number is shown on the x-axis because the cubic structure uses an $n \times n \times n$ k-point grid. . . . 67

2.2 Variation of the band gap of $CsPbI_3$ with the cutoff radius r_{cut} used in the trimming function for the I $5p$ orbital (a) and the Pb $6s$ orbital (b). 70

2.3 Schematic representation of an anharmonic double-well potential-energy surface. The high-symmetry monomorphous structure is located near the central maximum, while the symmetry-broken polymorphous structures correspond to the minima. 72

2.4 Surface slab models used in this work: (a) monomorphous and (b) polymorphous slabs. The regions marked by dashed boxes indicate the surface layers in which the atoms were allowed to relax during structural optimization, while the middle layers were kept fixed to preserve the bulk-like character of the slab. 77

2.5 Atomic model of the symmetric $CsPbBr_3$/$Cs_2PbI_2Cl_2$ interface with CsBr and $PbCl_2$ terminations. The symmetric construction on both sides of the interface avoids artificial dipole interactions. 78

2.6 Schematic planar-averaged and macroscopically averaged electrostatic potentials for the surface slab calculation. The vacuum plateau $V_{\text{slab}}^{\text{vac}}$ and the bulk-like plateau $V_{\text{slab}}^{\text{bulk}}$ are extracted from the slab macroscopic average, while V_{bulk} is obtained from the corresponding bulk calculation. 80
2.7 Schematic planar-averaged and macroscopically averaged electrostatic potentials for the interface calculation. The macroscopic averages on the left and right bulk-like regions give the interface lineup $\Delta V_{\text{int}} = V_R - V_L$. The quantities V_{bulk}^L and V_{bulk}^R are obtained from the separate bulk calculations of the left and right materials. 81

3.1 Monomorphous (a) and polymorphous (b) bulk structures and pair distribution function (PDF) (c) of $CsPbI_3$. 95
3.2 Phonon dispersion of monomorphous and polymorphous configurations of $CsPbI_3$ (a), $CsPbBr_3$ (b), $CsPbCl_3$ (c), $CsSnI_3$ (d), $CsSnBr_3$ (e), and $CsSnCl_3$ (f). M and P denote monomorphous and polymorphous configurations, respectively. 97
3.3 Energy gain of $CsBX_3$ compounds due to positional local disorder (a) and the relatioship between B–X–B angle change and Goldschmidt tolerance factor (b). 98
3.4 Band structures of monomorphous configurations and unfolded spectral functions of polymorphous configurations for $CsPbI_3$ (a), $CsPbBr_3$ (b), $CsPbCl_3$ (c), $CsSnI_3$ (d), $CsSnBr_3$ (e), and $CsSnCl_3$ (f). The color maps show the unfolded spectral functions of the polymorphous configurations, while the black lines show the band structures of the corresponding monomorphous configurations. 100
3.5 Correlation between the disorder-induced band-gap opening and the B–X–B bond-angle change. 101
3.6 Band-gap opening caused by octahedral tilting, B–X bond elongation, and full positional local disorder. 102
3.7 Comparison of the pair distribution functions of monomorphous, polymorphous, bond-length, and B–X–B angle configurations of $CsPbI_3$. 102
3.8 Comparison between experimental band gaps and band gaps calculated using different levels of theory for monomorphous and polymorphous bulk models. Experimental values are taken from Tao *et al.* [22]. 103
3.9 Average in-plane (panel a and c) and out-of-plane (panel b and d) B–X–B angles and B–X bond lengths in each layer of the monomorphous and polymorphous $CsPbI_3$ surface slabs. 105
3.10 Average in-plane B–X–B angles and B–X bond lengths in each layer of the reconstructed monomorphous surface slab. 106
3.11 The color map represents the lowest calculated surface energies, between CsX and BX_2 terminations (X=I,Br,Cl and B=Sn, Pb), [i.e., min(γ_{CsX}, γ_{BX_2})], as a function of B and X chemical potentials. Hatched regions correspond to stability regions of $CsBX_3$ and competing phases. Points A–D correspond to growth conditions: A (X-rich, B-rich), B (X-rich, B-poor), C (X-poor, B-rich), and D (X-poor, B-poor). The red line corresponds to points where the surface energies of CsX and BX_2 terminations are equal. Blue and orange arrows show regions where CsX and BX_2 terminations are stable, respectively. a) $CsPbI_3$, b) $CsPbBr_3$, c) $CsPbCl_3$, d) $CsSnI_3$, e) $CsSnBr_3$, and f) $CsSnCl_3$. 108

3.12 Surface energies of polymorphous and monomorphous surface slabs. (a,b) Surface energies of the CsX- and BX_2-terminated monomorphous (a) and polymorphous (b) $CsBX_2$ surface slabs under two possible growth conditions. (c) The correlation between the difference in surface energies of polymorphous and monomorphous surface slabs and the B–X–B angle at the surface. (d) Surface energies of monomorphous, polymorphous and reconstructed monomorphous $CsPbI_3$ surface slabs. The labels M, R, and P on the x-axis denote monomorphous, reconstructed monomorphous, and polymorphous structures, respectively. Surface energies in panel (d) are calculated under I-rich and Pb-rich growth conditions. 109

3.13 Planar-averaged and macroscopically averaged electrostatic potentials of $CsPbI_3$. **a** Planar-averaged electrostatic potential of monomorphous $CsPbI_3$ bulk and surface slabs with PbI_2 and CsI terminations. **b** Macroscopically averaged electrostatic potential of monomorphous and polymorphous $CsPbI_3$ surface slabs. The vacuum level is set to 0 eV. 111

3.14 Absolute band positions of monomorphous and polymorphous $CsBX_3$ slabs calculated using GGA and GGA+DFT-1/2. 112

3.15 Surface dipole density of monomorphous and polymorphous surface slabs. **a** Dependence of the surface dipole density of PbI_2 and CsI terminations of monomorphous $CsPbI_3$, and their difference, on the scaling factor used for the Gaussian width parameter σ. **b** Correlation between the surface dipole density difference of BX_2 and CsX terminations and the corresponding difference in absolute VBM for monomorphous and polymorphous $CsBX_3$ surface slabs. 113

3.16 Chemical trends in the absolute valence-band maximum (VBM) of Pb- and Sn-based $CsBX_3$ perovskites. The compounds on the x-axis are ordered by increasing halide electronegativity. **a** Absolute VBM computed using the optB86b+SOC. **b** Absolute VBM computed with the DFT-1/2+SOC. Black lines show the experimental VBM trends reported by Tao *et al.* [22]. 115

3.17 Work-function shift, bulk VBM shift, and absolute VBM shift between monomorphous and polymorphous surface slabs for **a** CsX and **b** BX_2 terminations. 117

3.18 Absolute band positions of monomorphous (M), reconstructed monomorphous (R), and polymorphous (P) $CsPbI_3$ surface slabs. 118

3.19 (a) Planar-averaged squared wave function of the CsI-terminated $CsPbI_3$ surface slab. (b) Planar-averaged squared wave function of the PbI_2-terminated $CsPbI_3$ surface slab. Here, E_n–E_{n-5} denote the six highest occupied Kohn-Sham states. 119

4.1 Structures of all-inorganic mixed-halide Ruddlesden–Popper 2D perovskites. **a** $Cs_2PbI_2Cl_2$ ($n = 1$) phase. **b** $Cs_3Pb_2I_3Cl_4$ ($n = 2$) phase. **c** $Cs_4Pb_3I_4Cl_6$ ($n = 3$) phase. **d** General structure of $Cs_{n+1}Pb_nI_{n+1}Cl_{2n}$. Here, n is the number of connected Pb-halide octahedral layers in one perovskite slab. **e** $CsPbICl_2$ 3D reference structure, corresponding to the limit $n \to \infty$. 126

4.2 Pb atom off-centering. **a** relationship between average Pb atom off-centering and octaheral layer thickness. **b,c,d** Structural representation of Pb atom off-centering in n=2 (b), n=3 (c) and n=4 (d) phases. Only a sequence of n octahedra perpedicular to the 2D stacking is shown. 127

4.3 Crystal structure (a) and decomposition energy (b) of Cs_2PbI_4. The considered decomposition reaction paths are: (1) $\mathrm{Cs_2PbI_4 \rightarrow 2CsI + PbI_2}$, (2) $\mathrm{Cs_2PbI_4 \rightarrow CsI + CsPbI_3}$, and (3) $\mathrm{Cs_2PbI_4 \rightarrow \frac{2}{3}CsPbI_3 + \frac{1}{3}Cs_4PbI_6}$. For comparison, the decomposition energy of $CsPbI_3$ through $\mathrm{CsPbI_3 \rightarrow CsI + PbI_2}$ is also shown. 129

4.4 Decomposition energies of the site-ordered and one of halide-disordered $Cs_2PbI_2Cl_2$ configurations. In the site-ordered configuration, I atoms occupy the apical sites and Cl atoms occupy the equatorial sites. In the halide-disordered configuration, I atoms occupy the equatorial sites and Cl atoms occupy the apical sites. A, B, C, and D on the x-axis correspond to the decomposition pathways defined in Eq. 4.2. 130

4.5 Phonon dispersion and structure of monomorphous and polymorphous structures. **a,b** Structures of monomorphous (a) and polymorphous (b) $Cs_3Pb_2I_3Cl_4$ (n=2). On top of each structure, there is topview of marker area. **c** Phonon dispersion of monomorphous configuration of Cs_2PbI_2 (n=1). **d** Phonon dispersion of monomorphous and polymorphous n=2 structure. 131

4.6 Accuracy check of phonon dispersion. **a** Phonon dispersion of n=2 polymorphous configuration calculated with cutoff of 50 Ry and 60 Ry. **b** Relationship between total energy and displacement of atoms along eigenvector of imaginary mode Z(0.0, 0.0, 0.5) 132

4.7 Structural and energetic consequences of local disordering. **a** Dependence of the changes in the Pb–Cl–Pb and Pb–I–Pb bond angles on the octahedral-layer thickness, n. The Pb–Cl–Pb (P) and Pb–I–Pb (P) angle changes arise from positional local disorder in the polymorphous structures, whereas the Pb–Cl–Pb (M) angle change in the $PbCl_2$ layer immediately adjacent to the CsI spacer originates from Pb off-centering in the monomorphous structures. P and M denote polymorphous and monomorphous structures, respectively. **b** Correlation between the energy gain and the average B-X-B angle change. The average B-X-B angle change is calculated as the average of the Pb-Cl-Pb and Pb-I-Pb angle changes. 134

4.8 Dependence of the decomposition enthalpy of monomorphous and polymorphous configurations on the octahedral layer thickness, n, of $\mathrm{Cs_{n+1}Pb_nI_{n+1}Cl_{2n}}$. Red full (blue dashed) horizontal line indicate the decomposition entahlpies of the monomophous (polymorphous) 3D reference structures, $CsPbICl_2$. 136

4.9 Band structure of 2D perovskites with octahedral layer thicknesses of $n = 1$ (a), $n = 2$ (b), and $n \rightarrow \infty$ (c). In panels (b) and (c), the colormap represents the polymorphous spectral function, while the red curves represent the monomorphous band structures. (d) Band gap evolution of the monomorphous and polymorphous configurations as a function of the octahedral layer thickness n. In the band structures, the VBM is aligned to 0 eV. For the comparison between monomorphous and polymorphous configurations, the VBM of the monomorphous structure is aligned to 0 eV. 138

4.10 Bonding scheme of $Cs_2PbI_2Cl_2$, adapted from Ref. [11]. 139

4.11 Band gap opening due to positional local disorder. **a** Contributions of equatorial (Pb–Cl–Pb) and apical (Pb–I–Pb) angle changes to the band gap opening induced by positional local disorder. **b** Relationship between the band gap opening and the in-plane Pb–Cl–Pb angle change. 140

4.12 Effective masses of 2D perovskites. **a** In-plane electron and hole effective masses calculated for the monomorphous and polymorphous configurations as a function of the octahedral layer thickness n. **b** Enhancement factors λ_e and λ_h for the electron and hole effective masses induced by positional local disorder. 142

4.13 Surface slab models of 2D perovskites. **a,b** Symmetric slab models of monomorphous (a) and polymorphous (b) $Cs_3Pb_2I_3Cl_4$ ($n = 2$). **c–e** CsI (c), double-CsI (d), and $PbCl_2$ (e) terminations of $Cs_2PbI_2Cl_2$ ($n = 1$). These slabs have the (001) orientation, normal to the stacking direction of the 2D perovskite. **f** Lateral surface slab with the (100) orientation, perpendicular to the stacking direction. 144

4.14 Phase diagram of the $n = 1$ 2D perovskite $Cs_2PbI_2Cl_2$. **a** Three-dimensional chemical-potential stability region as a function of $\Delta\mu_{\mathrm{Pb}}$, $\Delta\mu_{\mathrm{Cl}}$, and $\Delta\mu_{\mathrm{I}}$. Only the stability region of the $n = 1$ compound is shown. **b** Two-dimensional slice of the phase diagram under Pb-rich conditions, $\Delta\mu_{\mathrm{Pb}} = 0$, shown as a function of $\Delta\mu_{\mathrm{Cl}}$ and $\Delta\mu_{\mathrm{I}}$. The points A, B, and C mark representative limits of the stability region. 146

4.15 Surface energy of the $n = 1$ **(a)** and $n = 2$ **(b)** structures as a function of the Cl chemical potential. The background color maps show the stability regions of the 2D perovskites and the competing 3D phases. 146

4.16 Surface energy as a function of octahedral layer thickness n. The points A and C correspond to the Pb-rich growth conditions marked in Fig. 4.14b: A is Cl-poor and I-poor, while C is Cl-rich and I-poor. Because the surface energies of the CsI termination are identical at points A and C, they are represented by a single red curve. 147

4.17 **a** Planar-averaged electrostatic potentials of the $n = 1$ d-CsI-terminated surface slab and the bulk reference. **b** Ionisation potentials of the $n = 1$ surface slabs with $PbCl_2$, CsI, d-CsI, and lateral terminations, calculated using GGA and DFT-1/2. The black dashed line shows the experimental value reported by Liu *et al.* [37]. 148

4.18 Ionisation potentials of the 2D perovskites calculated using GGA and DFT-1/2 as a function of the octahedral layer thickness n. The dashed blue and red lines show the GGA ionisation potentials of the $n \to \infty$ surface slabs with $PbCl_2$ and CsI terminations, respectively. The dotted lines show the corresponding DFT-1/2 results. 150

4.19 **a** Electrostatic potentials of the monomorphous and polymorphous $n = 2$ structures with $PbCl_2$ termination. **b** Ionisation potentials of the monomorphous and polymorphous $n = 2$ structures with $PbCl_2$, CsI, and d-CsI terminations, calculated using DFT-1/2. 150

4.20 $CsPbBr_3/Cs_2PbI_2Cl_2$ interface terminations: a) CsBr/CsI, b) CsBr/d-CsI, c) CsBr/$PbCl_2$, d) $PbBr_2$/CsI, e) $PbBr_2$/d-CsI, and f) $PbBr_2/PbCl_2$. 152

4.21 The relationship between adhesion energy, E_{adh}, of $CsPbBr_3/Cs_2PbI_2Cl_2$ interfaces with different terminations and optimized interface distance. 153

4.22 Comparison of the band offsets of the CsBr/$PbCl_2$ and $PbBr_2$/CsI interfaces calculated using GGA and DFT-1/2. The blue bars represent $CsPbBr_3$, and the red bars represent $Cs_2PbI_2Cl_2$. 154
4.23 Band offsets of the $CsPbBr_3$/$Cs_2PbI_2Cl_2$ interfaces calculated using DFT-1/2 with the three-step strain correction. The experimental value is taken from Ref. [52]. 154

A.1 Calculated band gaps of the monomorphous and polymorphous configurations as a function of experimental band gap. Results are shown for the optB86b, PBE, and PBEsol exchange–correlation functionals. All calculations were performed at the fixed optB86b-vdW optimized geometries with SOC included. 170
A.2 Absolute VBM positions of the (a) monomorphous and (b) polymorphous configurations calculated using the optB86b, PBE, and PBEsol exchange–correlation functionals. The calculations were performed at the fixed optB86b-vdW optimized geometries with SOC included. The CsX and BX_2 labels denote the two surface terminations or alignment references used in the calculations. Blue points are not always visible because of overlapping with the greeen ones. 171

B.1 Relationship between the polymorphous energy gain and the average B–X–B bond-angle deviation, $\langle \Delta\theta_{\mathrm{BXB}} \rangle$, calculated using fixed lattice constants and volume-relaxed lattice constants. The nearly overlapping trends indicate that volume relaxation does not alter the correlation between structural distortion and energy stabilization. 174

C.1 Projected density of states of the $n = 1$ and $n = 2$ $Cs_{n+1}Pb_nI_{n+1}Cl_{2n}$ 2D perovskites. The zero of energy is set to the VBM. The upper valence band is mainly composed of I-$5p$ states with minor Cl-$3p$ and Pb-$6s$ contributions, while the lower conduction band is dominated by Pb-$6p$ states. 175

D.1 Phonon dispersion of monomorphous and polymorphous $CsPbICl_2$ ($n \to \infty$). Imaginary phonon modes in the monomorphous structure indicate the dynamical instability of the high-symmetry phase, while their suppression in the polymorphous structure indicates stabilization by local positional disorder. 176

E.1 Effect of biaxial strain on $Cs_2PbI_2Cl_2$. **a** Strain energy relative to the unstrained structure. **b** Strain-induced changes in the bulk VBM, CBM, and band gap relative to the unstrained bulk structure. Negative and positive strain values correspond to compressive and tensile strain, respectively. 177
E.2 Relative change in the out-of-plane c lattice parameter as a function of the applied in-plane biaxial strain. 178

List of Tables

2.1 Optimized cutoff radii r_{cut} (a.u.) used in the DFT-1/2 correction for the relevant atomic orbitals in the $CsBX_3$ compounds. 71

3.1 Optimized and experimental lattice constants of $CsBX_3$ perovskites. 94
3.2 High-frequency dielectric constant ε_∞, static dielectric constant ε_s, and element-averaged Born effective charges Z^* for monomorphous and polymorphous structures of inorganic halide perovskites. 96
3.3 Structural parameters of the surface layers of the monomorphous and polymorphous slabs. B–X_{in} and B–X_{out} denote the in-plane and out-of-plane bond lengths between the B-site atom and the halogen atom, respectively. BXB_{in} and BXB_{out} denote the in-plane and out-of-plane B–X–B bond angles. B–B_{out} is the out-of-plane B–B distance. dB_{in} and dB_{out} are the in-plane and out-of-plane off-centering displacements of the B-site atom. 107

4.1 Calculated lattice constants of $Cs_{n+1}Pb_nI_{n+1}Cl_{2n}$ structures. Experimental values are taken from Ref. [1] for $n = 1$ and Ref. [3] for $n = 2$. 125
4.2 Adhesion energy and optimized distance between the 3D $CsPbBr_3$ and 2D $Cs_2PbI_2Cl_2$ regions for different interface terminations. 152
4.3 Calculated valence band offsets for different models of the $CsPbBr_3/Cs_2PbI_2Cl_2$ interface. The experimental value is taken from Ref. [52]. 155

A.1 Difference between optB86b-vdW and optB86b electronic calculations performed without SOC at the same optB86b-vdW optimized geometries. The values quantify the electronic contribution of the nonlocal vdW term, independent of structural relaxation effects. Here, $\Delta E_g = E_g^{\text{optB86b-vdW}} - E_g^{\text{optB86b}}$ and $\Delta E_{\mathrm{VBM}} = E_{\mathrm{VBM}}^{\text{optB86b-vdW}} - E_{\mathrm{VBM}}^{\text{optB86b}}$ 170

B.1 Relative volume change and additional energy gain of 3D perovskites due to volume relaxation. 173
B.2 Relative changes in volume, lattice parameters, and additional energy gain of polymorphous $n > 1$ 2D perovskites due to volume relaxation. 173

Chapter 1

Introduction: Halide Perovskite Solar Cells, Theoretical Understanding, and Research Challenges

> I would put my money on the sun and solar energy. What a source of power! I hope we don't have to wait until oil and coal run out before we tackle that.
>
> Thomas Edison

In this introduction chapter, we first discuss the growing global energy demand and the environmental problems caused by fossil fuels, which increase the need for renewable energy sources, especially solar energy. We then explain why halide perovskites have become very promising materials for solar cells. Since perovskite solar cells still face important stability problems before commercialization, we also review the main challenges that limit their long-term use, including the instability of 3D perovskites and the possible benefits of 2D perovskites for improving stability and performance. We place special focus on surfaces and interfaces, particularly the interface between the perovskite layer and the charge transport layers, because these have a strong effect on device performance and stability. In addition, we review the theoretical methods used to study the bulk, surface, and interface properties of halide perovskites. Because these materials are soft and anharmonic, their theoretical study requires careful computational approaches. Finally, we present the main open questions addressed in this thesis.

1.1 Global energy challenge and motivation for photovoltaics

1.1.1 Rising energy demand and the environmental cost of fossil fuels

Global energy use continues to rise, showing that world demand is still increasing faster than the transition away from fossil fuels. According to the International Energy Agency (IEA), global electricity demand grew by 3.0% in 2025, after increasing by 4.4% in 2024 [1]. The IEA also projects that global electricity consumption will rise from 28 200 TWh in 2025 to 33 600 TWh by 2030, an increase of about 5 400 TWh in only five years [1].

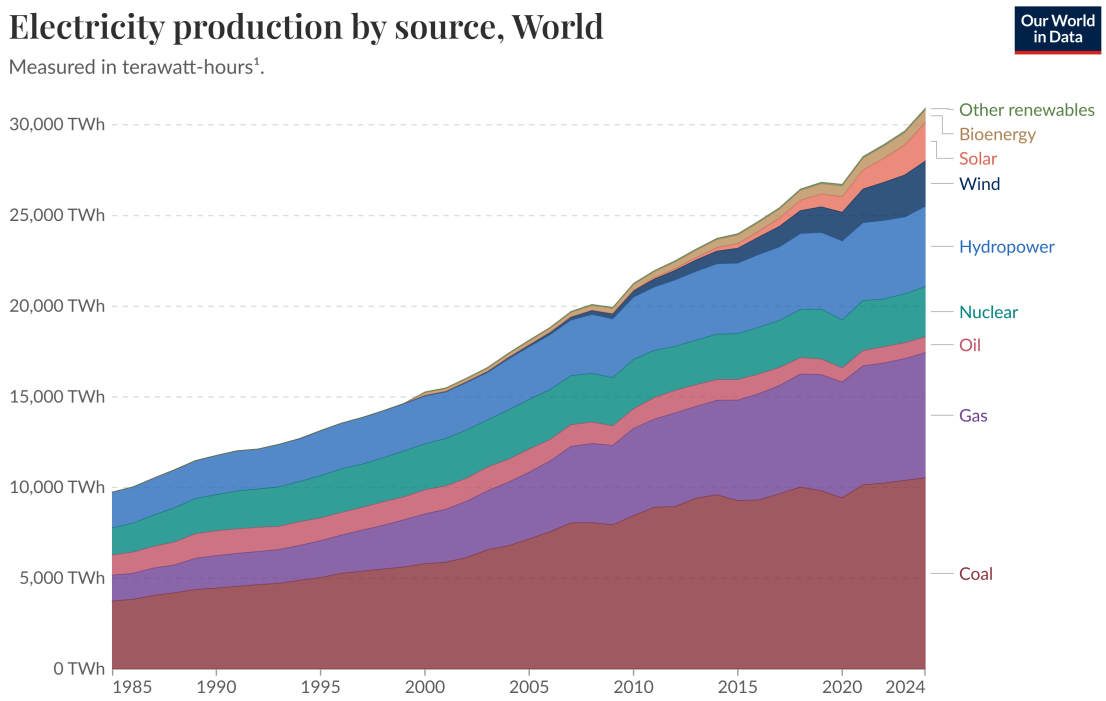

Figure 1.1: Global electricity production by source, measured in terawatt-hours (TWh). Coal remains the largest source of electricity worldwide, followed by gas, while renewable energy sources such as wind and solar have grown rapidly in recent years. Source: Our World in Data, based on Ember (2026) and Energy Institute (2025) [2].

The buildings sector is expected to be the largest contributor to this growth, accounting for 49% of additional global electricity demand between 2025 and 2030, mainly because of increasing use of air conditioning, heat pumps, and digital technologies such as data centres [1]. Industry will remain another important driver as more production processes become electrified [1]. Transport is also expected to play a growing role, with its share of electricity-demand growth rising to more than 10% by 2030, largely because of

the rapid expansion of electric vehicles (EVs) [1]. In the IEA Stated Policies Scenario, electricity use by EVs is projected to increase from about 180 TWh in 2024 to 780 TWh in 2030 [3]. Another important emerging driver is the rapid expansion of data centres. The IEA estimates that global data-centre electricity consumption will more than double to around 945 TWh by 2030, growing at about 15% per year and reaching just under 3% of total global electricity demand [4].

At the same time, much of global energy demand is still met by fossil fuels, especially coal and gas. As shown in Figure 1.1, global electricity production has increased strongly over time, but a large part of this growth has continued to rely on fossil-fuel sources, although wind and solar have expanded rapidly in recent years [2]. Fossil fuels also remain the dominant source of carbon emissions. The Global Carbon Budget 2025 projects that fossil CO_2 emissions reached 38.1 billion tonnes in 2025, which is 1.1% higher than in 2024 [5]. Coal, oil, and natural gas therefore remain closely linked to climate change and air pollution. Reducing dependence on fossil fuels while meeting rising energy demand is thus one of the major technological challenges of the present century.

1.1.2 Need for efficient, stable, and low-cost photovoltaic materials

Renewable energy is widely regarded as a long-term solution to rising energy demand because it can provide electricity with much lower greenhouse-gas emissions than fossil fuels while also improving energy security and long-term affordability. According to the IEA, renewables accounted for 32% of global electricity generation in 2024, and this share is projected to increase to 43% by 2030 [6]. The same report states that renewables are expected to provide more than 90% of the growth in global electricity demand between 2025 and 2030, showing that they are becoming the main source of new electricity supply worldwide [6]. In addition, the International Renewable Energy Agency (IRENA) reports that 92.5% of all new power capacity added in 2024 was renewable, and that the renewable share of total installed power capacity rose to 46.4% [7]. Renewable technologies are also becoming increasingly competitive in economic terms: IRENA reports that 91% of newly commissioned utility-scale renewable power projects in 2024 produced electricity at a lower cost than the cheapest new fossil-fuel alternative [8].

Among renewable technologies, photovoltaics are particularly attractive because solar energy is abundant, widely distributed, and directly convertible into electricity. Solar photovoltaic generation has increased rapidly in recent years compared with other renewable energy sources, especially wind and hydropower [2]. This rapid growth is mainly driven by continuous technological improvements, falling costs, and strong global investment in solar-energy systems. Government incentives, such as tax credits, subsidies, and policies allowing solar prosumers to sell excess electricity to the grid, have also encouraged wider adoption of solar energy in Europe [9]. As a result, solar power has become one of the fastest-growing sources of electricity worldwide and is expected to play a key role in future energy systems.

The continued expansion of photovoltaic deployment, however, depends not only on high conversion efficiency, but also on long-term stability, scalable processing, and low manufacturing cost. At present, silicon solar cells account for nearly 92% of the global PV market [10]. This dominant position is mainly due to the abundance of silicon and, historically, to the strong technological and industrial base already established by the microelectronics industry. In the early development of photovoltaics, silicon PV benefited from the availability of high-purity silicon, wafer-processing techniques, and manufacturing know-how developed for microelectronic devices. However, the production of high-quality crystalline silicon for solar cells requires advanced processing, high energy input, and expensive manufacturing steps.

From a physical point of view, silicon also has some important limitations. Silicon is an indirect-band-gap semiconductor with a band gap of about 1.12 eV. Because of its indirect band gap, its absorption coefficient near the band edge is relatively low, which means that thicker absorber layers are required to absorb sunlight efficiently [11]. For this reason, silicon solar cells are usually based on wafers with thicknesses on the order of 130–180 μm [12]. The need for relatively thick wafers increases material consumption and contributes to the overall cost of the device. In addition, the performance of single-junction solar cells is fundamentally limited by the Shockley-Queisser limit, which can be derived using detailed-balance theory [13]. In practice, the efficiencies of real silicon solar cells are further reduced by optical, electrical, and resistive losses. Another limitation of conventional crystalline silicon is its mechanical rigidity. Since silicon wafers are brittle, they are not well suited to flexible or curved surfaces, although recent progress in ultrathin silicon structures has partly mitigated this issue [14].

These limitations have motivated intensive research into alternative photovoltaic materials and device structures that can offer high efficiency, low production cost, mechanical flexibility, and long-term stability. Based on their development history and operating concepts, solar cells are commonly divided into three generations [15]. First-generation solar cells are mainly based on crystalline silicon and dominate the commercial market because of their high efficiency, long lifetime, and proven reliability. Second-generation solar cells are thin-film technologies such as amorphous silicon, CdTe, and CIGS ($CuIn_xGa_{1-x}Se_2$), which reduce material consumption and can be lighter and more flexible than silicon. Third-generation solar cells include emerging photovoltaic technologies such as dye-sensitized solar cells, organic solar cells, perovskite solar cells, and quantum-dot solar cells, which aim to overcome the limitations of conventional single-junction devices through tunable optical properties, lower-cost processing, or compatibility with flexible and semi-transparent applications [15].

The certified record efficiencies of representative photovoltaic technologies are shown in Figure 1.2. For example, record efficiencies of 27.9% for single-crystal silicon, 23.6% for CIGS, 23.1% for CdTe, and 27.3% for single-junction perovskite solar cells are reported [16]. These results show that, although remarkable progress has been achieved, the search for improved photovoltaic materials remains necessary. In particular, materials with strong light absorption, suitable band gaps, good stability, scalable processing,

and low cost are essential for the future development of solar-cell technologies. A key objective is also to identify materials that can be combined with existing photovoltaic technologies, especially silicon, to fabricate low-cost tandem solar cells capable of surpassing the Shockley–Queisser limit [13] of single-junction devices.

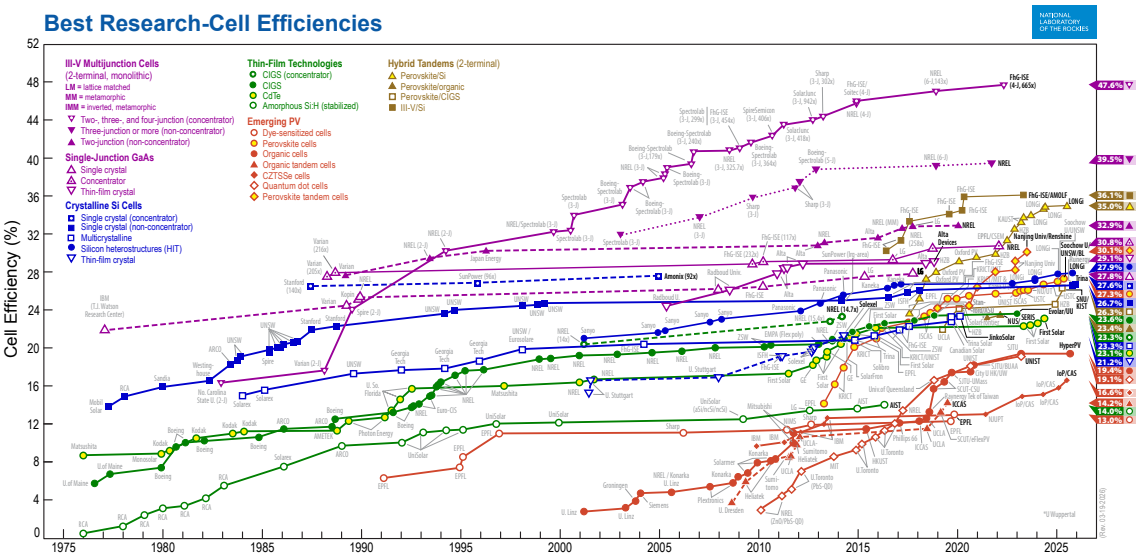

Figure 1.2: Best research-cell efficiency chart reported by NREL [16].

1.2 Halide perovskites as promising photovoltaic materials

1.2.1 Perovskite structure

Perovskites are a class of materials with the general chemical formula ABX_3, where A and B are cations and X is an anion. In the ideal three-dimensional perovskite crystal structure, the smaller B cation is located at the centre of an octahedron formed by six X anions, creating a network of corner-sharing BX_6 octahedra. The larger A cation occupies the cavity between these octahedra and helps stabilize the overall structure. For example, in $CsPbI_3$, shown in Figure 1.3, Cs is the A-site cation, Pb is the B-site cation, and I is the X-site anion.

For perovskite optoelectronic materials, especially those used in solar cells, the A site is commonly occupied by monovalent cations such as cesium (Cs^+), methylammonium (MA^+, $CH_3NH_3^+$), or formamidinium (FA^+, $HC(NH_2)_2^+$). The B site is most often occupied by lead (Pb^{2+}) as many lead-halide perovskites have favorable optoelectronic properties, although tin (Sn^{2+}) is also studied as a lead-reduced or lead-free alternative. The X site usually consists of halide anions such as iodide (I^-), bromide (Br^-), and chloride (Cl^-). Per-

ovskites can be classified as inorganic or hybrid, depending on whether the A-site cation is inorganic or an organic molecular ion.

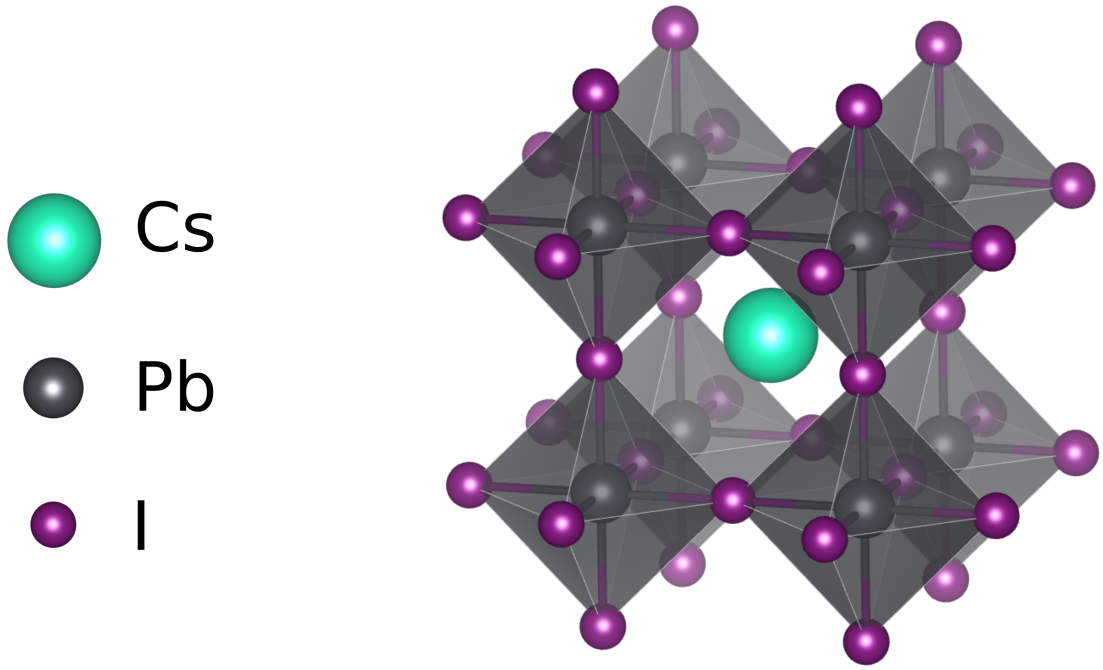

Figure 1.3: Structure of $CsPbI_3$.

Halide perovskites can adopt several structural phases, and $CsPbI_3$, shown in Figure 1.4, is a useful reference system for describing them. At room temperature, $CsPbI_3$ most commonly appears in the yellow δ phase, which is a non-perovskite orthorhombic structure and is not the desired light-absorbing form for optoelectronic devices [17, 18, 19, 20]. In contrast, the photoactive black phases belong to the perovskite family and are commonly described as α-$CsPbI_3$ (cubic), β-$CsPbI_3$ (tetragonal), and γ-$CsPbI_3$ (orthorhombic) [19, 20, 21, 17]. A range of phase-transition temperatures has been reported in the literature, depending on sample preparation, heating or cooling rate, and measurement method [17, 22, 19, 20]. Upon heating, the yellow δ phase transforms into black α-$CsPbI_3$ at about 310–$350\,^{\circ}\mathrm{C}$ [19, 23, 17]. During cooling, the black perovskite phase then undergoes successive transitions from α to β at about 200–$281\,^{\circ}\mathrm{C}$ and from β to γ at about 100–$184\,^{\circ}\mathrm{C}$ [19, 22, 20]. Although these black phases have much better optical properties than the yellow phase, they are metastable under ambient conditions and tend to revert to the yellow δ phase, especially in the presence of moisture [22, 18, 23].

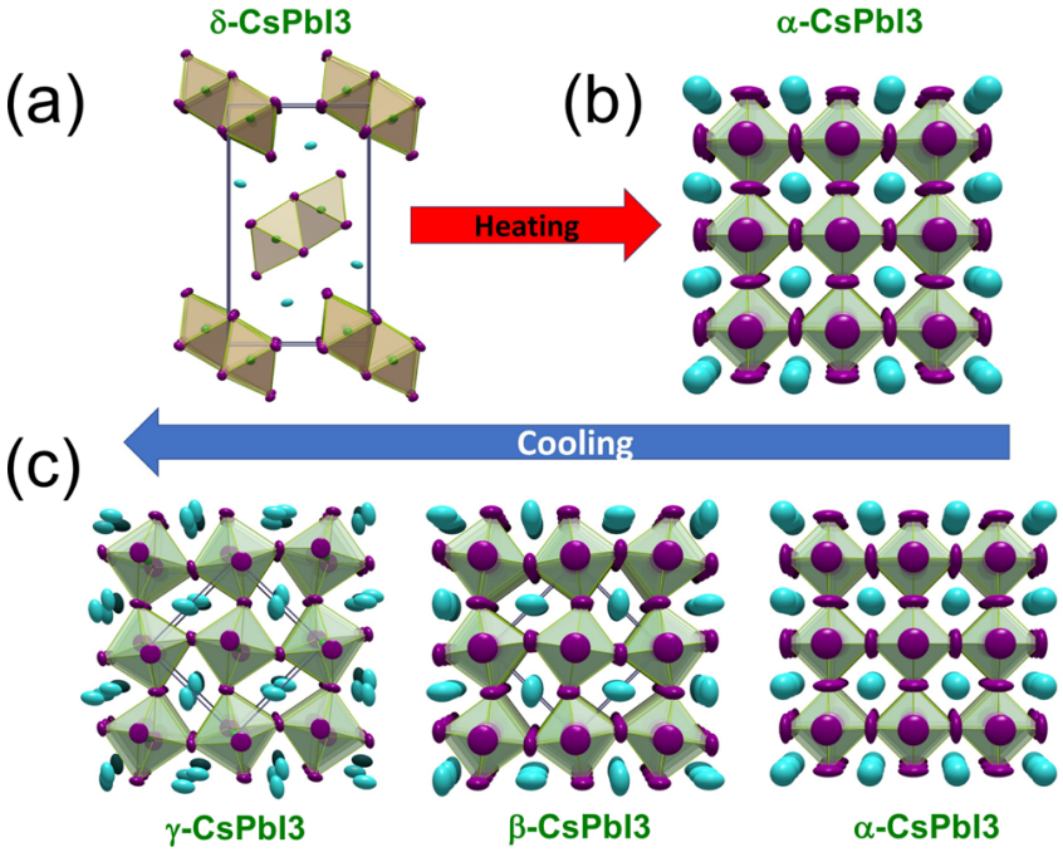

Figure 1.4: Schematic illustration of the structural phases of $CsPbI_3$ (α, β, γ, and δ). Adapted from Ref. [20].

1.2.2 Emergence and rapid development of perovskite solar cells

Perovskite solar cells were first reported by the Miyasaka group in 2009 [24]. In that work, methylammonium lead iodide ($CH_3NH_3PbI_3$ or MAPI) was used as the light-absorbing material in a dye-sensitized solar cell with a liquid electrolyte, achieving a power-conversion efficiency of 3.8%. In 2012, the transition from liquid-junction perovskite-sensitized cells to solid-state perovskite photovoltaic devices was marked by several important reports. Chung et al. demonstrated all-solid-state dye-sensitized cells using $CsSnI_3$ as a solid-state component, while Park et al. reported MAPI-sensitized mesoscopic cells with the solid hole-transport material spiro-MeOTAD, reaching a power conversion efficiency of 9.7% [25, 26]. In the same period, Lee et al. introduced meso-superstructured organometal halide perovskite solar cells with efficiencies of 10.9%, and Etgar et al. demonstrated hole-transport layer (HTL) free MAPI/TiO_2 heterojunction cells, in which MAPI acted both as light absorber and HTL [27, 28]. These studies collectively established solid-state perovskite photovoltaics as a rapidly developing technology. Following this breakthrough period, perovskite materials were rapidly extended to other optoelectronic devices [29], including light-emitting diodes [30], photodetectors [31], and lasers [32]. Within 12 years, the efficiency of perovskite solar cells increased from about 10% to 27.3%, making them one of the fastest-developing solar-cell technologies in history (see Fig. 1.2).

1.2.3 Optoelectronic properties that make halide perovskites attractive

One of the major reasons for the strong interest in hybrid organic–inorganic halide perovskites is their compatibility with relatively low-temperature, solution-based processing. Hybrid halide perovskites can be deposited from solution at comparatively low temperatures, which avoids the high-vacuum and often high-temperature processing required for many conventional photovoltaic technologies and therefore offers a route toward simpler, potentially lower-cost manufacturing [33]. This processing route is also compatible with scalable deposition methods such as blade coating, slot-die coating, and roll-to-roll manufacturing, which is why perovskites are considered promising for large-area production [34]. In addition, low-temperature solution processing has enabled flexible perovskite solar cells, making these materials especially attractive for lightweight and flexible photovoltaic technologies [35].

One of the most important advantages of halide perovskites is that their band gap can be readily tuned by mixing or substituting the halides, B-site atoms, and A-site cations. For example, halide mixing in $MAPb(I,Br)_3$ tunes the band gap from about 1.55 eV for $MAPbI_3$ to about 2.30 eV for $MAPbBr_3$ [36]; B-site mixing in $MASn_xPb_{1-x}I_3$ lowers it from about 1.55 eV to a minimum near 1.17 eV at intermediate Sn/Pb compositions [37]; and A-site substitution from MA to FA shifts it from about 1.55–1.57 eV for $MAPbI_3$ to about 1.48 eV for $FAPbI_3$ [38]. Band-gap engineering through compositional mixing in halide per-

ovskites was first explored theoretically by Castelli *et al.* [39] using first-principles calculations, which showed that variation of the A-, B-, and X-site species systematically tunes the electronic structure and can yield band gaps spanning from 0.5 eV to 5 eV. Knutson *et al.* [40] further showed that band-gap tuning in metal-halide perovskites is strongly correlated with the metal–halide–metal bond angle, such that steric control of the A-site cation modifies octahedral tilting and thereby tunes the optical gap.

The tunable band gap of halide perovskites is a major advantage for tandem photovoltaics, where the top and bottom subcells must have appropriately matched band gaps to utilize the solar spectrum efficiently. As a result, perovskites have been widely adopted as the top absorber in perovskite/silicon tandem solar cells, and a two-terminal crystalline silicon–perovskite tandem cell developed by LONGi reached a certified efficiency of 34.85% in 2025 [41] (see Figure 1.2).

The defect tolerance of halide perovskites contributes [42, 43, 44] to superior solar-cell performance by reducing non-radiative recombination losses, thereby helping to sustain high open-circuit voltage, long carrier lifetimes and diffusion lengths, and efficient photovoltaic operation despite structural imperfections. This behaviour arises in part from their antibonding band-edge electronic structure, which often favours the formation of shallow defect states rather than deep traps that would strongly promote non-radiative recombination [42]. This effect is further enhanced by the high dielectric constant and soft, deformable lattice, which screen charge–defect interactions and allow structural relaxation around defects, thereby reducing their electronic activity [45]. More recently, De Angelis and co-workers showed that defect tolerance is also related to the dynamic chemical nature of halide defects, particularly iodine, for which redox processes and structural reconfigurations can passivate or deactivate recombination centres even when defects are not strictly shallow [46]. In addition, Zhang *et al.* [47] found that all-inorganic halide perovskites suffer less from non-radiative recombination than their hybrid counterparts, making them attractive for photovoltaic applications despite material-specific limitations such as the relatively wide band gap and phase instability.

The high absorption coefficient of halide perovskites allows most incident light to be absorbed within a thin layer, thereby reducing material use and enabling material-efficient solar-cell fabrication [48]. At the same time, strong absorption supports high short-circuit current density, and the thin absorber shortens carrier-transport pathways. Since the diffusion length in efficient perovskites can exceed the absorption depth, photogenerated carriers are more likely to be extracted before recombination occurs [44]. The high absorption coefficient of halide perovskites originates from their favourable electronic band structure, in particular their direct band gap and strong optical transitions near the band edge. These materials exhibit large transition dipole moments because of significant orbital overlap between metal and halide states, which leads to a high probability of photon absorption and efficient generation of charge carriers [49]. In addition, the joint density of states near the band edges and the dispersive nature of the bands further enhance light absorption across the visible spectrum [50]. Halide perovskites also exhibit high dielectric permittivity and therefore relatively small exciton binding energies

[51, 52], which favours electron–hole separation at room temperature.

Despite these exceptional advantages, the practical use of halide perovskites in solar cells remains limited by insufficient stability under realistic operating conditions. As a result, understanding the microscopic origins of degradation and identifying strategies to suppress them have become central research directions in the field.

1.3 Stability challenges in halide perovskite solar cells

1.3.1 Instability of 3D halide perovskites

Although perovskite materials possess excellent properties that make them among the most promising candidates for optoelectronic applications, their instability under real operating conditions remains a major challenge that limits large-scale deployment. One of the main reasons for the instability of 3D halide perovskites is that they are soft and highly ionic crystals rather than rigid covalent semiconductors [53]. Because of this soft lattice, defects can form relatively easily, and ions, especially halide ions, can migrate through the crystal with fairly low energy barriers [54, 55]. Ion migration is now widely accepted as a key origin of electrical drift, hysteresis, and long-term operational instability in perovskite solar cells [54, 56]. De Angelis *et al.* reported that iodine-related defects, especially iodine interstitials and Frenkel defects, have lower formation energies at perovskite surfaces and interfaces than in the bulk, which makes defect formation and ion migration more favourable in these regions [57].

A second major reason is the strong sensitivity of halide perovskites to the environment. Moisture can enter the film, interact with the lattice, and promote hydrated intermediate phases and eventual decomposition, especially in iodide-based hybrid perovskites [58]. Oxygen under illumination is particularly harmful because light can drive the formation of reactive superoxide species, and theoretical calculations have shown that iodide vacancies are favourable sites for this reaction [59]. Heat also accelerates degradation by breaking down the perovskite into simpler compounds such as PbI_2 and volatile species; this has been clearly observed for $MAPbI_3$, including decomposition near 85 °C even under inert conditions [60, 61].

Another important source of instability is structural instability. In several high-performance iodide perovskites, the desired black photoactive phase is not always the most stable phase at room temperature. For example, $FAPbI_3$ and $CsPbI_3$ can transform into non-photoactive yellow phases, which greatly reduces device performance [62]. This behaviour can be understood from structural arguments such as the tolerance factor, which relates the size mismatch of the A, B, and X ions to the stability of the 3D perovskite framework [62]. In mixed-halide perovskites, light-induced halide segregation can also occur, where illumination drives the material to separate into iodide-rich and bromide-rich regions. Thermodynamic theory explains this behaviour by showing that

photogenerated carriers lower their energy in iodide-rich domains, thereby creating a driving force for demixing [63]. Therefore, the instability of 3D halide perovskites is best understood as a combination of intrinsic structural softness, ion migration, chemical reactivity, and structural instability.

1.3.2 Role of 2D perovskites in improving stability

To overcome the instability of halide perovskites, researchers have developed several strategies. These include compositional engineering to stabilize the crystal phase [64], defect and interface passivation to reduce trap formation and ion migration, and device-level approaches such as stable contact layers and encapsulation to protect the material from heat, moisture, and oxygen [65]. Among these approaches, the use of 2D perovskites has emerged as an effective way to improve both device stability and performance.

Two-dimensional perovskites are commonly classified into two main types according to the spacer layer: Ruddlesden–Popper (RP) and Dion–Jacobson (DJ) structures (see Figure 1.5). Their properties can be tuned by changing the number of connected metal-halide octahedral layers, usually denoted by n [66, 67]. An $n = 1$ structure is generally called a 2D perovskite, while almost pure phase with a higher n value have been also obtained. When processing thin-films of 2D perovskites, a distribution of phases is often obtained and an average <n> can be defined. Such mixed phases are sometimes quoted as quasi-2D perovskites. In most cases, the spacer is an organic molecule, and these materials are known as hybrid 2D perovskites [68]. However, layered perovskites can also be formed with inorganic ions such as Cs, leading to all-inorganic 2D perovskites [69].

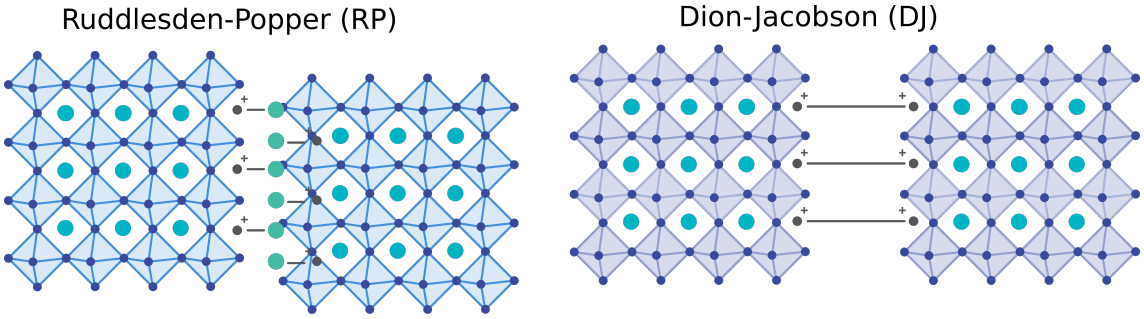

Figure 1.5: Schematic structure of Ruddlesden–Popper and Dion–Jacobson 2D perovskites [70].

Compared with their 3D counterparts, 2D perovskites generally show better environmental and structural stability [71, 72]. However, they are often less suitable as the sole absorber layer in solar cells because they usually have wider band gaps, less favourable charge-transport properties [73] and require vertical orientation as well as exciton dissociation centers [74]. In contrast, 3D perovskites are excellent light absorbers but suffer from instability during operation. For this reason, combining 2D and 3D perovskites has become an important strategy for building solar cells that are both efficient and stable.

One common approach is to use a 2D perovskite as an ultrathin layer on top of a 3D perovskite absorber [75]. This 2D/3D heterostructure can improve surface quality, reduce defect density, and enhance device durability. For example, a reported device with a 2D perovskite interfacial layer reached a power-conversion efficiency of 26.31% and retained 95% of its initial efficiency after 1000 hours [76]. Another approach is to intermix 2D and 3D perovskite phases. This can also improve stability while maintaining strong photovoltaic performance, as shown by Shao *et al.*, who reported stable 2D perovskite solar cells with efficiencies of around 21% [77]. Intermixing 2D and 3D perovskite phases led recently to the stabilization of pure $FAPbI_3$ 3D solar cells, thus avoiding instabilities related to alloying and leading to an optical band gap closer to the optimum for single junction solar cells (<1.5eV) [78, 79]. Using thick 2D and 3D bilayers is a last alternative that can be combined with the above approaches and was demonstrated thanks to solvent management in 2022 [80]. All these recent strategies often rely on pure phases with a n value greater than 1.

Two-dimensional perovskites generally show poor charge-carrier transport in the out-of-plane direction. Therefore, when they are used as a capping layer on 3D perovskites, the 2D layer is usually kept very thin so that it does not block charge extraction and reduce solar-cell performance. This limitation is closely related to the layered structure of 2D perovskites, which often does not favour carrier transport toward the electrodes. An alternative strategy is to grow the 2D perovskite with a vertical orientation rather than in the conventional horizontal arrangement [81]. Because 2D perovskites exhibit much better charge transport in the in-plane direction, such vertical alignment can facilitate charge extraction from the 3D perovskite. Moreover, the vertical growth of 2D perovskites opens the possibility of using them directly in solar cells. For example, Tsai *et al.* reported a 2D perovskite solar cell with a vertically aligned structure and a power-conversion efficiency of 12.52% [71]. In such a structure, the orientation of the inorganic layers allows photogenerated electrons and holes to move more effectively toward the contacts, thereby improving charge collection.

The main reason why 2D perovskites improve the stability of 3D perovskite solar cells is that they protect the most vulnerable regions of the 3D film, especially the surface and grain boundaries [76]. These regions usually contain more defects and are more easily damaged by moisture, oxygen, heat, and light. A thin 2D perovskite layer formed on the surface of a 3D perovskite absorber, or at the interface between the absorber and a charge transport layer, can act as a protective barrier by limiting the ingress of water and oxygen. This effect is particularly strong in many hybrid 2D perovskites because their large organic spacer molecules make the surface more water resistant [82].

At the same time, the 2D layer can passivate surface defects by interacting with undercoordinated ions and other defect sites [83]. This reduces non-radiative recombination and lowers chemical reactivity at the surface. It can also slow ion migration within the perovskite layer [83], which is important because ion movement is closely related to phase instability and long-term degradation during operation. In addition, the 2D layer can create a more stable interfaces between the perovskite and the charge-transport layers, which helps suppress harmful interfacial reactions and improves structural stability

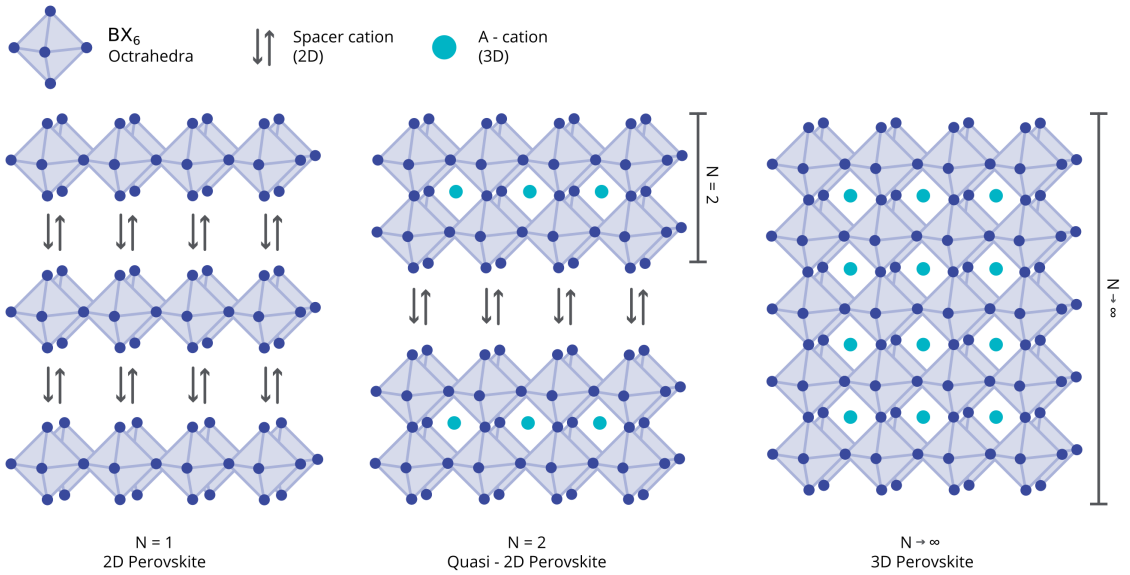

Figure 1.6: Schematic structure of 2D, quasi-2D, and 3D perovskites [70].

[84]. Therefore, 2D perovskites do more than simply cover the 3D absorber; they can improve chemical stability and reduce interfacial recombination, leading to better long-term solar-cell performance.

Although halide perovskites combine excellent optoelectronic properties with promising strategies for improving stability, many of the key mechanisms governing their behaviour originate at the atomic scale. In particular, local structural disorder, anharmonic lattice motion, ionic migration, surface termination, and interface formation strongly affect electronic structure, degradation pathways, and charge extraction. A predictive understanding of these materials therefore requires first-principles methods that go beyond idealized static bulk crystal models.

1.4 Theoretical description of halide perovskites

1.4.1 Electronic structure and optical properties of 3D halide perovskites

Even *et al.* provided one of the earliest clear theoretical explanations of the unusual electronic properties of hybrid lead-halide perovskites by showing that their band structure is strongly governed by spin–orbit coupling (SOC) [85]. They demonstrated that SOC mainly affects the Pb-derived conduction band, where it causes a large splitting of the band-edge states and strongly modifies the band gap, whereas the valence band is much less affected [85]. They also showed that the band gap remains direct, that the optical transitions are nearly isotropic and only weakly influenced by local lattice distortions, and that the band

alignment with TiO_2 is favourable for electron injection in perovskite solar cells [85]. In this way, their work provided one of the first simple and physically meaningful pictures of why these materials are excellent light absorbers for photovoltaics [85]. Importantly, Even *et al.* pointed out that several earlier theoretical studies [86, 87, 88, 89] had analysed the electronic structure of lead-halide perovskites without properly incorporating SOC into the published band structures, despite the heavy-element character of Pb and experimental indications [90, 91] that relativistic effects should be important. Although the role of SOC had been mentioned in the computational work of Mosconi *et al.* [92], it had still not been fully included in the reported band-structure analysis. They further emphasized that the apparent agreement between some non-SOC DFT band gaps and experiment was largely accidental, arising from error cancellation rather than from a physically correct description [85, 92].

In a related first-principles study, Yin *et al.* [93] showed that the superior photovoltaic properties of halide perovskites originate from a favourable combination of direct band-gap p–p transitions, enabled by the Pb lone-pair s orbitals and the perovskite symmetry, together with high ionicity, large lattice constants, and strong antibonding coupling between Pb s and I p orbitals. Their analysis helped clarify the orbital origin of the band-edge states and explained why these materials simultaneously exhibit strong optical absorption and defect-tolerant electronic properties [93].

Subsequent theoretical work went beyond semilocal density-functional theory and employed many-body perturbation methods, particularly the GW approximation [94] and the Bethe–Salpeter equation (BSE) [95], to obtain a more accurate description of quasiparticle energies and optical excitations in 3D halide perovskites. These studies confirmed the essential role of SOC in determining the electronic structure, but also showed that electron–electron interactions must be treated explicitly in order to predict reliable band gaps [96, 97] and absorption spectra [39, 98]. When relativistic effects and many-body corrections are taken into account simultaneously, theory yields a much more consistent description of the direct band gap and optical response than standard DFT alone.

Another important direction of theoretical work concerned the nature of the optical absorption edge and the role of excitonic effects [99]. Calculations showed that, although 3D halide perovskites are direct-gap semiconductors with strong optical absorption, their exciton binding energies are relatively small because of strong dielectric screening [51, 52]. As a result, photoexcited electron–hole pairs can dissociate efficiently at room temperature, which is highly favourable for photovoltaic applications. At the same time, BSE-based studies [100, 101] demonstrated that excitonic effects still influence the detailed line shape and onset of the absorption spectrum, thus providing a more complete microscopic picture of the optical properties near the band edge.

1.4.2 Theoretical description of 2D halide perovskites

Layered 2D halide perovskites have attracted early theoretical interest because their natural quantum-well-like structures give rise to strong quantum and dielectric confine-

ment. These effects make their excitonic, optical, and electronic properties particularly pronounced and accessible to theoretical modelling [102, 103, 104, 105, 106]. Early studies focused on excitonic states, dielectric confinement, and optical transitions in layered lead-halide perovskites, while later works combined density functional theory (DFT), effective-mass models, and quantum-well descriptions to rationalize their band structures and excitonic properties [107, 102].

However, simplified effective-mass and abrupt dielectric-confinement models are not always sufficient for ultrathin 2D hybrid perovskites, where the strength of dielectric confinement can depend sensitively on the organic spacer and the dielectric contrast between the organic and inorganic layers [67, 108]. Even *et al.* [67] showed that, for layered hybrid organic–inorganic perovskites, quantum confinement cannot be fully described by conventional semiconductor quantum-well models, and that a first-principles composite-material approach is more appropriate. Kepenekian *et al.* [109] further introduced a generic elastic model for layered hybrid perovskite quantum wells, showing that lattice-mismatch-induced mechanical energy can be relaxed through octahedral rotations. Above a critical inorganic layer thickness, this relaxation leads to surface reorganization, low-energy electronic states, band-gap shifts, and surface-assisted exciton dissociation.

Theoretical and computational studies have also been extended to all-inorganic 2D halide perovskites. The synthesis of the all-inorganic Ruddlesden–Popper mixed-halide compound $Cs_2PbI_2Cl_2$ [69] motivated subsequent first-principles investigations of related Pb- and Sn-based systems. For example, Xu *et al.* [110] investigated the optoelectronic properties of 2D $Cs_2PbI_2Cl_2$ and $Cs_2SnI_2Cl_2$, predicting high, layer-dependent in-plane carrier mobilities using deformation-potential theory. In particular, their results suggested electron-dominated transport in $Cs_2PbI_2Cl_2$ and hole-dominated transport in $Cs_2SnI_2Cl_2$.

1.4.3 Anharmonicity and local structural disorder

Theoretical studies [111, 112, 113, 114] have highlighted the central role of lattice dynamics and electron–phonon coupling [115] in determining the bulk electronic and optical properties of halide perovskites. Owing to their structural softness and dynamic disorder, these materials exhibit substantial fluctuations in the local atomic arrangement even when the average crystal symmetry is preserved [116, 117]. First-principles calculations have shown that such fluctuations can renormalize the band gap, broaden optical transitions, and contribute to the temperature dependence of optical spectra and carrier transport [111, 112, 113]. In addition, coupling between charge carriers and polar lattice vibrations has been proposed to promote large-polaron formation, which may help explain the long carrier lifetimes and diffusion lengths observed in these materials [118, 119, 120].

Anharmonicity refers to deviations from the harmonic approximation, in which the restoring force is no longer strictly proportional to atomic displacement. In halide perovskites, this behaviour is particularly pronounced. Early *ab initio* molecular-dynamics simulations revealed strong anharmonic motion at room temperature in MAPI, includ-

ing continuous rotation of the MA^+ molecular cations and significant distortions of the PbI_6 octahedra [116, 121, 122]. Subsequent lattice-dynamics studies identified imaginary phonon modes in the cubic phase, indicating dynamical instabilities and a breakdown of the harmonic picture [123, 124]. These results suggest that the high-symmetry structures reported by diffraction are often not the lowest-energy static configurations, but rather time- and space-averaged structures [116, 117], commonly described as monomorphous. Consistent with this view, Beecher *et al.* showed, using pair-distribution-function measurements, that MAPI exhibits local symmetry breaking that is not resolved by conventional Bragg X-ray diffraction [125]. Zhao *et al.* further demonstrated that polymorphous (i.e., locally disordered) structural models reproduce the experimental pair distribution function much more accurately than the ideal monomorphous cubic configuration [114] (see Fig. 1.7). Perovskite structures possess a multiwell potential-energy surface (PES) due to anharmonicity. In this multiwell PES, the monomorphous configuration corresponds to a local maximum, whereas the polymorphous configurations correspond to energetically favourable minima (see Fig. 1.8) [111].

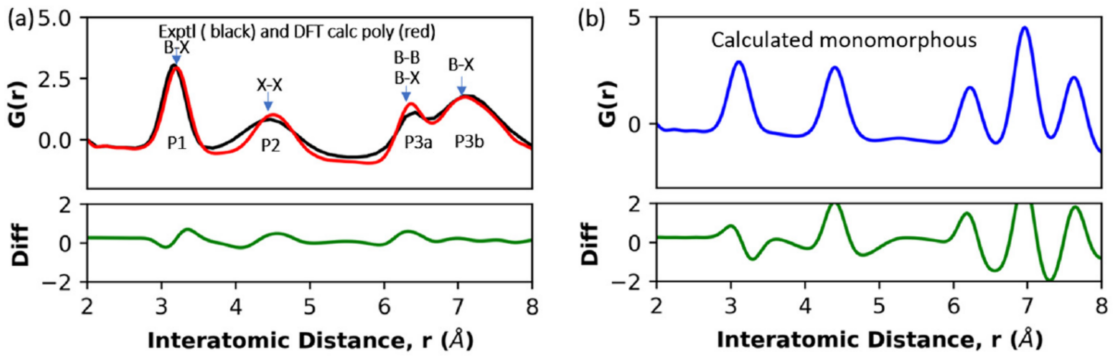

Figure 1.7: Comparison of the calculated pair distribution functions for polymorphous (a) and monomorphous (b) configurations of MAPI with experiment. Adapted from Ref. [114]

Related questions have also been discussed in terms of ferroelectricity and local polar behaviour. Ferroelectricity is characterized by a spontaneous electric polarization that can be reversed by an external electric field. In many materials, it originates from an anharmonic energy landscape that favours a polar distortion over a centrosymmetric configuration [126]. This mechanism is well established in oxide perovskites, where soft polar modes and anharmonic atomic displacements drive ferroelectric phase transitions [127]. Related ideas have also been explored for halide perovskites, whose soft and polarizable lattices can support local polar distortions and fluctuating dipoles [122, 126]. Roma *et al.* [126] showed, using first-principles calculations, that several alkali lead halides can exhibit collective ferroelectric polarization, at least on the nanoscale, and that some compounds may even display hyperferroelectric behaviour. However, for halide perovskites more broadly, the presence of local polar instabilities and dynamic dipoles does not necessarily imply robust long-range classical ferroelectric order. It is therefore more appro-

priate to describe this family as exhibiting strong polar fluctuations and, in some cases, ferroelectric-like or incipient ferroelectric behaviour.

Closely related to anharmonicity and polar fluctuations is local structural disorder. In halide perovskites, the average cubic or tetragonal structure often masks a distribution of locally distorted octahedra, off-centred cations, and fluctuating bond lengths and angles. This disorder is not merely a small correction to the ideal crystal structure; it is an intrinsic and more realistic structural description, which was initially described as static and non-thermal [114]. This picture was refined when low-frequency relaxations (in the μeV range) were experimentally observed by Brillouin scattering instead of neutron scattering at high temperature [128]. The polymorphous picture can thus be considered as a quasistatic aproximation to the structural disorder spead throughout the lattice [111]. Importantly, local disorder also helps explain why halide perovskites can sustain strong atomic motion and structural fluctuations while still retaining sharp absorption onsets and relatively small Urbach energies [129]. Gehrmann *et al.* showed theoretically that the disorder potential in halide perovskites is dynamically shortened by nuclear motion, thereby limiting long-range electronic disorder and preserving favourable band-edge distributions for optoelectronic performance [130]. Thus, the key issue is not only the magnitude of the disorder, but also its spatial correlations and dynamical character.

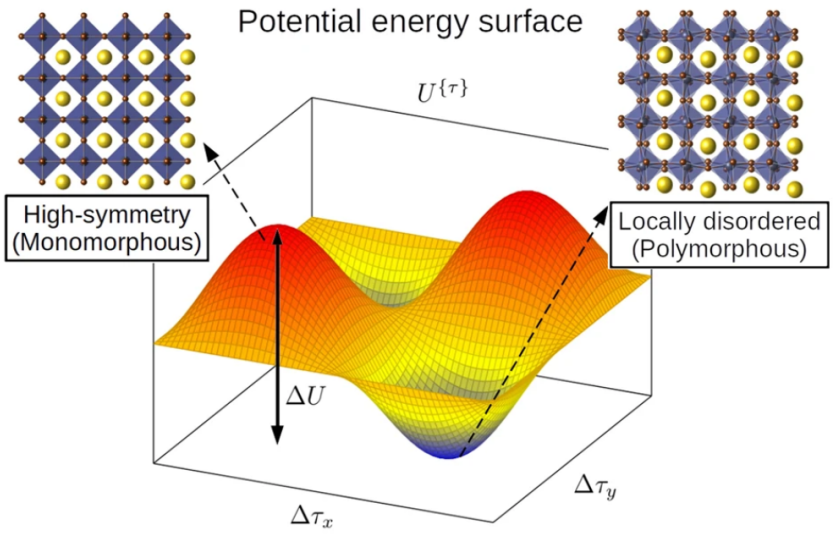

Figure 1.8: Schematic representation of the potential-energy surface of halide perovskites, illustrating the high-symmetry monomorphous configuration and the lower-energy polymorphous configurations [111].

Accounting for local disorder in atomistic models has led to significantly improved predictions of electronic and optical properties. Zhao *et al.* found that polymorphous networks yield lower energies, larger band gaps, and more realistic dielectric responses than ideal monomorphous structures [114]. More recent calculations beyond the high-symmetry picture have further shown that locally disordered structures strongly influ-

ence electron–phonon coupling and the temperature dependence of the band gap, bringing theory into better agreement with experiment [111, 115]. Accurate prediction of bulk halide-perovskite properties therefore requires models that explicitly capture local structural disorder rather than relying solely on averaged crystallographic structures [112, 131, 114]. For this reason, polymorphous and finite-temperature approaches are becoming increasingly important for understanding and predicting the electronic structure, optical spectra, and carrier dynamics of halide perovskites.

More recently, Hou *et al.* [132] examined local structural disorder in high-symmetry formamidinium-based Dion–Jacobson 2D perovskites. For the $n = 2$ compound (3AMP)FAPb_2I_7, this approach showed that reduced local octahedral distortion and structural disorder are associated with enhanced exciton transport, with exciton diffusion lengths exceeding 2 μm. This work highlights the importance of going beyond ideal high-symmetry crystal models when describing 2D perovskites, since local symmetry breaking and polymorphous distortions can strongly influence excitonic transport.

The limitations of idealized bulk models become even more important when one considers surfaces and interfaces. In perovskite solar cells, many of the most relevant processes for device operation and degradation begin at exposed surfaces or buried interfaces, where atomic coordination, chemical composition, and electrostatic alignment differ substantially from those in the bulk.

1.5 Role of surfaces and interfaces in perovskite solar cells

1.5.1 Surface orientation and termination

Surfaces and interfaces play a central role in halide perovskites because they directly affect crystal growth, environmental stability, defect formation, ion migration, and energy-level alignment with contact layers. Since many degradation and charge-transfer processes start at exposed surfaces or buried interfaces, an atomic-scale and electronic-structure understanding of these regions is essential for explaining device performance and stability. From a computational point of view, slab models within periodic boundary conditions are particularly useful for this purpose, because they allow one to evaluate surface energies, compare terminations, analyse defect formation, and determine band-edge positions with respect to the vacuum level.

ABX_3 perovskites can be viewed as stacks of alternating AX and BX_2 atomic layers along selected crystallographic directions. Among the low-index surfaces, the (001) family has been the most widely observed and studied in halide perovskites. Scanning tunnelling microscopy (STM) studies have reported that the exposed surfaces of halide perovskites are often associated with the (001) orientation or its equivalent low-index counterparts [133, 134, 135, 136]. For this reason, many theoretical studies have also focused on (001)-oriented slab models [137, 138, 139].

For ideal cubic perovskites, the (100), (010), and (001) surfaces are symmetry-equivalent. In lower-symmetry phases, however, such as the orthorhombic phase, these orientations are no longer equivalent and can exhibit different atomic structures and surface energies. For orthorhombic $MAPbI_3$, Wang *et al.* [140] compared several surface orientations, including (100), (010), (001), (110), (101), (011), and (111), and found that the (100) surface has the lowest calculated surface energy. This suggests that the (100) facet is the thermodynamically most favourable stoichiometric surface in that phase.

Nevertheless, the lowest-energy facet is not always the most robust under operating conditions. Halide perovskites commonly form (100)-type surfaces under standard synthesis conditions, but facet engineering can increase the fraction of other orientations, including (111) [141]. In $FAPbI_3$, Ma *et al.* showed that the (100) facet interacts more strongly with water, leading to elongated Pb–I bonds and facilitating the transition to the non-perovskite δ phase, whereas the (111) facet is more resistant to moisture-induced degradation [141]. In addition, Yao *et al.* reported that the (111) facet has a higher in-plane ion-migration activation energy and a lower diffusion coefficient than the (100) facet, which further supports its improved structural stability [142]. These results show that surface orientation influences not only surface formation energy, but also degradation pathways and ion transport.

For a (001)-type stoichiometric surface, cleavage of the ABX_3 lattice produces two ideal terminations: an AX termination and a BX_2 termination. In the case of $MAPbI_3$, these correspond to MAI-terminated and PbI_2-terminated surfaces. Both experiment and first-principles calculations suggest that the AX termination is often more favourable for ideal defect-free surfaces. STM measurements revealed that the exposed (001) surface of $MAPbI_3$ is predominantly MAI-terminated, with zigzag and dimer-like surface features [136]. Atomic-resolution STM combined with DFT further supported the assignment of the experimentally exposed orthorhombic $MAPbI_3$ surface to an MAI-terminated (001) surface [134].

This picture is consistent with first-principles studies of surface energetics. Haruyama *et al.* [143] and Geng *et al.* [144] found that the MAI-terminated $MAPbI_3$ (001) surface is more stable than the PbI_2-terminated surface under equilibrium growth conditions. Therefore, the AX termination is often used as the preferred starting point for modelling ideal perovskite surfaces. For all-inorganic halide perovskites, scanning tunnelling microscopy measurement revealed that the CsBr-terminated (001) surface is the most stable surface of $CsPbBr_3$ [135, 145]. This assignment was further supported by the theoretical study of Yang et al. [146, 145].

However, the relative stability of surface defects depends strongly on the chemical environment. Uratani and Yamashita [138] showed that under PbI_2-rich conditions, excess Pb and iodine vacancies are likely to form trap-producing surface defects, while under MAI-rich conditions excess iodine becomes more relevant. Under intermediate conditions, trap-forming surface defects are less favourable. This result highlights that the energetically preferred ideal termination does not by itself determine the electronic quality of the real surface; defect chemistry and growth conditions are equally important.

Surface defects are also closely related to ionic motion and degradation. *Ab initio* calcu-

lations have shown that surfaces and grain boundaries can lower the effective activation energy for ion migration in lead-halide perovskites [57]. In addition, Aristidou *et al.* [59] identified iodide vacancies at the surface as favourable sites for photo-induced superoxide formation from O_2, pointing to surface V_I defects as possible initiators of oxygen- and light-driven degradation. Overall, surface termination must therefore be considered together with defect formation and chemical-potential conditions.

1.5.2 Surface electronic structure and absolute band alignment

Surface slab calculations are also important for determining the absolute energy levels of perovskites. By aligning the electrostatic potential of the slab to the vacuum level, one can obtain the valence-band maximum and conduction-band minimum on an absolute energy scale. These quantities are directly relevant for band alignment at transport-layer/perovskite interfaces. In practice, however, the absolute band positions depend strongly on surface orientation, termination, reconstruction, and defect content.

This sensitivity is also reflected in experiments. For example, the reported valence-band position of $CsPbBr_3$ spans a broad range, approximately from -5.5 to -6.5 eV, depending on sample preparation and measurement method [147, 148, 149]. One reason for this spread is that the exact surface termination and surface condition are often not known experimentally. First-principles calculations help clarify this issue by comparing different ideal surfaces under controlled conditions. For several halide perovskites, it has been found that BX_2-terminated surfaces generally show deeper valence-band positions than AX-terminated surfaces [150, 151]. Traoré *et al.* explained these shifts in terms of different microscopic surface dipoles, which modify the vacuum-level alignment and therefore the absolute band positions [139]. Traoré *et al.* also proposed tuning absolute band positions through dipole engineering using molecular surface coatings.

Surface termination also determines whether electronic states appear inside the band gap. In principle, cleavage can leave undercoordinated atoms and create dangling-bond-related surface states. For $MAPbI_3$, Lodeiro *et al.* [152] showed that in-gap surface states are more likely for PbI_2-terminated surfaces than for MAI-terminated surfaces. This is consistent with experimental observations suggesting that Pb-rich surfaces can generate surface states associated with Pb-derived dangling bonds [153]. In many cases these states are shallow rather than deep, and are therefore less harmful than strong non-radiative recombination centres. For example, Delgado *et al.* found that $CsPbBr_3$ surfaces mainly exhibit shallow states located close to the valence-band edge [154]. Even so, shallow states can still influence interfacial charge transfer and band alignment, and should not be neglected when modeling of perovskite surfaces.

1.5.3 Interface properties in perovskite solar cells

Atomistic simulations of perovskite interfaces are important because they help us understand interfacial phenomena at the atomic scale and can guide experiments toward improved interface design. In halide perovskite solar cells, the interfaces between the perovskite absorber and the charge-transport layers are among the key factors that determine both device performance and stability [155]. One of the first theoretical studies of such interfaces was reported by Mosconi *et al.* [156], who investigated the TiO_2/organohalide-perovskite interface using first-principles calculations. Their work showed that interfacial chemistry can strongly affect binding, stability, and electronic coupling between the perovskite and TiO_2. Later studies on TiO_2/$MAPbI_3$ interfaces confirmed that strong interfacial coupling can promote electron transfer, while the detailed interface structure and surface termination can shift the band edges and change the transfer barrier [157]. These findings were important because they helped explain why the choice of electron-transport layer and interface treatment strongly influences charge extraction and hysteresis in real devices [158].

Similar ideas were later extended to HTL/perovskite interfaces [159, 160, 161, 162, 163]. For NiO/$MAPbI_3$, Li et al. showed that the band alignment and calculated device response depend strongly on the exposed $MAPbI_3$ plane and termination; among the interfaces considered, the NiO(100)/$MAPbI_3$(001)-PbI_2 contact gave the most favorable J_{sc} and V_{oc} [161]. Traore et al. further showed that defects in the NiO contact, especially Ni vacancies, can improve the valence-band alignment with the perovskite, while Li doping provides an additional way to tune the interface energetics [160]. Experimentally, Liu et al. related the hysteresis behavior of inverted devices to the HTL/perovskite contact and found reduced hysteresis for NiO_x compared with PEDOT:PSS, mainly through changes in trap density and interfacial carrier accumulation [159]. More generally, Stolterfoht et al. quantified voltage losses caused by interfacial recombination and energy-level offsets at charge-transport-layer contacts [162], while Torres Merino et al. showed that the valence-band alignment at the hole-transport interface also affects the photostability of wide-bandgap perovskites by influencing hole extraction and halide segregation [163]. These studies show that HTL selection cannot be based only on separately measured bulk energy levels; the actual atomic termination, defect chemistry, and interfacial energetics must also be considered.

Capping and interfacial layers play a related role at the perovskite surface. Cho and Park reviewed how interlayers can reduce recombination losses, modify energy-level alignment, and improve device stability through passivation and barrier effects [164]. Grancini et al. demonstrated this concept experimentally by forming a 2D/3D perovskite junction, which improved long-term stability in carbon-based devices and modules [75]. More recently, Zhi et al. used machine learning to identify molecular descriptors of ammonium-salt passivation materials, highlighting hydrogen-bonding ability, hydrogen content, and hydrophobicity as important selection criteria [165]. Together, these results indicate that capping layers should be treated not merely as protective coatings, but as chemically active interfaces that can passivate defects, alter dipoles and band offsets,

and either facilitate or limit charge extraction depending on their composition and structure.

1.6 Open questions addressed in this thesis

Despite major progress in understanding halide perovskites, several important questions remain unresolved from a computational point of view. In particular, many key properties relevant to photovoltaic performance and stability are governed by surfaces, interfaces, and locally disordered structures, which are difficult to describe accurately using idealized high-symmetry models. This challenge is especially important for halide perovskites because their soft and anharmonic lattices make local symmetry breaking and interface-specific effects central to their behaviour. The present thesis addresses three such open problems.

1.6.1 Accurate prediction of surface properties of cubic halide perovskites

Recent work has shown that local structural disorder is essential for obtaining accurate bulk electronic properties of cubic halide perovskites, including band gaps, effective masses, and dielectric response [112, 111, 166, 113, 115]. For example, molecular-dynamics sampling and polymorphous structural models have been shown to improve agreement between theory and experiment, and to correct the underestimation of band gaps obtained from more idealized descriptions [167, 111, 166, 113]. Since local disorder can also shift absolute band-edge positions [111], it is expected to influence surface ionization energies, electron affinities, surface dipoles, and band alignment at interfaces.

However, most atomistic studies of cubic perovskite surfaces have relied on monomorphous slab models derived from average crystallographic structures [168, 169, 151, 170, 171]. Such models may overlook the influence of local symmetry breaking on surface relaxation, reconstruction, energetics, and vacuum-level alignment. As a consequence, the role of local disorder in determining surface stability and electronic structure remains insufficiently understood. In this thesis, we therefore investigate the surfaces of cubic $CsBX_3$ (B = Pb, Sn; X = I, Br, Cl) perovskites while explicitly incorporating local disorder, with the aim of clarifying its impact on surface energetics and absolute electronic levels. We further analyze the trends of relevant quantities across compositions.

1.6.2 Anharmonicity and local disorder in all-inorganic 2D and quasi-2D perovskites

All-inorganic layered perovskites have attracted increasing attention because they are expected to offer improved robustness under harsh operating conditions while retaining useful optoelectronic properties [110]. In particular, the mixed-halide RP compounds

$Cs_2PbI_2Cl_2$ and $Cs_2SnI_2Cl_2$ were synthesized by Li *et al.* [69], opening a route toward all-inorganic 2D perovskites that are thermodynamically more stable than their single-halide analogues [172]. Since then, $Cs_2PbI_2Cl_2$ has attracted interest as a capping or passivation material in 3D inorganic perovskite solar cells and related optoelectronic devices [84, 173, 174, 175].

Nevertheless, most theoretical studies of these systems have focused on ideal bulk structures, especially for the $n = 1$ phase, while 2D perovskites with larger quantum wells ($n > 1$) are still commonly described using high-symmetry structural models. This is a significant limitation because, in 3D halide perovskites, local disorder and anharmonicity are known to play a decisive role in determining structural stability and electronic properties [111, 114]. Since 2D perovskites with higher n values lie between the strictly 2D and 3D limits, similar effects may also be important in these layered materials. In this thesis, we therefore study the bulk and surface properties of all-inorganic n=1 and n>1 2D perovskites, with particular emphasis on the role of local disorder and the possibility of lower-energy polymorphous structures.

1.6.3 Interfaces between all-inorganic 2D and 3D perovskites

Interfaces between 2D and 3D perovskites play a central role in mixed-dimensional solar cells because they can modify defect formation, carrier extraction, interfacial dipoles, and long-term device stability. While interfaces involving organic-spacer 2D perovskites have been widely studied theoretically [109], interfaces between all-inorganic 2D and 3D perovskites remain largely unexplored. This is partly because such interfaces are more difficult to construct: in systems such as $Cs_2PbI_2Cl_2/CsPbX_3$, the in-plane lattice mismatch can be substantial and must be treated carefully to avoid artificial strain effects.

This problem is particularly relevant from a device perspective because $Cs_2PbI_2Cl_2$ has already been used experimentally as a capping or interfacial layer for 3D inorganic perovskites such as $CsPbI_3$ and $CsPbBr_3$ [84, 176]. However, the atomistic structure, band offsets and adhesion energies of these interfaces have not yet been clarified theoretically. In this thesis, we address this gap by studying $Cs_2PbI_2Cl_2/CsPbX_3$ interfaces from first principles, with particular attention to interface structure, electronic band alignment, and the role of strain.

References

[1] International Energy Agency. Demand – Electricity 2026. IEA. 2026. URL: https://www.iea.org/reports/electricity-2026/demand (visited on 04/13/2026). Available at: https://www.iea.org/reports/electricity-2026/demand (accessed: 2026-04-13).

[2] Hannah Ritchie and Pablo Rosado. Electricity Mix. *Our World in Data*, 2020. Available at: https://ourworldindata.org/electricity-mix (accessed: 2026-04-13).

[3] International Energy Agency. Outlook for Energy Demand – Global EV Outlook 2025. IEA. 2025. URL: https://www.iea.org/reports/global-ev-outlook-2025/outlook-for-energy-demand (visited on 04/13/2026). Available at: https://www.iea.org/reports/global-ev-outlook-2025/outlook-for-energy-demand (accessed: 2026-04-13).

[4] International Energy Agency. Energy and AI. IEA. 2025. URL: https://www.iea.org/reports/energy-and-ai (visited on 04/13/2026). Available at: https://www.iea.org/reports/energy-and-ai (accessed: 2026-04-13).

[5] Global Carbon Project. Fossil Fuel CO_2 Emissions Hit Record High in 2025. 2025. URL: https://globalcarbonbudget.org/fossil-fuel-co2-emissions-hit-record-high-in-2025/ (visited on 04/13/2026). Available at: https://globalcarbonbudget.org/fossil-fuel-co2-emissions-hit-record-high-in-2025/ (accessed: 2026-04-13).

[6] International Energy Agency. Renewable Electricity – Renewables 2025. IEA. 2025. URL: https://www.iea.org/reports/renewables-2025/renewable-electricity (visited on 04/13/2026). Available at: https://www.iea.org/reports/renewables-2025/renewable-electricity (accessed: 2026-04-13).

[7] International Renewable Energy Agency. Renewable Capacity Highlights 2025. IRENA. 2025. URL: https://www.irena.org/-/media/Files/IRENA/Agency/Publication/2025/Mar/IRENA_DAT_RE_Capacity_Highlights_2025.pdf (visited on 04/13/2026). Available at: https://www.irena.org/-/media/Files/IRENA/Agency/Publication/2025/Mar/IRENA_DAT_RE_Capacity_Highlights_2025.pdf (accessed: 2026-04-13).

[8] International Renewable Energy Agency. Renewable Power Generation Costs in 2024. IRENA. 2025. URL: https://www.irena.org/Publications/2025/Jun/Renewable-Power-Generation-Costs-in-2024 (visited on 04/13/2026). Available at: https://www.irena.org/Publications/2025/Jun/Renewable-Power-Generation-Costs-in-2024 (accessed: 2026-04-13).

[9] European Commission. EU Solar Energy Strategy, 2022. Communication from the Commission to the European Parliament, the Council, the European Economic and Social Committee and the Committee of the Regions, COM(2022) 221 final.

[10] Atelier SolairePV. Le solaire photovoltaïque en France : réalité, potentiel et défis. October 22, 2025. URL: https://solairepv.fr/wp-content/uploads/SolairePVEnFranceV3.1.pdf (visited on 06/20/2026). Guide collectif préparé par des chercheuses et chercheurs du CNRS et de la Fédération de Recherche du Photovoltaïque; sous la supervision de Stéphane Collin et Jean-François Guillemoles. Available at: https://solairepv.fr/wp-content/uploads/SolairePVEnFranceV3.1.pdf.

[11] G. G. Macfarlane, T. P. McLean, J. E. Quarrington, and V. Roberts. Fine Structure in the Absorption-Edge Spectrum of Si. *Physical Review*, 111(5):1245–1254, September 1958.

[12] Markus Fischer, Michael Woodhouse, Susanne Herritsch, Jutta Trube, et al. International technology roadmap for photovoltaic (ITRPV). *VDMA EV https://itrpv. vdma. org/en/ueber-uns*, 2021.

[13] William Shockley and Hans J. Queisser. Detailed Balance Limit of Efficiency ofp-nJunction Solar Cells. *Journal of Applied Physics*, 32(3):510–519, March 1961.

[14] Taojian Wu, Zhaolang Liu, Hao Lin, Pingqi Gao, and Wenzhong Shen. Free-standing ultrathin silicon wafers and solar cells through edges reinforcement. *Nature Communications*, 15(1), May 2024.

[15] Justyna Pastuszak and Paweł Węgierek. Photovoltaic Cell Generations and Current Research Directions for Their Development. *Materials*, 15(16):5542, August 2022.

[16] National Renewable Energy Laboratory (NREL). Best Research-Cell Efficiency Chart, 2025. Avialable at: https://www.nrel.gov/pv/cell-efficiency.html (accessed: 2026-04-13).

[17] Chong Dong, Dayu Liu, Liang Wang, Kanghua Li, Xuke Yang, Zhe Li, Haisheng Song, Ling Xu, Chao Chen, and Jiang Tang. Growth Mechanism of Thermally Evaporated γ-$CsPbI_3$ Film. *Advanced Functional Materials*, 33(28), April 2023.

[18] Zhun Yao, Wangen Zhao, and Shengzhong (Frank) Liu. Stability of the $CsPbI_3$ perovskite: from fundamentals to improvements. *Journal of Materials Chemistry A*, 9(18):11124–11144, 2021.

[19] Rebecca J. Sutton, Marina R. Filip, Amir A. Haghighirad, Nobuya Sakai, Bernard Wenger, Feliciano Giustino, and Henry J. Snaith. Cubic or Orthorhombic? Revealing the Crystal Structure of Metastable Black-Phase $CsPbI_3$ by Theory and Experiment. *ACS Energy Letters*, 3(8):1787–1794, June 2018.

[20] Arthur Marronnier, Guido Roma, Soline Boyer-Richard, Laurent Pedesseau, Jean-Marc Jancu, Yvan Bonnassieux, Claudine Katan, Constantinos C. Stoumpos, Mercouri G. Kanatzidis, and Jacky Even. Anharmonicity and Disorder in the Black Phases of Cesium Lead Iodide Used for Stable Inorganic Perovskite Solar Cells. *ACS Nano*, 12(4):3477–3486, March 2018.

[21] Boya Zhao, Shi-Feng Jin, Sheng Huang, Ning Liu, Jing-Yuan Ma, Ding-Jiang Xue, Qiwei Han, Jie Ding, Qian-Qing Ge, Yaqing Feng, and Jin-Song Hu. Thermodynamically Stable Orthorhombic γ-$CsPbI_3$ Thin Films for High-Performance Photovoltaics. *Journal of the American Chemical Society*, 140(37):11716–11725, August 2018.

[22] Handong Jin, Yu-Jia Zeng, Julian A. Steele, Maarten B. J. Roeffaers, Johan Hofkens, and Elke Debroye. Phase stabilization of cesium lead iodide perovskites for use in efficient optoelectronic devices. *NPG Asia Materials*, 16(1), May 2024.

[23] Feng Ke, Chenxu Wang, Chunjing Jia, Nathan R. Wolf, Jiejuan Yan, Shanyuan Niu, Thomas P. Devereaux, Hemamala I. Karunadasa, Wendy L. Mao, and Yu Lin. Preserving a robust $CsPbI_3$ perovskite phase via pressure-directed octahedral tilt. *Nature Communications*, 12(1), January 2021.

[24] Akihiro Kojima, Kenjiro Teshima, Yasuo Shirai, and Tsutomu Miyasaka. Organometal Halide Perovskites as Visible-Light Sensitizers for Photovoltaic Cells. *Journal of the American Chemical Society*, 131(17):6050–6051, April 2009.

[25] In Chung, Byunghong Lee, Jiaqing He, Robert P. H. Chang, and Mercouri G. Kanatzidis. All-solid-state dye-sensitized solar cells with high efficiency. *Nature*, 485(7399):486–489, May 2012.

[26] Hui-Seon Kim, Chang-Ryul Lee, Jeong-Hyeok Im, Ki-Beom Lee, Thomas Moehl, Arianna Marchioro, Soo-Jin Moon, Robin Humphry-Baker, Jun-Ho Yum, Jacques E. Moser, Michael Grätzel, and Nam-Gyu Park. Lead Iodide Perovskite Sensitized All-Solid-State Submicron Thin Film Mesoscopic Solar Cell with Efficiency Exceeding 9%. *Scientific Reports*, 2(1), August 2012.

[27] Michael M. Lee, Joël Teuscher, Tsutomu Miyasaka, Takurou N. Murakami, and Henry J. Snaith. Efficient Hybrid Solar Cells Based on Meso-Superstructured Organometal Halide Perovskites. *Science*, 338(6107):643–647, November 2012.

[28] Lioz Etgar, Peng Gao, Zhaosheng Xue, Qin Peng, Aravind Kumar Chandiran, Bin Liu, Md. K. Nazeeruddin, and Michael Grätzel. Mesoscopic $CH_3NH_3PbI_3/TiO_2$ Heterojunction Solar Cells. *Journal of the American Chemical Society*, 134(42):17396–17399, October 2012.

[29] Jiachen Sun, Jiang Wu, Xin Tong, Feng Lin, Yanan Wang, and Zhiming M. Wang. Organic/Inorganic Metal Halide Perovskite Optoelectronic Devices beyond Solar Cells. *Advanced Science*, 5(5), March 2018.

[30] Zhi-Kuang Tan, Reza Saberi Moghaddam, May Ling Lai, Pablo Docampo, Ruben Higler, Felix Deschler, Michael Price, Aditya Sadhanala, Luis M. Pazos, Dan Credgington, Fabian Hanusch, Thomas Bein, Henry J. Snaith, and Richard H. Friend. Bright light-emitting diodes based on organometal halide perovskite. *Nature Nanotechnology*, 9(9):687–692, August 2014.

[31] Mahshid Ahmadi, Ting Wu, and Bin Hu. A Review on Organic-Inorganic Halide Perovskite Photodetectors: Device Engineering and Fundamental Physics. *Advanced Materials*, 29(41), September 2017.

[32] Qing Zhang, Qiuyu Shang, Rui Su, T. Thu Ha Do, and Qihua Xiong. Halide Perovskite Semiconductor Lasers: Materials, Cavity Design, and Low Threshold. *Nano Letters*, 21(5):1903–1914, January 2021.

[33] Henry J. Snaith. Perovskites: The Emergence of a New Era for Low-Cost, High-Efficiency Solar Cells. *The Journal of Physical Chemistry Letters*, 4(21):3623–3630, October 2013.

[34] Chunyang Zhang and Nam-Gyu Park. Materials and methods for cost-effective fabrication of perovskite photovoltaic devices. *Communications Materials*, 5(1), September 2024.

[35] Jingbi You, Ziruo Hong, Yang (Michael) Yang, Qi Chen, Min Cai, Tze-Bin Song, Chun-Chao Chen, Shirong Lu, Yongsheng Liu, Huanping Zhou, and Yang Yang. Low-Temperature Solution-Processed Perovskite Solar Cells with High Efficiency and Flexibility. *ACS Nano*, 8(2):1674–1680, January 2014.

[36] Jun Hong Noh, Sang Hyuk Im, Jin Hyuck Heo, Tarak N. Mandal, and Sang Il Seok. Chemical Management for Colorful, Efficient, and Stable Inorganic-Organic Hybrid Nanostructured Solar Cells. *Nano Letters*, 13(4):1764–1769, March 2013.

[37] Feng Hao, Constantinos C. Stoumpos, Robert P. H. Chang, and Mercouri G. Kanatzidis. Anomalous Band Gap Behavior in Mixed Sn and Pb Perovskites Enables Broadening of Absorption Spectrum in Solar Cells. *Journal of the American Chemical Society*, 136(22):8094–8099, May 2014.

[38] Norman Pellet, Peng Gao, Giuliano Gregori, Tae-Youl Yang, Mohammad K. Nazeeruddin, Joachim Maier, and Michael Grätzel. Mixed-Organic-Cation Perovskite Photovoltaics for Enhanced Solar-Light Harvesting. *Angewandte Chemie International Edition*, 53(12):3151–3157, February 2014.

[39] Ivano E. Castelli, Juan María García-Lastra, Kristian S. Thygesen, and Karsten W. Jacobsen. Bandgap calculations and trends of organometal halide perovskites. *APL Materials*, 2(8), August 2014.

[40] Jeremy L. Knutson, James D. Martin, and David B. Mitzi. Tuning the band gap in hybrid tin iodide perovskite semiconductors using structural templating. *Inorganic Chemistry*, 44(13):4699–4705, May 2005.

[41] LONGi. 34.85%! LONGi Breaks World Record for Crystalline Silicon-Perovskite Tandem Solar Cell Efficiency Again. LONGi. April 2025. URL: `https://www.longi.com/en/news/silicon-perovskite-tandem-solar-cells-new-world-efficiency/` (visited on 04/16/2026). Available at: `https://www.longi.com/en/news/silicon-perovskite-tandem-solar-cells-new-world-efficiency/` (accessed: 2026-04-16).

[42] Wan-Jian Yin, Tingting Shi, and Yanfa Yan. Unique Properties of Halide Perovskites as Possible Origins of the Superior Solar Cell Performance. *Advanced Materials*, 26(27):4653–4658, May 2014.

[43] Xie Zhang, Mark E. Turiansky, and Chris G. Van de Walle. Correctly Assessing Defect Tolerance in Halide Perovskites. *The Journal of Physical Chemistry C*, 124(11):6022–6027, February 2020.

[44] Samuel D. Stranks, Giles E. Eperon, Giulia Grancini, Christopher Menelaou, Marcelo J. P. Alcocer, Tomas Leijtens, Laura M. Herz, Annamaria Petrozza, and Henry J. Snaith. Electron-Hole Diffusion Lengths Exceeding 1 Micrometer in an Organometal Trihalide Perovskite Absorber. *Science*, 342(6156):341–344, October 2013.

[45] Aron Walsh, David O. Scanlon, Shiyou Chen, X. G. Gong, and Su-Huai Wei. Self-Regulation Mechanism for Charged Point Defects in Hybrid Halide Perovskites. *Angewandte Chemie International Edition*, 54(6):1791–1794, December 2014.

[46] Daniele Meggiolaro, Silvia G. Motti, Edoardo Mosconi, Alex J. Barker, James Ball, Carlo Andrea Riccardo Perini, Felix Deschler, Annamaria Petrozza, and Filippo De Angelis. Iodine chemistry determines the defect tolerance of lead-halide perovskites. *Energy & Environmental Science*, 11(3):702–713, 2018.

[47] Xie Zhang, Mark E. Turiansky, and Chris G. Van de Walle. All-inorganic halide perovskites as candidates for efficient solar cells. *Cell Reports Physical Science*, 2(10):100604, October 2021.

[48] Stefaan De Wolf, Jakub Holovsky, Soo-Jin Moon, Philipp Löper, Bjoern Niesen, Martin Ledinsky, Franz-Josef Haug, Jun-Ho Yum, and Christophe Ballif. Organometallic Halide Perovskites: Sharp Optical Absorption Edge and Its Relation to Photovoltaic Performance. *The Journal of Physical Chemistry Letters*, 5(6):1035–1039, March 2014.

[49] Joseph S. Manser, Jeffrey A. Christians, and Prashant V. Kamat. Intriguing Optoelectronic Properties of Metal Halide Perovskites. *Chemical Reviews*, 116(21):12956–13008, June 2016.

[50] Laura M. Herz. Charge-Carrier Dynamics in Organic-Inorganic Metal Halide Perovskites. *Annual Review of Physical Chemistry*, 67(1):65–89, May 2016.

[51] Jacky Even, Laurent Pedesseau, and Claudine Katan. Analysis of Multivalley and Multibandgap Absorption and Enhancement of Free Carriers Related to Exciton Screening in Hybrid Perovskites. *The Journal of Physical Chemistry C*, 118(22):11566–11572, May 2014.

[52] Atsuhiko Miyata, Anatolie Mitioglu, Paulina Plochocka, Oliver Portugall, Jacob Tse-Wei Wang, Samuel D. Stranks, Henry J. Snaith, and Robin J. Nicholas. Direct measurement of the exciton binding energy and effective masses for charge carriers in organic-inorganic tri-halide perovskites. *Nature Physics*, 11(7):582–587, 2015.

[53] Runda Li, Yixin Luo, Libing Yao, Liuwen Tian, Zengyi Sun, Rui Wang, and Jingjing Xue. Structural softness in photovoltaic perovskites. *Applied Physics Letters*, 126(14), April 2025.

[54] Christopher Eames, Jarvist M. Frost, Piers R. F. Barnes, Brian C. O'Regan, Aron Walsh, and M. Saiful Islam. Ionic transport in hybrid lead iodide perovskite solar cells. *Nature Communications*, 6(1), June 2015.

[55] Wolfgang Tress. Metal Halide Perovskites as Mixed Electronic-Ionic Conductors: Challenges and Opportunities—From Hysteresis to Memristivity. *The Journal of Physical Chemistry Letters*, 8(13):3106–3114, June 2017.

[56] Jarla Thiesbrummel, Sahil Shah, Emilio Gutierrez-Partida, Fengshuo Zu, Francisco Peña-Camargo, Stefan Zeiske, Jonas Diekmann, Fangyuan Ye, Karol P. Peters, Kai O. Brinkmann, Pietro Caprioglio, Akash Dasgupta, Seongrok Seo, Fatai A. Adeleye, Jonathan Warby, Quentin Jeangros, Felix Lang, Shuo Zhang, Steve Albrecht, Thomas Riedl, Ardalan Armin, Dieter Neher, Norbert Koch, Yongzhen Wu, Vincent M. Le Corre, Henry Snaith, and Martin Stolterfoht. Ion-induced field screening as a dominant factor in perovskite solar cell operational stability. *Nature Energy*, 9(6):664–676, March 2024.

[57] Daniele Meggiolaro, Edoardo Mosconi, and Filippo De Angelis. Formation of Surface Defects Dominates Ion Migration in Lead-Halide Perovskites. *ACS Energy Letters*, 4(3):779–785, February 2019.

[58] Bowei Li and Wei Zhang. Improving the stability of inverted perovskite solar cells towards commercialization. *Communications Materials*, 3(1), September 2022.

[59] Nicholas Aristidou, Christopher Eames, Irene Sanchez-Molina, Xiangnan Bu, Jan Kosco, M. Saiful Islam, and Saif A. Haque. Fast oxygen diffusion and iodide defects mediate oxygen-induced degradation of perovskite solar cells. *Nature Communications*, 8(1), May 2017.

[60] Emilio J. Juarez-Perez, Luis K. Ono, Maki Maeda, Yan Jiang, Zafer Hawash, and Yabing Qi. Photodecomposition and thermal decomposition in methylammonium halide lead perovskites and inferred design principles to increase photovoltaic device stability. *Journal of Materials Chemistry A*, 6(20):9604–9612, 2018.

[61] Bert Conings, Jeroen Drijkoningen, Nicolas Gauquelin, Aslihan Babayigit, Jan D'Haen, Lien D'Olieslaeger, Anitha Ethirajan, Jo Verbeeck, Jean Manca, Edoardo Mosconi, Filippo De Angelis, and Hans-Gerd Boyen. Intrinsic Thermal Instability of Methylammonium Lead Trihalide Perovskite. *Advanced Energy Materials*, 5(15), June 2015.

[62] Zhen Li, Mengjin Yang, Ji-Sang Park, Su-Huai Wei, Joseph J. Berry, and Kai Zhu. Stabilizing Perovskite Structures by Tuning Tolerance Factor: Formation of Formamidinium and Cesium Lead Iodide Solid-State Alloys. *Chemistry of Materials*, 28(1):284–292, December 2015.

[63] Zehua Chen, Geert Brocks, Shuxia Tao, and Peter A. Bobbert. Unified theory for light-induced halide segregation in mixed halide perovskites. *Nature Communications*, 12(1), May 2021.

[64] Nam Joong Jeon, Jun Hong Noh, Woon Seok Yang, Young Chan Kim, Seungchan Ryu, Jangwon Seo, and Sang Il Seok. Compositional engineering of perovskite materials for high-performance solar cells. *Nature*, 517(7535):476–480, January 2015.

[65] Yifan Lv, Hui Zhang, Ruqing Liu, Yanan Sun, and Wei Huang. Composite Encapsulation Enabled Superior Comprehensive Stability of Perovskite Solar Cells. *ACS Applied Materials & Interfaces*, 12(24):27277–27285, May 2020.

[66] J. Calabrese, N. L. Jones, R. L. Harlow, N. Herron, D. L. Thorn, and Y. Wang. Preparation and characterization of layered lead halide compounds. *Journal of the American Chemical Society*, 113(6):2328–2330, March 1991.

[67] Jacky Even, Laurent Pedesseau, and Claudine Katan. Understanding Quantum Confinement of Charge Carriers in Layered 2D Hybrid Perovskites. *ChemPhysChem*, 15(17):3733–3741, September 2014.

[68] Guangbao Wu, Tinghuan Yang, Xing Li, Nafees Ahmad, Xuning Zhang, Shengli Yue, Jin Zhou, Yanxun Li, Hui Wang, Xinghua Shi, Shengzhong (Frank) Liu, Kui Zhao, Huiqiong Zhou, and Yuan Zhang. Molecular Engineering for Two-Dimensional Perovskites with Photovoltaic Efficiency Exceeding 18%. *Matter*, 4(2):582–599, February 2021.

[69] Jiangwei Li, Qin Yu, Yihui He, Constantinos C. Stoumpos, Guangda Niu, Giancarlo G. Trimarchi, Hang Guo, Guifang Dong, Dong Wang, Liduo Wang, and Mercouri G. Kanatzidis. $Cs_2PbI_2Cl_2$, All-Inorganic Two-Dimensional Ruddlesden–Popper Mixed Halide Perovskite with Optoelectronic Response. *Journal of the American Chemical Society*, 140(35):11085–11090, August 2018.

[70] Mary O'Kane. What Are 2D Perovskites? n.d. URL: `https://www.ossila.com/pages/what-are-2d-perovskites`. Available at: `https://www.ossila.com/pages/what-are-2d-perovskites` (accessed: 2026-04-17).

[71] Hsinhan Tsai, Wanyi Nie, Jean-Christophe Blancon, Constantinos C. Stoumpos, Reza Asadpour, Boris Harutyunyan, Amanda J. Neukirch, Rafael Verduzco, Jared J. Crochet, Sergei Tretiak, Laurent Pedesseau, Jacky Even, Muhammad A. Alam, Gautam Gupta, Jun Lou, Pulickel M. Ajayan, Michael J. Bedzyk, Mercouri G. Kanatzidis, and Aditya D. Mohite. High-efficiency two-dimensional Ruddlesden–Popper perovskite solar cells. *Nature*, 536(7616):312–316, July 2016.

[72] Jacky Even, Siraj Sidhik, Mikael kepenekian, boubacar traoré boubacar, Claudine Katan, Mercouri G. Kanatzidis, and Aditya D. Mohite. 2D multilayered perovskites and 2D/3D bilayers for stable solar cells. In Alexandre Freundlich, Karin Hinzer, and Stéphane Collin, editors, *Physics, Simulation, and Photonic Engineering of Photovoltaic Devices XII*, page 4. SPIE, March 2023.

[73] Laurent Pedesseau, Jean-Marc Jancu, Alain Rolland, Emmanuelle Deleporte, Claudine Katan, and Jacky Even. Electronic properties of 2D and 3D hybrid organic/inorganic perovskites for optoelectronic and photovoltaic applications. *Optical and Quantum Electronics*, 46(10):1225–1232, November 2013.

[74] J.-C. Blancon, H. Tsai, W. Nie, C. C. Stoumpos, L. Pedesseau, C. Katan, M. Kepenekian, C. M. M. Soe, K. Appavoo, M. Y. Sfeir, S. Tretiak, P. M. Ajayan, M. G. Kanatzidis, J. Even, J. J. Crochet, and A. D. Mohite. Extremely efficient internal exciton dissociation through edge states in layered 2D perovskites. *Science*, 355(6331):1288–1292, March 2017.

[75] G. Grancini, C. Roldán-Carmona, I. Zimmermann, E. Mosconi, X. Lee, D. Martineau, S. Narbey, F. Oswald, F. De Angelis, M. Graetzel, and Mohammad Khaja Nazeeruddin. One-Year stable perovskite solar cells by 2D/3D interface engineering. *Nature Communications*, 8(1), June 2017.

[76] Yuping Gao, Hang Liu, Zonglong Song, Yu Chen, Liu Yang, Ziyang Hu, Yu Zou, Yongsheng Chen, and Yongsheng Liu. Spontaneous 2D perovskite formation at the buried interface of perovskite solar cells enhances crystallization uniformity and defect passivation. *Nature Photonics*, 20(2):178–185, November 2025.

[77] Ming Shao, Tong Bie, Lvpeng Yang, Yerun Gao, Xing Jin, Feng He, Nan Zheng, Yu Yu, and Xinliang Zhang. Over 21% Efficiency Stable 2D Perovskite Solar Cells. *Advanced Materials*, 34(1):2107211, 2022.

[78] Siraj Sidhik, Isaac Metcalf, Wenbin Li, Tim Kodalle, Connor J. Dolan, Mohammad Khalili, Jin Hou, Faiz Mandani, Andrew Torma, Hao Zhang, Rabindranath Garai, Jessica Persaud, Amanda Marciel, Itzel Alejandra Muro Puente, G. N. Manjunatha Reddy, Adam Balvanz, Muhammad A. Alam, Claudine Katan, Esther Tsai, David Ginger, David P. Fenning, Mercouri G. Kanatzidis, Carolin M. Sutter-Fella, Jacky Even, and Aditya D. Mohite. Two-dimensional perovskite templates for durable, efficient formamidinium perovskite solar cells. *Science*, 384(6701):1227–1235, 2024.

[79] Rabindranath Garai, Isaac Metcalf, Nilanjana Nandi, Paramvir Ahlawat, Braulio Reyes-Suárez, Faiz Mandani, Hao Zhang, Tim Kodalle, Michael D. Irwin, Claudine Katan, Carolin M. Sutter-Fella, Mercouri G. Kanatzidis, G. N. Manjunatha Reddy, Jacky Even, and Aditya D. Mohite. Bypassing the yellow phase for extremely stable formamidinium lead iodide perovskite solar cells. *Science*, 392(6797), April 2026.

[80] Siraj Sidhik, Yafei Wang, Michael De Siena, Reza Asadpour, Andrew J. Torma, Tanguy Terlier, Kevin Ho, Wenbin Li, Anand B. Puthirath, Xinting Shuai, Ayush Agrawal, Boubacar Traore, Matthew Jones, Rajiv Giridharagopal, Pulickel M. Ajayan, Joseph Strzalka, David S. Ginger, Claudine Katan, Muhammad Ashraful Alam, Jacky Even, Mercouri G. Kanatzidis, and Aditya D. Mohite. Deterministic fabrication of 3D/2D perovskite bilayer stacks for durable and efficient solar cells. *Science*, 377(6613):1425–1430, 2022.

[81] Xing Li, Lei Gu, Yang Feng, Chao Wu, Chunming Yang, and Lin Song. Vertically Oriented 2D Perovskite Layer with n = 1 Phase Enables Efficient and Stable Inverted Perovskite Solar Cells. *ACS Applied Materials & Interfaces*, 16(44):60387–60393, October 2024.

[82] Bhushan P. Kore, Wei Zhang, Billy W. Hoogendoorn, Majid Safdari, and James M. Gardner. Moisture tolerant solar cells by encapsulating 3D perovskite with long-chain alkylammonium cation-based 2D perovskite. *Communications Materials*, 2(1), September 2021.

[83] Guangbao Wu, Rui Liang, Mingzheng Ge, Guoxing Sun, Yuan Zhang, and Guichuan Xing. Surface Passivation Using 2D Perovskites toward Efficient and Stable Perovskite Solar Cells. *Advanced Materials*, 34(8), January 2022.

[84] Syed-Fawad-Ali Shah, Inyoung Jeong, Jaewang Park, Donghyeop Shin, Inchan Hwang, Nikolai Tsvetkov, Dohyung Kim, Jihye Gwak, Joo Hyung Park, Sang Il Seok, Kihwan Kim, and Hanul Min. Efficient and stable $CsPbI_3$ perovskite solar cells with spontaneously formed 2D-$Cs_2PbI_2Cl_2$ at the buried interface. *Cell Reports Physical Science*, 5(5):101935, May 2024.

[85] Jacky Even, Laurent Pedesseau, Jean-Marc Jancu, and Claudine Katan. Importance of Spin-Orbit Coupling in Hybrid Organic/Inorganic Perovskites for Photovoltaic Applications. *The Journal of Physical Chemistry Letters*, 4(17):2999–3005, August 2013.

[86] G. Murtaza and Iftikhar Ahmad. First principle study of the structural and optoelectronic properties of cubic perovskites $CsPbM_3$ (M = Cl, Br, I). *Physica B: Condensed Matter*, 406(17):3222–3229, September 2011.

[87] Ivo Borriello, Giovanni Cantele, and Domenico Ninno. Ab initioinvestigation of hybrid organic-inorganic perovskites based on tin halides. *Physical Review B*, 77(23):235214, June 2008.

[88] Y. H. Chang, C. H. Park, and K. Matsuishi. First-Principles Study of the Structural and the Electronic Properties of the Lead-Halide-Based Inorganic-Organic Perovskites $(CH_3NH_3)PbX_3$ and $CsPbX_3$ (X = Cl, Br, I). *Journal of the Korean Physical Society*, 44(4):889–893, 2004.

[89] T. Umebayashi, K. Asai, T. Kondo, and A. Nakao. Electronic structures of lead iodide based low-dimensional crystals. *Physical Review B*, 67(15), April 2003.

[90] Kenichiro Tanaka, Takayuki Takahashi, Takuma Ban, Takashi Kondo, Kazuhito Uchida, and Noboru Miura. Comparative study on the excitons in lead-halide-based perovskite-type crystals $CH_3NH_3PbBr_3$ $CH_3NH_3PbI_3$. *Solid State Communications*, 127(9-10):619–623, September 2003.

[91] Masakatsu Hirasawa, Teruya Ishihara, and Takenari Goto. Exciton Features in 0-, 2-, and 3-Dimensional Networks of [PbI6]4-Octahedra. *Journal of the Physical Society of Japan*, 63(10):3870–3879, October 1994.

[92] Edoardo Mosconi, Anna Amat, Md. K. Nazeeruddin, Michael Grätzel, and Filippo De Angelis. First-Principles Modeling of Mixed Halide Organometal Perovskites for Photovoltaic Applications. *The Journal of Physical Chemistry C*, 117(27):13902–13913, July 2013.

[93] Wan-Jian Yin, Tingting Shi, and Yanfa Yan. Superior Photovoltaic Properties of Lead Halide Perovskites: Insights from First-Principles Theory. *The Journal of Physical Chemistry C*, 119(10):5253–5264, February 2015.

[94] Mark S. Hybertsen and Steven G. Louie. Electron correlation in semiconductors and insulators: Band gaps and quasiparticle energies. *Physical Review B*, 34(8):5390–5413, October 1986.

[95] E. E. Salpeter and H. A. Bethe. A Relativistic Equation for Bound-State Problems. *Physical Review*, 84(6):1232–1242, December 1951.

[96] Paolo Umari, Edoardo Mosconi, and Filippo De Angelis. Relativistic GW calculations on $CH_3NH_3PbI_3$ and $CH_3NH_3SnI_3$ Perovskites for Solar Cell Applications. *Scientific Reports*, 4(1), March 2014.

[97] Marina R. Filip and Feliciano Giustino. GW quasiparticle band gap of the hybrid organic-inorganic perovskite $CH_3NH_3PbI_3$: Effect of spin-orbit interaction, semicore electrons, and self-consistency. *Physical Review B*, 90(24), December 2014.

[98] T. J. Whitcher, J.-X. Zhu, X. Chi, H. Hu, Daming Zhao, T. C. Asmara, X. Yu, M. B. H. Breese, A. H. Castro Neto, Y. M. Lam, A. T. S. Wee, Elbert E. M. Chia, and A. Rusydi. Importance of Electronic Correlations and Unusual Excitonic Effects in Formamidinium Lead Halide Perovskites. *Physical Review X*, 8(2), May 2018.

[99] Michal Baranowski and Paulina Plochocka. Excitons in Metal-Halide Perovskites. *Advanced Energy Materials*, 10(26), February 2020.

[100] Menno Bokdam, Tobias Sander, Alessandro Stroppa, Silvia Picozzi, D. D. Sarma, Cesare Franchini, and Georg Kresse. Role of Polar Phonons in the Photo Excited State of Metal Halide Perovskites. *Scientific Reports*, 6(1), June 2016.

[101] Towfiq Ahmed, C. La-o-vorakiat, T. Salim, Y. M. Lam, Elbert E. M. Chia, and Jian-Xin Zhu. Optical properties of organometallic perovskite: An ab initio study using relativistic GW correction and Bethe-Salpeter equation. *EPL (Europhysics Letters)*, 108(6):67015, December 2014.

[102] Teruya Ishihara, Jun Takahashi, and Takenari Goto. Exciton state in two-dimensional perovskite semiconductor $(C_{10}H_{21}NH_3)_2PbI_4$. *Solid State Communications*, 69(9):933–936, March 1989.

[103] Teruya Ishihara, Jun Takahashi, and Takenari Goto. Optical properties due to electronic transitions in two-dimensional semiconductors $(C_nH_{2n+1}NH_3)_2PbI_4$. *Physical Review B*, 42(17):11099–11107, December 1990.

[104] N. A. GIPPIUS, T. ISHIHARA, L. V. KELDYSH, E. A. MULJAROV, and S. G. TIKHODEEV. Dielectrically confined excitons and polaritons in natural superlattices - perovskite lead iodide semiconductors. *Le Journal de Physique IV*, 03(C5):437–440, October 1993.

[105] Claudine Katan, Nicolas Mercier, and Jacky Even. Quantum and Dielectric Confinement Effects in Lower-Dimensional Hybrid Perovskite Semiconductors. *Chemical Reviews*, 119(5):3140–3192, January 2019.

[106] Catherine M. Mauck and William A. Tisdale. Excitons in 2D Organic-Inorganic Halide Perovskites. *Trends in Chemistry*, 1(4):380–393, July 2019.

[107] Sebastien Sourisseau, Nicolas Louvain, Wenhua Bi, Nicolas Mercier, David Rondeau, Florent Boucher, Jean-Yves Buzaré, and Christophe Legein. Reduced Band Gap Hybrid Perovskites Resulting from Combined Hydrogen and Halogen Bonding at the Organic-Inorganic Interface. *Chemistry of Materials*, 19(3):600–607, January 2007.

[108] Bin Cheng, Ting-You Li, Partha Maity, Pai-Chun Wei, Dennis Nordlund, Kang-Ting Ho, Der-Hsien Lien, Chun-Ho Lin, Ru-Ze Liang, Xiaohe Miao, Idris A. Ajia, Jun Yin, Dimosthenis Sokaras, Ali Javey, Iman S. Roqan, Omar F. Mohammed, and Jr-Hau He. Extremely reduced dielectric confinement in two-dimensional hybrid perovskites with large polar organics. *Communications Physics*, 1(1), November 2018.

[109] Mikaël Kepenekian, Boubacar Traore, Jean-Christophe Blancon, Laurent Pedesseau, Hsinhan Tsai, Wanyi Nie, Constantinos C. Stoumpos, Mercouri G. Kanatzidis, Jacky Even, Aditya D. Mohite, Sergei Tretiak, and Claudine Katan. Concept of Lattice Mismatch and Emergence of Surface States in Two-dimensional Hybrid Perovskite Quantum Wells. *Nano Letters*, 18(9):5603–5609, August 2018.

[110] Zhuo Xu, Ming Chen, and Shengzhong Frank Liu. Layer-Dependent Ultrahigh-Mobility Transport Properties in All-Inorganic Two-Dimensional $Cs_2PbI_2Cl_2$ and $Cs_2SnI_2Cl_2$ Perovskites. *The Journal of Physical Chemistry C*, 123(45):27978–27985, October 2019.

[111] Marios Zacharias, George Volonakis, Feliciano Giustino, and Jacky Even. Anharmonic electron-phonon coupling in ultrasoft and locally disordered perovskites. *npj Computational Materials*, 9(1), August 2023.

[112] Marios Zacharias and Jacky Even. Local Structural Disorder in Crystalline Materials. *ACS Energy Letters*, 10(11):5635–5643, October 2025.

[113] Marios Zacharias, George Volonakis, Laurent Pedesseau, Claudine Katan, Feliciano Giustino, and Jacky Even. Roadmap for electronic structure, anharmonicity, and electron-phonon calculations in locally disordered inorganic and hybrid halide perovskites. *Physical Review B*, 113(8), February 2026.

[114] Xin-Gang Zhao, Gustavo M. Dalpian, Zhi Wang, and Alex Zunger. Polymorphous nature of cubic halide perovskites. *Physical Review B*, 101(15), April 2020.

[115] Marios Zacharias, George Volonakis, Laurent Pedesseau, Claudine Katan, Feliciano Giustino, and Jacky Even. Electron-phonon couplings in polymorphous crystals. *Physical Review B*, 113(8), February 2026.

[116] Claudio Quarti, Edoardo Mosconi, and Filippo De Angelis. Structural and electronic properties of organo-halide hybrid perovskites from ab initio molecular dynamics. *Physical Chemistry Chemical Physics*, 17(14):9394–9409, 2015.

[117] Marcelo A. Carignano, S. Assa Aravindh, Iman S. Roqan, Jacky Even, and Claudine Katan. Critical Fluctuations and Anharmonicity in Lead Iodide Perovskites from Molecular Dynamics Supercell Simulations. *The Journal of Physical Chemistry C*, 121(38):20729–20738, September 2017.

[118] X.-Y. Zhu and V. Podzorov. Charge Carriers in Hybrid Organic-Inorganic Lead Halide Perovskites Might Be Protected as Large Polarons. *The Journal of Physical Chemistry Letters*, 6(23):4758–4761, November 2015.

[119] Kiyoshi Miyata, Daniele Meggiolaro, M. Tuan Trinh, Prakriti P. Joshi, Edoardo Mosconi, Skyler C. Jones, Filippo De Angelis, and X.-Y. Zhu. Large polarons in lead halide perovskites. *Science Advances*, 3(8), August 2017.

[120] Y. Chen, H. T. Yi, X. Wu, R. Haroldson, Y. N. Gartstein, Y. I. Rodionov, K. S. Tikhonov, A. Zakhidov, X. -Y. Zhu, and V. Podzorov. Extended carrier lifetimes and diffusion in hybrid perovskites revealed by Hall effect and photoconductivity measurements. *Nature Communications*, 7(1), August 2016.

[121] Aurelien M. A. Leguy, Jarvist Moore Frost, Andrew P. McMahon, Victoria Garcia Sakai, W. Kockelmann, ChunHung Law, Xiaoe Li, Fabrizia Foglia, Aron Walsh, Brian C. O'Regan, Jenny Nelson, João T. Cabral, and Piers R. F. Barnes. The dynamics of methylammonium ions in hybrid organic–inorganic perovskite solar cells. *Nature Communications*, 6(1), May 2015.

[122] Jarvist M. Frost, Keith T. Butler, and Aron Walsh. Molecular ferroelectric contributions to anomalous hysteresis in hybrid perovskite solar cells. *APL MATERIALS*, 2(8), July 2014.

[123] Federico Brivio, Jarvist M. Frost, Jonathan M. Skelton, Adam J. Jackson, Oliver J. Weber, Mark T. Weller, Alejandro R. Goñi, Aurélien M. A. Leguy, Piers R. F. Barnes, and Aron Walsh. Lattice dynamics and vibrational spectra of the orthorhombic, tetragonal, and cubic phases of methylammonium lead iodide. *Physical Review B*, 92(14), October 2015.

[124] Lucy D. Whalley, Jonathan M. Skelton, Jarvist M. Frost, and Aron Walsh. Phonon anharmonicity, lifetimes, and thermal transport in $CH_3NH_3PbI_3$ from many-body perturbation theory. *Physical Review B*, 94(22), December 2016.

[125] Alexander N. Beecher, Octavi E. Semonin, Jonathan M. Skelton, Jarvist M. Frost, Maxwell W. Terban, Haowei Zhai, Ahmet Alatas, Jonathan S. Owen, Aron Walsh, and Simon J. L. Billinge. Direct Observation of Dynamic Symmetry Breaking above Room Temperature in Methylammonium Lead Iodide Perovskite. *ACS Energy Letters*, 1(4):880–887, October 2016.

[126] Guido Roma, Arthur Marronnier, and Jacky Even. From latent ferroelectricity to hyperferroelectricity in alkali lead halide perovskites. *Physical Review Materials*, 4(9), September 2020.

[127] Weili Luo, Hao Wang, Rodney S. Ruoff, Jerzy Cioslowski, and Steven Phelps. Susceptibility Discontinuity in Single Crystal C_{60}. *Physical Review Letters*, 73(1):186–188, July 1994.

[128] B. Hehlen, P. Bourges, B. Rufflé, S. Clément, R. Vialla, A. C. Ferreira, C. Ecolivet, S. Paofai, S. Cordier, C. Katan, A. Létoublon, and J. Even. Pseudospin-phonon pretransitional dynamics in lead halide hybrid perovskites. *Physical Review B*, 105(2), January 2022.

[129] David A. Egger, Achintya Bera, David Cahen, Gary Hodes, Thomas Kirchartz, Leeor Kronik, Robert Lovrincic, Andrew M. Rappe, David R. Reichman, and Omer Yaffe. What Remains Unexplained about the Properties of Halide Perovskites? *Advanced Materials*, 30(20), March 2018.

[130] Christian Gehrmann and David A. Egger. Dynamic shortening of disorder potentials in anharmonic halide perovskites. *Nature Communications*, 10(1), July 2019.

[131] Haiyuan Wang, Alexey Tal, Thomas Bischoff, Patrick Gono, and Alfredo Pasquarello. Accurate and efficient band-gap predictions for metal halide perovskites at finite temperature. *npj Computational Materials*, 8(1), November 2022.

[132] Jin Hou, Jared Fletcher, Siedah J. Hall, Hao Zhang, Marios Zacharias, George Volonakis, Claire Welton, Stefan Zeiske, Isaiah W. Gilley, Donghoon Shin, Faiz Mandani, Isaac Metcalf, Shuo Sun, Bo Zhang, Yinsheng Guo, Bin Chen, G. N. Manjunatha Reddy, Claudine Katan, Jacky Even, Matthew Y. Sfeir, Mercouri G. Kanatzidis, and Aditya D. Mohite. Exciton diffusion beyond 2 μm enabled by maximum symmetry in two-dimensional perovskites. *Nature Synthesis*, April 2026.

[133] Robin Ohmann, Luis K. Ono, Hui-Seon Kim, Haiping Lin, Michael V. Lee, Youyong Li, Nam-Gyu Park, and Yabing Qi. Real-Space Imaging of the Atomic Structure of Organic-Inorganic Perovskite. *Journal of the American Chemical Society*, 137(51):16049–16054, December 2015.

[134] Limin She, Meizhuang Liu, and Dingyong Zhong. Atomic Structures of $CH_3NH_3PbI_3$ (001) Surfaces. *ACS Nano*, 10(1):1126–1131, December 2015.

[135] Wei Zhang, Luis K. Ono, Jiamin Xue, and Yabing Qi. Atomic Level Insights into Metal Halide Perovskite Materials by Scanning Tunneling Microscopy and Spectroscopy. *Angewandte Chemie International Edition*, 61(5), November 2021.

[136] Limin She, Meizhuang Liu, Xiaoli Li, Zeying Cai, and Dingyong Zhong. Growth and interfacial structure of methylammonium lead iodide thin films on Au(111). *Surface Science*, 656:17–23, February 2017.

[137] Azimatu Seidu, Marc Dvorak, Jari Järvi, Patrick Rinke, and Jingrui Li. Surface reconstruction of tetragonal methylammonium lead triiodide. *APL Materials*, 9(11), November 2021.

[138] Hiroki Uratani and Koichi Yamashita. Charge Carrier Trapping at Surface Defects of Perovskite Solar Cell Absorbers: A First-Principles Study. *The Journal of Physical Chemistry Letters*, 8(4):742–746, February 2017.

[139] Boubacar Traoré, Pooja Basera, Alexandra J. Ramadan, Henry J. Snaith, Claudine Katan, and Jacky Even. A Theoretical Framework for Microscopic Surface and Interface Dipoles, Work Functions, and Valence Band Alignments in 2D and 3D Halide Perovskite Heterostructures. *ACS Energy Letters*, 7(1):349–357, December 2021.

[140] Yun Wang, Bobby G. Sumpter, Jingsong Huang, Haimin Zhang, Porun Liu, Huagui Yang, and Huijun Zhao. Density Functional Studies of Stoichiometric Surfaces of Orthorhombic Hybrid Perovskite $CH_3NH_3PbI_3$. *The Journal of Physical Chemistry C*, 119(2):1136–1145, January 2015.

[141] Chunqing Ma, Felix T. Eickemeyer, Sun-Ho Lee, Dong-Ho Kang, Seok Joon Kwon, Michael Grätzel, and Nam-Gyu Park. Unveiling facet-dependent degradation and facet engineering for stable perovskite solar cells. *Science*, 379(6628):173–178, January 2023.

[142] Yuxin Yao, Biao Li, Degong Ding, Chenxia Kan, Pengjie Hang, Daoyong Zhang, Zechen Hu, Zhenyi Ni, Xuegong Yu, and Deren Yang. Oriented wide-bandgap perovskites for monolithic silicon-based tandems with over 1000 hours operational stability. *Nature Communications*, 16(1), January 2025.

[143] Jun Haruyama, Keitaro Sodeyama, Liyuan Han, and Yoshitaka Tateyama. Termination Dependence of Tetragonal $CH_3NH_3PbI_3$ Surfaces for Perovskite Solar Cells. *The Journal of Physical Chemistry Letters*, 5(16):2903–2909, August 2014.

[144] Wei Geng, Chuan-Jia Tong, Zhen-Kun Tang, ChiYung Yam, Yan-Ning Zhang, Woon-Ming Lau, and Li-Min Liu. Effect of surface composition on electronic properties of methylammonium lead iodide perovskite. *Journal of Materiomics*, 1(3):213–220, September 2015.

[145] Jeremy Hieulle, Shulin Luo, Dae-Yong Son, Afshan Jamshaid, Collin Stecker, Zonghao Liu, Guangren Na, Dongwen Yang, Robin Ohmann, Luis K. Ono, Lijun Zhang, and Yabing Qi. Imaging of the Atomic Structure of All-Inorganic Halide Perovskites. *The Journal of Physical Chemistry Letters*, 11(3):818–823, January 2020.

[146] Yi Yang, Chunju Hou, and Tong-Xiang Liang. Energetic and electronic properties of $CsPbBr_3$ surfaces: a first-principles study. *Physical Chemistry Chemical Physics*, 23(12):7145–7152, 2021.

[147] Yun Hu, Qiang Wang, Ying-Li Shi, Meng Li, Lei Zhang, Zhao-Kui Wang, and Liang-Sheng Liao. Vacuum-evaporated all-inorganic cesium lead bromine perovskites for high-performance light-emitting diodes. *Journal of Materials Chemistry C*, 5(32):8144–8149, 2017.

[148] Alagesan Subramanian, Zhenghui Pan, Zhenbo Zhang, Imtiaz Ahmad, Jing Chen, Meinan Liu, Shuang Cheng, Yijun Xu, Jun Wu, Wei Lei, Qasim Khan, and Yuegang Zhang. Interfacial Energy-Level Alignment for High-Performance All-Inorganic Perovskite $CsPbBr_3$ Quantum Dot-Based Inverted Light-Emitting Diodes. *ACS Applied Materials & Interfaces*, 10(15):13236–13243, March 2018.

[149] Shuxia Tao, Ines Schmidt, Geert Brocks, Junke Jiang, Ionut Tranca, Klaus Meerholz, and Selina Olthof. Absolute energy level positions in tin- and lead-based halide perovskites. *Nature Communications*, 10(1), June 2019.

[150] Claudio Quarti, Filippo De Angelis, and David Beljonne. Influence of Surface Termination on the Energy Level Alignment at the $CH_3NH_3PbI_3$ Perovskite/C_{60} Interface. *Chemistry of Materials*, 29(3):958–968, January 2017.

[151] Xin Huang, Tula R. Paudel, Peter A. Dowben, Shuai Dong, and Evgeny Y. Tsymbal. Electronic structure and stability of the $CH_3NH_3PbBr_3$ (001) surface. *Physical Review B*, 94(19), November 2016.

[152] Lucas Lodeiro, Felipe Barría-Cáceres, Karla Jiménez, Renato Contreras, Ana L. Montero-Alejo, and Eduardo Menéndez-Proupin. Methodological Issues in First-Principle Calculations of $CH_3NH_3PbI_3$ Perovskite Surfaces: Quantum Confinement and Thermal Motion. *ACS Omega*, 5(45):29477–29491, November 2020.

[153] Weiguang Kong, Tao Ding, Gang Bi, and Huizhen Wu. Optical characterizations of the surface states in hybrid lead–halide perovskites. *Physical Chemistry Chemical Physics*, 18(18):12626–12632, 2016.

[154] Frederico P. Delgado, Frederico Simões, Leeor Kronik, Waldemar Kaiser, and David A. Egger. Machine-Learning Force Fields Reveal Shallow Electronic States on Dynamic Halide Perovskite Surfaces. *ACS Energy Letters*, 10(7):3367–3374, June 2025.

[155] Shuyan Shao and Maria Antonietta Loi. The Role of the Interfaces in Perovskite Solar Cells. *Advanced Materials Interfaces*, 7(1), November 2019.

[156] Edoardo Mosconi, Enrico Ronca, and Filippo De Angelis. First-Principles Investigation of the TiO2/Organohalide Perovskites Interface: The Role of Interfacial Chlorine. *The Journal of Physical Chemistry Letters*, 5(15):2619–2625, July 2014.

[157] Run Long, Wei-Hai Fang, and Oleg V. Prezhdo. Strong Interaction at the Perovskite/TiO2 Interface Facilitates Ultrafast Photoinduced Charge Separation: A Nonadiabatic Molecular Dynamics Study. *The Journal of Physical Chemistry C*, 121(7):3797–3806, February 2017.

[158] Bo Chen, Mengjin Yang, Shashank Priya, and Kai Zhu. Origin of J-V Hysteresis in Perovskite Solar Cells. *The Journal of Physical Chemistry Letters*, 7(5):905–917, February 2016.

[159] Jie Liu, Xingtian Yin, Yuxiao Guo, Meidan Que, Jing Chen, Zhong Chen, and Wenxiu Que. Influence of Hole Transport Layers/Perovskite Interfaces on the Hysteresis Behavior of Inverted Perovskite Solar Cells. *ACS Applied Energy Materials*, 3(7):6391–6399, June 2020.

[160] Boubacar Traore, Laurent Pedesseau, Jean-Christophe Blancon, Sergei Tretiak, Aditya D. Mohite, Jacky Even, Claudine Katan, and Mikaël Kepenekian. Importance of Vacancies and Doping in the Hole-Transporting Nickel Oxide Interface with Halide Perovskites. *ACS Applied Materials & Interfaces*, 12(5):6633–6640, January 2020.

[161] Longhua Li, Jianli Mi, Yangchun Yong, Baodong Mao, and Weidong Shi. First-principles study on the lattice plane and termination dependence of the electronic properties of the NiO/$CH_3NH_3PbI_3$ interfaces. *Journal of Materials Chemistry C*, 6(30):8226–8233, 2018.

[162] Martin Stolterfoht, Pietro Caprioglio, Christian M. Wolff, José A. Márquez, Joleik Nordmann, Shanshan Zhang, Daniel Rothhardt, Ulrich Hörmann, Yohai Amir, Alex Redinger, Lukas Kegelmann, Fengshuo Zu, Steve Albrecht, Norbert Koch, Thomas Kirchartz, Michael Saliba, Thomas Unold, and Dieter Neher. The impact of energy alignment and interfacial recombination on the internal and external open-circuit voltage of perovskite solar cells. *Energy & Environmental Science*, 12(9):2778–2788, 2019.

[163] Luis Victor Torres Merino, Christopher E. Petoukhoff, Oleksandr Matiash, Anand Selvin Subbiah, Carolina Villamil Franco, Pia Dally, Badri Vishal, Sofiia Kosar, Diego Rosas Villalva, Vladyslav Hnapovskyi, Esma Ugur, Sahil Shah, Francisco Peña Camargo, Orestis Karalis, Hannes Hempel, Igal Levine, Rakesh R. Pradhan, Suzana Kralj, Nikhil Kalasariya, Maxime Babics, Bumin Kagan Yildirim, Ahmed A. Said, Erkan Aydin, Helen Bristow, Subhashri Mannar, Waseem Raja, Anil Reddy Pininti, Adi Prasetio, Arsalan

Razzaq, Hamza Al Nasser, Thomas G. Allen, Furkan H. Isikgor, Derya Baran, Thomas D. Anthopoulos, Monica Morales Masis, Udo Schwingenschlögl, Thomas Unold, Martin Stolterfoht, Frédéric Laquai, and Stefaan De Wolf. Impact of the valence band energy alignment at the hole-collecting interface on the photostability of wide band-gap perovskite solar cells. *Joule*, 8(9):2585–2606, September 2024.

[164] An-Na Cho and Nam-Gyu Park. Impact of Interfacial Layers in Perovskite Solar Cells. *ChemSusChem*, 10(19):3687–3704, September 2017.

[165] Chongyang Zhi, Suo Wang, Shijing Sun, Can Li, Zhihao Li, Zhi Wan, Hongqiang Wang, Zhen Li, and Zhe Liu. Machine-Learning-Assisted Screening of Interface Passivation Materials for Perovskite Solar Cells. *ACS Energy Letters*, 8(3):1424–1433, February 2023.

[166] Ibrahim Buba Garba, Lorenzo Trombini, Claudine Katan, Jacky Even, Marios Zacharias, Mikael Kepenekian, and George Volonakis. Three-Dimensional to Layered Halide Perovskites: A Parameter-Free Hybrid Functional Method for Predicting Electronic Band Gaps. *ACS Materials Letters*, 7(5):1922–1929, April 2025.

[167] Julia Wiktor, Ursula Rothlisberger, and Alfredo Pasquarello. Predictive Determination of Band Gaps of Inorganic Halide Perovskites. *The Journal of Physical Chemistry Letters*, 8(22):5507–5512, October 2017.

[168] Yan-Jin Chen, Chunju Hou, and Yi Yang. Surface energy and surface stability of cesium tin halide perovskites: a theoretical investigation. *Physical Chemistry Chemical Physics*, 25(15):10583–10590, 2023.

[169] C.-G. Ma, V. Krasnenko, and M.G. Brik. First-principles calculations of different (001) surface terminations of three cubic perovskites CsCaBr3, CsGeBr3, and CsSnBr3. *Journal of Physics and Chemistry of Solids*, 115:289–299, April 2018.

[170] Ruo Xi Yang and Liang Z. Tan. First-Principles Characterization of Surface Phonons of Halide Perovskite $CsPbI_3$ and Their Role in Stabilization. *The Journal of Physical Chemistry Letters*, 12(38):9253–9261, September 2021.

[171] Jakoah Brgoch, Anna J. Lehner, Michael Chabinyc, and Ram Seshadri. Ab Initio Calculations of Band Gaps and Absolute Band Positions of Polymorphs of $RbPbI_3$ and $CsPbI_3$: Implications for Main-Group Halide Perovskite Photovoltaics. *The Journal of Physical Chemistry C*, 118(48):27721–27727, November 2014.

[172] M. Oluchi Anunobi and Robert F. Berger. Energetic Stability and Band-Edge Orbitals of Layered Inorganic Perovskite Compounds for Solar Energy Applications. *The Journal of Physical Chemistry C*, 127(41):20217–20225, October 2023.

[173] Zhenzhen Li, Xiaolong Liu, Jia Xu, Shujie Yang, Hang Zhao, Hui Huang, Shengzhong Frank Liu, and Jianxi Yao. 2D–3D $Cs_2PbI_2Cl_2$–$CsPbI_{2.5}Br_{0.5}$ Mixed-Dimensional Films for All-Inorganic Perovskite Solar Cells with Enhanced Efficiency and Stability. *The Journal of Physical Chemistry Letters*, 11(10):4138–4146, May 2020.

[174] Shaomin Yang, Weiduan Liu, Yu Han, Zhike Liu, Wenjing Zhao, Chenyang Duan, Yuhang Che, Haoshuang Gu, Yuebin Li, and Shengzhong (Frank) Liu. 2D $Cs_2PbI_2Cl_2$ Nanosheets for Holistic Passivation of Inorganic $CsPbI_2Br$ Perovskite Solar Cells for Improved Efficiency and Stability. *Advanced Energy Materials*, 10(46), October 2020.

[175] Xiaoming Zhao, Tianran Liu, Quinn C. Burlingame, Tianjun Liu, Rudolph Holley, Guangming Cheng, Nan Yao, Feng Gao, and Yueh-Lin Loo. Accelerated aging of all-inorganic, interface-stabilized perovskite solar cells. *Science*, 377(6603):307–310, July 2022.

[176] Xing Huang, Kuanxin Lv, Wenqiang Zhu, Zhenzhen Li, and Hang Zhao. Accessible New Non-Quantum Dot $Cs_2PbI_2Cl_2$-Based Photocatalysts for Efficient Hole-Driven Photocatalytic Applications. *Molecules*, 29(14):3249, July 2024.

Chapter 2

Theoretical Framework and Electronic-Structure Calculations

In this chapter, we present the theoretical methods and computational details used throughout this work, including the employed code, basis sets, and convergence criteria to insure reproducibility. We first briefly discuss the limitations of semilocal generalized gradient approximation (GGA) functionals in electronic-structure calculations and outline the theoretical background of the DFT-1/2 quasiparticle correction. We then describe in detail the generation of locally disordered structures and the underlying theory. For the study of surfaces and interfaces, we also present the methods used to calculate absolute band positions, band offsets, surface energies, and adhesion energies.

2.1 Computational Details and Quasiparticle Correction

2.1.1 Computational details

All electronic-structure calculations in this work were carried out within Density Functional Theory (DFT). For all calculations, we used a plane-wave basis set as implemented in the open-source Quantum ESPRESSO package [1]. The interaction between core and valence electrons was described using ultrasoft pseudopotentials. The studied materials include $CsBX_3$ (B = Pb, Sn; X = I, Br, Cl) and $Cs_{n+1}Pb_nI_{n+1}Cl_{2n}$ structures. In the valence configuration, 9 electrons were considered for Cs ($5s^25p^66s^1$), 7 for I ($5s^25p^5$), 7 for Br ($4s^24p^5$), 7 for Cl ($3s^23p^5$), 14 for Sn ($4d^{10}5s^25p^2$), and 14 for Pb ($5d^{10}6s^26p^2$).

Spin–orbit coupling (SOC) was included in all electronic-property calculations by using fully relativistic pseudopotentials, since the studied systems contain heavy elements. However, SOC was not included in structural relaxations or phonon calculations. For electronic-structure and relaxation calculations, the self-consistent field (SCF) convergence threshold was set to 10^{-7} Ry. For phonon calculations, a tighter SCF threshold of 10^{-14} Ry was used. The force convergence threshold was set to 10^{-3} Ry/Å for high-symmetry bulk, slab, and interface structures. For positional local disordered bulk structures, a tighter force threshold of 10^{-5} Ry/Å was used. All structural relaxations were performed using the Broyden–Fletcher–Goldfarb–Shanno (BFGS) algorithm.

Phonon dispersion calculations for high-symmetry structures were performed using density functional perturbation theory (DFPT). For positional local disordered structures, the frozen-phonon method was used. The optB86b-vdW [2] exchange–correlation functional was employed, which is a GGA functional that includes a non-local correlation term to describe weak van der Waals interactions. The vdW term was used only for structural relaxations. For calculations including SOC, the optB86b exchange–correlation functional without the vdW term was used.

The Brillouin zone was sampled using a Monkhorst–Pack $6 \times 6 \times 6$ k-point grid for the primitive bulk structure. This value was selected based on total-energy convergence, as shown in Fig. 2.1b. The k-point grid was scaled according to the size of the supercell or surface slab. The plane-wave cutoff energy was also tested by checking the convergence of the total energy. As shown in Fig. 2.1a, a wavefunction cutoff energy of 80 Ry was sufficient for bulk calculations. Therefore, all bulk electronic, phonon, and relaxation calculations were carried out using an 80 Ry cutoff.

For surface and interface calculations, the convergence of the absolute band position and surface energy was used as the main criterion. Based on these tests, a wavefunction cutoff energy of 50 Ry was found to be sufficient for surface and interface calculations. Since ultrasoft pseudopotentials were used, the charge-density cutoff energy was set to eight times the wavefunction cutoff energy.

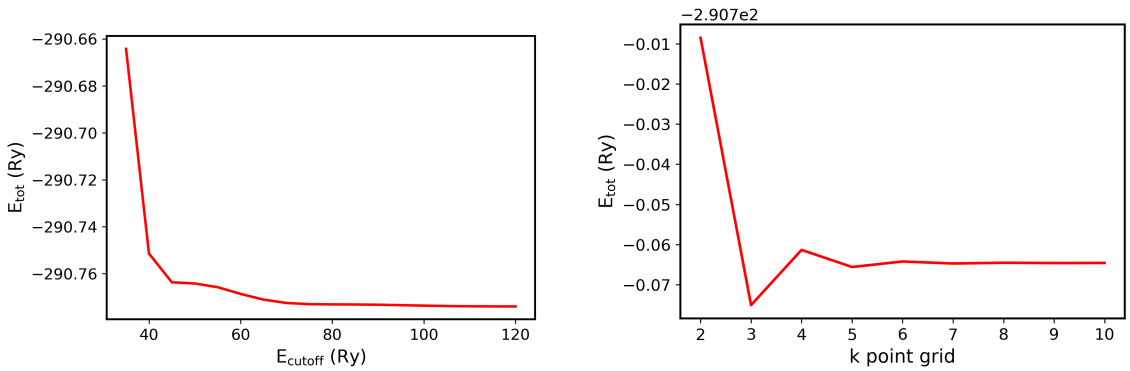

Figure 2.1: Convergence of the total energy of high-symmetry cubic $CsPbI_3$ with respect to the plane-wave cutoff energy (a) and the k-point grid (b). In panel (b), only one number is shown on the x-axis because the cubic structure uses an $n \times n \times n$ k-point grid.

2.1.2 DFT-1/2 method

Semilocal GGA functionals generally underestimate the band gap and ionization potential of semiconductors. This mainly arises from the self-interaction error inherent to semilocal functionals and their inability to account for the discontinuity of the derivative of the energy versus the number of electrons. In GGA, an electron can interact spuriously with its own charge density, which tends to over-delocalize the electronic states and gives an incorrect description of localized states. Several approaches have been developed to improve the prediction of band gaps and ionization potentials, including many-body perturbation theory within the GW approximation [3], hybrid functionals [4], self-interaction correction schemes [5], and the DFT-1/2 method [6].

Among these methods, GW is one of the most accurate approaches for quasiparticle energies, but it becomes computationally very expensive for large systems. Hybrid functionals can also improve the electronic structure significantly, but they remain costly for large-scale calculations. In addition, their accuracy may depend on the choice of mixing parameters, which are often material dependent. Although parameter-free dielectric-dependent hybrid functionals have been developed, they are still computationally demanding, and the self-consistent evaluation of the dielectric constant further increases the cost [7]. In contrast, DFT-1/2 is much less expensive computationally. Its cost is close to that of semilocal GGA, while its accuracy for band gaps can approach that of more advanced methods such as GW [8].

The theoretical basis of DFT-1/2 comes from Slater's half-occupation idea, which had previously been successful in atomic ionization problems [6, 9, 10]. The main idea is that the energy required to remove an electron can be described well by a state with half occupation, and this can be converted into a correction to the Kohn–Sham potential.

The starting point of the method is Janak's theorem [11],

$$\frac{\partial E}{\partial f_i} = \varepsilon_i(f_i), \tag{2.1}$$

where E is the total energy, f_i is the occupation of the Kohn–Sham state i, and ε_i is the corresponding eigenvalue. This relation shows that the change in total energy with respect to the occupation number is directly given by the eigenvalue of that state.

If $\varepsilon_i(f_i)$ is assumed to vary approximately linearly with occupation, integration between the neutral system and the ionized system gives

$$E(0) - E(-1) = \varepsilon_i(-1/2). \tag{2.2}$$

This means that the eigenvalue of the half-ionized state approximates the ionization energy. Therefore, instead of removing one full electron at once, the excitation can be described by a state in which half an electron is removed.

For the exact functional, the total energy is piecewise linear with respect to fractional electron number, and the relevant Kohn–Sham eigenvalue is approximately constant over the fractional-occupation interval. In semilocal DFT, this condition is violated, leading to an occupation dependence of the eigenvalue. In the DFT-1/2 formalism, this dependence is written as

$$\frac{\partial \varepsilon_i}{\partial f_i} = 2S_i, \tag{2.3}$$

where S_i is the self-energy associated with the hole created in state i. This quantity represents the energetic contribution arising from the interaction of the hole with its own electrostatic and exchange-correlation fields. In this sense, S_i can be viewed as the self-interaction contribution that should be removed, at least approximately, in order to obtain a better excitation energy.

Using the approximate linearity of $\varepsilon_i(f_i)$, one obtains

$$\varepsilon_i(-1/2) = \varepsilon_i(0) - S_i. \tag{2.4}$$

This is the central idea of the DFT-1/2 method [6]. It shows that the half-ionized eigenvalue can be obtained from the ground-state eigenvalue by subtracting the self-energy of the hole. In this way, the correction is directly connected to the reduction of self-interaction error.

The self-energy is written as the expectation value of a self-energy potential $V_S(\mathbf{r})$,

$$S_i = \int |\psi_i(\mathbf{r})|^2 \, V_S(\mathbf{r}) \, d^3r, \tag{2.5}$$

where $\psi_i(\mathbf{r})$ is the wave function of state i. This expression gives a practical interpretation of S_i: it is the average value of an effective correction potential over the orbital from which half an electron is removed. In this way, DFT-1/2 introduces the self-energy through a local potential that can be added directly to the one-electron equations.

Using this idea, the Kohn–Sham equation is modified by subtracting the self-energy potential,

$$\left[-\nabla^2 + V_{\mathrm{eff}}(\mathbf{r}) - V_S(\mathbf{r})\right]\psi_i(\mathbf{r}) = \left[\varepsilon_i(0) - S_i\right]\psi_i(\mathbf{r}) = \varepsilon_i(-1/2)\psi_i(\mathbf{r}). \tag{2.6}$$

Here, $V_{\mathrm{eff}}(\mathbf{r})$ is the usual Kohn–Sham effective potential, which includes the external, Hartree, and exchange-correlation terms. Thus, the role of DFT-1/2 is to correct the Kohn–Sham Hamiltonian through the subtraction of $V_S(\mathbf{r})$. This correction mainly affects the valence states, which are more strongly influenced by the hole, and as a result it improves the calculated band gap.

For an isolated atom, the self-energy potential is approximated as the difference between the effective potential of the neutral atom and that of the half-ionized atom,

$$V_S(\mathbf{r}) \approx -V(-1/2, \mathbf{r}) + V(0, \mathbf{r}). \tag{2.7}$$

This provides the practical recipe used in DFT-1/2 calculations: one first performs atomic calculations for the neutral and half-ionized states, and then uses the difference between their effective potentials as the correction potential. In this way, the physical picture of half ionization is retained, but it is expressed in a form that can be used in solid-state calculations.

When this atomic self-energy potential is repeated in a periodic crystal, its long-range Coulomb tail would lead to an unphysical divergence. To avoid this problem, the potential is multiplied by a trimming function,

$$\Theta(r) = \begin{cases} \left[1 - \left(\dfrac{r}{\mathrm{r_{cut}}}\right)^n\right]^3, & r \le \mathrm{r_{cut}}, \\ 0, & r > \mathrm{r_{cut}}, \end{cases} \tag{2.8}$$

so that the final correction used in the solid becomes $\Theta(r)V_S(r)$. This cutoff localizes the correction in the region where the hole has atomic character and removes the long-range part that should not extend through the entire crystal.

The parameter $\mathrm{r_{cut}}$ is determined by requiring the band gap to become extremal,

$$\frac{\partial(e_c - e_v)}{\partial V_S} = 0, \tag{2.9}$$

where e_c and e_v are the conduction-band minimum and valence-band maximum eigenvalues, respectively. This condition reflects the physical idea that the most suitable correction corresponds to a localized hole with maximum self-energy.

The DFT-1/2 correction was implemented in Quantum ESPRESSO through the `ld1.x` tool. This tool was used to generate modified pseudopotentials in which half an electron is removed from selected atomic orbitals. The resulting pseudopotentials therefore include the DFT-1/2 self-energy correction and can be used directly in the subsequent bulk calculations. In this way, the correction is introduced at the pseudopotential level while the overall computational cost remains close to that of standard semilocal DFT.

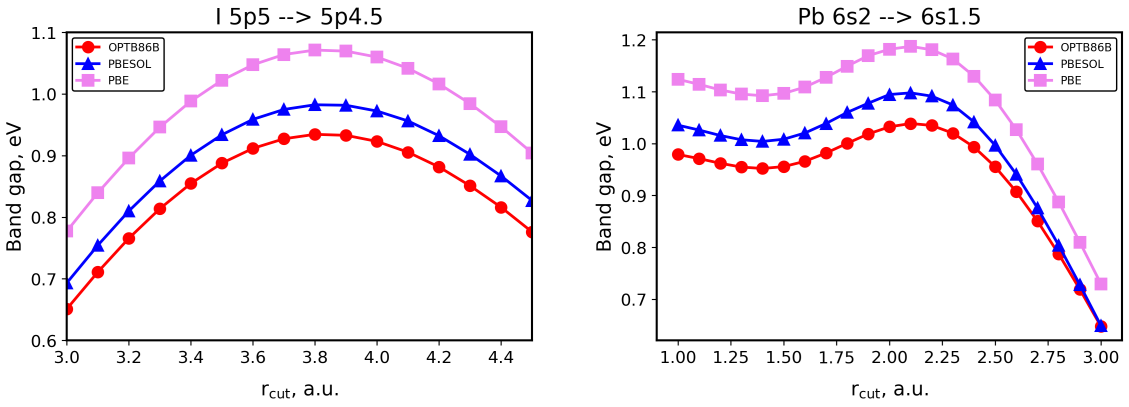

Figure 2.2: Variation of the band gap of $CsPbI_3$ with the cutoff radius r_{cut} used in the trimming function for the I $5p$ orbital (a) and the Pb $6s$ orbital (b).

For solid compounds, the choice of the orbital from which half an electron is removed is crucial. To identify the relevant orbitals, the projected density of states (PDOS) was analyzed in order to determine the main atomic-orbital contributions to the valence-band maximum. In halide perovskites $CsBX_3$ ($B = \mathrm{Pb}, \mathrm{Sn}$ and $X = \mathrm{I}, \mathrm{Br}, \mathrm{Cl}$), the top of the valence band is known to arise mainly from the antibonding hybridization between the halogen p states and the s states of the B-site cation [12]. Based on this electronic structure, the pseudopotentials of both the B cation and the halogen atom were modified by removing half an electron from the corresponding orbitals. As discussed above, the cutoff radius r_{cut} must be optimized for each corrected orbital by using the condition of maximum band gap. In the present work, the optimal r_{cut} values were determined in $CsPbI_3$ by sequentially sweeping the cutoff radii of the Pb $6s$ and I $5p$ orbitals, as shown in Fig. 2.2. A full two-dimensional optimization was not necessary, since the optimal cutoff radius of each orbital was essentially independent of that of the other. Thus, one cutoff radius was optimized first, and the obtained value was then kept fixed while optimizing the second. The results show that the optimal r_{cut} values are nearly independent of the choice of exchange-correlation functional, although the absolute band-gap values change slightly. The final optimized r_{cut} values used for the $CsBX_3$ compounds are listed in Table 2.1.

2.2 Lattice Dynamics and Generation/Analysis of Locally Positionally Disordered Structures

2.2.1 Anharmonic Special Displacement Method (ASDM)

In many perovskites, the ideal high-symmetry structure is not the true local ground-state arrangement of the atoms due to anharmonicity. Although the average crystal may ap-

Table 2.1: Optimized cutoff radii r_{cut} (a.u.) used in the DFT-1/2 correction for the relevant atomic orbitals in the $CsBX_3$ compounds.

Material	Pb	Sn	I	Br	Cl
$CsPbI_3$	2.1		3.8		
$CsPbBr_3$	2.2			3.4	
$CsPbCl_3$	2.2				3.2
$CsSnI_3$		2.3	3.6		
$CsSnBr_3$		2.3		3.2	
$CsSnCl_3$		2.4			3.0

pear highly symmetric, the atoms often prefer to move away from their ideal Wyckoff positions through octahedral tilting, cation off-centering, or other local distortions. For this reason, the ideal high-symmetry structure is commonly called the *monomorphous* structure, while the supercell with positional local disorder is called the *polymorphous* structure. A supercell is needed to represent the polymorphous structure because these local symmetry-breaking distortions cannot be accounted for within the small primitive cell. In a harmonic crystal, the potential-energy surface is well approximated by a single parabolic well around the equilibrium position. By contrast, strongly anharmonic perovskites are often described by a double-well potential-energy surface, as illustrated in Fig. 2.3. In this picture, the high-symmetry monomorphous structure lies near the central maximum or saddle-point region of the potential-energy surface, whereas the polymorphous structures correspond to the lower-energy minima. There are some methods to generate the polymorphous structures; in this work we employed the Anharmonic Special Displacement Method (ASDM) developed by Zacharias *et al.* [13]. We explain the theoretical framework of ASDM and the procedure for generating the polymorphous structure below.

The starting point is the potential-energy surface expanded around a chosen reference structure:

$$U(\{\tau\}) = U_0 + \frac{1}{2}\sum_{i,i'} C_{ii'}\Delta\tau_i\Delta\tau_{i'}, \tag{2.10}$$

where U_0 is the energy of the reference structure, $\Delta\tau_i$ is the displacement of atomic coordinate i, and

$$C_{ii'} = \frac{\partial^2 U}{\partial\tau_i\partial\tau_{i'}} \tag{2.11}$$

are the interatomic force constants (IFCs). Phonons are obtained from the IFCs, which describe the curvature of the potential-energy surface around a reference structure. If the reference structure is dynamically stable, all phonon frequencies are real. By contrast, imaginary phonon frequencies indicate that the structure is unstable and can lower its energy through a symmetry-breaking distortion. Therefore, the eigenvectors of the unstable soft modes provide the physically meaningful directions used to construct the initial distorted supercell.

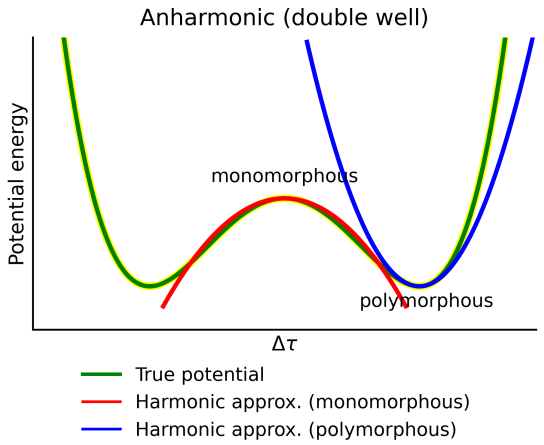

Figure 2.3: Schematic representation of an anharmonic double-well potential-energy surface. The high-symmetry monomorphous structure is located near the central maximum, while the symmetry-broken polymorphous structures correspond to the minima.

The special displacement method (SDM) provides a systematic way to construct such a symmetry-broken supercell. The idea of SDM [14] comes from the Williams–Lax [15, 16] picture of lattice vibrations, where a temperature-dependent observable is written as an average over many nuclear configurations. In the harmonic approximation, this average becomes a multidimensional Gaussian integral over the phonon normal coordinates. In practice, evaluating this integral directly would require many randomly displaced structures, for example from Monte Carlo sampling [17] or molecular dynamics [18]. The key idea of SDM is that, for a sufficiently large supercell, this configurational average can be approximated by *one carefully chosen displacement pattern*. This single configuration is called the Zacharias–Giustino (ZG) displacement [14].

To understand the ZG displacement, it is useful to recall that the displacement of atom κ in cell p can be expanded in phonon normal modes as

$$\Delta\tau_{p\kappa\alpha} = \frac{1}{\sqrt{N_p}} \left(\frac{M_0}{M_\kappa}\right)^{1/2} \sum_{\mathbf{q}\nu} e^{i\mathbf{q}\cdot\mathbf{R}_p} e_{\kappa\alpha,\nu}(\mathbf{q})\, z_{\mathbf{q}\nu}, \tag{2.12}$$

where N_p is the number of primitive cells in the supercell, M_κ is the mass of atom κ, M_0 is a reference mass, $\mathbf{R}_p$ is the lattice vector of cell p, $e_{\kappa\alpha,\nu}(\mathbf{q})$ is the phonon eigenvector, and $z_{\mathbf{q}\nu}$ is the normal coordinate of mode $(\mathbf{q}\nu)$. This equation shows that any atomic distortion can be written as a sum of phonon eigenvectors. Therefore, the phonons already contain the physically correct distortion patterns of the crystal.

In the SDM, the many possible values of $z_{\mathbf{q}\nu}$ are replaced by one special choice that reproduces the thermal average as closely as possible. This leads to the ZG displacement:

$$\Delta\tau^{\mathrm{ZG}}_{p\kappa\alpha} = \left(\frac{M_0}{N_p M_\kappa}\right)^{1/2} \sum_{\mathbf{q}\nu} S_{\mathbf{q}\nu}\, u_{\mathbf{q}\nu}(T)\, \mathrm{Re}\left[e^{i\mathbf{q}\cdot\mathbf{R}_p} e_{\kappa\alpha,\nu}(\mathbf{q})\right]. \tag{2.13}$$

This is the central equation of the method. Its meaning is simple. The *direction* of each atomic displacement is given by the phonon eigenvector $e_{\kappa\alpha,\nu}(\mathbf{q})$. The phase factor $e^{i\mathbf{q}\cdot\mathbf{R}_p}$ tells how the distortion changes from one cell to another across the supercell. The real part is taken because the final atomic positions must be real. The factor $S_{\mathbf{q}\nu} = \pm 1$ is a sign chosen so that the combined supercell distortion best reproduces the average effect of many vibrational configurations. The sign factors $S_{\mathbf{q}\nu}$ are not chosen from a fixed physical convention. Instead, Zacharias and Giustino [14] introduced a normalized error function $E(\{S_{\mathbf{q}\nu}\})$ to determine the most suitable sign pattern for a given supercell. This function measures the unwanted cross terms between different phonon modes that remain in a finite supercell representation. The optimal set of signs is chosen by minimizing this error function, so that the ZG-displaced supercell reproduces the vibrational mean-square displacements as accurately as possible. Therefore, the signs are selected algorithmically within the ASDM implementation. In this way, the ZG displacement is not an arbitrary distortion, but a compact and physically motivated representation of lattice disorder written in terms of phonon modes.

The amplitude $u_{\mathbf{q}\nu}(T)$ is determined by the mean-square displacement of each phonon mode. In the harmonic approximation,

$$u^2_{\mathbf{q}\nu}(T) = \frac{\hbar}{2M_0\omega_{\mathbf{q}\nu}} \left(2n_{\mathbf{q}\nu,T} + 1\right), \tag{2.14}$$

where $\omega_{\mathbf{q}\nu}$ is the phonon frequency and

$$n_{\mathbf{q}\nu,T} = \frac{1}{\exp(\hbar\omega_{\mathbf{q}\nu}/k_BT) - 1} \tag{2.15}$$

is the Bose–Einstein occupation factor. This equation shows that soft modes have larger displacement amplitudes because their frequencies are small. It also shows that the displacement does not vanish even at $T = 0$.

At zero temperature, $n_{\mathbf{q}\nu,T} = 0$, and the amplitude becomes

$$u^2_{\mathbf{q}\nu}(0) = \frac{\hbar}{2M_0\omega_{\mathbf{q}\nu}}, \qquad u_{\mathbf{q}\nu}(0) = \sqrt{\frac{\hbar}{2M_0\omega_{\mathbf{q}\nu}}}. \tag{2.16}$$

This is the quantum zero-point displacement. It comes directly from the ground state of the quantum harmonic oscillator. For this reason, the SDM provides a natural scale for the initial atomic distortion even when the goal is only to generate a ground-state polymorphous structure [13] and can be used to treat anharmonicity; therefore, it is called ASDM.

Although Zacharias *et al.* [13] showed that random displacements, all-mode ZG displacements, and soft-mode ZG displacements can all relax to similar polymorphous structures with comparable energy lowering, the use of soft-mode ZG displacements is more practical for generating the initial structure. The reason is that the soft-mode eigenvectors already describe the main structural instabilities of the monomorphous phase, such as octahedral tilting and related symmetry-breaking motions. Therefore, they move the

atoms directly along the physically relevant directions of energy lowering and place the initial supercell closer to the local minimum of the potential-energy surface. Random displacements can also break the symmetry, but they are less controlled because their effectiveness depends on the chosen displacement pattern and amplitude. For this reason, soft-mode ZG displacements provide a more systematic and physically motivated route for generating the polymorphous ground-state structure. This is the main idea of ASDM and explains the main difference from SDM. The polymorphous concept introduced by Zunger and coworkers [19] in fact provides a quansistatic picture of a lattice disorder, and does not describe the ultra-low frequency structural relaxations at the origin of this disorder. This is also a limit for the approach based on the ASDM method. Simulating explicitely these low-frequency structural relaxations could be in principle achieve with molecular dynamics (MD) , but this would require very long and accurate MD simulation run including a proper description of strain relaxation (NPT ensemble).

A practical difficulty is that unstable soft modes of the monomorphous phase have imaginary frequencies. In that case, the harmonic amplitude formula above cannot be used directly, because it contains $1/\omega_{\mathbf{q}\nu}$. Therefore, for unstable modes, the ZG expression should be understood mainly as a way to define the *pattern* of the distortion rather than its final amplitude. In practice, one applies a finite trial amplitude along the soft-mode eigenvectors to generate an initial symmetry-broken supercell. This trial amplitude should be chosen by replacing the imaginary frequency with a positive auxiliary value only for the construction of the initial displacement. This step is only a numerical procedure to start the relaxation.

The EPW `ZG.x` tool [13] was developed to implement the ASDM framework and can be used to generate symmetry-broken supercells based on the ZG displacement. In the same development, the `bands_unfold.x` tool was also introduced to unfold from the (small) supercell Brillouin zone to the Brillouin zone of the high symmetry unit cell. In the present work, both `ZG.x` and `bands_unfold.x`, as implemented in the Quantum ESPRESSO code, were used for the generation and analysis of polymorphous structures.

In practice, the ground-state polymorphous structure was generated using the following procedure:

- First, the phonon dispersion of the monomorphous structure was calculated using DFPT.
- From the DFPT calculations, the IFCs were obtained.
- In the `ZG.x` code, the eigenvectors of the unstable soft modes were identified using the IFCs of the monomorphous structure. These soft-mode eigenvectors were then combined, following the ASDM approach, to define the symmetry-breaking displacement pattern. In this way, an initial supercell containing the ZG displacement was generated.
- This distorted supercell was then fully relaxed within DFT so that the atoms could move toward the nearest local minimum of the potential-energy surface. The re-

laxed structure was taken as the candidate polymorphous ground-state configuration.

- To verify its dynamical stability, the phonon dispersion of the relaxed supercell was subsequently calculated using the frozen-phonon method (FPM).

- When no imaginary phonon modes were present, the relaxed structure was considered to be the polymorphous ground-state configuration and was used for the subsequent calculations.

The advantage of this approach is that it is more physical than applying completely random displacements [19]. Random displacements may also break the symmetry, but they do not necessarily follow the true lattice-instability directions of the crystal. In contrast, the ASDM-based construction uses the phonon eigenvectors of the unstable modes, so the initial distortion is directly connected to the intrinsic structural instability of the material. For this reason, it provides a systematic and physically motivated route for generating the polymorphous ground-state supercell of anharmonic perovskites.

2.2.2 Pair Distribution Function (PDF)

Conventional X-ray diffraction mainly provides information about the *average* crystal structure because the measured Bragg peaks reflect long-range periodic order. However, materials contain positional local disorder that is not fully captured by the average structure. For this reason, the PDF is used to analyze the local atomic arrangement. With more advanced experimental setups, the PDF can be measured experimentally from total-scattering data by Fourier transforming the properly corrected scattering signal [20, 21].

In the present work, the PDF was calculated directly from atomistic structural models. For this purpose, a custom Python script was developed instead of using an external package such as PDFgui [22]. The script reads the structural information from the input file, generates a supercell large enough to include all interatomic distances up to the chosen cutoff, and then calculates the distribution of pair distances. The implementation therefore provides a direct real-space description of the local structure from the atomic coordinates.

First, the distance between atoms i and j is calculated from their Cartesian coordinates:

$$r_{ij} = |\mathbf{R}_j - \mathbf{R}_i| \,. \tag{2.17}$$

Here, $\mathbf{R}_i$ and $\mathbf{R}_j$ are the position vectors of two atoms in the supercell. To avoid missing any relevant neighbors, the unit cell was repeated in all directions until the supercell size exceeded the maximum PDF distance used in the calculation. In this way, all pair distances in the range $r_{\min} \leq r_{ij} \leq r_{\max}$ were included.

After the pair distances were obtained, they were sorted into distance bins of width Δr. For each atom-pair type α-β, the partial PDF was normalized by the volume of the

spherical shell and by the number of central atoms:

$$g_{\alpha\beta}(r) = \frac{N_{\alpha\beta}(r)}{4\pi r^2 \, \Delta r \, N_\alpha}, \tag{2.18}$$

where $N_{\alpha\beta}(r)$ is the number of α-β pairs found in the interval $[r, r + \Delta r]$, and N_α is the number of atoms of type α. This normalization is important because the number of possible neighbors naturally increases with distance as the surface area of a sphere, $4\pi r^2$. The same procedure was also used to obtain the total PDF, where the normalization was performed using the total number of atoms in the structure. This is the central expression used in the script for the PDF calculation.

Because a histogram of discrete pair distances produces sharp spikes, a Gaussian broadening was applied to obtain a smooth PDF curve:

$$G(r) = \sum_m y_m \frac{1}{\sigma\sqrt{2\pi}} \exp\left[-\frac{(r - r_m)^2}{2\sigma^2}\right]. \tag{2.19}$$

Here, r_m is the position of a histogram peak, y_m is its intensity, and σ is the Gaussian width. In the present implementation, $\sigma = 0.1$ Å was used. This step converts the discrete histogram into a continuous curve that is easier to compare between different structural models and also experimental results.

Using this approach, the PDFs of the monomorphous and polymorphous structures were calculated on the same distance grid and compared directly [19]. Since the calculation starts from the atomic coordinates, the resulting PDF is sensitive to local bond-length variations and short-range distortions, making it a useful tool for distinguishing structures that may appear similar in the average crystallographic description.

2.3 Surface and Interface Property Calculations

2.3.1 Surface and interface slab construction

In *ab initio* calculations of surface properties, constructing a reliable surface slab is essential. In general, there are two main types of slab models: symmetric and asymmetric. Asymmetric slabs usually require a dipole correction, whereas in symmetric slabs the dipole moments from the two surfaces cancel because of symmetry. As a result, symmetric slabs usually show better convergence. For this reason, all surface calculations in this work were performed using symmetric slab models.

Among the surfaces of halide perovskites, the (001) surface is one of the most stable and commonly studied orientations [23, 24, 25, 26]. Therefore, we constructed slabs with the (001) orientation. The crystal structure of $CsBX_3$ consists of alternating CsX and BX_2 layers, which gives rise to two possible surface terminations: CsX and BX_2. To construct a symmetric slab with the same termination on both sides, one CsX or BX_2 layer was removed from one side of the supercell, and the same amount of vacuum was added on both sides of the slab. In addition, a $2 \times 2 \times 8$ supercell was constructed to account

for possible surface reconstructions. Based on convergence tests of the absolute valence-band maximum (VBM) and surface energy, a slab thickness of 8 octahedral layers and a vacuum thickness of 20 were found to be sufficient.

Figure 2.4 shows the monomorphous and polymorphous surface slabs of $CsPbI_3$ with CsI and PbI_2 terminations. The monomorphous slab was constructed from the monomorphous unit cell, whereas the polymorphous slab was built from a $2 \times 2 \times 2$ polymorphous bulk supercell generated using ASDM. During structural relaxation, the atoms in the middle layers of the slab were fixed, while the atoms near the two surfaces, corresponding to two octahedral layers, were allowed to relax. In this way, the central region of the slab retains a bulk-like structure, which better represents a realistic surface model, as illustrated in Figure 2.4 [27].

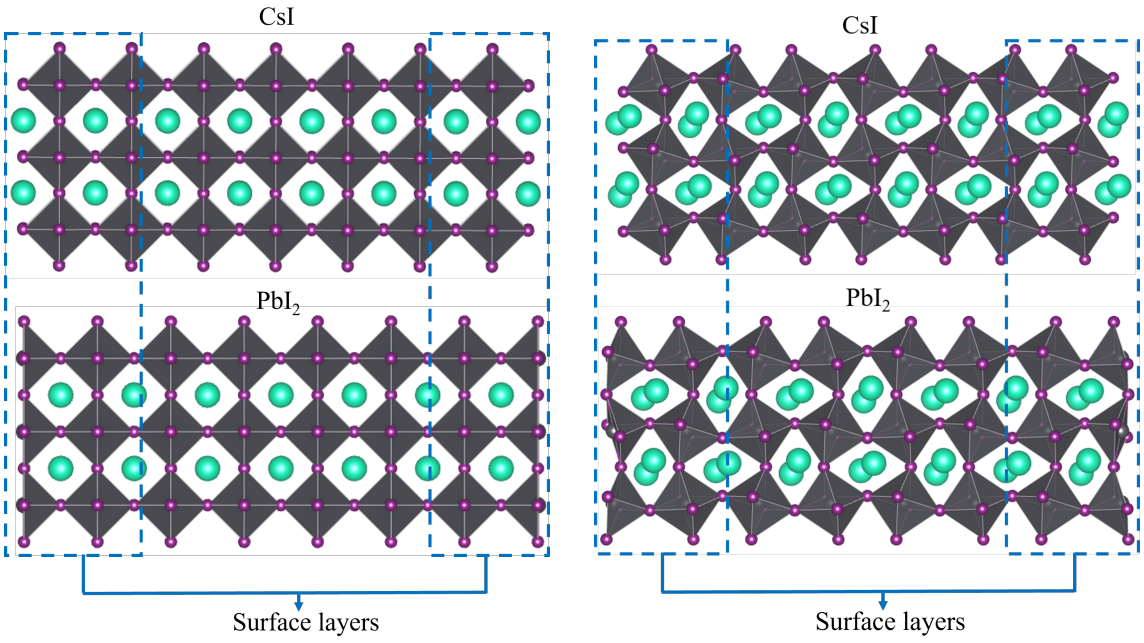

Figure 2.4: Surface slab models used in this work: (a) monomorphous and (b) polymorphous slabs. The regions marked by dashed boxes indicate the surface layers in which the atoms were allowed to relax during structural optimization, while the middle layers were kept fixed to preserve the bulk-like character of the slab.

We also investigated the surface properties of all-inorganic 2D perovskites $Cs_{n+1}Pb_nI_{n+1}Cl_{2n}$ for $n = 1$ to $n = 5$. Monomorphous surface slabs were constructed for all phases from $n = 1$ to $n = 5$, while a polymorphous slab was built only for the $n = 2$ phase. For phases with $n > 2$, polymorphous slabs become too large and computationally too expensive for *ab initio* calculations. In these 2D perovskites, three main surface terminations are possible: CsI, double-CsI, and $PbCl_2$. Symmetric slabs with identical terminations on both sides were constructed for all 2D systems. For the 2D

perovskite surface calculations also, 8 octahedral layers and a 20 Å vacuum region were sufficient to achieve convergence in both the absolute VBM and the surface energy.

For the 2D/3D interface models, symmetric regions were built on both the left and right sides of the interface in order to avoid spurious dipole–dipole interactions. In total, six types of interfaces are possible, because the 2D perovskite has three possible terminations and the 3D perovskite has two. As an example, the CsBr/$PbCl_2$-terminated interface is shown in Figure 2.5.

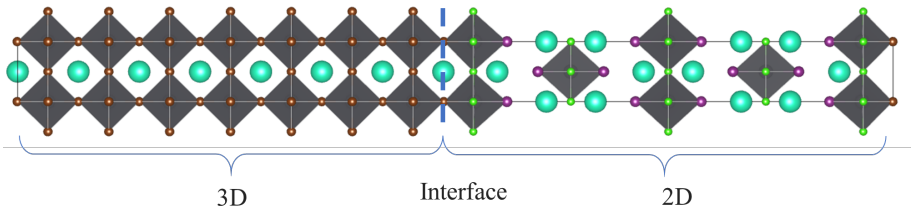

Figure 2.5: Atomic model of the symmetric $CsPbBr_3/Cs_2PbI_2Cl_2$ interface with CsBr and $PbCl_2$ terminations. The symmetric construction on both sides of the interface avoids artificial dipole interactions.

2.3.2 Planar and macroscopic averages of physical quantities for surfaces and interfaces

For a surface slab or an interface, the electrostatic potential and the charge density vary strongly at the atomic scale. These rapid oscillations make it difficult to identify quantities such as the vacuum level, interface dipole, and potential lineup directly from the raw three-dimensional data. A useful way to remove the atomic-scale oscillations is to first calculate the planar average and then the macroscopic average.

This approach has been widely used in band alignment studies. In particular, Baldereschi, Baroni, and Resta introduced the potential-lineup method for heterojunctions, and later reviews discussed the use of macroscopic averaging in a more general way for surfaces and interfaces [28].

Planar average. For any physical quantity $F(\mathbf{r})$ (for example, the electrostatic potential or charge density), the planar average along the z direction is defined as

$$\overline{F}(z) = \frac{1}{A}\int_A F(x,y,z)\,dx\,dy, \tag{2.20}$$

where A is the area of the plane parallel to the surface or interface. This averaging removes the in-plane variation and gives a one-dimensional function of z.

Macroscopic average for a surface slab. The planar-averaged quantity still contains oscillations due to the atomic layers. For a surface slab, these oscillations can be

smoothed by averaging over one lattice period L along the surface-normal direction:

$$\langle F\rangle_{\mathrm{surf}}(z) = \frac{1}{L}\int_{z-L/2}^{z+L/2} \overline{F}(z')\,dz'. \tag{2.21}$$

Here, L is chosen as the lattice periodicity of the slab material along the z direction. The resulting macroscopic average varies slowly with position and is useful for determining the bulk-like reference potential and the vacuum level, because in a perfect bulk this quantity is, by definition, constant..

Macroscopic average for an interface. For an interface between two materials, the two regions generally have different lattice periods along the interface-normal direction. In this case, the macroscopic average is obtained by smoothing the planar average twice, once with the period L_1 of material 1 and once with the period L_2 of material 2:

$$\langle F\rangle_{\mathrm{int}}(z) = \frac{1}{L_2}\int_{z-L_2/2}^{z+L_2/2}\left[\frac{1}{L_1}\int_{z'-L_1/2}^{z'+L_1/2}\overline{F}(z'')\,dz''\right]dz'. \tag{2.22}$$

This double smoothing removes the oscillations associated with both materials and gives a slowly varying profile across the interface. From the plateau values in the two bulk-like regions, one can obtain the interface potential lineup.

2.3.3 Absolute band positions of surfaces and band offsets of interfaces

The absolute band positions and the band offsets were obtained from the planar-averaged and macroscopic-averaged electrostatic potentials using the standard lineup approach introduced by Van de Walle [29]. In addition, a correction to the bulk VBM from DFT-1/2 was included to improve the band-edge positions, and the DFT-1/2 band gap was used to determine the conduction-band minimum (CBM) [9].

For the surface slab calculation, we first evaluated the planar-averaged electrostatic potential and then obtained its macroscopic average. A schematic example is shown in Fig. 2.6. From the macroscopic average of the slab, two plateau regions were identified: a bulk-like plateau inside the slab, denoted by $V_{\mathrm{slab}}^{\mathrm{bulk}}$, and a vacuum plateau, denoted by $V_{\mathrm{slab}}^{\mathrm{vac}}$, as illustrated in Fig. 2.6. The difference between these two quantities gives the electrostatic-potential alignment between the bulk-like region of the slab and the vacuum level.

The bulk calculation was used to determine the position of the VBM with respect to the bulk macroscopic average electrostatic potential, written as $E_{\mathrm{VBM}}^{\mathrm{bulk}} - V_{\mathrm{bulk}}$. To account for the self-interaction correction, we added the DFT-1/2 shift of the bulk VBM, denoted by $\Delta E_{\mathrm{VBM}}^{\mathrm{DFT}-1/2}$. In practice, semilocal DFT usually describes the ground-state charge density and electrostatic potential reasonably well, but it often underestimates the band gap and can yield inaccurate band-edge energies relative to the reference potential. This term

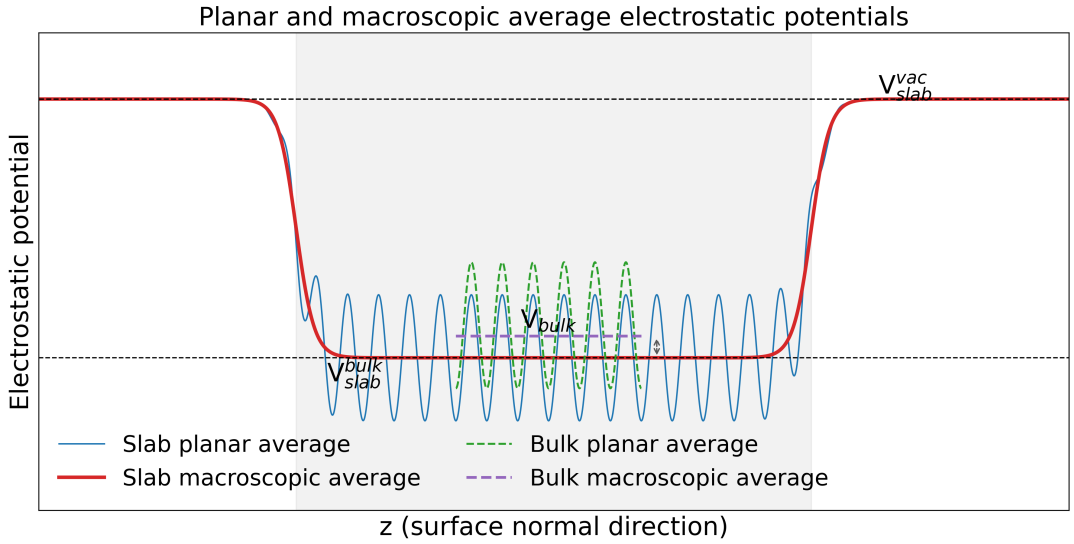

Figure 2.6: Schematic planar-averaged and macroscopically averaged electrostatic potentials for the surface slab calculation. The vacuum plateau $V^{\mathrm{vac}}_{\mathrm{slab}}$ and the bulk-like plateau $V^{\mathrm{bulk}}_{\mathrm{slab}}$ are extracted from the slab macroscopic average, while V_{bulk} is obtained from the corresponding bulk calculation.

therefore corrects the bulk VBM position relative to the bulk electrostatic potential. The absolute VBM, referenced to the vacuum level, is then calculated as

$$E^{\mathrm{abs}}_{\mathrm{VBM}} = \left(E^{\mathrm{bulk}}_{\mathrm{VBM}} - V_{\mathrm{bulk}}\right) + \left(V^{\mathrm{bulk}}_{\mathrm{slab}} - V^{\mathrm{vac}}_{\mathrm{slab}}\right) + \Delta E^{\mathrm{DFT}-1/2}_{\mathrm{VBM}}. \tag{2.23}$$

The CBM was then calculated from the absolute VBM and the DFT-1/2 band gap,

$$E^{\mathrm{abs}}_{\mathrm{CBM}} = E^{\mathrm{abs}}_{\mathrm{VBM}} + E^{\mathrm{DFT}-1/2}_{g}. \tag{2.24}$$

For the interface supercell calculation, the planar-averaged electrostatic potential was first evaluated along the interface-normal direction and then macroscopically averaged. From the macroscopic average of the interface supercell, two bulk-like plateau regions were identified on the left and right sides of the interface, denoted by V_L and V_R, respectively, as shown in Fig. 2.7. Their difference,

$$\Delta V_{\mathrm{int}} = V_R - V_L, \tag{2.25}$$

represents the potential lineup across the interface.

The bulk calculations of the two isolated materials were then used to determine the position of each VBM with respect to its own bulk macroscopic average electrostatic potential, namely $E^{L}_{\mathrm{VBM}} - V^{L}_{\mathrm{bulk}}$ for the left side material and $E^{R}_{\mathrm{VBM}} - V^{R}_{\mathrm{bulk}}$ for the material on the right side of the interface. The DFT-1/2 correction was included through the VBM shifts of the two bulk materials. These shifts correct the bulk VBM positions relative to

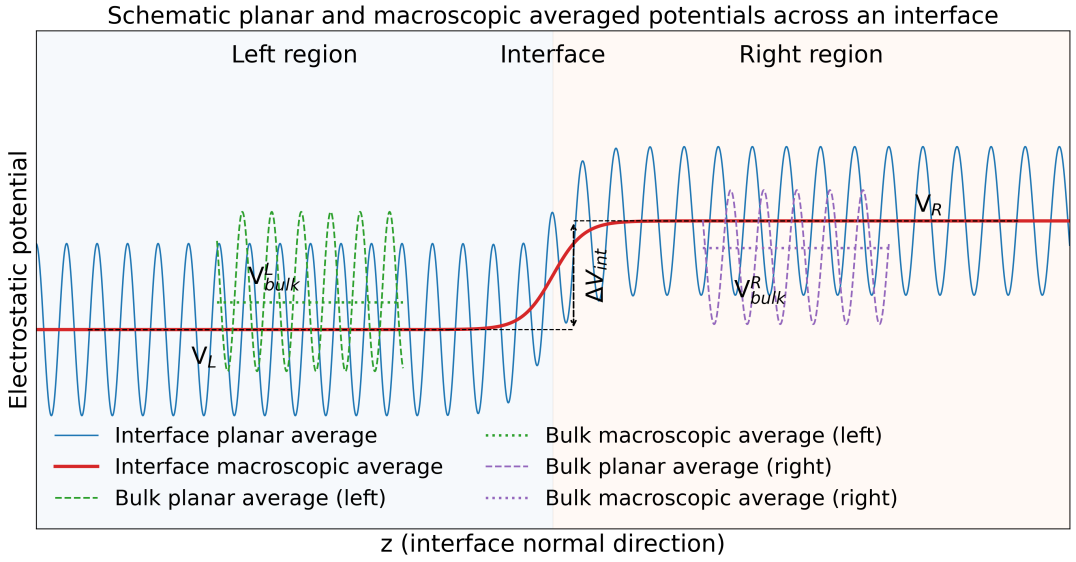

Figure 2.7: Schematic planar-averaged and macroscopically averaged electrostatic potentials for the interface calculation. The macroscopic averages on the left and right bulk-like regions give the interface lineup $\Delta V_{\mathrm{int}} = V_R - V_L$. The quantities V^L_{bulk} and V^R_{bulk} are obtained from the separate bulk calculations of the left and right materials.

their corresponding bulk electrostatic potentials. Accordingly, the valence band offset (VBO) is calculated as

$$\begin{aligned} \mathrm{VBO} = &\left[\left(E^R_{\mathrm{VBM}} - V^R_{\mathrm{bulk}}\right) + \Delta E^{\mathrm{DFT}-1/2,R}_{\mathrm{VBM}} \right] \\ -&\left[\left(E^L_{\mathrm{VBM}} - V^L_{\mathrm{bulk}}\right) + \Delta E^{\mathrm{DFT}-1/2,L}_{\mathrm{VBM}} \right] + \Delta V_{\mathrm{int}}. \end{aligned} \tag{2.26}$$

In the present 2D/3D perovskite interface, DFT-1/2 was found to describe the ionization potential and the bulk VBM shift well, but it underestimates the band gap of the 2D perovskites [9]. For this reason, the conduction-band offset (CBO) was not calculated from the DFT-1/2 band gap. Instead, we used the experimental band gaps of the two materials. The CBO is given by

$$\mathrm{CBO} = \mathrm{VBO} + E_g^{\mathrm{exp},R} - E_g^{\mathrm{exp},L}. \tag{2.27}$$

Thus, in the interface analysis, the DFT-1/2 correction enters only through the bulk VBM shifts, whereas the CBO is evaluated using the experimental band gaps.

2.3.4 Strain correction of band offsets

For coherent interfaces with negligible or modest strain effects, the VBO can be obtained directly from the standard lineup approach given in Eq. 2.26. However, for lattice-mismatched pseudomorphic interfaces, strain modifies the VBM positions of the two materials, and this effect should be included explicitly. We explore two correction

schemes, the first based on the so-called Absolute Deformation Potentials (ADP) [30], the second, called the three step approach [31], relies on a decomposition of the interface strain. Following the model-solid approach of Van de Walle [30], the strain-corrected valence-band offset can be written as

$$\mathrm{VBO}_{\mathrm{ADP}} = \mathrm{VBO} + \Delta E_{\mathrm{VBM}}^{\mathrm{strain},R} - \Delta E_{\mathrm{VBM}}^{\mathrm{strain},L}, \tag{2.28}$$

where the strain-induced VBM shift of each material is expressed, to first order, as

$$\Delta E_{\mathrm{VBM}}^{\mathrm{strain}} \approx a_v \,\mathrm{Tr}(\varepsilon) + \Delta E_{\mathrm{VBM}}^{\mathrm{shear}}. \tag{2.29}$$

Here, a_v is the hydrostatic valence-band absolute deformation potential (ADP), ε is the strain tensor, and $\Delta E_{\mathrm{VBM}}^{\mathrm{shear}}$ denotes the shear-strain contribution to the VBM shift. For small hydrostatic strain, $\mathrm{Tr}(\varepsilon) \approx \Delta\Omega/\Omega$.

The hydrostatic valence-band ADP of each material is obtained from the shift of the bulk VBM under hydrostatic strain as [32]

$$a_v = \frac{\Delta\left(E_{\mathrm{VBM}} - V_{\mathrm{bulk}}\right)}{\mathrm{Tr}(\varepsilon)}. \tag{2.30}$$

Thus, a_v measures the hydrostatic change in the VBM position relative to the bulk macroscopic average electrostatic potential, while $\Delta E_{\mathrm{VBM}}^{\mathrm{shear}}$ accounts for the additional shift, and possible band splitting, induced by the non-hydrostatic part of the strain.

This deformation-potential treatment is most reliable when the lattice mismatch is small and the strain-induced band-edge shift remains approximately linear. For larger mismatch, or for low-symmetry systems, the approximation becomes less accurate [31, 33]. In that regime, the error in the ADP-based correction may become significant. Lang *et al.* [31] showed that the difference between the ADP result and the three-step result increases with increasing deformation, while Hu *et al.* [34] also noted that the ADP-based treatment is useful mainly for cases with small lattice mismatch.

For this reason, the three-step approach is preferred when one wants a more direct treatment of strain. Instead of correcting the final VBO through a linear deformation-potential expression, the method calculates the potential alignment step by step from first-principles heterostructures. This makes it better suited for large-lattice-mismatched systems.

The basic idea of the three-step approach is to connect the left material L and the right material R through intermediate strained structures, so that the lattice mismatch is introduced gradually rather than all at once. In this way, the lineup of the macroscopic average electrostatic potential is obtained as a sum of smaller and better-defined contributions.

Let the equilibrium lattice constants of the two materials be

$$L : (a_1, a_2, a_3), \qquad R : (b_1, b_2, b_3). \tag{2.31}$$

Two intermediate structures are introduced starting from material L:

$$L' : (b_1, a_2, a_3), \tag{2.32}$$

$$L'' : (b_1, b_2, a_3). \tag{2.33}$$

Thus, the lattice constant is changed first along one in-plane direction, then along the second in-plane direction, and finally the resulting structure L'' is aligned with the equilibrium structure of material R. The method can be generalized to other interface orientations in the same way.

In a direct interface calculation, the potential lineup is obtained from Eq. 2.25. In the three-step approach, this total lineup is decomposed into three successive contributions,

$$\Delta V_{\mathrm{int}}^{\mathrm{3step}} = \Delta V_{L/L'} + \Delta V_{L'/L''} + \Delta V_{L''/R}, \tag{2.34}$$

with

$$\Delta V_{L/L'} = V_{L'} - V_{L}, \tag{2.35}$$
$$\Delta V_{L'/L''} = V_{L''} - V_{L'}, \tag{2.36}$$
$$\Delta V_{L''/R} = V_{R} - V_{L''}. \tag{2.37}$$

Here, each ΔV term is obtained from a separate heterostructure calculation between two neighboring structures in the sequence. The terms $\Delta V_{L/L'}$ and $\Delta V_{L'/L''}$ represent the strain-induced potential lineups associated with the progressive lattice transformation, while $\Delta V_{L''/R}$ represents the final interface lineup. Therefore, the full potential alignment between L and R is recovered as the sum of three smaller potential lineups.

The three-step valence-band offset can then be written as

$$\begin{aligned} \mathrm{VBO}_{\mathrm{3step}} = &\Big[\left(E_{\mathrm{VBM}}^{R} - V_{\mathrm{bulk}}^{R}\right) + \Delta E_{\mathrm{VBM}}^{\mathrm{DFT}-1/2,R} \Big] \\ -&\Big[\left(E_{\mathrm{VBM}}^{L} - V_{\mathrm{bulk}}^{L}\right) + \Delta E_{\mathrm{VBM}}^{\mathrm{DFT}-1/2,L} \Big] + \Delta V_{\mathrm{int}}^{\mathrm{3step}}. \end{aligned} \tag{2.38}$$

This equation has the same structure as the standard lineup expression in Eq. 2.26, but the single interface lineup ΔV_{int} is replaced by the sum of three stepwise lineups. The advantage of this formulation is that strain is treated explicitly through actual interface calculations between neighboring structures, rather than through a linear deformation-potential correction. For this reason, the method remains more reliable when the deformation is too large for the ADP approximation to be accurate.

Once the strain-corrected valence-band offset is obtained from Eq. (2.38), the CBO can be evaluated from $\mathrm{VBO}_{\mathrm{3step}}$ and the experimental band gaps using Eq. (2.27).

2.3.5 Surface dipoles

The difference in the absolute valence-band maximum (VBM) among different surface terminations can be understood in terms of the surface dipole [27]. In a slab geometry, termination-dependent charge redistribution near the surface modifies the electrostatic potential step between the bulk-like region of the slab and the vacuum region. This potential step shifts the vacuum level and therefore changes the vacuum-referenced band energies, including the absolute VBM.

To define the surface dipole, we start from the electric displacement field,

$$\mathbf{D} = \varepsilon_0 \mathbf{E} + \mathbf{P}, \tag{2.39}$$

where $\mathbf{E}$ is the electric field, $\mathbf{P}$ is the polarization density, and ε_0 is the vacuum permittivity. Taking the divergence of Eq. (2.39) and using Gauss's law gives

$$\nabla \cdot \mathbf{D} = \rho_{\text{free}}, \qquad -\nabla \cdot \mathbf{P} = \rho_b, \tag{2.40}$$

where ρ_{free} and ρ_b are the free-charge and bound-charge densities, respectively. For an insulating slab, $\rho_{\text{free}} = 0$, so the relevant microscopic charge redistribution is described by the bound charge density. For a slab normal to the z direction, using planar averaging,

$$\overline{\rho_b}(z) = -\frac{dP_z(z)}{dz}. \tag{2.41}$$

The dipole moment density associated with one surface is given by the first moment of the bound charge density,

$$p_s = \int_{z_0}^{c/2} (z - z_0)\overline{\rho_b}(z)\, dz, \tag{2.42}$$

where z_0 is chosen at the center of the bulk-like region of the symmetric slab and $c/2$ is the center of the vacuum region. Substituting Eq. (2.41) into Eq. (2.42) gives

$$p_s = -\int_{z_0}^{c/2} (z - z_0)\frac{dP_z(z)}{dz}\, dz. \tag{2.43}$$

Integrating by parts,

$$p_s = -\left[(z - z_0)P_z(z)\right]_{z_0}^{c/2} + \int_{z_0}^{c/2} P_z(z)\, dz. \tag{2.44}$$

For a symmetric slab, the polarization vanishes at the slab center and at the middle of the vacuum region, so the boundary term is zero. Therefore,

$$p_s = \int_{z_0}^{c/2} P_z(z)\, dz. \tag{2.45}$$

To relate the surface dipole to the electrostatic potential step, we now use Poisson's equation for the planar-averaged electrostatic potential,

$$\frac{d^2\overline{V}(z)}{dz^2} = -\frac{\overline{\rho_b}(z)}{\varepsilon_0}, \tag{2.46}$$

together with

$$E(z) = -\frac{d\overline{V}(z)}{dz}. \tag{2.47}$$

Using Eq. (2.41), Poisson's equation becomes

$$\frac{dE(z)}{dz} = \frac{\rho_b(z)}{\varepsilon_0} = -\frac{1}{\varepsilon_0}\frac{dP_z(z)}{dz}. \tag{2.48}$$

Integrating with respect to z gives

$$E(z) = -\frac{P_z(z)}{\varepsilon_0} + C. \tag{2.49}$$

For a symmetric slab, the electric field vanishes in the vacuum region and P_z also vanishes there, so the integration constant is zero. Thus,

$$E(z) = -\frac{P_z(z)}{\varepsilon_0}. \tag{2.50}$$

The potential step associated with one surface is then

$$\Delta V = V\left(\frac{c}{2}\right) - V(z_0) = -\int_{z_0}^{c/2} E(z)\, dz. \tag{2.51}$$

Substituting Eq. (2.50) yields

$$\Delta V = \frac{1}{\varepsilon_0}\int_{z_0}^{c/2} P_z(z)\, dz. \tag{2.52}$$

Using Eq. (2.45), we finally obtain

$$\Delta V = \frac{p_s}{\varepsilon_0}. \tag{2.53}$$

Therefore, differences in surface dipole directly produce differences in the electrostatic potential step, which in turn shift the vacuum level, the work function, and the absolute VBM.

In practice, the surface dipole was evaluated from the planar-averaged total microscopic charge density. The electronic contribution was obtained from Quantum ESPRESSO, which outputs only the electronic charge density. To construct the total charge density, the ionic contribution was added separately using Gaussian distributions centered at the atomic positions:

$$\rho(z) = \rho_{\mathrm{ion}}(z) + \rho_{\mathrm{el}}(z), \tag{2.54}$$

with

$$\rho_{\mathrm{ion}}(z) = \sum_{i=1}^{N} \frac{q_i}{\sigma_i\sqrt{2\pi}} \exp\left[-\frac{(z-z_i)^2}{2\sigma_i^2}\right], \tag{2.55}$$

where q_i is the ionic charge assigned to atom i, z_i is the atomic position along the surface-normal direction, and σ_i is the Gaussian width. Electronic density calculated by Quantum ESPRESSO is given as a positive electron-number density; its sign must be reversed when constructing the physical charge density.

2.3.6 Surface energy

Non-stoichiometric surface slabs require introducing elemental chemical potentials, which vary with the experimental conditions during growth and operation [35, 36]. We write each elemental chemical potential as a deviation from its most stable elemental reference:

$$\mu_i = \mu_i^0 + \Delta\mu_i \qquad \mu_i^0 \equiv E_i \tag{2.56}$$

where E_i is the total energy per atom of the elemental reference phase of species i, and $\Delta\mu_i \leq 0$ under equilibrium with that reference, to prevent elemental precipitation.

A symmetric slab generally contains a different number of atoms than an integer multiple of the bulk formula, that is, the slab is not stoichiometric. There are thus excess atoms ΔN_i of each species relative to N_{bulk} bulk formula units. The surface energy of a symmetric slab is calculated as follows [36]:

$$\gamma(\Delta\mu_i) = \frac{1}{2A}\left(E_{\mathrm{slab}} - N_{\mathrm{bulk}}E_{\mathrm{bulk}} - \sum_i \Delta N_i E_i - \sum_i \Delta N_i \Delta\mu_i\right) \tag{2.57}$$

where E_{slab} is the total energy of the surface slab, A is the surface area of one face, N_{bulk} is the number of bulk unit cells, and E_{bulk} is the total energy of the bulk unit cell.

For sufficiently large crystals, the surface is equilibrated with the corresponding bulk phase, which acts as a thermodynamic reservoir. This imposes constraints on the allowed chemical potentials.

For the 3D perovskite $CsPbX_3$, equilibrium with the bulk phase gives

$$\Delta\mu_{\mathrm{Cs}} + \Delta\mu_{\mathrm{Pb}} + 3\Delta\mu_X = \Delta H(\mathrm{CsPbX_3}) \tag{2.58}$$

where ΔH denotes the formation enthalpy from the elemental references. Competing secondary phases CsX and PbX_2 further bound the chemical potentials:

$$\Delta\mu_{\mathrm{Cs}} + \Delta\mu_X \leq \Delta H(\mathrm{CsX}) \tag{2.59}$$

$$\Delta\mu_{\mathrm{Pb}} + 2\Delta\mu_X \leq \Delta H(\mathrm{PbX_2}) \tag{2.60}$$

Using the bulk-equilibrium condition, we can eliminate the chemical potential of Cs,

$$\Delta\mu_{\mathrm{Cs}} = \Delta H(\mathrm{CsPbX_3}) - \Delta\mu_{\mathrm{Pb}} - 3\Delta\mu_X \tag{2.61}$$

and calculate the surface energy $\gamma(\Delta\mu_{\mathrm{Pb}}, \Delta\mu_X)$ as a function of the two remaining independent chemical potentials.

The same formalism can be applied to the 2D perovskite $Cs_{n+1}Pb_nI_{n+1}Cl_{2n}$. In this case, the surface is equilibrated with bulk $Cs_{n+1}Pb_nI_{n+1}Cl_{2n}$, and the corresponding bulk-equilibrium condition becomes

$$(n+1)\Delta\mu_{\mathrm{Cs}} + n\Delta\mu_{\mathrm{Pb}} + (n+1)\Delta\mu_{\mathrm{I}} + 2n\Delta\mu_{\mathrm{Cl}} = \Delta H(\mathrm{Cs_{n+1}Pb_nI_{n+1}Cl_{2n}}) \tag{2.62}$$

where $\Delta H(\mathrm{Cs_{n+1}Pb_nI_{n+1}Cl_{2n}})$ is the formation enthalpy of the 2D bulk phase from the elemental reference states.

Competing secondary phases further restrict the allowed chemical-potential range. For the present system, the relevant competing phases are $CsPbI_3$, $CsPbCl_3$, CsI, CsCl, PbI_2, and $PbCl_2$, which impose the following conditions:

$$\Delta\mu_{\mathrm{Cs}} + \Delta\mu_{\mathrm{I}} \leq \Delta H(\mathrm{CsI}) \tag{2.63}$$

$$\Delta\mu_{\mathrm{Cs}} + \Delta\mu_{\mathrm{Cl}} \leq \Delta H(\mathrm{CsCl}) \tag{2.64}$$

$$\Delta\mu_{\mathrm{Pb}} + 2\Delta\mu_{\mathrm{I}} \leq \Delta H(\mathrm{PbI_2}) \tag{2.65}$$

$$\Delta\mu_{\mathrm{Pb}} + 2\Delta\mu_{\mathrm{Cl}} \leq \Delta H(\mathrm{PbCl_2}) \tag{2.66}$$

$$\Delta\mu_{\mathrm{Cs}} + \Delta\mu_{\mathrm{Pb}} + 3\Delta\mu_{\mathrm{I}} \leq \Delta H(\mathrm{CsPbI_3}) \tag{2.67}$$

$$\Delta\mu_{\mathrm{Cs}} + \Delta\mu_{\mathrm{Pb}} + 3\Delta\mu_{\mathrm{Cl}} \leq \Delta H(\mathrm{CsPbCl_3}). \tag{2.68}$$

Using the bulk-equilibrium condition, we can again eliminate the chemical potential of Cs,

$$\Delta\mu_{\mathrm{Cs}} = \frac{\Delta H(\mathrm{Cs}_{n+1}\mathrm{Pb}_n\mathrm{I}_{n+1}\mathrm{Cl}_{2n}) - n\Delta\mu_{\mathrm{Pb}} - (n+1)\Delta\mu_{\mathrm{I}} - 2n\Delta\mu_{\mathrm{Cl}}}{n+1} \tag{2.69}$$

and calculate the surface energy $\gamma(\Delta\mu_{\mathrm{Pb}}, \Delta\mu_{\mathrm{I}}, \Delta\mu_{\mathrm{Cl}})$ as a function of the remaining independent chemical potentials, constrained by the competing phases listed above.

2.3.7 Adhesion energy

In first-principles calculations, interface stability is commonly evaluated using the adhesion energy, or work of adhesion, which is obtained from the total energies of the interface and the two separated surfaces [37]. This approach has been used for several halide perovskite interfaces, including TiO_2/perovskite and perovskite/HTL contacts, to assess interface stability and bonding strength [38, 39]. For 2D/3D perovskite systems, related binding-energy calculations have also been used to examine whether interface formation is energetically favorable [40]. In experiments, adhesion is usually evaluated indirectly through mechanical quantities such as fracture energy or pull-off strength. For example, double-cantilever-beam measurements showed that the $CH_3NH_3PbI_3$/HTM interface has a low fracture energy, which indicates weak mechanical adhesion [41]. Later studies further showed that stronger interfacial adhesion can improve both efficiency and operational stability in perovskite solar cells [42].

In this work, we calculate the adhesion energy to evaluate the stability of the 2D/3D perovskite interface. The adhesion energy is the energy required to separate the interface into its 2D and 3D components. First, the 2D/3D interface model is constructed and fully relaxed to obtain its total energy. Surface slabs of the 2D and 3D perovskites are then built with the same thickness as in the interface model and fully relaxed to obtain their total energies. The adhesion energy is calculated as [37]

$$E_{\mathrm{adh}} = \frac{E_{2D} + E_{3D} - E_{2D/3D}}{A} \tag{2.70}$$

where $E_{2D/3D}$ is the total energy of the relaxed interface, E_{2D} and E_{3D} are the total energies of the relaxed 2D and 3D surface slabs, and A is the interfacial area. A larger adhesion energy means that more energy is needed to separate the interface, which indicates a more stable interface.

References

[1] P Giannozzi, O Andreussi, T Brumme, O Bunau, M Buongiorno Nardelli, M Calandra, R Car, C Cavazzoni, D Ceresoli, M Cococcioni, N Colonna, I Carnimeo, A Dal Corso, S de Gironcoli, P Delugas, R A DiStasio, A Ferretti, A Floris, G Fratesi, G Fugallo, R Gebauer, U Gerstmann, F Giustino, T Gorni, J Jia, M Kawamura, H-Y Ko, A Kokalj, E Küçükbenli, M Lazzeri, M Marsili, N Marzari, F Mauri, N L Nguyen, H-V Nguyen, A Otero-de-la-Roza, L Paulatto, S Poncé, D Rocca, R Sabatini, B Santra, M Schlipf, A P Seitsonen, A Smogunov, I Timrov, T Thonhauser, P Umari, N Vast, X Wu, and S Baroni. Advanced capabilities for materials modelling with Quantum ESPRESSO. *Journal of Physics: Condensed Matter*, 29(46):465901, October 2017.

[2] Jiří Klimeš, David R. Bowler, and Angelos Michaelides. Van der Waals density functionals applied to solids. *Physical Review B*, 83(19), May 2011.

[3] Wilfried G. Aulbur, Lars Jönsson, and John W. Wilkins. *Quasiparticle Calculations in Solids*. In *Solid State Physics*. Elsevier, 2000, pages 1–218.

[4] Cesare Franchini. Hybrid functionals applied to perovskites. *Journal of Physics: Condensed Matter*, 26(25):253202, May 2014.

[5] J. P. Perdew and Alex Zunger. Self-interaction correction to density-functional approximations for many-electron systems. *Physical Review B*, 23(10):5048–5079, May 1981.

[6] Luiz G. Ferreira, Marcelo Marques, and Lara K. Teles. Approximation to density functional theory for the calculation of band gaps of semiconductors. *Physical Review B*, 78(12), September 2008.

[7] Ibrahim Buba Garba, Lorenzo Trombini, Claudine Katan, Jacky Even, Marios Zacharias, Mikael Kepenekian, and George Volonakis. Three-Dimensional to Layered Halide Perovskites: A Parameter-Free Hybrid Functional Method for Predicting Electronic Band Gaps. *ACS Materials Letters*, 7(5):1922–1929, April 2025.

[8] K. Amnuyswat and P. Thanomngam. Band gap prediction of the alloying halide perovskites using GW compare to DFT-1/2 method. In *THE SECOND MATERIALS RESEARCH SOCIETY OF THAILAND INTERNATIONAL CONFERENCE*, volume 2279, page 110002. AIP Publishing, 2020.

[9] Boubacar Traore, Jacky Even, Laurent Pedesseau, Mikaël Képénekian, and Claudine Katan. Band gap, effective masses, and energy level alignment of 2D and 3D halide perovskites and heterostructures using DFT-1/2. *Physical Review Materials*, 6(1), January 2022.

[10] Luiz G. Ferreira, Ronaldo R. Pelá, Lara K. Teles, Marcelo Marques, Mauro Ribeiro Jr., and Jürgen Furthmüller. The LDA-1/2 technique: Recent developments. In *AIP Conference Proceedings*, pages 27–28. AIP, 2013.

[11] J. F. Janak. Proof that $\partial E/\partial n_i = \epsilon_i$ in density-functional theory. *Physical Review B*, 18(12):7165–7168, December 1978.

[12] Jacky Even, Laurent Pedesseau, Jean-Marc Jancu, and Claudine Katan. Importance of Spin-Orbit Coupling in Hybrid Organic/Inorganic Perovskites for Photovoltaic Applications. *The Journal of Physical Chemistry Letters*, 4(17):2999–3005, August 2013.

[13] Marios Zacharias, George Volonakis, Feliciano Giustino, and Jacky Even. Anharmonic lattice dynamics via the special displacement method. *Physical Review B*, 108(3), July 2023.

[14] Marios Zacharias and Feliciano Giustino. Theory of the special displacement method for electronic structure calculations at finite temperature. *Physical Review Research*, 2(1), March 2020.

[15] Ferd E. Williams. Theoretical Low Temperature Spectra of the Thallium Activated Potassium Chloride Phosphor. *Physical Review*, 82(2):281–282, April 1951.

[16] Melvin Lax. The Franck-Condon Principle and Its Application to Crystals. *The Journal of Chemical Physics*, 20(11):1752–1760, November 1952.

[17] Stefan Goedecker. Minima hopping: An efficient search method for the global minimum of the potential energy surface of complex molecular systems. *The Journal of Chemical Physics*, 120(21):9911–9917, June 2004.

[18] Xin-Gang Zhao, Zhi Wang, Oleksandr I. Malyi, and Alex Zunger. Effect of static local distortions vs. dynamic motions on the stability and band gaps of cubic oxide and halide perovskites. *Materials Today*, 49:107–122, October 2021.

[19] Xin-Gang Zhao, Gustavo M. Dalpian, Zhi Wang, and Alex Zunger. Polymorphous nature of cubic halide perovskites. *Physical Review B*, 101(15), April 2020.

[20] Simon Billinge. *Chapter 16. Local Structure from Total Scattering and Atomic Pair Distribution Function (PDF) Analysis*. In *Powder Diffraction*. Royal Society of Chemistry, 2008, pages 464–493.

[21] B. H. Toby and T. Egami. Accuracy of pair distribution function analysis applied to crystalline and non-crystalline materials. *Acta Crystallographica Section A Foundations of Crystallography*, 48(3):336–346, May 1992.

[22] C L Farrow, P Juhas, J W Liu, D Bryndin, E S Božin, J Bloch, Th Proffen, and S J L Billinge. PDFfit2 and PDFgui: computer programs for studying nanostructure in crystals. *Journal of Physics: Condensed Matter*, 19(33):335219, July 2007.

[23] Robin Ohmann, Luis K. Ono, Hui-Seon Kim, Haiping Lin, Michael V. Lee, Youyong Li, Nam-Gyu Park, and Yabing Qi. Real-Space Imaging of the Atomic Structure of Organic-Inorganic Perovskite. *Journal of the American Chemical Society*, 137(51):16049–16054, December 2015.

[24] Limin She, Meizhuang Liu, and Dingyong Zhong. Atomic Structures of CH3NH3PbI3 (001) Surfaces. *ACS Nano*, 10(1):1126–1131, December 2015.

[25] Wei Zhang, Luis K. Ono, Jiamin Xue, and Yabing Qi. Atomic Level Insights into Metal Halide Perovskite Materials by Scanning Tunneling Microscopy and Spectroscopy. *Angewandte Chemie International Edition*, 61(5), November 2021.

[26] Limin She, Meizhuang Liu, Xiaoli Li, Zeying Cai, and Dingyong Zhong. Growth and interfacial structure of methylammonium lead iodide thin films on Au(111). *Surface Science*, 656:17–23, February 2017.

[27] Boubacar Traoré, Pooja Basera, Alexandra J. Ramadan, Henry J. Snaith, Claudine Katan, and Jacky Even. A Theoretical Framework for Microscopic Surface and Interface Dipoles, Work Functions, and Valence Band Alignments in 2D and 3D Halide Perovskite Heterostructures. *ACS Energy Letters*, 7(1):349–357, December 2021.

[28] Alfonso Baldereschi, Stefano Baroni, and Raffaele Resta. Band Offsets in Lattice-Matched Heterojunctions: A Model and First-Principles Calculations for GaAs/AlAs. *Physical Review Letters*, 61(6):734–737, August 1988.

[29] Chris G. Van de Walle and Richard M. Martin. Theoretical calculations of heterojunction discontinuities in the Si/Ge system. *Physical Review B*, 34(8):5621–5634, October 1986.

[30] Chris G. Van de Walle. Band lineups and deformation potentials in the model-solid theory. *Physical Review B*, 39(3):1871–1883, January 1989.

[31] Li Lang, Yue-Yu Zhang, Peng Xu, Shiyou Chen, H. J. Xiang, and X. G. Gong. Three-step approach for computing band offsets and its application to inorganic ABX_3 halide perovskites. *Phys. Rev. B*, 92:075102, 7, August 2015.

[32] Yong-Hua Li, X. G. Gong, and Su-Huai Wei. Ab initio calculation of hydrostatic absolute deformation potential of semiconductors. *Applied Physics Letters*, 88(4), January 2006.

[33] Yue-Yu Zhang, Li Lang, Hui-Jun Gu, Shiyou Chen, Zhi-Pan Liu, Hongjun Xiang, and Xin-Gao Gong. Origin of the type-II band offset between rutile and anatase titanium dioxide: Classical and quantum-mechanical interactions between O ions. *Physical Review B*, 95(15), April 2017.

[34] Yuying Hu, Chen Qiu, Tao Shen, Kaike Yang, and Huixiong Deng. Direct calculations on the band offsets of large-lattice-mismatched and heterovalent Si and III-V semiconductors. *Journal of Semiconductors*, 42(11):112102, November 2021.

[35] Xiao-Gang Wang, Anne Chaka, and Matthias Scheffler. Effect of the Environment on α-Al_2O_3(0001) Surface Structures. *Physical Review Letters*, 84(16):3650–3653, April 2000.

[36] Karsten Reuter and Matthias Scheffler. First-Principles Atomistic Thermodynamics for Oxidation Catalysis: Surface Phase Diagrams and Catalytically Interesting Regions. *Physical Review Letters*, 90(4), January 2003.

[37] D. E. Jiang and Emily A. Carter. First-principles study of the interfacial adhesion between $\mathrm{SiO_2}$ and $\mathrm{MoSi_2}$. *Phys. Rev. B*, 72:165410, 16, October 2005.

[38] W. Xiao, W.H. Pu, J.W. Wang, X. Wang, L. Sun, J.D. Cui, and L.G. Wang. Theoretical investigation of the structural and electronic properties of Al-decorated TiO2/perovskite interfaces. *Applied Surface Science*, 492:369–373, October 2019.

[39] Adriana Pecoraro, Francesca Fasulo, Michele Pavone, and Ana B. Muñoz-García. First-principles study of interfacial features and charge dynamics between spiro-MeOTAD and photoactive lead halide perovskites. *Chemical Communications*, 59(34):5055–5058, 2023.

[40] Andrew H. Proppe, Andrew Johnston, Sam Teale, Arup Mahata, Rafael Quintero-Bermudez, Eui Hyuk Jung, Luke Grater, Teng Cui, Tobin Filleter, Chang-Yong Kim, Shana O. Kelley, Filippo De Angelis, and Edward H. Sargent. Multication perovskite 2D/3D interfaces form via progressive dimensional reduction. *Nature Communications*, 12(1), 2021.

[41] Jae Hoon Yun, Inhwa Lee, Taek-Soo Kim, Min Jae Ko, Jin Young Kim, and Hae Jung Son. Synergistic enhancement and mechanism study of mechanical and moisture stability of perovskite solar cells introducing polyethyleneimine into the CH3NH3PbI3/HTM interface. *Journal of Materials Chemistry A*, 3(44):22176–22182, 2015.

[42] Zhenghong Dai, Shuai You, Dwaipayan Chakraborty, Shunran Li, Yadong Zhang, Anush Ranka, Stephen Barlow, Joseph J. Berry, Seth R. Marder, Peijun Guo, Yue Qi, Kai Zhu, and Nitin P. Padture. Connecting Interfacial Mechanical Adhesion, Efficiency, and Operational Stability in High Performance Inverted Perovskite Solar Cells. *ACS Energy Letters*, 9(4):1880–1887, April 2024.

Chapter 3

Polymorphism in bulk and surfaces of 3D inorganic halide perovskites: stability and electronic structure

In this chapter, we investigate the bulk and surface properties of the cubic phase of inorganic 3D halide perovskites. In particular, we focus on how local positional disorder affects structural stability, electronic properties, surface stability, and band alignment. Part of these results have been submitted for publication [1]. First, we analyze the structural properties of the generated polymorphous configurations. We discuss their dynamical and energetic stability using phonon calculations and total-energy comparisons. This allows us to show how local disorder stabilizes the perovskite structure compared with the ideal monomorphous cubic phase. Next, we examine the bulk electronic properties of both monomorphous and polymorphous structures using different levels of theory. These calculations show the importance of including local disorder and self-interaction correction for accurate band-gap prediction. We also quantify how B–X bond elongation and octahedral tilting contribute to band-gap opening in the locally distorted structures. Finally, we construct surface slabs that include local positional disorder and use them to study surface properties. We analyze the effect of local disorder on surface energy, surface dipoles, surface states, and absolute band positions. These results show that including local disorder improves the prediction of surface properties and gives a more realistic description of inorganic halide perovskite surfaces.

3.1 Structural Origin and Stabilization of Local Positional Disorder

3.1.1 Ideal cubic perovskite structure

Perovskite materials can exist in several structural phases. Among them, the cubic phase is the high-temperature and high-symmetry phase. In this chapter, we study the cubic phases of all-inorganic halide perovskites with the chemical formula $CsBX_3$, where B = Pb or Sn and X = Cl, Br, or I. The ideal cubic perovskite structure belongs to the $Pm\bar{3}m$ space group. In this structure, the Cs atom occupies the 1a Wyckoff position, the B-site cation occupies the 1b position, and the halogen atom occupies the 3c position. The lattice constants were optimized by fitting the total energy as a function of volume using the Murnaghan–Birch equation of state. The optimized lattice constants for the investigated compositions range from 5.546 to 6.282 Å, as summarized in Table 3.1.

Table 3.1: Optimized and experimental lattice constants of $CsBX_3$ perovskites.

Structure	Optimized lattice constant (Å)	Experimental lattice constant (Å)
$CsPbI_3$	6.282	6.297 [2]
$CsPbBr_3$	5.902	5.874 [3]
$CsPbCl_3$	5.647	5.605 [3]
$CsSnI_3$	6.177	6.219 [4]
$CsSnBr_3$	5.800	5.804 [5]
$CsSnCl_3$	5.546	5.563 [6]

The difference between the optimized and experimental lattice constants is less than 1% for all compounds. Previous theoretical studies reported that lattice constants calculated using the PBE exchange-correlation functional differ from experiment by about 1.5% [7]. In comparison, our optB86b+vdW calculations give lattice constants that are in better agreement with experimental values.

3.1.2 Dynamical instability of the cubic phase

The high-temperature cubic phases of halide perovskites are often dynamically unstable within the harmonic approximation. This instability arises because the ideal cubic structure represents a high-symmetry average configuration rather than a true minimum of the potential-energy surface. In the cubic $CsBX_3$ structure, the B–X–B bonds are linear, the BX_6 octahedra are untilted, and the B-site cation occupies a centrosymmetric position (see Fig. 3.1). However, lower-symmetry distortions, including octahedral tilting and local cation off-centering, modify the bond lengths (see Fig. 3.1c) and can lower the total energy [8]. These distortions appear as imaginary phonon frequencies in harmonic phonon calculations.

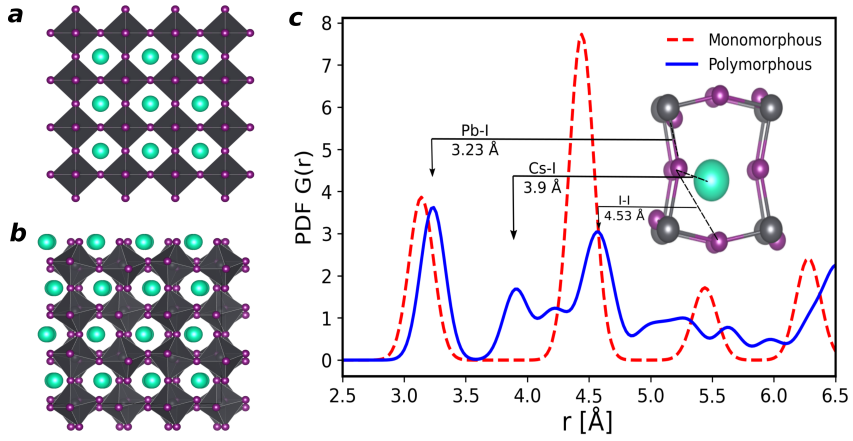

Figure 3.1: Monomorphous (a) and polymorphous (b) bulk structures and pair distribution function (PDF) (c) of $CsPbI_3$.

In this work, phonon dispersions were calculated for both monomorphous and polymorphous configurations of the $CsBX_3$ compounds, as shown in Fig. 3.2. The phonon dispersions show that the monomorphous structures of all investigated compounds have imaginary phonon modes, which are plotted as negative frequencies in Fig. 3.2. These imaginary modes indicate that the ideal cubic structure is dynamically unstable within the harmonic approximation. In particular, strong instabilities are observed at the M and R high-symmetry points of the Brillouin zone. These zone-boundary instabilities are characteristic of octahedral-rotation modes in cubic perovskites [9]. The M-point instability is commonly associated with in-phase octahedral rotations between neighboring unit cells, whereas the R-point instability corresponds to out-of-phase octahedral rotations [10]. Several theoretical studies reported similar M- and R-point imaginary phonon modes for cubic halide perovskites, where these instabilities were attributed to long-range spontaneous octahedral tilting [10, 11, 12].

In contrast, the polymorphous configurations show a surpression of the imaginary phonon modes. This indicates that local symmetry breaking stabilizes the phonon dispersion by allowing the lattice to relax toward lower-energy local configurations. However, this stabilization should not be interpreted as harmonic stability of the ideal cubic arrangement itself. Instead, it shows that the average cubic phase can be represented as an ensemble of locally distorted structures. This interpretation is consistent with the polymorphous description of cubic halide perovskites, in which local octahedral tilting, bond-length variations, and cation displacements coexist with average cubic symmetry [13].

In addition to stabilizing the imaginary modes, the polymorphous configurations also modify the optical phonon modes. In several cases, the optical phonon frequencies are reduced compared with the corresponding monomorphous structures. This reduction can be attributed to the distribution of local force constants in the distorted lattice. In the ideal monomorphous structure, equivalent bonds experience identical restoring forces,

whereas in the polymorphous structure the local environments are inequivalent. This produces a broader distribution of vibrational frequencies and can lead to optical-phonon softening, band flattening, and phonon bunching, which is clustering of optical modes within narrow frequency ranges. Zacharias *et al.* showed that local disorder in halide perovskites can strongly modify the vibrational dynamics, producing broadened and overdamped optical phonon modes [8]. The reduction of optical phonon frequencies observed in the present polymorphous structures is therefore consistent with the soft and locally disordered nature of halide-perovskite lattices.

The optical phonons near the Brillouin-zone center provide information about polar lattice dynamics. In particular, the separation between longitudinal optical (LO) and transverse optical (TO) phonon modes near Γ reflects the strength of the long-range dipole–dipole interaction. All investigated compounds have pronounced LO–TO splitting in both monomorphous and polymorphous configurations. This splitting originates from the macroscopic electric field generated by longitudinal polar optical vibrations. For an LO mode, the relative displacement of charged sublattices produces a long-range electric field, which adds an additional restoring force and increases the LO phonon frequency relative to the corresponding TO mode. This effect is described by the non-analytic contribution to the dynamical matrix [14].

The magnitude of the LO–TO splitting is mainly governed by the Born effective charges and the electronic dielectric screening. In a simplified scalar picture, the splitting strength can be expressed as

$$\Delta\omega^2_{\mathrm{LO-TO}} = \omega^2_{\mathrm{LO}} - \omega^2_{\mathrm{TO}} \propto \frac{|Z^*|^2}{\varepsilon_\infty}, \tag{3.1}$$

where Z^* is the Born effective charge and ε_∞ is the high-frequency dielectric constant. Thus, larger Born effective charge magnitudes enhance the long-range dipole–dipole interaction, whereas a larger ε_∞ screens the macroscopic electric field and reduces the LO–TO splitting. More generally, the non-analytic correction depends on the full Born effective charge tensors, phonon eigenvectors, atomic masses, unit-cell volume, and the direction of the phonon wave vector approaching Γ [14].

Table 3.2: High-frequency dielectric constant ε_∞, static dielectric constant ε_s, and element-averaged Born effective charges Z^* for monomorphous and polymorphous structures of inorganic halide perovskites.

Structure	Monomorphous					Polymorphous				
	ε_∞	ε_s	Z^*_{B}	Z^*_{X}	Z^*_{Cs}	ε_∞	ε_s	Z^*_{B}	Z^*_{X}	Z^*_{Cs}
$CsPbI_3$	6.59	13.76	4.97	-5.11	1.39	5.37	22.89	4.36	-4.08	1.29
$CsPbBr_3$	4.93	41.57	4.30	-4.31	1.32	4.35	18.69	3.98	-3.79	1.27
$CsSnI_3$	28.85	69.49	5.89	-9.98	1.45	7.81	64.01	5.15	-5.56	1.32
$CsSnBr_3$	13.13	59.85	5.05	-6.51	1.36	6.28	96.67	4.65	-4.81	1.30

The dielectric constants and element-averaged Born effective charges listed in Table 3.2 help explain the LO–TO splitting observed near Γ. In all compounds, the B-site

cations have large positive Born effective charges, while the halide ions have negative values. This shows that the polar response is mainly governed by relative motion of the B cation and the halide framework. The Cs ions have smaller positive values and therefore contribute less to the polar optical modes. The relatively large Z^*_{B} and Z^*_{X} values indicate strong dynamic charge transfer during lattice vibrations, which enhances the long-range dipole–dipole interaction responsible for LO–TO splitting. The large Born effective charges are consistent with previous reports [10, 15] for lead-halide perovskites, where dynamic charge transfer and soft polar lattice response produce strong dielectric and LO–TO effects.

Comparing the monomorphous and polymorphous structures, the element-averaged Born effective charges slightly decrease in the polymorphous configurations. Therefore, the LO–TO splitting in the polymorphous structures cannot be explained by larger Born effective charges alone. Instead, the reduced high-frequency dielectric constant ε_∞, especially in $CsSnI_3$ and $CsSnBr_3$, indicates weaker electronic screening of the macroscopic electric field. This weaker screening can strengthen the LO–TO splitting even when the average Born effective charges are slightly reduced. The large static dielectric constants ε_s further confirm the soft and highly polarizable nature of these lattices, although the non-analytic LO–TO correction is governed by ε_∞ rather than ε_s. The validity of the semi-classical Fröhlich Hamiltonian was inspected in details for $CsPbBr_3$ in a recent paper [16], by quantifying the LO-TO splitting and the electron-phonon coupling strength for individual polar optical phonons, analyzing the mixing induced by long-range polar interactions and the relative contributions to the dielectric spectrum, tracing their symmetry evolution across phase transitions using group theory and a band folding approach.

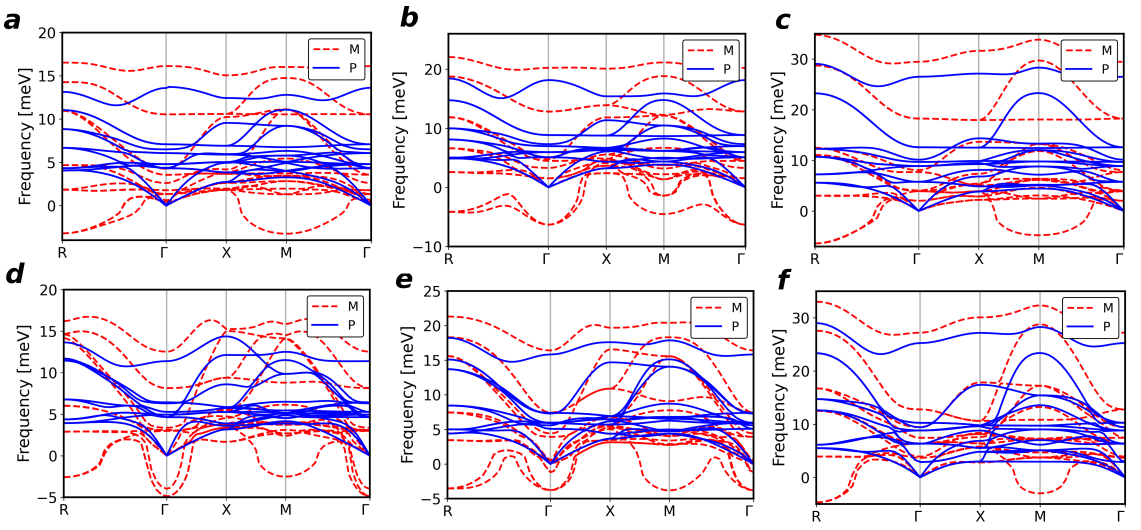

Figure 3.2: Phonon dispersion of monomorphous and polymorphous configurations of $CsPbI_3$ (a), $CsPbBr_3$ (b), $CsPbCl_3$ (c), $CsSnI_3$ (d), $CsSnBr_3$ (e), and $CsSnCl_3$ (f). M and P denote monomorphous and polymorphous configurations, respectively.

3.1.3 Energy gain with local positional disorder

As discussed in the previous chapter, the potential energy surfaces (PESs) of halide perovskites are characterized by double-well due to strong anharmonicity. The monomorphous structure corresponds to a local maximum or saddle point on the PES, whereas the locally distorted polymorphous structure corresponds to a lower-energy minimum [17]. When positional local disorder is introduced, the atoms relax away from the high-symmetry configuration, lowering the total energy of the system. The energy difference between the monomorphous and polymorphous configurations is therefore referred to here as the energy gain.

Figure 3.3a shows the relationship between the energy gain and the average change in the B–X–B bond angle, $\langle \Delta\theta_{\mathrm{BXB}} \rangle$. The energy gain shows a clear correlation with the magnitude of the B–X–B angle change, indicating that compounds with larger local distortions gain more energy upon relaxation into the polymorphous configuration.

The magnitude of the B–X–B angle change depends on the structural flexibility of each compound. To rationalize this trend, we use the Goldschmidt tolerance factor [18]. The tolerance factor provides a measure of whether a perovskite structure is likely to remain close to the ideal cubic geometry or undergo octahedral tilting and distortion. For an ideal cubic perovskite, the tolerance factor is typically close to 1. In the $CsBX_3$ compounds considered here, the tolerance factors are smaller than 0.9 [1], indicating a tendency toward structural distortion.

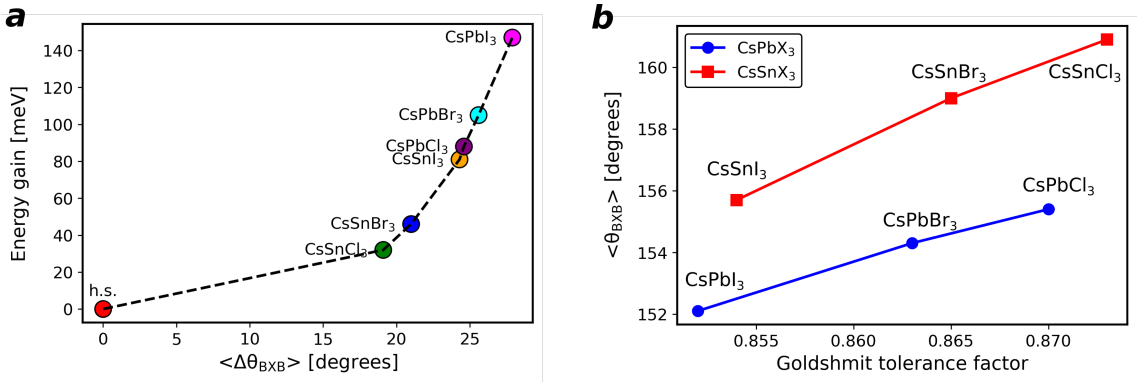

Figure 3.3: Energy gain of $CsBX_3$ compounds due to positional local disorder (a) and the relatioship between B–X–B angle change and Goldschmidt tolerance factor (b).

As shown in Figure 3.3b, compounds with smaller Goldschmidt tolerance factors exhibit larger changes in the B–X–B angle. This trend arises because larger halide ions reduce the tolerance factor and enhance the tendency for octahedral distortion. In addition, Pb-based compounds have smaller tolerance factors than their Sn-based counterparts,

[1] We use Shannon ionic radii to calculate the tolerance factor, assuming oxidation states of $+1$, $+2$, and -1 for cesium, the B-site atom, and the halogens, respectively. The coordination number is taken as 6 for the B-site atom and the halogens, and 12 for cesium.

and consequently show larger B–X–B angle changes and larger energy gains. Thus, compounds with larger tolerance factors remain closer to the cubic geometry, have smaller B–X–B change, and gain less energy from positional local disorder.

Among the compounds studied, $CsPbI_3$ has the largest B–X–B angle change, approximately $27.9°$, and the largest energy gain, about 147 meV/f.u. In contrast, $CsSnCl_3$ shows the smallest B–X–B angle change, approximately $19.1°$, and one of the smallest energy gains, about 35 meV/f.u. Zacharias *et al.* [8] reported energy gains of 111 meV/f.u. for $CsPbI_3$, 80 meV/f.u. for $CsPbBr_3$, and 61 meV/f.u. for $CsSnI_3$. Zhao *et al.* [13] reported corresponding values of 123 meV/f.u. for $CsPbI_3$ and 55 meV/f.u. for $CsSnI_3$. The variation among the reported and calculated energy gains can be attributed to the use of different exchange–correlation functionals. However, the overall trend in energy gain across the different compounds remains similar.

3.2 Impact of Local Disorder on Bulk Electronic Structure

3.2.1 Band structure modification due to disorder

Figure 3.4 compares the electronic spectral functions of the polymorphous configurations with the band structures of the corresponding monomorphous configurations for $CsBX_3$ compounds. The polymorphous spectral functions are shown as color maps, while the monomorphous band structures are shown as black lines. This comparison shows that local structural disorder significantly modifies the electronic structure of halide perovskites.

In the monomorphous configurations, the electronic bands appear as sharp and well-defined dispersions because of the translational symmetry of the idealized structure. In contrast, local disorder breaks the local symmetry and leads to a broadening of the unfolded spectral features. As a result, the electronic states in the polymorphous configurations are distributed over a finite energy range rather than appearing as sharp bands. This disorder-induced broadening is especially visible near the valence-band maximum (VBM) and conduction-band minimum (CBM), where local structural distortions modify both the band-edge energies and the band dispersion.

Local disorder increases the band gap relative to the monomorphous reference structures. The band-gap opening is defined as

$$\Delta E_g = E_g^{\mathrm{poly}} - E_g^{\mathrm{mono}}. \tag{3.2}$$

In addition, the dispersion near the VBM and CBM becomes flatter in the polymorphous configurations. This suggests an increase in the electron and hole effective masses, although effective masses were not explicitly calculated in this work. A similar disorder-induced enhancement of carrier effective masses was reported by Zacharias *et al.* for $CsPbBr_3$ and $CsPbI_3$, with enhancement factors in the range of 1.3–4.7 [8].

For some compounds, the band structure of the monomorphous configuration presents a band edge orbital character exchange, resulting in negative band gaps. In

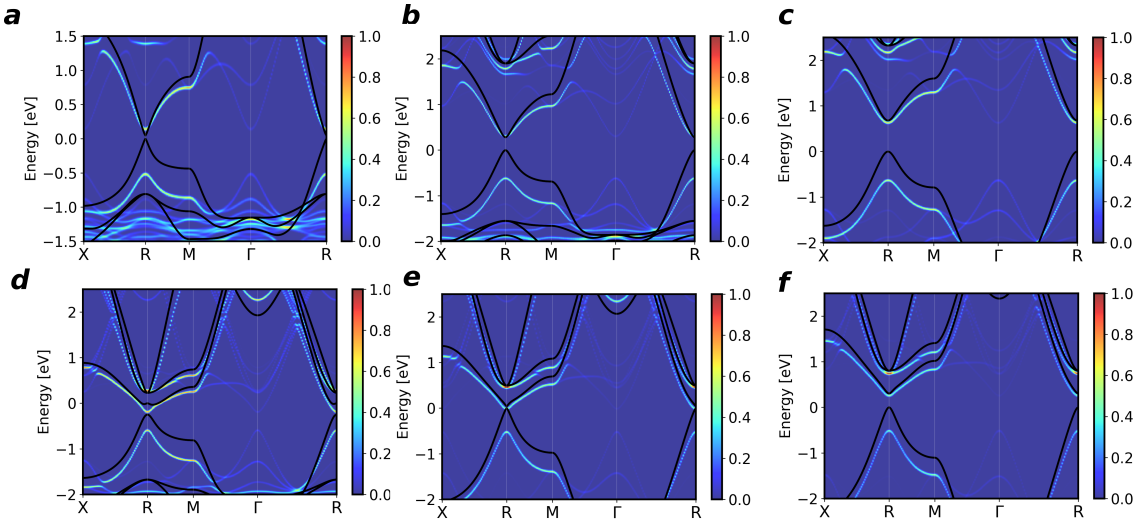

Figure 3.4: Band structures of monomorphous configurations and unfolded spectral functions of polymorphous configurations for $CsPbI_3$ (a), $CsPbBr_3$ (b), $CsPbCl_3$ (c), $CsSnI_3$ (d), $CsSnBr_3$ (e), and $CsSnCl_3$ (f). The color maps show the unfolded spectral functions of the polymorphous configurations, while the black lines show the band structures of the corresponding monomorphous configurations.

particular, the monomorphous structures of $CsSnI_3$, $CsSnBr_3$, and $CsPbI_3$ have negative band gaps of -0.25 eV, -0.04 eV, and -0.05 eV, respectively. These negative values indicate a band-edge exchange in the idealized high-symmetry structures. When local disorder is included, the correct band-edge ordering is recovered and a finite band gap opens.

The disorder-induced band-gap opening correlates with the change in the average B–X–B bond angle. In this work, the band gaps of both monomorphous and polymorphous structures were calculated using GGA+SOC. As shown in Fig. 3.5, larger deviations from the linear B–X–B angle are associated with larger band-gap openings. This trend is observed for both Pb- and Sn-based compounds, and the fitted slopes of ΔE_g as a function of $\Delta\theta$ are similar for the two families. The magnitude of the band-gap opening increases from lighter to heavier halides, consistent with the larger B–X–B bond-angle distortion in the heavier-halide compounds.

This behavior is also consistent with previous studies. Zhao *et al.* [13] reported disorder-induced band-gap openings of 0.64 eV for $CsPbI_3$ and 0.65 eV for $CsSnI_3$. A similar correlation between band-gap opening and B–X–B bond-angle distortion was reported by Zacharias *et al.* [19]. Sabino *et al.* [20] also reported an increase in the disorder-induced band-gap opening from Cl- to I-based compounds.

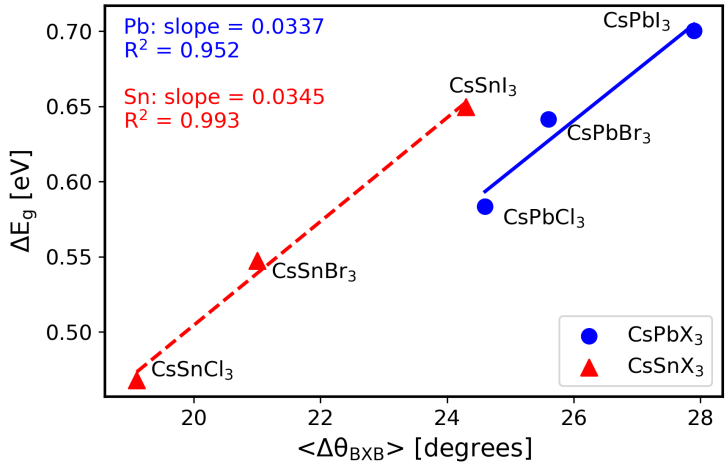

Figure 3.5: Correlation between the disorder-induced band-gap opening and the B–X–B bond-angle change.

3.2.2 Role of bond-length variation and octahedral tilting

The physical origin of the disorder-induced band-gap opening can be understood in terms of reduced orbital overlap caused by local distortions. In the ideal monomorphous structure, the linear B–X–B angle maximizes the orbital overlap between the B-site s orbitals and halide p orbitals. Local deviations from the linear B–X–B angle, together with an increase in the B–X bond length, reduce this overlap and increase the band gap.

This behavior is related to the orbital character of the band edges. The valence-band maximum is mainly formed by antibonding hybridization between the B-site s orbital and the halide p orbitals [21]. When the B–X orbital overlap is reduced, the antibonding interaction at the top of the valence band becomes weaker, which lowers the VBM energy and contributes to the band-gap opening. Local disorder induces both octahedral tilting and B–X bond-length variations. The pair distribution function analysis shows a clear elongation of the B–X bond due to local disorder, as shown in Fig. 3.1c. In this section, we quantify the separate contributions of octahedral tilting and B–X bond elongation to the disorder-induced band-gap opening.

Figure 3.6 shows the calculated band-gap opening caused by octahedral tilting, B–X bond elongation, and full local positional disorder. In the polymorphous structures, bond-angle distortions and bond-length variations occur simultaneously. To separate these two effects, we constructed two idealized model structures. In the first bond length model, the B–X bond lengths are taken from the polymorphous configuration, while the B–X–B angles are constrained to remain $180°$, as in the monomorphous structure. In the second B–X–B angle model, the B–X–B angles are taken from the polymorphous configuration, while the B–X bond lengths are kept equal to those of the monomorphous structure.

The structural character of these two models is illustrated for $CsPbI_3$ in Fig. 3.7. The bond length model has PDF peak positions close to those of the polymorphous structure,

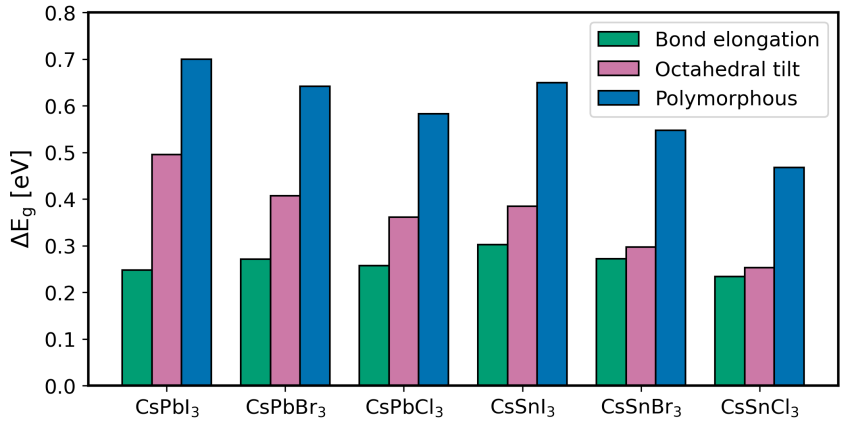

Figure 3.6: Band-gap opening caused by octahedral tilting, B–X bond elongation, and full positional local disorder.

confirming that it preserves the polymorphous bond-length distribution, while its overall lineshape remains closer to the monomorphous structure because the B–X–B angle is not distorted. Conversely, the B–X–B angle model shows a lineshape similar to the polymorphous structure, reflecting the presence of octahedral tilting, while its main peak positions remain close to those of the monomorphous structure because the B–X bond lengths are unchanged.

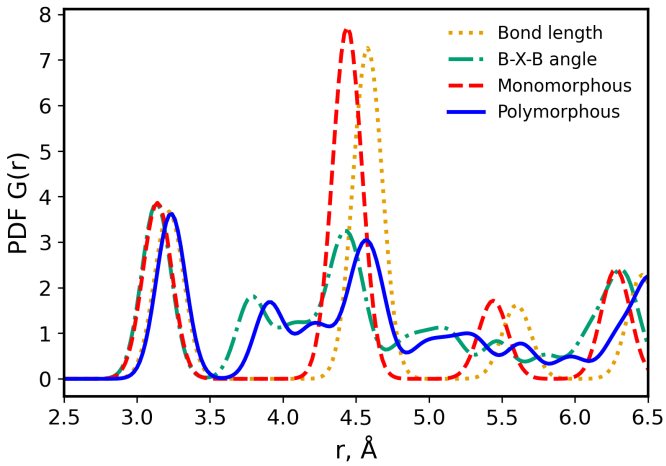

Figure 3.7: Comparison of the pair distribution functions of monomorphous, polymorphous, bond-length, and B–X–B angle configurations of $CsPbI_3$.

For the Pb-based compounds, octahedral tilting dominates the band-gap opening. However, the contribution of octahedral tilting decreases from I to Br to Cl, consistent with the decreasing B–X–B bond-angle distortion across this series. In contrast, for the Sn-based compounds, octahedral tilting and B–X bond elongation contribute almost equally to the band-gap opening. This can be attributed to the smaller B–X–B bond-angle changes

in the Sn-based compounds compared with the Pb-based compounds. A similar trend for Sn- and Pb-based halide perovskites was also reported by Sabino *et al.* [20].

3.2.3 Accurate Band-Gap Prediction

Figure 3.8 compares the calculated band gaps obtained using GGA+SOC and GGA+SOC+DFT-1/2 for monomorphous and polymorphous bulk structures with experimental values reported by Tao *et al.* [22]. The GGA+SOC calculations for both monomorphous and polymorphous structures show a severe underestimation of the band gap relative to experiment. This underestimation is expected because standard GGA functionals suffer from self-interaction error and lack the derivative discontinuity of the exchange-correlation potential.

To improve the band-gap prediction, we used the DFT-1/2 method proposed by Ferreira *et al.*, which partially corrects the self-interaction error and has been shown to improve band gaps for many semiconductors. However, our GGA+SOC+DFT-1/2 calculations based on monomorphous structures still underestimate the experimental band gaps, as shown in Fig. 3.8.

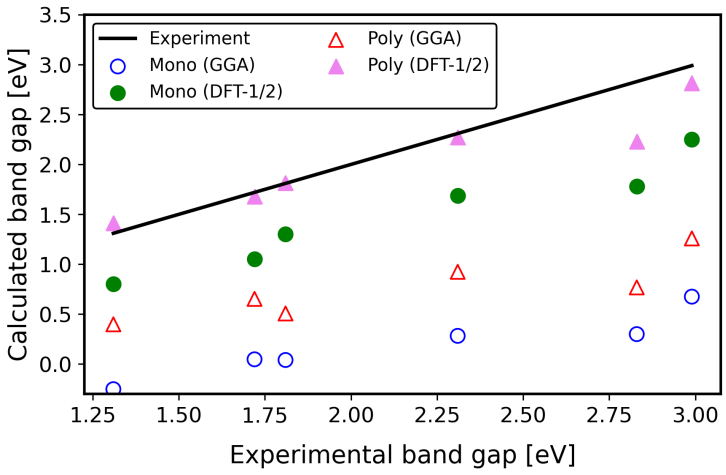

Figure 3.8: Comparison between experimental band gaps and band gaps calculated using different levels of theory for monomorphous and polymorphous bulk models. Experimental values are taken from Tao *et al.* [22].

The remaining discrepancy is not only due to the electronic-structure method, but also to the use of an idealized high-symmetry structural model. Indeed previous studies have shown that both self-consistent GW and DFT-1/2 can accurately predict band gaps for many conventional semiconductors [23]. However, these approaches may still underestimate the band gaps of cubic halide perovskites when calculations are performed using monomorphous structures [24]. For example, self-consistent GW calculations were reported to underestimate the band gap of cubic $CsPbI_3$ by approximately 0.6 eV [25]. This

discrepancy can be attributed, at least in part, to the neglect of local structural disorder in the ideal monomorphous model.

Our results demonstrate that incorporating local disorder significantly improves the agreement between calculated and experimental band gaps. In particular, the GGA+SOC+DFT-1/2 calculations using polymorphous structures yield band gaps that are much closer to experiment, as shown by the magenta diamonds in Fig. 3.8. This improvement arises from the disorder-induced band-gap opening discussed in the previous sections. The importance of local disorder is also consistent with previous self-consistent GW [26] and hybrid DFT calculations using the PBE0 functional [19] for polymorphous cubic perovskite structures.

Therefore, accurate band-gap prediction in cubic halide perovskites requires not only an improved electronic-structure method [8], such as DFT-1/2, but also a realistic polymorphous structural description that captures local disorder. The combination of GGA+SOC+DFT-1/2 with polymorphous structures provides a more reliable description of the experimental band gaps than calculations based on ideal monomorphous structures.

3.3 Surface Structural Relaxation and Stability

3.3.1 Surface relaxation in different structural models

To model the [001] surfaces of monomorphous and polymorphous $CsPbI_3$, we started from the structures shown in Figure 1.4a,b of section 2. In these slab models, only the atoms in the outermost two CsX and two BX_2 layers were allowed to relax, as indicated by the dashed lines, while the atoms in the central region were fixed at their bulk positions. This setup preserves the bulk-like structure in the center of the slab and allows us to compare how the different surface models respond to relaxation.

The surface relaxation shows opposite trends in the monomorphous and polymorphous slabs. For the polymorphous $CsPbI_3$ slabs, the average in-plane B–X–B angles in the surface region increase by 4.5° and 3.1° for the CsI- and PbI_2-terminated surfaces, respectively, relative to the bulk value of 152.1°. In contrast, for the monomorphous slabs, the corresponding in-plane angles decrease by 13.2° and 9.2° relative to the ideal cubic value of 180°. The structural parameters for all compounds studied in this work are summarized in Table 3.3.

This opposite behavior originates from the different starting geometries of the two structural models. The monomorphous slab starts from an ideal high-symmetry cubic structure with linear B–X–B angles. This configuration is unstable at the surface, and relaxation introduces octahedral tilting, which reduces the in-plane B–X–B angles. In contrast, the polymorphous slab already contains local octahedral tilts in the bulk. At the surface, the reduced number of structural constraints allows the octahedra to relax slightly toward a more linear geometry. As a result, the surface B–X–B angles increase compared with the bulk polymorphous value.

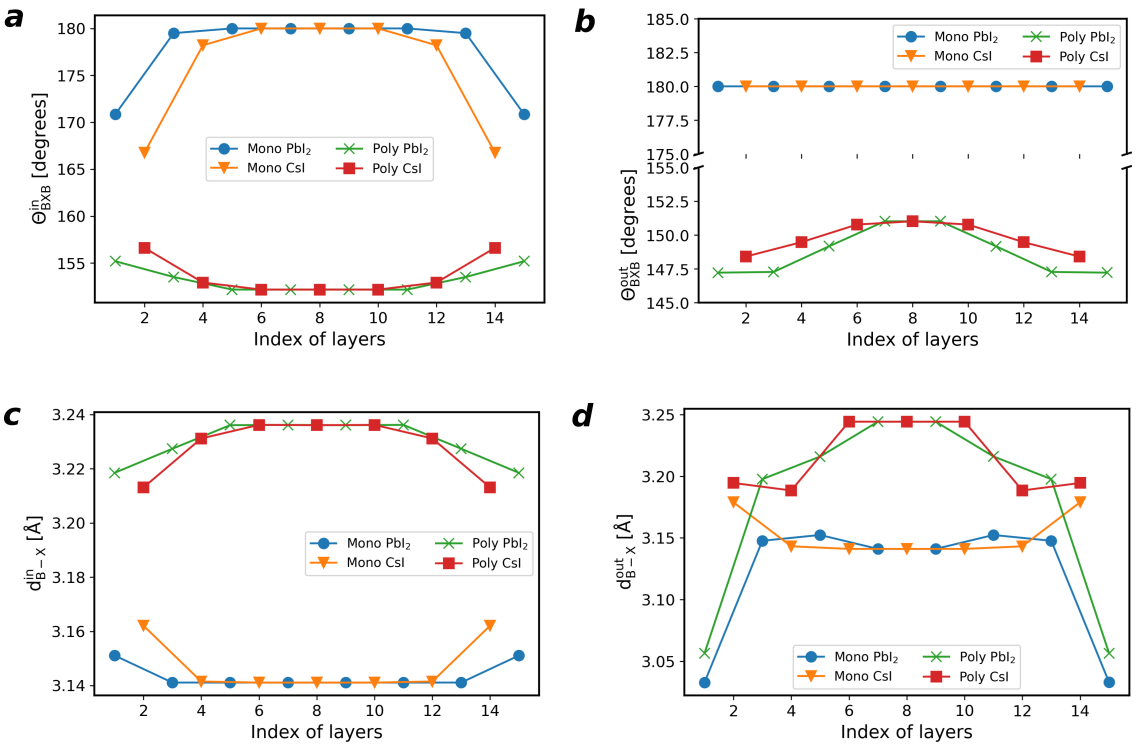

Figure 3.9: Average in-plane (panel a and c) and out-of-plane (panel b and d) B–X–B angles and B–X bond lengths in each layer of the monomorphous and polymorphous $CsPbI_3$ surface slabs.

The magnitude of the surface relaxation also depends on the termination. The CsI-terminated surface shows a larger change in the B–X–B angle than the PbI_2-terminated surface. This is because the outermost CsI layer does not contain B-site cations, giving the surface iodide atoms more freedom to move. Similar behavior has also been reported by Traoré et al. [27].

The out-of-plane relaxation further highlights the difference between the monomorphous and polymorphous models. In the ideal monomorphous slab, the symmetry of the starting structure restricts lateral atomic motion. As a result, the surface atoms mainly relax inward along the surface-normal direction, while the out-of-plane B–X–B angle remains fixed at 180°, consistent with previous reports [27, 28]. This constrained relaxation leads to only a small contraction of the surface B–B distance, about 1%. In the polymorphous slab, however, the local structural disorder allows octahedra to tilt and deform in all directions. Consequently, the out-of-plane B–X–B angle decreases by about 5°, and the surface B–B distance contracts by about 4% for $CsPbI_3$ (Table 3.3). These results show that local disorder provides additional structural degrees of freedom, allowing the surface to accommodate strain more effectively.

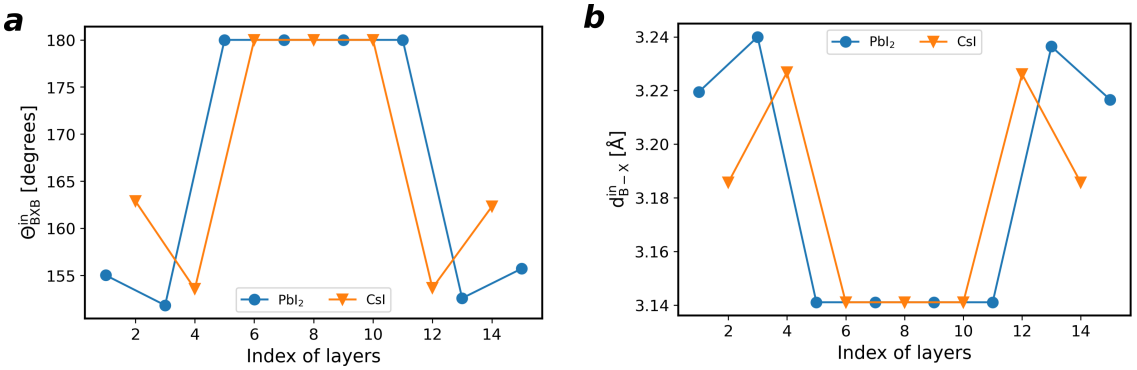

Figure 3.10: Average in-plane B–X–B angles and B–X bond lengths in each layer of the reconstructed monomorphous surface slab.

To test whether the limited relaxation of the ideal monomorphous slab is caused by the imposed symmetry, we introduced small random displacements to the surface atoms of the monomorphous slab before relaxation. The central bulk-like layers were kept fixed, as in the other slab models. We refer to this model as the reconstructed monomorphous slab. This procedure breaks the artificial in-plane symmetry of the ideal monomorphous surface without changing the bulk reference structure.

After relaxation, the reconstructed monomorphous slab shows substantial changes in both the in-plane B–X–B angles and the B–X bond lengths compared with the ideal monomorphous slab. However, the way these distortions extend into the subsurface region is different from the behavior observed in the polymorphous slab. In both the ideal monomorphous and polymorphous slabs, the surface geometry gradually approaches the bulk-like geometry toward the center of the slab, as shown in Fig. 3.9. In contrast, in the reconstructed monomorphous slab, the distortions do not propagate smoothly.

Table 3.3: Structural parameters of the surface layers of the monomorphous and polymorphous slabs. B–X_{in} and B–X_{out} denote the in-plane and out-of-plane bond lengths between the B-site atom and the halogen atom, respectively. BXB_{in} and BXB_{out} denote the in-plane and out-of-plane B–X–B bond angles. B–B_{out} is the out-of-plane B–B distance. dB_{in} and dB_{out} are the in-plane and out-of-plane off-centering displacements of the B-site atom.

Compound	Termination	Type	B–X_{in} (Å)	BXB_{in} (°)	B–X_{out} (Å)	BXB_{out} (°)	B–B_{out} (Å)	dB_{in} (Å)	dB_{out} (Å)
$CsPbI_3$	CsI	Mono	3.16	166.8	3.18	180.0	6.40	0.00	0.28
		Poly	3.21	156.6	3.19	148.4	6.20	0.07	0.11
	PbI_2	Mono	3.15	170.8	3.03	180.0	6.22	0.00	0.81
		Poly	3.22	155.2	3.06	147.2	6.02	0.13	0.64
$CsPbBr_3$	CsBr	Mono	2.96	169.7	2.98	180.0	5.99	0.00	0.20
		Poly	3.00	159.4	3.00	151.7	5.86	0.05	0.08
	$PbBr_2$	Mono	2.97	166.0	2.83	180.0	5.82	0.00	0.86
		Poly	2.99	162.4	2.84	153.5	5.70	0.11	0.73
$CsPbCl_3$	CsCl	Mono	2.83	172.8	2.84	180.0	5.72	0.00	0.14
		Poly	2.87	160.5	2.86	153.1	5.61	0.04	0.06
	$PbCl_2$	Mono	2.85	164.5	2.68	180.0	5.54	0.00	0.84
		Poly	2.85	166.8	2.69	160.7	5.50	0.09	0.77
$CsSnI_3$	CsI	Mono	3.10	169.8	3.15	180.0	6.33	0.00	0.22
		Poly	3.13	161.4	3.14	154.4	6.18	0.06	0.13
	SnI_2	Mono	3.09	173.9	2.98	180.0	6.10	0.00	0.73
		Poly	3.15	158.5	3.00	152.9	5.98	0.21	0.68
$CsSnBr_3$	CsBr	Mono	2.90	174.0	2.94	180.0	5.92	0.00	0.13
		Poly	2.93	165.6	2.94	158.2	5.82	0.04	0.10
	$SnBr_2$	Mono	2.92	167.0	2.77	180.0	5.72	0.00	0.82
		Poly	2.93	166.3	2.79	161.7	5.67	0.15	0.77
$CsSnCl_3$	CsCl	Mono	2.77	176.3	2.80	180.0	5.65	0.00	0.09
		Poly	2.79	167.6	2.80	160.2	5.57	0.03	0.07
	$SnCl_2$	Mono	2.80	164.4	2.61	180.0	5.45	0.00	0.83
		Poly	2.81	164.4	2.64	166.4	5.44	0.18	0.83

Instead, the in-plane B–X–B angles show abrupt layer-dependent changes, including a clear jump between the first and second layers, as shown in Fig. 3.10. This indicates that simply breaking the surface symmetry of the monomorphous slab does not reproduce the smooth structural relaxation of the polymorphous model. The polymorphous structure provides a more natural description of local surface relaxation because its bulk already contains local tilts and distortions.

3.3.2 Surface energy and stability

We calculated the surface energies of monomorphous and polymorphous $CsBX_3$ surface slabs with CsX and BX_2 terminations. Since symmetric slabs were used in this work, the surface models are non-stoichiometric. Therefore, the surface energy depends on the chemical potentials of elements. For this reason, the surface energies of the polymorphous $CsBX_3$ slabs were evaluated as a function of the B and X chemical potentials, as shown in Fig. 3.11. This allows different growth conditions to be considered.

The hatched regions in Fig. 3.11 indicate the thermodynamic stability region of $CsBX_3$ with respect to the competing CsX and BX_2 phases. The color map shows the lowest sur-

face energy between the CsX- and BX_2-terminated surfaces, min(γ_{CsX}, $\gamma_{\mathrm{BX_2}}$), at each point in chemical-potential space. The red line marks the condition where the two terminations have equal surface energy. On one side of this line, the CsX termination is more stable, whereas on the other side, the BX_2 termination is favored. These regions are indicated by the blue and orange arrows, respectively.

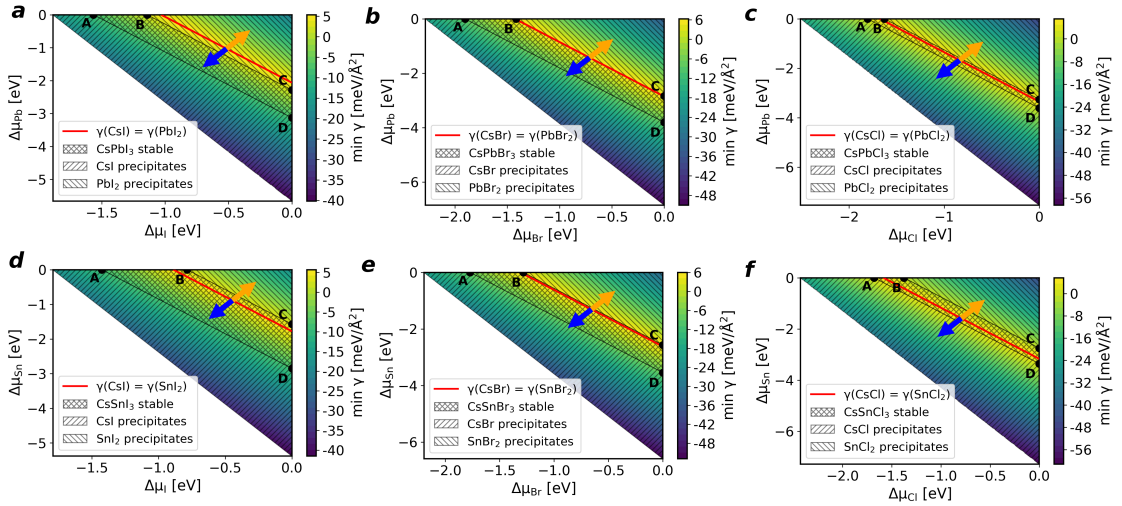

Figure 3.11: The color map represents the lowest calculated surface energies, between CsX and BX_2 terminations (X=I,Br,Cl and B=Sn, Pb), [i.e., min(γ_{CsX}, γ_{BX_2})], as a function of B and X chemical potentials. Hatched regions correspond to stability regions of $CsBX_3$ and competing phases. Points A–D correspond to growth conditions: A (X-rich, B-rich), B (X-rich, B-poor), C (X-poor, B-rich), and D (X-poor, B-poor). The red line corresponds to points where the surface energies of CsX and BX_2 terminations are equal. Blue and orange arrows show regions where CsX and BX_2 terminations are stable, respectively. a) $CsPbI_3$, b) $CsPbBr_3$, c) $CsPbCl_3$, d) $CsSnI_3$, e) $CsSnBr_3$, and f) $CsSnCl_3$.

For $CsPbI_3$, the CsI-terminated surface has the lowest surface energy throughout the entire stability region. This result agrees with previous computational studies, which reported that CsX-terminated surfaces are energetically favored [28, 29]. It is also consistent with STM experiments showing that perovskite surfaces are predominantly CsX-terminated [30, 31]. For the other compounds, the line where $\gamma_{\mathrm{CsX}} = \gamma_{\mathrm{BX_2}}$ lies inside or close to the $CsBX_3$ stability region. This means that the preferred surface termination depends on the B and X chemical potentials. In $CsPbBr_3$, this line lies near the boundary between the $CsPbBr_3$ and $PbBr_2$ stability regions, so the CsBr termination remains stable over nearly the whole stability region. In $CsPbCl_3$, $CsSnI_3$, and $CsSnBr_3$, the equality line is also close to the BX_2-rich boundary, indicating that the CsX termination is favored over most of the stability region. In contrast, for $CsSnCl_3$, the equality line is closer to the CsCl boundary. As a result, the $SnCl_2$-terminated surface becomes more stable over a larger part of the stability region.

Because some of the growth conditions labeled in Fig. 3.11 give equivalent surface en-

ergies, only two representative conditions are shown in Fig. 3.12. Specifically, conditions C and D are used to compare the surface energies of monomorphous and polymorphous $CsBX_3$ slabs with CsX and BX_2 terminations. Under condition D, the CsX termination is the most stable for all compositions. Under condition C, the CsX termination is favored only for $CsPbI_3$, whereas the BX_2 termination becomes more stable for the other compounds. This behavior follows directly from the position of the equality line in Fig. 3.11. For $CsPbI_3$, this line lies outside the stability region, while for the other compounds it crosses or approaches the stability region.

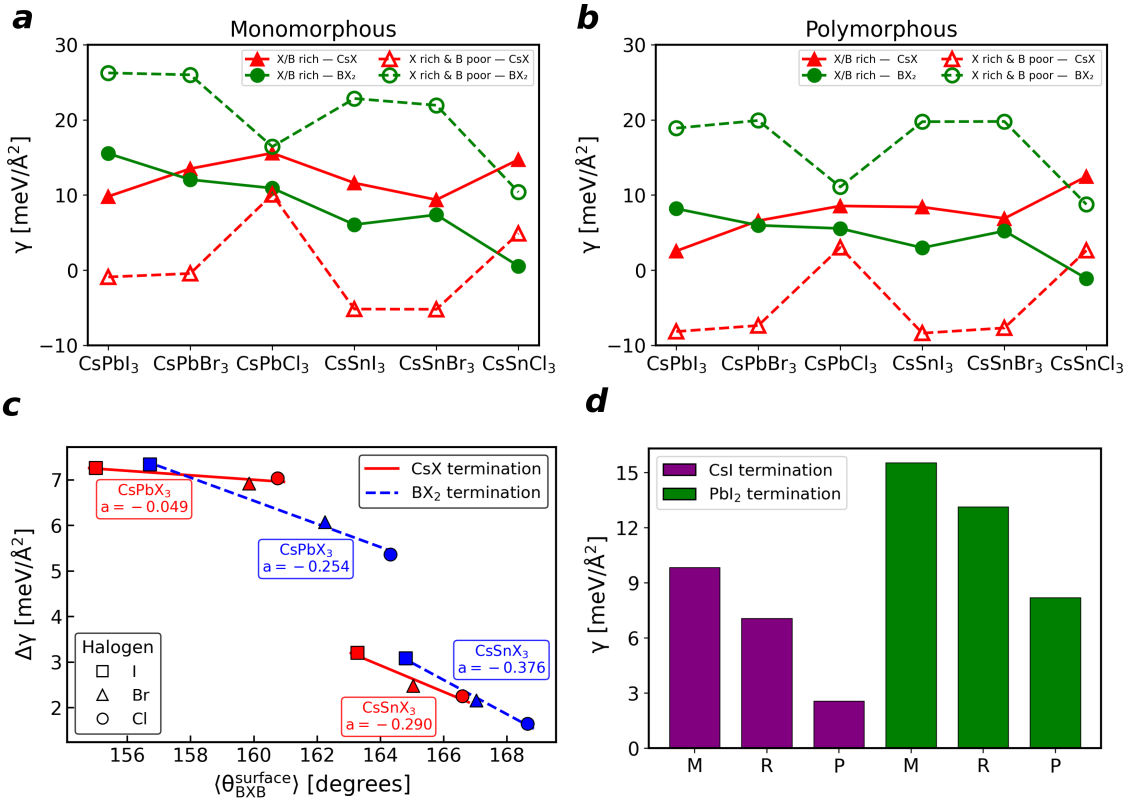

Figure 3.12: Surface energies of polymorphous and monomorphous surface slabs. (a,b) Surface energies of the CsX- and BX_2-terminated monomorphous (a) and polymorphous (b) $CsBX_2$ surface slabs under two possible growth conditions. (c) The correlation between the difference in surface energies of polymorphous and monomorphous surface slabs and the B–X–B angle at the surface. (d) Surface energies of monomorphous, polymorphous and reconstructed monomorphous $CsPbI_3$ surface slabs. The labels M, R, and P on the x-axis denote monomorphous, reconstructed monomorphous, and polymorphous structures, respectively. Surface energies in panel (d) are calculated under I-rich and Pb-rich growth conditions.

The effect of positional local disorder on surface stability is shown in Fig. 3.12a,b. In general, polymorphous slabs have lower surface energies than monomorphous slabs. This shows that local disorder stabilize the surface. Although reconstructed monomor-

phous slabs also have lower surface energies than unreconstructed monomorphous slabs, the polymorphous slabs remain the most stable structures, as shown in Fig. 3.12d. Therefore, the energy lowering is not simply due to surface reconstruction, but is strongly connected to the presence of local structural disorder.

The reduction in surface energy from the monomorphous to the polymorphous structure, $\Delta\gamma$, depends mainly on composition rather than on the chosen growth condition. As shown in Fig. 3.12c, $\Delta\gamma$ correlates with the surface B–X–B bond angle, $\theta_{\mathrm{BXB}}^{\mathrm{surface}}$. For both $CsPbX_3$ and $CsSnX_3$, and for both terminations, a nearly linear relationship is observed between $\Delta\gamma$ and $\theta_{\mathrm{BXB}}^{\mathrm{surface}}$. This indicates that surfaces with stronger octahedral tilting gain more surface energy from local disorder.

Fig. 3.12d compares the monomorphous, reconstructed monomorphous, and polymorphous $CsPbI_3$ surface slabs under I-rich and Pb-rich conditions. As expected, reconstruction lowers the surface energy of the monomorphous slab. However, the reduction is smaller than that obtained in the fully polymorphous slab for both terminations. This suggests that a symmetry-constrained monomorphous slab cannot fully reach the lowest-energy surface configuration. In contrast, the polymorphous slab can relax through local distortions and non-uniform octahedral tilting, leading to a more stable surface. Therefore, monomorphous slabs should be regarded mainly as reference structures, while polymorphous slabs provide a more realistic description of the ground-state surface geometry.

3.4 Surface Electronic Properties and Band Alignment

3.4.1 Absolute band positions

Experimentally reported absolute valence-band maxima (VBMs) for halide perovskites show substantial scatter. This variability arises from challenges in film preparation and from the intrinsic complexity of these materials. Polycrystalline films can contain multiple surface terminations, different defect densities at the surface and in the bulk, and strong sensitivity to the initial stoichiometry [32]. Moreover, the low density of states near the band edges further complicates reliable spectral analysis. For $CsPbI_3$, reported VBMs span from -4.89 to -6.25 eV [33, 34, 22]. This spread in experimental ionization potentials largely reflects differences in sample quality and data-analysis protocols. Tao *et al.* applied consistent experimental protocols across a wide range of halide perovskites [22]. We therefore use this dataset as our experimental reference because it provides measurements from the same research group for a broad range of compositions.

We first computed the planar-averaged and macroscopically averaged electrostatic potentials, as shown in Figure 3.13 for $CsPbI_3$. The electrostatic potential in the middle of the slab is lower than the corresponding bulk electrostatic potential (Figure 3.13a). This shift arises from surface dipoles, which modify the internal electrostatic potential of the

slab. Positional local disorder also affects the surface dipole and changes the electrostatic potential in the middle of the slab, as shown by the macroscopically averaged electrostatic potential in Figure 3.13b. The effect of local disorder is discussed in more detail in the following sections.

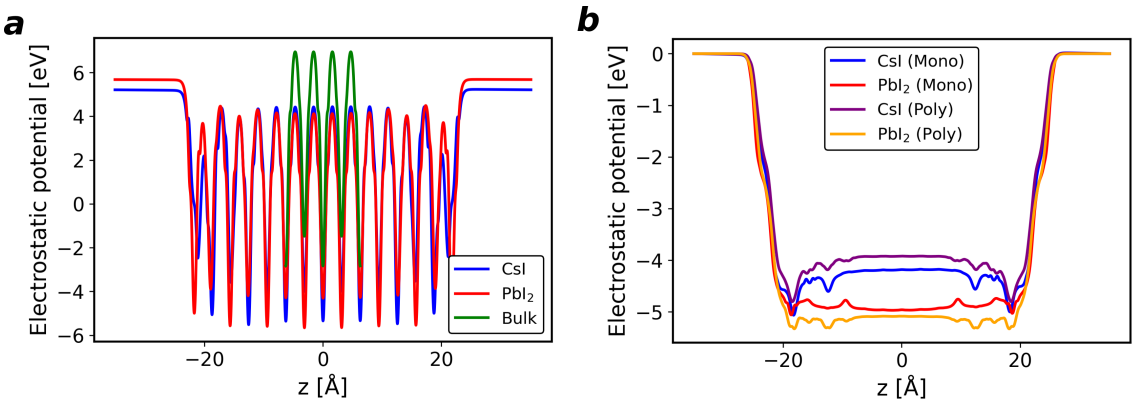

Figure 3.13: Planar-averaged and macroscopically averaged electrostatic potentials of $CsPbI_3$. **a** Planar-averaged electrostatic potential of monomorphous $CsPbI_3$ bulk and surface slabs with PbI_2 and CsI terminations. **b** Macroscopically averaged electrostatic potential of monomorphous and polymorphous $CsPbI_3$ surface slabs. The vacuum level is set to 0 eV.

We computed the absolute band positions for monomorphous and polymorphous $CsBX_3$ compounds (B = Pb, Sn; X = I, Br, Cl) using GGA and GGA+DFT-1/2 (Figure 3.14). For all compounds, the calculated VBM of the CsX-terminated surface is closer to the experimental values reported by Tao *et al.* [22]. When combined with the surface-energy calculations, this result suggests that the experimentally probed surfaces are likely CsX-rich or contain a mixture of CsX and BX_2 terminations. Therefore, the experimentally measured VBM onset is likely dominated by CsX-terminated regions.

In VBM measurements, the exact surface termination of $CsBX_3$ samples is generally not determined. It is therefore possible that both CsX and BX_2 terminations coexist on the surface. However, ultraviolet photoelectron spectroscopy (UPS) mainly probes the most superficial electronic states. Since our calculations show that the BX_2 termination has a deeper VBM, its contribution would appear at higher binding energy and may not determine the UPS onset. Therefore, if CsX and BX_2 terminations coexist, the measured VBM onset is expected to be dominated by the CsX-terminated regions.

For all compounds, GGA+DFT-1/2 gives absolute band positions that are closer to experiment than those obtained with standard GGA. For example, $CsSnI_3$ (Figure 3.14d) clearly shows that GGA+DFT-1/2 gives a better description of the experimental absolute band positions than standard GGA. The experimental VBM and CBM, referenced to the vacuum level, are located at -5.69 eV and -4.38 eV, respectively [22]. For the CsI-terminated surface, standard GGA places the VBM too high, at -3.32 eV for the monomorphous structure and -3.74 eV for the polymorphous structure. In contrast, GGA+DFT-1/2 gives much

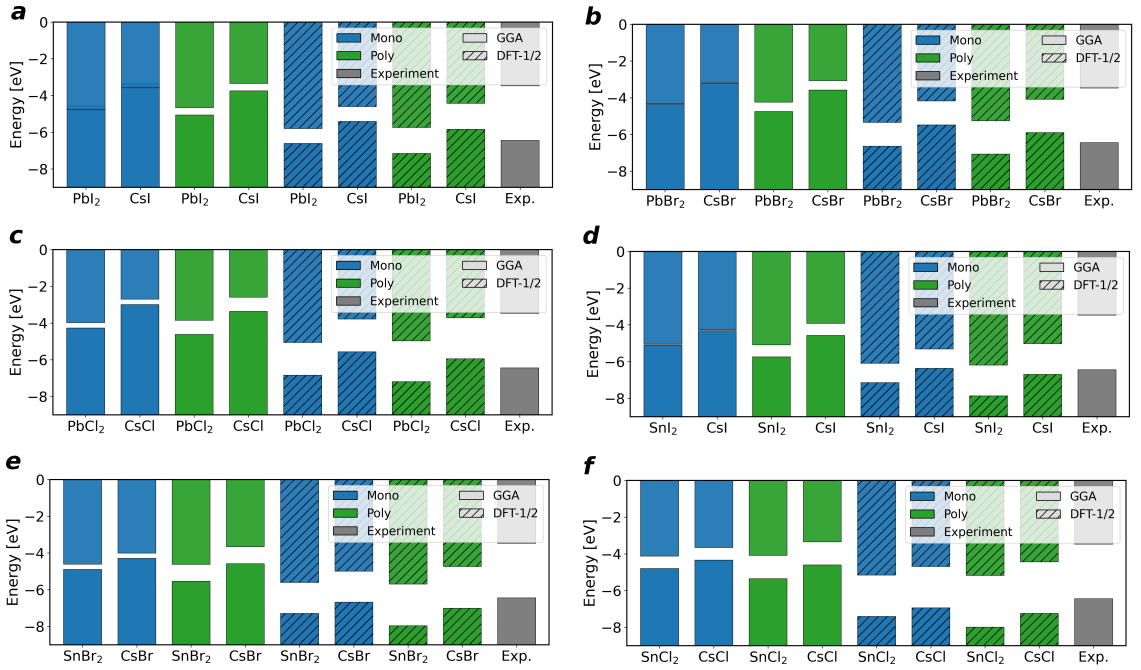

Figure 3.14: Absolute band positions of monomorphous and polymorphous $CsBX_3$ slabs calculated using GGA and GGA+DFT-1/2.

closer values of -5.40 eV and -5.83 eV for the monomorphous and polymorphous structures, respectively. The polymorphous GGA+DFT-1/2 result is particularly close to the experimental VBM. Across the full $CsBX_3$ series, standard GGA systematically places the VBM too shallow relative to vacuum, whereas GGA+DFT-1/2 shifts the VBM downward and brings it closer to experiment.

3.4.2 Role of surface dipoles

The CsX and BX_2 terminations have different absolute VBM positions. For both Pb- and Sn-based compounds, BX_2-terminated surfaces have deeper, more negative VBMs than CsX-terminated surfaces (Figure 3.14). We attribute this difference to the orientation of the local surface dipole in the topmost layer. The local dipole points inward for BX_2 terminations and outward for CsX terminations. In our sign convention, an outward dipole points from the slab center toward the vacuum, while an inward dipole points from the vacuum toward the slab center.

To quantify this effect, we calculated the surface dipole density of the CsI and PbI_2 terminations of $CsPbI_3$, and their difference, as a function of the Gaussian width, σ, used for the calculation of ionic charges (see section 2, equation 2.55) (Figure 3.15a). We tested different values of σ to ensure that the ionic charges remained well localized and surface dipoles are converged. As the starting value, we used the ionic radius of each element and then scaled it. The surface dipole density and their difference converge when σ for each

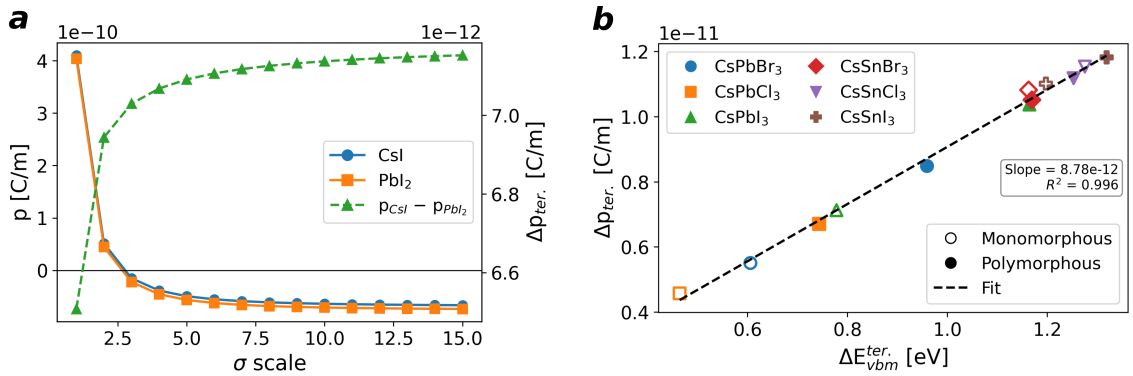

Figure 3.15: Surface dipole density of monomorphous and polymorphous surface slabs. **a** Dependence of the surface dipole density of PbI_2 and CsI terminations of monomorphous $CsPbI_3$, and their difference, on the scaling factor used for the Gaussian width parameter σ. **b** Correlation between the surface dipole density difference of BX_2 and CsX terminations and the corresponding difference in absolute VBM for monomorphous and polymorphous $CsBX_3$ surface slabs.

atom is smaller than 1/8 of the corresponding atomic radius (see Figure 3.15a). Therefore, we used a σ scaling factor of 8 for all surface-dipole calculations.

We then calculated the surface dipole density difference between BX_2 and CsX terminations for the monomorphous and polymorphous configurations of all studied compounds (Figure 3.15b). The surface-dipole difference is defined as

$$\Delta p_{\mathrm{term}} = p_{\mathrm{CsX}} - p_{\mathrm{BX_2}}, \tag{3.3}$$

where p_{CsX} and $p_{\mathrm{BX_2}}$ are the surface dipole density of the CsX- and BX_2-terminated slabs, respectively. The corresponding absolute VBM difference between the two terminations is defined as

$$\Delta E^{\mathrm{term}}_{\mathrm{VBM}} = E^{\mathrm{CsX}}_{\mathrm{VBM}} - E^{\mathrm{BX_2}}_{\mathrm{VBM}}. \tag{3.4}$$

With these definitions, both Δp_{term} and $\Delta E^{\mathrm{term}}_{\mathrm{VBM}}$ are positive, because the CsX-terminated surfaces have shallower the absolute VBMs than the BX_2-terminated surfaces.

Figure 3.15b shows that the surface-dipole difference is linearly related to the VBM difference between the two terminations. The relationship between the work-function shift and the change in surface dipole can be written as [27]

$$\Delta W_f = e\frac{\Delta p_{\mathrm{term}}}{\epsilon_0}, \tag{3.5}$$

where Δp_{term} is the change in the surface dipole moment per unit area, ϵ_0 is the vacuum permittivity, $\epsilon_0 = 8.85 \times 10^{-12}$ F m^{-1}, and e is the elementary charge, $e = 1.60 \times 10^{-19}$ C. When Δp_{term} is plotted against $\Delta V^{\mathrm{term}}_{\mathrm{VBM}}$, the fitted slope is 8.78×10^{-12} F m^{-1}, close to ϵ_0. The fit also gives a high correlation coefficient, $R^2 = 0.996$. This agreement supports

the interpretation that the absolute VBM difference between the two terminations mainly comes from their different surface dipoles. Although ΔW_f in Eq. 3.5 has units of energy in joules, $\Delta V_{\mathrm{VBM}}^{\mathrm{term}}$ was expressed in electronvolts in the fitting procedure. Therefore, the factor e is effectively included in the eV to J conversion, making the fitted slope directly comparable to ϵ_0.

Both monomorphous and polymorphous structures follow the same linear trend. This result shows that the dipole-controlled band alignment is not limited to ideal high-symmetry slabs, but also holds when positional local disorder is included. Among the studied surfaces, polymorphous $CsSnI_3$ has the largest surface-dipole difference, $\Delta p_{\mathrm{term}} = 1.18 \times 10^{-11}$ C m^{-1}, and also the largest VBM difference between terminations, $\Delta E_{\mathrm{VBM}}^{\mathrm{term}} = 1.32$ eV. In contrast, monomorphous $CsPbCl_3$ has the smallest surface-dipole difference, $\Delta p_{\mathrm{term}} = 0.46 \times 10^{-11}$ C m^{-1}, and the smallest VBM difference, $\Delta E_{\mathrm{VBM}}^{\mathrm{term}} = 0.46$ eV.

3.4.3 Chemical trends in the absolute valence-band position

The absolute VBM changes with substitution of both the B-site cation and the halogen atom. Figure 3.16 shows the absolute band positions of all studied monomorphous and polymorphous compounds calculated using GGA and GGA+DFT-1/2. The figure also compares the calculated trends with the experimental values reported by Tao *et al.* [22].

B-site substitution. The VBM of halide perovskites mainly originates from antibonding interactions between the B-site s orbitals and the halide p orbitals. Replacing Pb with Sn raises the VBM for two reasons. First, Sn^{2+} is smaller than Pb^{2+}, which shortens the B–X bond length. The shorter bond increases the overlap between the B-site s orbital and the halide p orbital, raising the energy of the antibonding VBM state. Second, Sn is less electronegative than Pb. As a result, the Sn-5s orbital lies higher in energy, closer to the vacuum level, than the Pb-6s orbital. This also pushes the antibonding VBM upward. Therefore, Sn-based perovskites have shallower, less negative VBMs than the corresponding Pb-based compounds. This trend agrees with previous reports [35]. It is also not limited to corner-sharing ABX_3 perovskites, but has been observed in edge- and face-sharing octahedral networks as well [36].

X-site substitution. Replacing the halogen atom from I to Br to Cl affects the VBM through two competing effects. The first effect is chemical. The halogen electronegativity increases from I to Br to Cl, which lowers the energy of the halide p orbitals. This effect is expected to shift the VBM downward. The second effect is structural. The B–X bond length decreases from I to Br to Cl, which increases the overlap between the B-site s orbital and the halide p orbital. Stronger orbital overlap raises the antibonding VBM state and therefore tends to shift the VBM upward.

In semi-local GGA calculations, the structural contribution spuriously dominates. For both monomorphous and polymorphous structures, the calculated VBM shifts upward from I to Br to Cl, as shown in Figure 3.16a. This trend is opposite to the experimental trend. This behavior can be attributed to the self-interaction error intrinsic to the GGA,

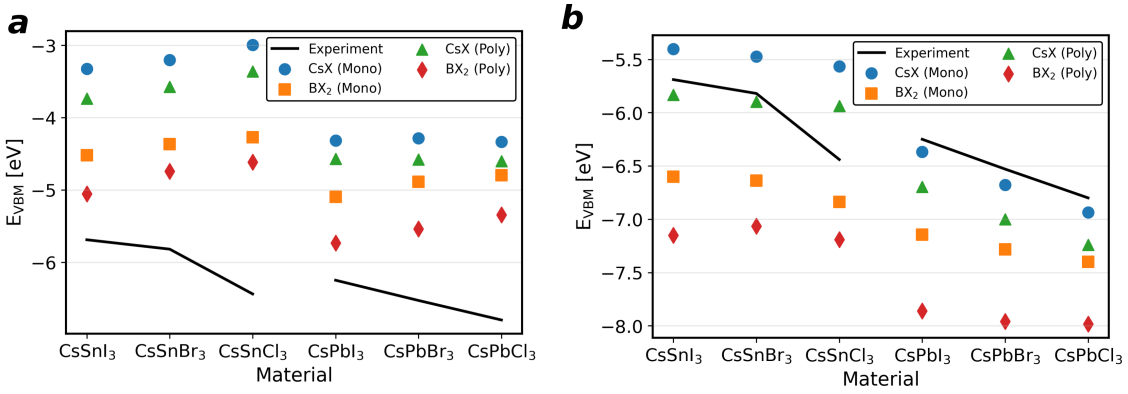

Figure 3.16: Chemical trends in the absolute valence-band maximum (VBM) of Pb- and Sn-based $CsBX_3$ perovskites. The compounds on the x-axis are ordered by increasing halide electronegativity. **a** Absolute VBM computed using the optB86b+SOC. **b** Absolute VBM computed with the DFT-1/2+SOC. Black lines show the experimental VBM trends reported by Tao *et al.* [22].

which over-delocalizes the halogen p orbitals. We therefore applied the DFT-1/2 method, which effectively reduces self-interaction errors and improves the localization of the halogen p states. As a result, the trend is reversed, and the VBM shifts downward in the order I $\rightarrow$ Br $\rightarrow$ Cl (Figure 3.16b). This trend agrees with the experimental results of Tao *et al.* [22]. Therefore, after reducing the self-interaction error, the chemical effect of halide electronegativity becomes dominant over the structural bond-length effect. This result shows that DFT-1/2 is important not only for improving the absolute VBM values, but also for reproducing the correct chemical trend across the halide series.

3.4.4 Effect of local disorder on band alignment

For both CsX- and BX_2-terminated surfaces, the polymorphous structures show deeper VBMs than the corresponding monomorphous structures (Figure 3.14). This shift has two contributions. First, local disorder changes the surface dipole, which modifies the electrostatic potential relative to the vacuum level. Second, local disorder elongates B–X bonds and tilts the octahedra, which stabilizes the bulk VBM. On average, local disorder lowers the bulk VBM by ~ 0.55 eV.

The bar plots in Figure 3.17 show these three quantities: the work-function shift estimated from the surface-dipole change using Eq. 3.5, the bulk VBM shift, and the total absolute VBM shift. Although the bulk VBM shift is large, the surface-dipole contribution partly compensates it. Therefore, the total vacuum-referenced VBM shift is smaller than the bulk contribution alone. Surfaces with a larger compensating surface-dipole shift show a smaller total absolute VBM shift.

Among the studied compounds, the CsCl-terminated surface of $CsPbCl_3$ shows the largest work-function shift, -0.37 eV. This shift partly compensates the band-edge change

caused by positional local disorder, so the absolute VBM shifts by only 0.27 eV. In contrast, positive work-function shifts are found only for the PbI_2- and $PbBr_2$-terminated surfaces of $CsPbI_3$ and $CsPbBr_3$, with values of 0.09 eV and 0.01 eV, respectively. These two surfaces also show some of the largest absolute VBM shifts, 0.64 eV and 0.65 eV. Overall, CsX-terminated surfaces show a stronger compensating work-function shift than BX_2-terminated surfaces. Therefore, when positional local disorder is included, the absolute VBM of CsX-terminated surfaces shifts less than that of BX_2-terminated surfaces.

The stronger compensation in CsX-terminated surfaces can be explained by a larger change in the surface dipole. In these surfaces, local disorder reduces the coherent Cs–X surface rumpling, mainly by pulling the outer halide layer inward. At the same time, the increase in surface B–B contraction also helps to reduce the surface dipole (Table 3.3). Thus, both structural changes act in the same direction and lead to a larger decrease in the surface dipole. In BX_2-terminated surfaces, however, the situation is more complex because several structural changes compete with each other. The increased B–B contraction tends to reduce the surface dipole, whereas the change in the out-of-plane B–X–B angle can push some surface halide atoms toward the vacuum, which increases the surface dipole. As a result, these two effects partly cancel each other, giving a smaller net dipole change than in CsX-terminated surfaces. In some cases, the dipole increase caused by the outward displacement of surface halides is larger than the dipole decrease caused by B–B contraction. This explains the positive work-function shifts of the PbI_2- and $PbBr_2$-terminated $CsPbI_3$ and $CsPbBr_3$ slabs. In these two cases, the large change in the out-of-plane B–X–B angle promotes an outward displacement of surface halides. This outward displacement increases the surface dipole and can overcome the dipole reduction caused by the simultaneous increase in out-of-plane B–B contraction. As a result, the PbI_2- and $PbBr_2$-terminated $CsPbI_3$ and $CsPbBr_3$ slabs show positive work-function shifts.

Overall, the absolute VBM shift is well described by the sum of the bulk VBM shift and the surface-dipole-induced work-function shift. Thus, local disorder stabilizes the bulk VBM, while the accompanying change in surface dipole partly compensates this stabilization in the the absolute VBM.

We also compared the effect of surface reconstruction on the absolute VBM of monomorphous $CsPbI_3$ (Figure 3.18). Surface reconstruction does not significantly affect the absolute VBM of the CsI-terminated monomorphous slab, giving values similar to those of the unreconstructed monomorphous slab (Figure 3.18a). For the PbI_2 termination, reconstruction lowers the VBM of the monomorphous slab, but the shift remains smaller than that observed in the fully polymorphous slab, as expected (Figure 3.18b).

For $CsPbX_3$ and $CsSnX_3$, the agreement between monomorphous or polymorphous structures and experiment is different (Figure 3.16). This difference can be understood by considering both the accuracy of DFT-1/2 and the uncertainty in the experimental ionization potentials. For $CsPbX_3$, the monomorphous structures appear to give ionization potentials closer to experiment. However, this should not be interpreted as evidence that the monomorphous model is more realistic. Several studies have shown that DFT-1/2 can slightly overcorrect self-interaction errors in halide perovskites and even more strongly

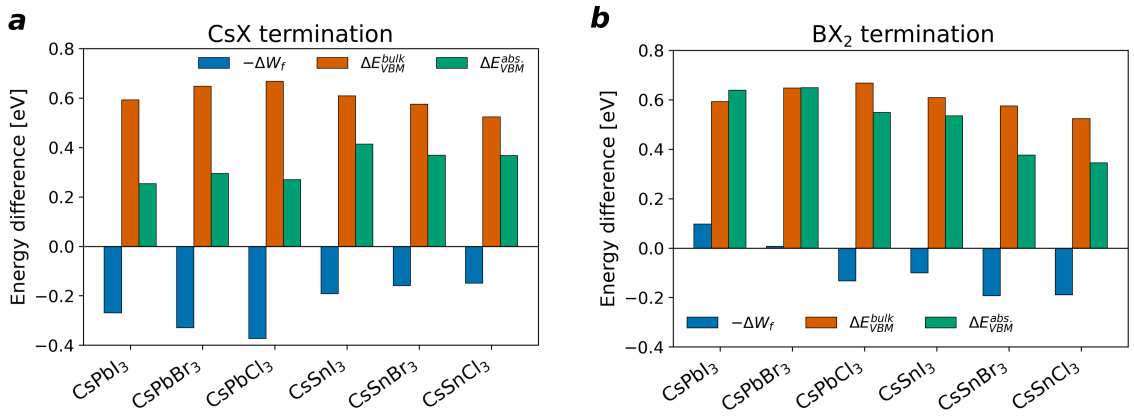

Figure 3.17: Work-function shift, bulk VBM shift, and absolute VBM shift between monomorphous and polymorphous surface slabs for **a** CsX and **b** BX_2 terminations.

in other semiconductors [37, 38]. This can lead to errors in band-edge energies of about 0.2 eV in perovskites [39, 40, 41]. In addition, Tao *et al.* reported ionization potentials averaged over several samples, with a spread of up to about 0.3 eV for Pb-based compounds [22]. This spread indicates that the measured values are sensitive to sample-dependent factors such as surface condition and stoichiometry.

Therefore, the apparent agreement between the monomorphous $CsPbX_3$ structures and experiment is likely caused by error compensation. The polymorphous structures remain physically more meaningful because they include local symmetry breaking and structural disorder, which are expected in real materials. For $CsSnX_3$, the polymorphous structures give more accurate ionization potentials. This is consistent with the smaller experimental spread reported for Sn-based compounds, around 0.07 eV [22], and with the smaller DFT-1/2 error reported for Sn-based perovskites [41]. Taken together, these results support the use of polymorphous structures as the more realistic model for both Pb- and Sn-based compounds, while the apparently better agreement of monomorphous $CsPbX_3$ with experiment is most likely an artifact of partial error compensation.

3.4.5 Surface states

Dangling bonds may be present on the surface and could induce surface states inside the band gap. We computed the planar-averaged squared wavefunctions of the last six highest occupied Kohn-Sham states ($E_n \ldots E_{n-5}$) including SOC at the Gamma point to identify surface states within the band gap (Figure 3.19). For the CsI termination, we did not find any surface states in either the polymorphous or monomorphous structures, consistent with the results of Delgado *et al.* [42]. This is expected because the outermost octahedra remain intact. In a PbI_2-terminated polymorphous $CsPbI_3$ surface slab, the two highest occupied Kohn-Sham states are well localized in the surface region of the slab and can therefore be assigned to surface states. The E_{n-2} state is localized in the bulk region of the slab and can be assigned to the VBM. In the monomorphous PbI_2-terminated slab, we

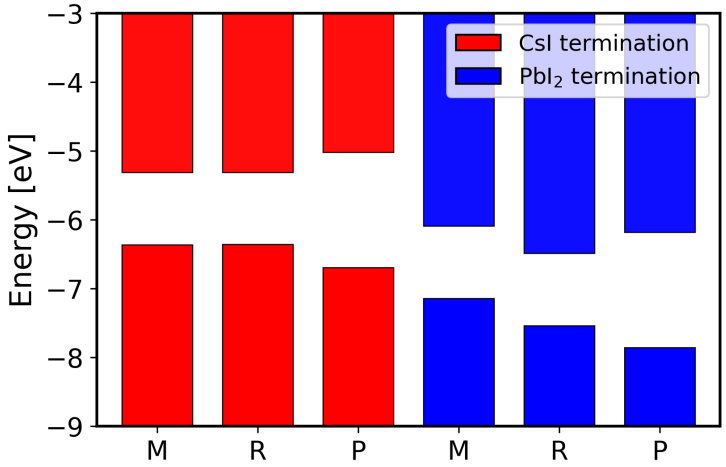

Figure 3.18: Absolute band positions of monomorphous (M), reconstructed monomorphous (R), and polymorphous (P) $CsPbI_3$ surface slabs.

did not identify any surface states within the band gap however, surface-localized states are present within the valence band. This arises because the formation of surface states depends strongly on the Pb coordination. In the polymorphous case, the out-of-plane B–X–B bond angle decreases due to local disorder in addition to surface reconstruction, whereas in the monomorphous structure it remains 180 °. The calculated energy separation between that surface state and the VBM (E_n - E_{n-2}) is 0.11 eV. The asymmetry in the planar-averaged squared wavefunctions for the PbI_2-terminated slab arises from the degeneracy of the Kohn-Sham states rather than from a net dipole. This is confirmed by the symmetry of the planar-averaged total charge density and electrostatic potential, as well as the flat vacuum electrostatic potential, all of which indicate the absence of any net dipole. Overall, the polymorphous configuration can possibly present surface states, whereas their formation is hindered in the monomorphous configuration by its symmetry constraints.

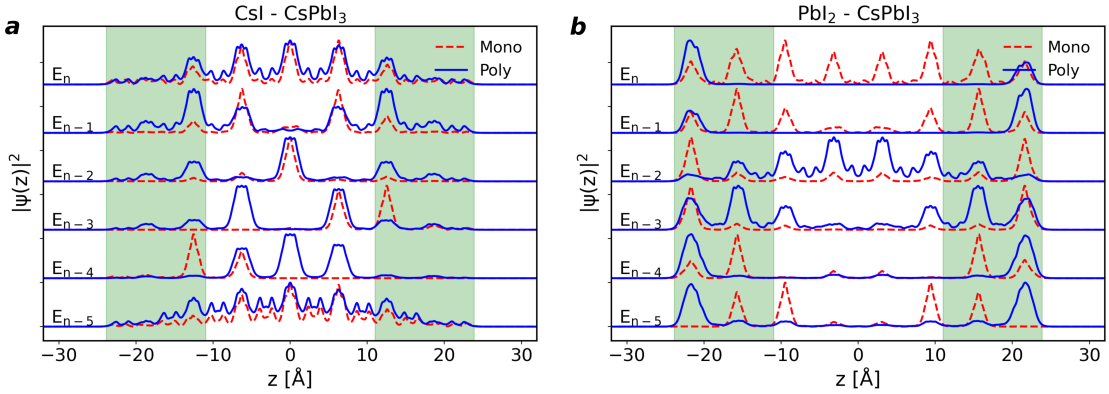

Figure 3.19: (a) Planar-averaged squared wave function of the CsI-terminated $CsPbI_3$ surface slab. (b) Planar-averaged squared wave function of the PbI_2-terminated $CsPbI_3$ surface slab. Here, E_n–E_{n-5} denote the six highest occupied Kohn-Sham states.

References

[1] Jasurbek Gulomov, Guido Roma, Marios Zacharias, Jacky Even, and Claudine Katan. The role of local disorder in surface properties of inorganic halide perovskites. Manuscript submitted to Physical Review Materials, 2026.

[2] Arthur Marronnier, Guido Roma, Soline Boyer-Richard, Laurent Pedesseau, Jean-Marc Jancu, Yvan Bonnassieux, Claudine Katan, Constantinos C. Stoumpos, Mercouri G. Kanatzidis, and Jacky Even. Anharmonicity and Disorder in the Black Phases of Cesium Lead Iodide Used for Stable Inorganic Perovskite Solar Cells. *ACS Nano*, 12(4):3477–3486, March 2018.

[3] Chr. Kn. Møller. Crystal Structure and Photoconductivity of Cæsium Plumbohalides. *Nature*, 182(4647):1436–1436, November 1958.

[4] Koji Yamada, Shinya Funabiki, Hiromi Horimoto, Takashi Matsui, Tsutomu Okuda, and Sumio Ichiba. Structural Phase Transitions of the Polymorphs of $CsSnI_3$ by Means of Rietveld Analysis of the X-Ray Diffraction. *Chemistry Letters*, 20(5):801–804, May 1991.

[5] M Mori and H Saito. An X-ray study of successive phase transitions in $CsSnBr_3$. *Journal of Physics C: Solid State Physics*, 19(14):2391–2401, May 1986.

[6] G. G. Bulanova, A. B. Podlesskaya, L. V. Soboleva, and A. I. Soklakov. Study of Cesium Tin Chloride $CsSnCl_3$ and Cs_2SnCl_6. *Izvestiya Akademii Nauk SSSR, Neorganicheskie Materialy*, 8:1930–1932, 1972.

[7] Li Lang, Ji-Hui Yang, Heng-Rui Liu, H.J. Xiang, and X.G. Gong. First-principles study on the electronic and optical properties of cubic ABX_3 halide perovskites. *Physics Letters A*, 378(3):290–293, January 2014.

[8] Marios Zacharias, George Volonakis, Feliciano Giustino, and Jacky Even. Anharmonic electron-phonon coupling in ultrasoft and locally disordered perovskites. *npj Computational Materials*, 9(1):153, August 2023.

[9] Jonathon S. Bechtel and Anton Van der Ven. Octahedral tilting instabilities in inorganic halide perovskites. *Physical Review Materials*, 2(2), February 2018.

[10] Sebastián Caicedo-Dávila, Adi Cohen, Silvia G. Motti, Masahiko Isobe, Kyle M. McCall, Manuel Grumet, Maksym V. Kovalenko, Omer Yaffe, Laura M. Herz, Douglas H. Fabini, and David A. Egger. Disentangling the effects of structure and lone-pair electrons in the lattice dynamics of halide perovskites. *Nature Communications*, 15(1), May 2024.

[11] Arthur Marronnier, Heejae Lee, Bernard Geffroy, Jacky Even, Yvan Bonnassieux, and Guido Roma. Structural Instabilities Related to Highly Anharmonic Phonons in Halide Perovskites. *The Journal of Physical Chemistry Letters*, 8(12):2659–2665, June 2017.

[12] Hiroki Kawai, Giacomo Giorgi, Andrea Marini, and Koichi Yamashita. The Mechanism of Slow Hot-Hole Cooling in Lead-Iodide Perovskite: First-Principles Calculation on Carrier Lifetime from Electron–Phonon Interaction. *Nano Letters*, 15(5):3103–3108, April 2015.

[13] Xin-Gang Zhao, Gustavo M. Dalpian, Zhi Wang, and Alex Zunger. Polymorphous nature of cubic halide perovskites. *Physical Review B*, 101(15), April 2020.

[14] Xavier Gonze and Changyol Lee. Dynamical matrices, Born effective charges, dielectric permittivity tensors, and interatomic force constants from density-functional perturbation theory. *Physical Review B*, 55(16):10355–10368, April 1997.

[15] Jacob N. Wilson, Jarvist M. Frost, Suzanne K. Wallace, and Aron Walsh. Dielectric and ferroic properties of metal halide perovskites. *APL Materials*, 7(1), January 2019.

[16] Zeli Xu, Simon Thébaud, Marios Zacharias, Laurent Pedesseau, Claudine Katan, and Jacky Even. Influence of lattice anharmonicity and structural phase transitions on the Fröhlich interaction in $CsPbBr_3$: a first-principles study. *Physical Review B*, 113(23), June 2026.

[17] Marios Zacharias, George Volonakis, Feliciano Giustino, and Jacky Even. Anharmonic lattice dynamics via the special displacement method. *Physical Review B*, 108(3), July 2023.

[18] V. M. Goldschmidt. Die Gesetze der Krystallochemie. *Die Naturwissenschaften*, 14(21):477–485, May 1926.

[19] Marios Zacharias, George Volonakis, Laurent Pedesseau, Claudine Katan, Feliciano Giustino, and Jacky Even. Roadmap for electronic structure, anharmonicity, and electron-phonon calculations in locally disordered inorganic and hybrid halide perovskites. *Physical Review B*, 113(8), February 2026.

[20] Fernando P. Sabino, Xin Gang Zhao, Gustavo M. Dalpian, and Alex Zunger. Impact of symmetry breaking and spin-orbit coupling on the band gap of halide perovskites. *Physical Review B*, 110(3), July 2024.

[21] Jacky Even, Laurent Pedesseau, Jean-Marc Jancu, and Claudine Katan. Importance of Spin-Orbit Coupling in Hybrid Organic/Inorganic Perovskites for Photovoltaic Applications. *The Journal of Physical Chemistry Letters*, 4(17):2999–3005, August 2013.

[22] Shuxia Tao, Ines Schmidt, Geert Brocks, Junke Jiang, Ionut Tranca, Klaus Meerholz, and Selina Olthof. Absolute energy level positions in tin- and lead-based halide perovskites. *Nature Communications*, 10(1), June 2019.

[23] Saeid Abedi, Mahdi Tarighi Ahmadpour, Samira Baninajarian, Hamideh Kahnouji, S. Javad Hashemifar, Zhong-Kang Han, and Sergey V. Levchenko. Statistical analysis of the performance of a variety of first-principles schemes for accurate prediction of binary semiconductor band gaps. *The Journal of Chemical Physics*, 158(18), May 2023.

[24] Boubacar Traore, Jacky Even, Laurent Pedesseau, Mikaël Képénekian, and Claudine Katan. Band gap, effective masses, and energy level alignment of 2D and 3D halide perovskites and heterostructures using DFT-1/2. *Physical Review Materials*, 6(1), January 2022.

[25] Rebecca J. Sutton, Marina R. Filip, Amir A. Haghighirad, Nobuya Sakai, Bernard Wenger, Feliciano Giustino, and Henry J. Snaith. Cubic or Orthorhombic? Revealing the Crystal Structure of Metastable Black-Phase $CsPbI_3$ by Theory and Experiment. *ACS Energy Letters*, 3(8):1787–1794, June 2018.

[26] Julia Wiktor, Ursula Rothlisberger, and Alfredo Pasquarello. Predictive Determination of Band Gaps of Inorganic Halide Perovskites. *The Journal of Physical Chemistry Letters*, 8(22):5507–5512, October 2017.

[27] Boubacar Traoré, Pooja Basera, Alexandra J. Ramadan, Henry J. Snaith, Claudine Katan, and Jacky Even. A Theoretical Framework for Microscopic Surface and Interface Dipoles, Work Functions, and Valence Band Alignments in 2D and 3D Halide Perovskite Heterostructures. *ACS Energy Letters*, 7(1):349–357, December 2021.

[28] Azimatu Seidu, Marc Dvorak, Patrick Rinke, and Jingrui Li. Atomic and electronic structure of cesium lead triiodide surfaces. *The Journal of Chemical Physics*, 154(7), February 2021.

[29] Lixia Long, Dan Cao, Jiapeng Fei, Jianfeng Wang, Yun Zhou, Zhouting Jiang, Zhiwei Jiao, and Haibo Shu. Effect of surface intrinsic defects on the structural stability and electronic properties of the all-inorganic halide perovskite $CsPbI_3$(001) film. *Chemical Physics Letters*, 734:136719, November 2019.

[30] Limin She, Zhitao Shen, and Dingyong Zhong. Surface Structures of $CsSnI_3$(001) Films on Au(111). *The Journal of Physical Chemistry C*, 127(40):20101–20105, October 2023.

[31] Jeremy Hieulle, Shulin Luo, Dae-Yong Son, Afshan Jamshaid, Collin Stecker, Zonghao Liu, Guangren Na, Dongwen Yang, Robin Ohmann, Luis K. Ono, Lijun Zhang, and Yabing Qi. Imaging of the Atomic Structure of All-Inorganic Halide Perovskites. *The Journal of Physical Chemistry Letters*, 11(3):818–823, January 2020.

[32] Biao Yuan, Zeyu Wang, Shuchen Zhang, Christoph Hofer, Chuang Gao, Tamazouzt Chennit, Hongsheng Shi, Xiaoyan Wu, Yu Han, Letian Dou, Yi Yu, and Timothy J. Pennycook. Atomically resolved edges and defects in lead halide perovskites. *Nature*, 647(8089):364–368, October 2025.

[33] Jingya Mi, Yuetian Chen, Xiaomin Liu, Xingtao Wang, Yanfeng Miao, Yabing Qi, and Yixin Zhao. Synergistic stabilization of $CsPbI_3$ inorganic perovskite via 1D capping and secondary growth. *Journal of Energy Chemistry*, 68:387–392, May 2022.

[34] Pengyang Wang, Xingwang Zhang, Yuqin Zhou, Qi Jiang, Qiufeng Ye, Zema Chu, Xingxing Li, Xiaolei Yang, Zhigang Yin, and Jingbi You. Solvent-controlled growth of inorganic perovskite films in dry environment for efficient and stable solar cells. *Nature Communications*, 9(1), June 2018.

[35] Simone Meloni, Giulia Palermo, Negar Ashari-Astani, Michael Grätzel, and Ursula Rothlisberger. Valence and conduction band tuning in halide perovskites for solar cell applications. *Journal of Materials Chemistry A*, 4(41):15997–16002, 2016.

[36] Robert P. Reynolds, Jessica H. Persaud, George Volonakis, Andrew J. Torma, Patricia E. Meza, Zek E. Kelly, Constantinos C. Stoumpos, Vinayak P. Dravid, Claudine Katan, Aditya D. Mohite, and Mercouri G. Kanatzidis. Design Principles for Narrow-Gap Hybrid Semiconductors: Insights from Viologen-Tin and Viologen-Lead Iodides. *Journal of the American Chemical Society*, 147(28):24573–24593, July 2025.

[37] I. Guilhon, D. S. Koda, L. G. Ferreira, M. Marques, and L. K. Teles. Approximate quasiparticle correction for calculations of the energy gap in two-dimensional materials. *Physical Review B*, 97(4), January 2018.

[38] Joshua Claes, Bart Partoens, and Dirk Lamoen. Decoupled DFT-$\frac{1}{2}$ method for defect excitation energies. *Physical Review B*, 108(12), September 2023.

[39] Fernando Valadares, Ivan Guilhon, Lara K. Teles, and Marcelo Marques. Electronic Structure Panorama of Halide Perovskites: Approximated DFT-1/2 Quasiparticle and Relativistic Corrections. *The Journal of Physical Chemistry C*, 124(34):18390–18400, August 2020.

[40] Fernando Valadares, Ivan Guilhon, Lara K. Teles, and Marcelo Marques. Tunable Band Gap and Rhombohedral Distortion in Lead-Free $CsSn_{1-x}Ge_xI_3$ Mixed Perovskites. *The Journal of Physical Chemistry C*, 125(39):21740–21747, September 2021.

[41] Shu Xia Tao, Xi Cao, and Peter A. Bobbert. Accurate and efficient band gap predictions of metal halide perovskites using the DFT-1/2 method: GW accuracy with DFT expense. *Scientific Reports*, 7(1), October 2017.

[42] Frederico P. Delgado, Frederico Simões, Leeor Kronik, Waldemar Kaiser, and David A. Egger. Machine-Learning Force Fields Reveal Shallow Electronic States on Dynamic Halide Perovskite Surfaces. *ACS Energy Letters*, 10(7):3367–3374, June 2025.

Chapter 4

Bulk, Surface, and Interface Properties of All-Inorganic 2D Perovskites

In this chapter, we investigate the bulk, surface, and interface properties of all-inorganic 2D with different octahedral layer thickness. Building on the previous chapter, where local positional disorder was shown to play an important role in the structural and electronic properties of 3D inorganic halide perovskites, this chapter examines whether similar effects are present in lower-dimensional perovskite systems. First, we discuss the structural models and thermodynamic stability of single-halide and mixed-halide 2D perovskites. We then analyze the role of local positional disorder in their dynamical and thermodynamic stability. After that, we examine how positional local disorder affects the bulk electronic structure, band gap, and effective mass. Finally, we extend the analysis to surface properties and 2D/3D interfaces, including surface energies, ionization potentials, adhesion energies, and band offsets.

4.1 Structures and Thermodynamic Stability of 2D perovskites

4.1.1 Structures of 2D perovskites

The all-inorganic layered halide perovskite $Cs_2PbI_2Cl_2$ was synthesized by Li *et al.* [1]. In this work, we used the reported experimental structure as the starting model and then fully relaxed it. $Cs_2PbI_2Cl_2$ has a tetragonal K_2NiF_4-type Ruddlesden–Popper structure with the I4/mmm space group, as shown in Fig. 4.1a [2]. The relaxed lattice constants are $a = b = 5.650$ Å and $c = 18.912$ Å (Table 4.1). The experimental values are $a = b = 5.63$ Å and $c = 18.87$ Å (Table 4.1). Therefore, the calculated lattice constants agree with experiment within 0.4%, showing that the relaxed structure is reliable. In this mixed-halide 2D perovskite, I atoms occupy the apical sites, while Cl atoms occupy the equatorial sites of the Pb-halide octahedra.

Table 4.1: Calculated lattice constants of $Cs_{n+1}Pb_nI_{n+1}Cl_{2n}$ structures. Experimental values are taken from Ref. [1] for $n = 1$ and Ref. [3] for $n = 2$.

Compound	$a = b$ (Å)	c (Å)	Experimental lattice constants (Å)
$Cs_2PbI_2Cl_2$ ($n = 1$)	5.650	18.912	$a = b = 5.63$, $c = 18.87$
$Cs_3Pb_2I_3Cl_4$ ($n = 2$)	5.668	31.162	$a = b = 5.66$, $c = 30.1$
$Cs_4Pb_3I_4Cl_6$ ($n = 3$)	5.666	43.660	–
$Cs_5Pb_4I_5Cl_8$ ($n = 4$)	5.668	56.295	–
$Cs_6Pb_5I_6Cl_{10}$ ($n = 5$)	5.667	69.056	–
$CsPbICl_2$ ($n = \infty$)	5.657	6.295	–

As far as we know, the highest experimentally reported member of the $Cs_{n+1}Pb_nI_{n+1}Cl_{2n}$ family is the $n = 2$, $Cs_3Pb_2I_3Cl_4$, which was synthesized by Shuai *et al.* using chemical vapor deposition (CVD) [3]. They reported lattice constants of $a = b = 5.66$ Å and $c = 30.1$ Å (Table 4.1). Here the discrepancy might be increased by the fact that the measured sample is reported as slightly Cl-richer. However the complete crystallographic structure of the $n = 2$ compound could not be experimentally accessed directly by single crystal diffractometry, and only the lattice parameters and space group are reported. The authors of Ref. [3] discuss the uncertainty on the $n = 2$ compound stoichiometry, especially the I/Cl ratio. Our relaxed lattice constants are $a = b = 5.668$ Å and $c = 31.162$ Å (Table 4.1), as shown in Fig. 4.1b. The in-plane lattice constant agrees very well with experiment, while the out-of-plane lattice constant is overestimated by about 3.5%. Overestimation of lattice constants is commonly observed in semilocal GGA calculations. During relaxation, the structure shows a small out-of-plane displacement of Pb and Cl atoms. This distortion is mainly an off-centering along the out-of-plane direction, rather than an octahedral tilt that would break the I4/mmm space group

symmetry. We checked the symmetry of the relaxed $n = 2$ structure using the spglib Python package with a tolerance of 10^{-5} Å [4]. The relaxed structure was still identified as having the same I4/mmm space group. A similar out-of-plane off-centering after DFT relaxation was also reported by Shuai *et al.* [3].

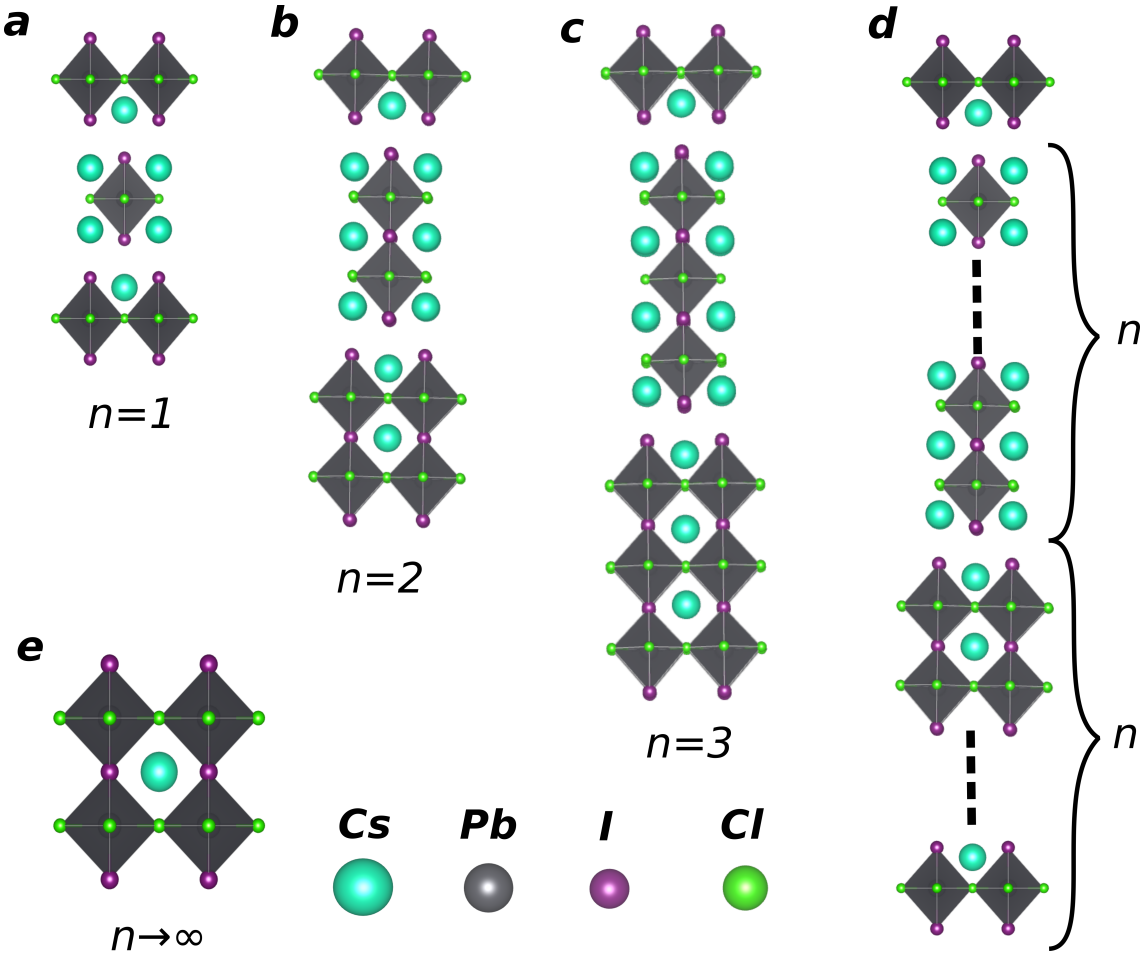

Figure 4.1: Structures of all-inorganic mixed-halide Ruddlesden–Popper 2D perovskites. **a** $Cs_2PbI_2Cl_2$ ($n = 1$) phase. **b** $Cs_3Pb_2I_3Cl_4$ ($n = 2$) phase. **c** $Cs_4Pb_3I_4Cl_6$ ($n = 3$) phase. **d** General structure of $Cs_{n+1}Pb_nI_{n+1}Cl_{2n}$. Here, n is the number of connected Pb-halide octahedral layers in one perovskite slab. **e** $CsPbICl_2$ 3D reference structure, corresponding to the limit $n \to \infty$.

In this work, we studied structures from $n = 1$ to $n = 5$. The 2D structures thicker octahedral layer (higher-n) were built by adding Pb-halide octahedral layers to both sides of the Ruddlesden–Popper perovskite slab, as shown schematically in Fig. 4.1d. All structures were then fully relaxed. In the limit $n \to \infty$, the layered structure approaches the 3D $CsPbICl_2$ reference structure. The relaxed $CsPbICl_2$ structure is also tetragonal because the I and Cl atoms have different ionic sizes and occupy different crystallographic positions. Its relaxed lattice constants are $a = b = 5.657$ Å and $c = 6.295$ Å (Table 4.1).

The in-plane lattice constant is almost unchanged with increasing n, remaining very close to 5.66 Å (Table 4.1). In contrast, the out-of-plane lattice constant increases as (2n+1)a* where a*, fitted to the calculated c values, is 6.261 Å, only 0.5% smaller than the relaxed c value for n=∞.

We also examined how the out-of-plane Pb off-centering changes with the thickness of the octahedral layer, as shown in Fig. 4.2a. In the n = 1 structure, the Pb off-centering is zero because the Pb atoms remain at the centers of the octahedra. For thicker layers, Pb atoms near the CsI spacer are slightly displaced in the out-of-plane direction. The largest average displacement is found for the n = 2 structure, where the Pb off-centering is about 0.16 Å.

When the octahedral layer becomes thicker, the average Pb off-centering gradually decreases. This is because Pb off-centering mainly occurs in the outer octahedra close to the CsI spacer, while the Pb atoms remain at the centers of the inner-region octahedra, as shown in Fig. 4.2b–d. Therefore, increasing n adds more inner, undisplaced Pb atoms, which lowers the average Pb off-centering. In the 3D reference structure $CsPbICl_2$, the average Pb off-centering disappears.

Traore *et al.* [5] found that the length of the organic spacer plays an important role in the distortion of 2D perovskites, with longer spacers leading to larger distortions. In the fully inorganic $Cs_{n+1}Pb_nI_{n+1}Cl_{2n}$ structure, the spacer is an inorganic CsI layer; therefore, it introduces only a very small distortion, mainly Pb off-centering, rather than octahedral tilting as observed for organic spacers. Most of the distortion is present in the octahedra close to the spacer, which is consistent with the results of Kepenekian *et al.* [6].

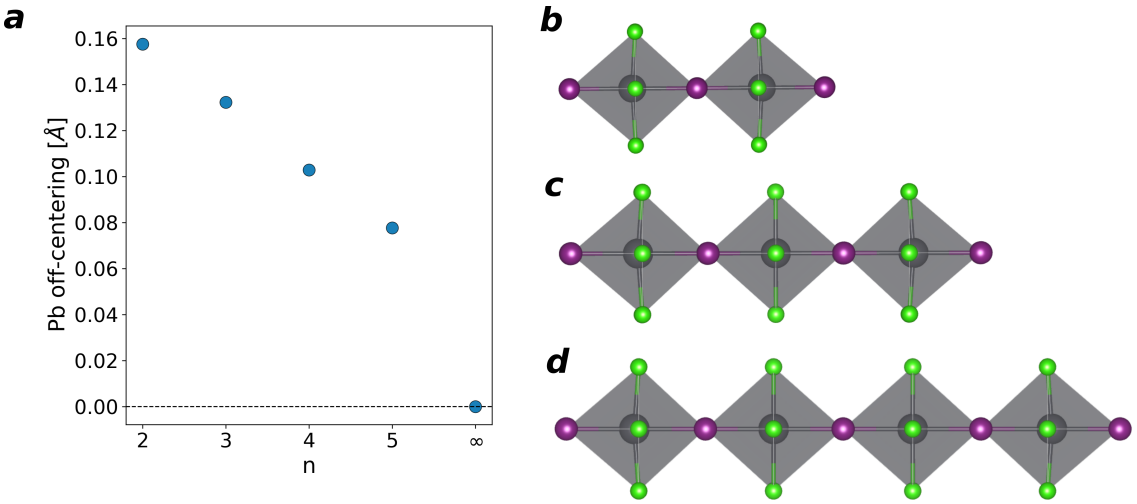

Figure 4.2: Pb atom off-centering. **a** relationship between average Pb atom off-centering and octaheral layer thickness. **b,c,d** Structural representation of Pb atom off-centering in n=2 (b), n=3 (c) and n=4 (d) phases. Only a sequence of n octahedra perpedicular to the 2D stacking is shown.

4.1.2 Single-halide 2D perovskites

Although Cs_2PbI_4 has not yet been synthesized, we theoretically studied this single-halide, all-inorganic 2D perovskite, as shown in Figure 4.3a. After structural relaxation, the calculated lattice constants are $a = b = 6.23$ Å and $c = 19.11$ Å. These lattice constants are larger than those of $Cs_2PbI_2Cl_2$, which is expected because I^- has a larger ionic radius than Cl^-.

To evaluate the thermodynamic stability of Cs_2PbI_4, we calculated its decomposition enthalpy. The decomposition enthalpy is defined as

$$\Delta H_{\mathrm{d}} = \sum_i \nu_i H^i_{\mathrm{prod}} - H_{\mathrm{struc}}, \tag{4.1}$$

where H^i_{prod} is the enthalpy of each decomposition product, ν_i is its stoichiometric coefficient, and H_{struc} is the enthalpy of the original structure. A positive ΔH_{d} means that decomposition into the selected products is energetically unfavorable. Therefore, the structure is stable against that reaction path. In contrast, a negative ΔH_{d} means that the decomposition reaction is energetically favorable, and the structure may decompose into those products.

We calculated the decomposition energy of Cs_2PbI_4 for three possible reaction paths, as listed in the caption of Figure 4.3. The results show that Cs_2PbI_4 is stable against reaction paths (1) and (2), but unstable against reaction path (3). Reaction path (3) produces the 3D $CsPbI_3$ phase and the 0D Cs_4PbI_6 phase. Therefore, Cs_2PbI_4 is expected to decompose into 3D and 0D phases rather than form as a stable 2D perovskite.

This result agrees with previous experimental and theoretical studies. Ray *et al.* [7] reported the formation of Cs_4PbBr_6 0D and $CsPbBr_3$ 3D phases instead of the Cs_2PbBr_4 2D phase in experiments. Previous DFT studies [1, 8] also found negative decomposition enthalpies for Cs_2PbX_4 against decomposition into 3D and 0D products. Therefore, Cs_2PbX_4 compounds, where X = I, Br, or Cl, have mainly been studied as theoretical model systems. These models are useful for understanding quantum confinement, layered crystal structures, and the differences between 2D Cs_2PbX_4 and 3D $CsPbX_3$ perovskites [8, 9, 10].

4.1.3 Different configurations of $Cs_2PbI_2Cl_2$

Li *et al.* [1] reported the synthesis of a site-ordered mixed-halide 2D perovskite, $Cs_2PbI_2Cl_2$, in which iodide ions occupy the apical sites and chloride ions occupy the equatorial sites (see Fig. 4.1a). In this work, we also generated several ordered halide configurations while keeping the same stoichiometry. These configurations were obtained by exchanging the positions of I and Cl atoms within the crystal structure. The structural model contains two formula units, corresponding to 14 atoms in total. After considering symmetry, 16 symmetry-inequivalent configurations were obtained and tested.

For each configuration, we calculated the decomposition energy using Eq. 4.1. Four possible decomposition pathways were considered:

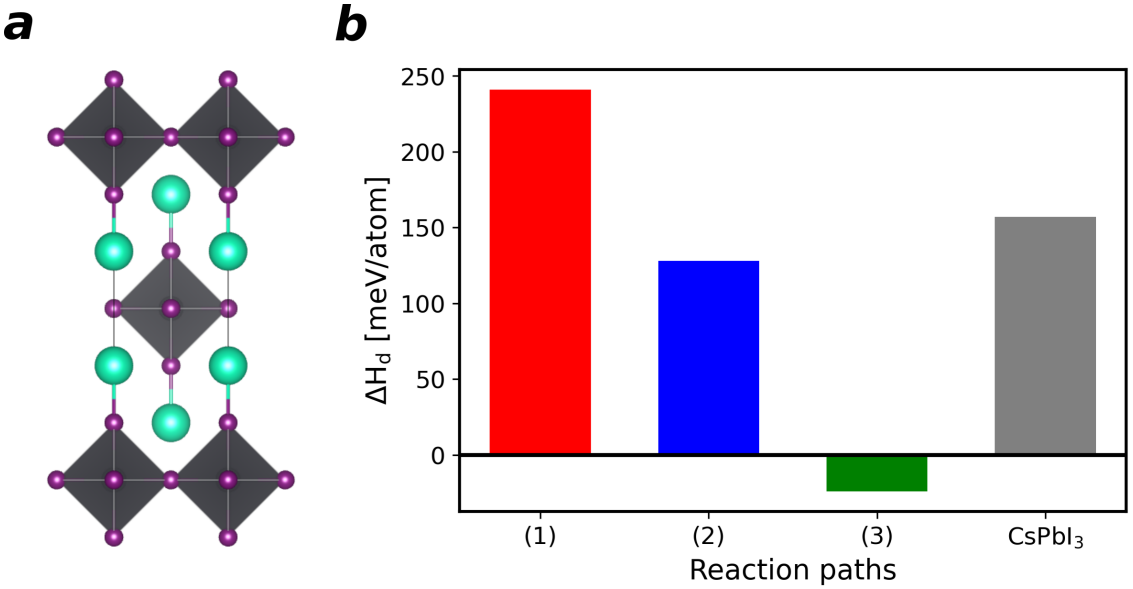

Figure 4.3: Crystal structure (a) and decomposition energy (b) of Cs_2PbI_4. The considered decomposition reaction paths are: (1) $Cs_2PbI_4 \rightarrow 2CsI + PbI_2$, (2) $Cs_2PbI_4 \rightarrow CsI + CsPbI_3$, and (3) $Cs_2PbI_4 \rightarrow \frac{2}{3}CsPbI_3 + \frac{1}{3}Cs_4PbI_6$. For comparison, the decomposition energy of $CsPbI_3$ through $CsPbI_3 \rightarrow CsI + PbI_2$ is also shown.

$$
\begin{aligned}
&\textbf{A.}\ Cs_2PbI_2Cl_2 \rightarrow 2CsI + PbCl_2 \\
&\textbf{B.}\ Cs_2PbI_2Cl_2 \rightarrow 2CsCl + PbI_2 \\
&\textbf{C.}\ Cs_2PbI_2Cl_2 \rightarrow \frac{2}{3}CsPbCl_3 + \frac{1}{3}Cs_4PbI_6 \\
&\textbf{D.}\ Cs_2PbI_2Cl_2 \rightarrow \frac{2}{3}CsPbI_3 + \frac{1}{3}Cs_4PbCl_6
\end{aligned}
\tag{4.2}
$$

Figure 4.4 shows the decomposition energies of the site-ordered configuration and the halide-exchanged configurations. The site-ordered configuration, where I occupies the apical sites and Cl occupies the equatorial sites, is stable against all four decomposition pathways. In contrast, the halide-disordered configurations become unstable against pathways C and D, which produce 3D and 0D perovskite-related phases. Among all tested configurations, only the site-ordered structure has positive decomposition energies for all considered pathways. This indicates that the specific ordering of I and Cl atoms plays an important role in stabilizing the $Cs_2PbI_2Cl_2$ structure.

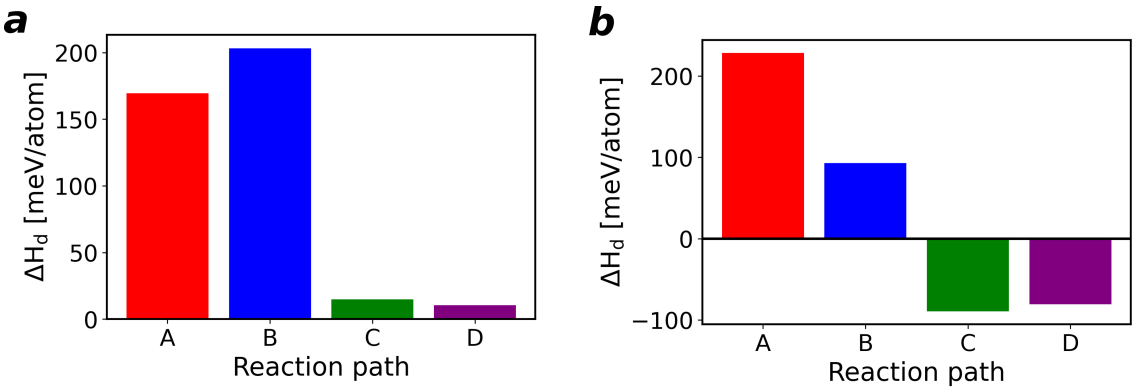

Figure 4.4: Decomposition energies of the site-ordered and one of halide-disordered $Cs_2PbI_2Cl_2$ configurations. In the site-ordered configuration, I atoms occupy the apical sites and Cl atoms occupy the equatorial sites. In the halide-disordered configuration, I atoms occupy the equatorial sites and Cl atoms occupy the apical sites. A, B, C, and D on the x-axis correspond to the decomposition pathways defined in Eq. 4.2.

4.2 Role of Local Positional Disorder in the Dynamical and Thermodynamic Stability of 2D Perovskites

4.2.1 Lattice dynamics of layered halide perovskites

We calculated the phonon dispersion of the monomorphous configuration of $Cs_2PbI_2Cl_2$ ($n = 1$), as shown in Fig. 4.5c. No imaginary modes are observed, indicating that the monomorphous configuration of the $n = 1$ 2D perovskite is dynamically stable. This behavior differs from the high-symmetry 3D perovskites discussed in Chapter 3, where dynamical instabilities were observed. Xu *et al.* [11] reported an imaginary mode at the M point for $Cs_2PbI_2Cl_2$. However, their calculation was performed using a flake model with a 15 Å vacuum layer along the out-of-plane direction, rather than a fully periodic structure.

The reason for this discrepancy can be found in the different boundary conditions used in the two calculations. In the flake model used by Xu *et al.* [11], the vacuum region along the out-of-plane direction removes part of the periodic constraint and weakens the out-of-plane interaction with neighboring layers. Similarly, Shao *et al.* [12] studied surface octahedral tilting in exfoliated 2D RP perovskites and showed that surfaces can unlock octahedral tilts that are constrained in the bulk-like structure. Therefore, the octahedral layers in the flake model have more structural freedom, which allow octahedral rotations and lead to the imaginary mode at the M point. In contrast, in the fully periodic structure (bulk-like) used in the present work, the CsI rock-salt spacer layers constrain the Pb–halide octahedral layers and suppress such rotations. Therefore, the high-symmetry $Cs_2PbI_2Cl_2$ structure is dynamically stable under fully periodic boundary conditions.

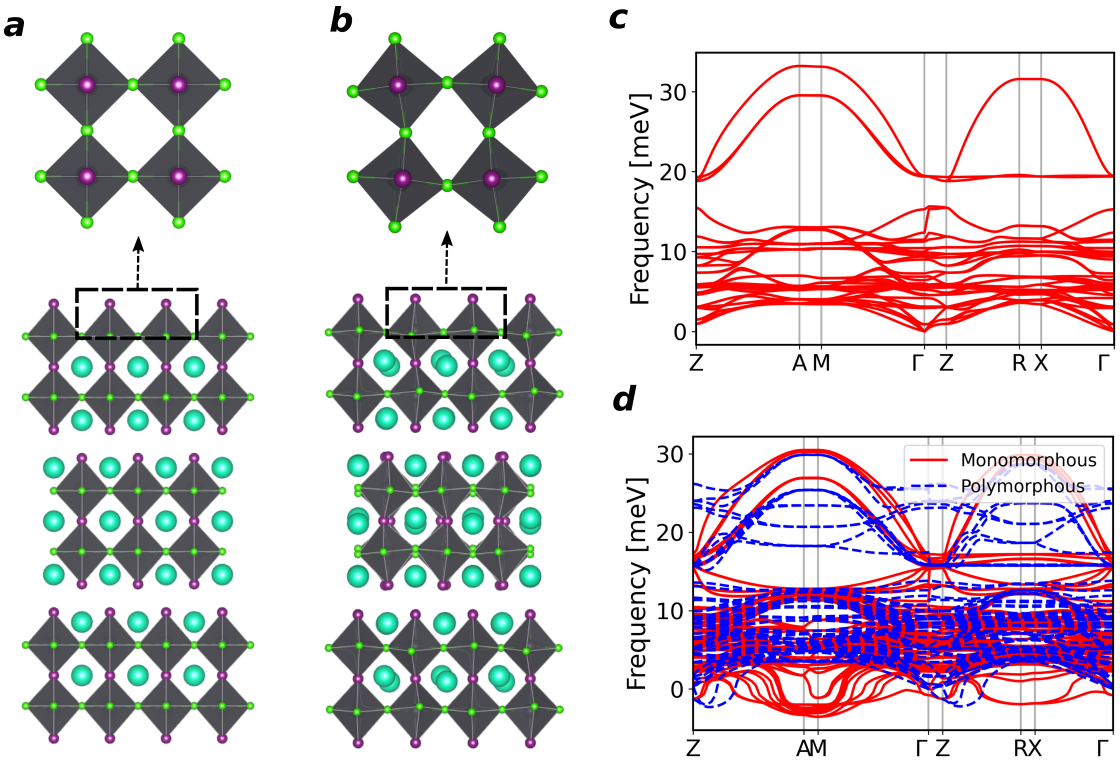

Figure 4.5: Phonon dispersion and structure of monomorphous and polymorphous structures. **a,b** Structures of monomorphous (a) and polymorphous (b) $Cs_3Pb_2I_3Cl_4$ (n=2). On top of each structure, there is topview of marker area. **c** Phonon dispersion of monomorphous configuration of Cs_2PbI_2 (n=1). **d** Phonon dispersion of monomorphous and polymorphous n=2 structure.

We also calculated the phonon dispersion of the $n = 2$ structure, $Cs_3Pb_2I_3Cl_4$, as shown in Fig. 4.5d. The monomorphous $n = 2$ structure shows imaginary modes along the A–M and R–X directions, which are associated with octahedral tilting [13]. A small imaginary mode is also observed at the Z high-symmetry point. To examine the effect of local structural disorder, we generated a polymorphous network for the $n = 2$ phase using ASDM with a $2 \times 2 \times 1$ supercell. We did not double the structure along the out-of-plane direction because the conventional unit cell already contains two formula units in this direction.

The introduction of positional local disorder removes the imaginary phonon modes along the A–M and R–X directions. Although polymorphism breaks the local structural symmetry, it does not necessarily produce a net electric dipole. The unstable modes observed along the A–M and R–X directions are consistent with alternating displacement patterns. Thus, in these layered perovskites, the dominant distortions are antiferrodistortive octahedral tilts rather than coherent polar displacements. There is still a small imaginary mode, with an energy scale of about 1 meV (8 cm^{-1}), at the Z point after the introduction of positional local disorder. Since the Z point corresponds to the out-of-plane direction, this mode may indicate either a weak residual instability along this direction or a numerical artifact. To clarify its origin, we performed several tests.

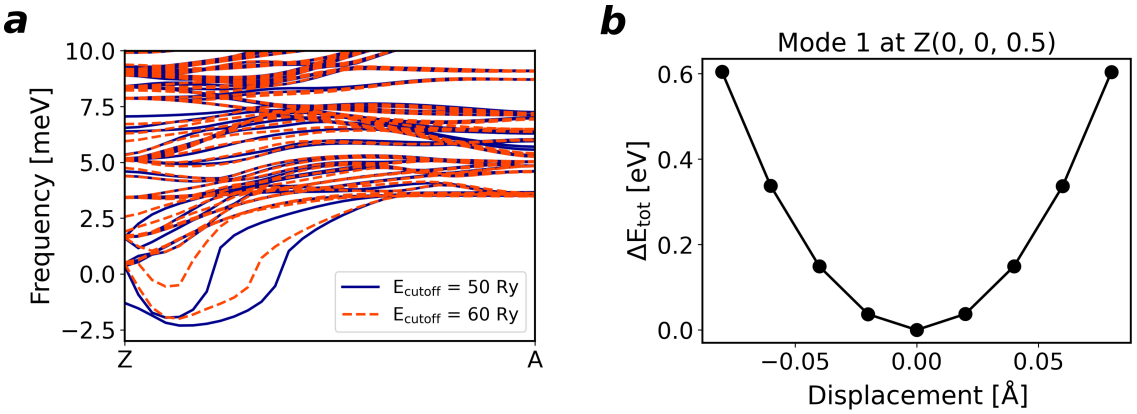

Figure 4.6: Accuracy check of phonon dispersion. **a** Phonon dispersion of n=2 polymorphous configuration calculated with cutoff of 50 Ry and 60 Ry. **b** Relationship between total energy and displacement of atoms along eigenvector of imaginary mode Z(0.0, 0.0, 0.5)

First, we regenerated the polymorphous structure using a $2 \times 2 \times 2$ supercell in order to accomodate possible distortions along the out-of-plane direction. However, doubling the polymorphous structure along this direction did not remove the imaginary mode at the Z point. Second, we displaced the structure with a very small amplitude along the eigenvector of the imaginary mode to check whether the mode corresponds to a double-well potential energy surface. Instead of a double-well shape, we obtained a parabolic relationship between displacement and total energy, as shown in Fig. 4.6b. This behavior indicates that the structure is dynamically stable against this displacement. Finally, we

tested the effect of numerical convergence by calculating the phonon dispersion using energy cutoffs of 50 Ry and 60 Ry. Increasing the cutoff energy reduced the magnitude of the negative frequency at the Z point, as shown in Fig. 4.6a. Given the non-negligible computational burden for the calculations of the phonons of the polymorphous configuration of the $n = 2$ structure is computationally large, we did not increase further the cutoff energy. Based on these tests, the small imaginary mode at the Z point is likely due to numerical error rather than a real structural instability. A similar issue was reported for a hybrid 2D perovskite by Chen *et al.* [14], where a small imaginary mode along the out-of-plane direction was also attributed to numerical error.

Both the $n = 1$ $Cs_2PbI_2Cl_2$ and $n = 2$ $Cs_3Pb_2I_3Cl_4$ structures show nearly flat phonon branches along the out-of-plane direction, indicating weak interlayer vibrational coupling in these layered 2D perovskite structures, as shown in Fig. 4.5c,d. This weak dispersion is related to the localized vibrations of Cs and I atoms [15]. In contrast, the stronger Pb–halide connectivity within the inorganic layers leads to more dispersive phonon branches along the in-plane directions. Local disorder also lowers the optical phonon frequencies, similar to the behavior observed in 3D perovskites [16] (see also chapter 3, figure 3.2). This softening indicates that local distortions modify the force constants and reduce the vibrational energies of optical modes.

4.2.2 Energy gain due to positional local disorder

Positional local disorder introduces changes in the B–X–B bond angles and B–X bond lengths. Figure 4.7(a) shows the bond-angle changes due to local disorder and Pb off-centering as a function of the octahedral-layer thickness, n. The data include the Pb–Cl–Pb changes (blue discs) and Pb–I–Pb changes (red squares) caused by local disorder in polymorphous structures, as well as the Pb–Cl–Pb change (green triangle) in the $PbCl_2$ layer adjacent to the CsI spacer due to Pb off-centering in the monomorphous structure.

The B–X–B angle change due to positional local disorder is defined as the difference between the average angles in the monomorphous and polymorphous structures. Since the monomorphous configuration of the $n = 1$ structure is already stable, it does not form a polymorphous network. Therefore, the angle changes for both Pb–Cl–Pb and Pb–I–Pb are 0° for $n = 1$. Pb off-centering in the monomorphous configuration affects only the Pb–Cl–Pb angle. The Pb–Cl–Pb angle change in the monomorphous structure is defined as its deviation from the linear configuration, $180^\circ - \theta_{\mathrm{Pb{-}{-}Cl{-}{-}Pb}}$.

The angle changes increase as the octahedral-layer thickness increases. The magnitude of the Pb–I–Pb angle change is higher than that of the Pb–Cl–Pb angle because the Pb–Cl–Pb angle has already deviated from 180° in the monomorphous structure due to Pb off-centering. For the $n = 2$ phase, the Pb–I–Pb and Pb–Cl–Pb angle changes are 11.6° and 8.43°, respectively. In the $n \to \infty$ 3D reference structure, the Pb–Cl–Pb and Pb–I–Pb angle changes become almost the same, reaching about 23.6°. To the best of our knowledge, Hou *et al.* [17] are the only authors who have studied the role of positional local disorder in 2D perovskites. They reported a B–X–B angle change of 12.8° in the $n = 2$ phase of a

hybrid DJ perovskite.

Positional local disorder extends the B–X bond length. The elongation of the B–X bond length also increases with increasing octahedral-layer thickness. The average B–X bond-length elongation is 0.011 Å for $n = 2$ and 0.065 Å for $n \to \infty$.

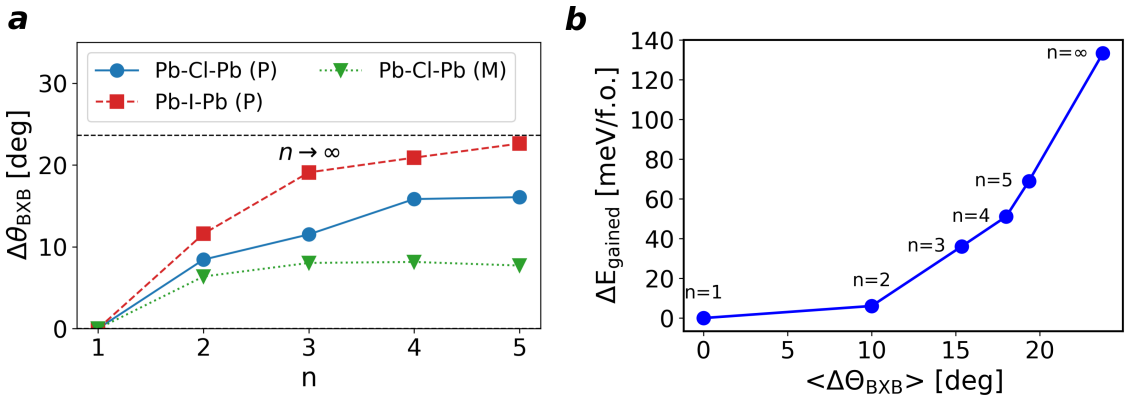

Figure 4.7: Structural and energetic consequences of local disordering. **a** Dependence of the changes in the Pb–Cl–Pb and Pb–I–Pb bond angles on the octahedral-layer thickness, n. The Pb–Cl–Pb (P) and Pb–I–Pb (P) angle changes arise from positional local disorder in the polymorphous structures, whereas the Pb–Cl–Pb (M) angle change in the $PbCl_2$ layer immediately adjacent to the CsI spacer originates from Pb off-centering in the monomorphous structures. P and M denote polymorphous and monomorphous structures, respectively. **b** Correlation between the energy gain and the average B-X-B angle change. The average B-X-B angle change is calculated as the average of the Pb-Cl-Pb and Pb-I-Pb angle changes.

The ground-state polymorphous structure has lower potential energy than the average high-symmetry structure. Therefore, introducing positional local disorder in perovskites leads to an energy gain. The energy gain is 6.09 meV/f.o. for the $n = 2$ and 133.3 meV/f.o. for the $n \to \infty$ structures. The energy gain of $CsPbICl_2$ ($n \to \infty$) is close to that of 3D cubic $CsPbI_3$ (147 meV/f.o.). In $n > 1$ 2D perovskites, the energy gain due to positional local disorder also shows a strong correlation with the average B-X-B angle change, as shown in Fig. 4.7b. A similar trend was reported for 3D perovskites by Zacharias *et al.* [16] (see also chapter 3, figure 3.3). So, a larger B-X-B angle change leads to a higher energy gain in both layered and 3D perovskites.

In all-inorganic $n = 1$ 2D perovskites the CsI rocksalt layer contrains the octahedral layers and suppresses structural fluctuations. In $n > 1$ 2D perovskites, this constraint becomes weaker as the octahedral layer thickness increases. As a result, structures with thicker octahedral layer show larger B-X-B angle changes, B-X bond length elongation and higher energy gains.

4.2.3 Effect of positional local disorder on thermodynamic stability

In the previous section, we discussed the thermodynamic stability of the $Cs_2PbI_2Cl_2$ $n = 1$ 2D perovskite with respect to competing phases on the basis of the enthalpy of the decomposition reaction, ΔH_d. In this section, we focus on the trend of ΔH_d vs n ($n = 1-5$) and the influence of local positional disorder on this trend as shown in Fig. 4.8. As shown in Fig. 4.4a, the decomposition enthalpies associated with reaction paths C and D are significantly lower than those of reaction paths A and B. Therefore, we mainly focus on the decomposition enthalpies of reaction paths C and D. The reaction paths given in Eq. 4.2 were defined for the $n = 1$ structure. For the general case, reaction paths C and D can be written as follows:

$$\begin{aligned} \textbf{C.}\ & \mathrm{Cs_{n+1}Pb_nI_{n+1}Cl_{2n}} \rightarrow \frac{\mathrm{n-1}}{3}\mathrm{CsPbI_3} + \frac{\mathrm{2n}}{3}\mathrm{CsPbCl_3} + \frac{1}{3}\mathrm{Cs_4PbI_6} \\ \textbf{D.}\ & \mathrm{Cs_{n+1}Pb_nI_{n+1}Cl_{2n}} \rightarrow \frac{\mathrm{n+1}}{3}\mathrm{CsPbI_3} + \frac{\mathrm{2(n-1)}}{3}\mathrm{CsPbCl_3} + \frac{1}{3}\mathrm{Cs_4PbCl_6} \end{aligned} \tag{4.3}$$

In the 3D reference structure, reaction paths C and D converge to a single reaction because, as n increases, the contribution of the 0D phase decreases and becomes negligible in the infinite-layer-thickness limit. Therefore, the limiting decomposition reaction involves only the 3D iodide- and chloride-based perovskites:

$$\mathrm{CsPbICl_2} \rightarrow \frac{1}{3}\mathrm{CsPbI_3} + \frac{2}{3}\mathrm{CsPbCl_3}. \tag{4.4}$$

The decomposition enthalpy decreases with increasing octahedral layer thickness. For the monomorphous configurations, larger octahedral layer thickness leads to negative decomposition enthalpy for the higher-n structures. For the monomorphous 3D reference structure, the decomposition enthalpy is -15 meV/atom, indicating that this configuration is unfavorable with respect to decomposition into the 3D Cl- and I-based cubic perovskites in Eq. 4.4. In the polymorphous configurations, the decomposition enthalpy also decreases with increasing octahedral layer thickness; however, it saturates after $n > 4$ and approaches the decomposition enthalpy of the polymorphous 3D reference structure. The decomposition enthalpy of the polymorphous 3D reference structure is 11.5 meV/atom. Therefore, within the polymorphous description, all 2D $\mathrm{Cs_{n+1}Pb_nI_{n+1}Cl_{2n}}$ perovskites considered here are thermodynamically stable against the selected decomposition pathways. The stabilization obtained with the polymorphous description indicates that local positional disorder plays an important role in stabilizing the mixed-halide layered perovskites. This conclusion is consistent with the polymorphous-network picture of cubic halide perovskites, where local symmetry-breaking distortions lower the total energy relative to the ideal monomorphous cubic structure [18]. The saturation of the decomposition enthalpy for $n > 4$ is physically reasonable because high-n 2D structures approach the 3D mixed-halide limit. While this specific saturation trend has not been reported for the present all-inorganic mixed-halide series, previous studies have shown that the thermodynamic stability of organic-spacer layered halide perovskites depends strongly on octahedral layer thickness [19, 20].

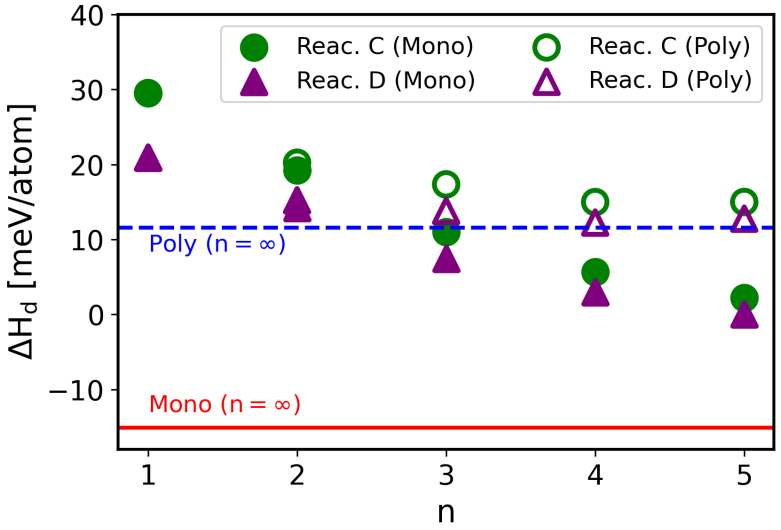

Figure 4.8: Dependence of the decomposition enthalpy of monomorphous and polymorphous configurations on the octahedral layer thickness, n, of $Cs_{n+1}Pb_nI_{n+1}Cl_{2n}$. Red full (blue dashed) horizontal line indicate the decomposition entahlpies of the monomophous (polymorphous) 3D reference structures, $CsPbICl_2$.

4.3 Bulk Electronic Properties of 2D Perovskites

4.3.1 Electronic structure

Figure 4.9a shows the electronic bands of the high-symmetry $Cs_2PbI_2Cl_2$ structure ($n = 1$) at the GGA+SOC level. The bands are almost flat along the out-of-plane directions (A–M and R–X). This indicates weak charge transport along the stacking direction, which is consistent with the layered nature of 2D perovskites and with previous theoretical studies [11, 3]. Figures 4.9b and 4.9c show the band structures of the monomorphous and polymorphous configurations for the $n = 2$ and $n \to \infty$ structures, respectively. The monomorphous bands are shown by red lines, while the polymorphous electronic states are represented by the spectral function (blue). Similar to the $n = 1$ systems, the $n = 2$ structure also shows weak dispersion along the out-of-plane direction.

Positional local disorder opens the band gap in both the $n = 2$ and $n \to \infty$ structures. The band gap opening is 0.12 eV for the $n = 2$ and 0.56 eV for the $n \to \infty$ compound. According to the calculated electronic bands at the GGA+SOC level, all studied materials are direct semiconductors. This is consistent with the strong optical response reported experimentally for all-inorganic layered mixed-halide perovskites [1]. The calculated band gap is 1.48 eV for the $n = 1$ and 1.23 eV for the monomorphous $n = 2$ structure. These values are much smaller than the experimental band gaps reported by Shuai *et al.*, which are 2.95 eV and 2.99 eV for the $n = 1$ and $n = 2$ systems, respectively [3]. This underestimation is expected because the calculations were performed using GGA+SOC. Therefore, in

this work, we focus mainly on the band gap trend rather than on the absolute comparison with experiment.

Figure 4.9d shows the evolution of the band gap as a function of the octahedral layer thickness n for both monomorphous and polymorphous configurations. In both cases, the band gap decreases as n increases. This trend is consistent with previous theoretical studies on $Cs_{n+1}Pb_nI_{n+1}Cl_{2n}$ [21], layered $A_{n+1}M_nX_{3n+1}$ structures (A = Cs, M = Pb or Sn, and X = Cl, Br, or I) [22], and hybrid layered halide perovskites with organic spacer cations [23, 24, 25].

However, the rate of band gap reduction is different for the two configurations. The band gap of the monomorphous configuration decreases more sharply with increasing n, whereas the polymorphous configuration shows a weaker dependence on the octahedral layer thickness. This difference can be qualitatively understood using the ideal effective-mass quantum confinement model for layered halide perovskites, assuming infinite confinement barriers [24]:

$$E_g = E_g^{3D} + \frac{\hbar^2 \pi^2}{2\mu L_{QW}^2}. \tag{4.5}$$

Here, E_g^{3D} is the band gap of the $n \to \infty$ 3D reference structure, L_{QW} is the quantum-well thickness, μ denotes the reduced effective mass of the 3D reference structure along the stacking direction, and $\hbar$ is the reduced Planck constant. This model is physically justified for $n > 1$, whereas for $n = 1$ it should be regarded only as an empirical fitting law, since the extremely small quantum-well thickness leads to confinement wave vectors outside the parabolic region in which the 3D effective-mass approximation is valid [24].

Positional local disorder flattens the band dispersion near the VBM and CBM, as shown in Figure 4.9c. This flattening increases the effective masses of the charge carriers and therefore increases the reduced effective mass μ. According to Eq. 4.5, a larger μ reduces the confinement term. As a result, the band gap becomes less sensitive to the quantum-well thickness. In other words, the increase in reduced effective mass weakens the energetic effect of quantum confinement and leads to a smaller confinement-induced band gap shift. In addition, the band gap opening due to positional local disorder also contributes to the change in the band gap slope. This effect is discussed in more detail in the next section.

Only two experimental band gaps are currently available for $Cs_{n+1}Pb_nI_{n+1}Cl_{2n}$, corresponding to the $n = 1$ and $n = 2$ structures reported by Shuai *et al.* [3]. Experimentally, the band gap changes by only 0.04 eV from $n = 1$ to $n = 2$. In our calculations, this difference is 0.25 eV for the monomorphous configurations and 0.13 eV for the polymorphous configurations. Therefore, including positional local disorder improves the calculated trend and gives a result closer to experiment. The remaining difference may be partly related to the absence of many-body corrections in the present GGA+SOC calculations.

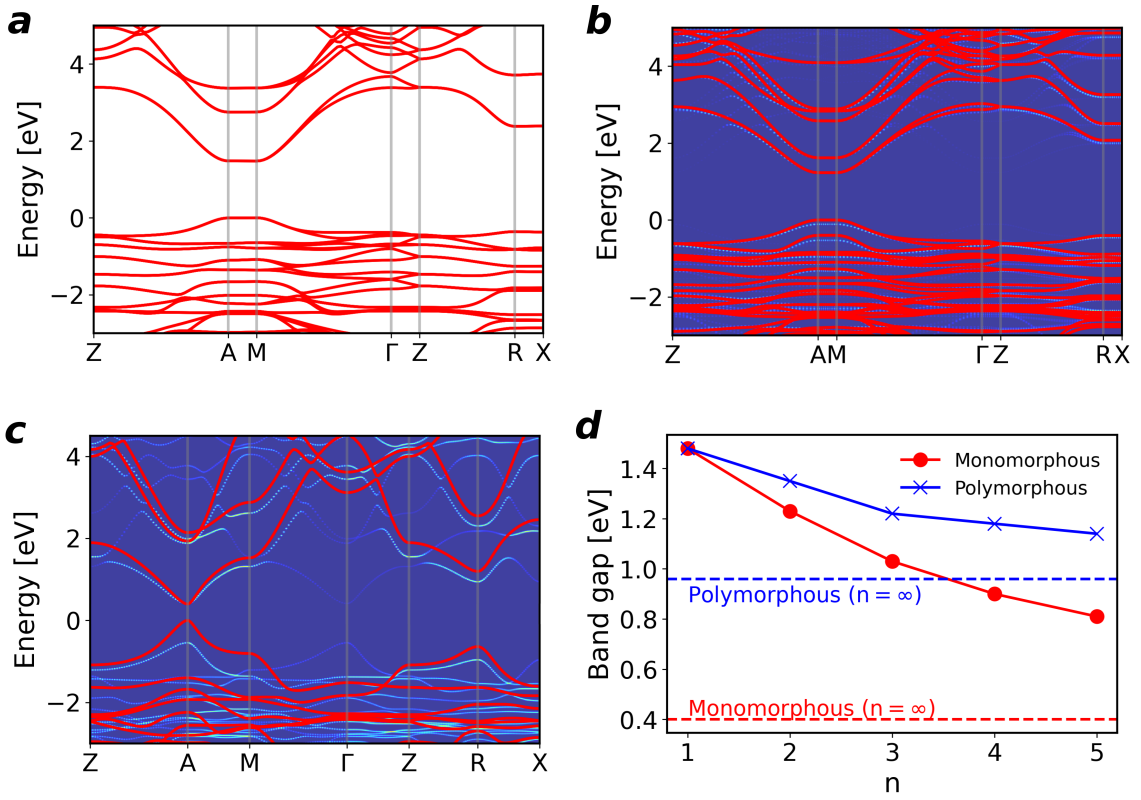

Figure 4.9: Band structure of 2D perovskites with octahedral layer thicknesses of $n = 1$ (a), $n = 2$ (b), and $n \to \infty$ (c). In panels (b) and (c), the colormap represents the polymorphous spectral function, while the red curves represent the monomorphous band structures. (d) Band gap evolution of the monomorphous and polymorphous configurations as a function of the octahedral layer thickness n. In the band structures, the VBM is aligned to 0 eV. For the comparison between monomorphous and polymorphous configurations, the VBM of the monomorphous structure is aligned to 0 eV.

4.3.2 Band gap opening due to local disorder

Figure 4.10 shows the bonding scheme of $Cs_2PbI_2Cl_2$ ($n = 1$), adapted from Ref. [11]. According to this scheme, the VBM is mainly formed by σ-antibonding interactions between Pb(6s) and halogen p orbitals. The CBM is formed by antibonding Pb(6p)-based states, including Pb(6p)–Cl(3s) σ-antibonding and Pb(6p)–Cl(3p) π-antibonding interactions. This is different from 3D lead halide perovskites, where the CBM is mainly derived from Pb(6p) orbitals. Symmetry analysis further shows that the VBM contains Pb(6s)–Cl($p_{x,y}$) and Pb(6s)–I(p_z) antibonding contributions [26, 27]. In our structure, Cl atoms occupy the equatorial positions, whereas I atoms occupy the apical positions. Therefore, the Pb–Cl bond length and Pb–Cl–Pb angle mainly affect the in-plane Pb(6s)–Cl($p_{x,y}$) interaction, while the Pb–I bond length and Pb–I–Pb angle affect the out-of-plane Pb(6s)–I(p_z) interaction. Variations in these bond lengths and bond angles can modify the VBM energy and contribute to the band gap opening.

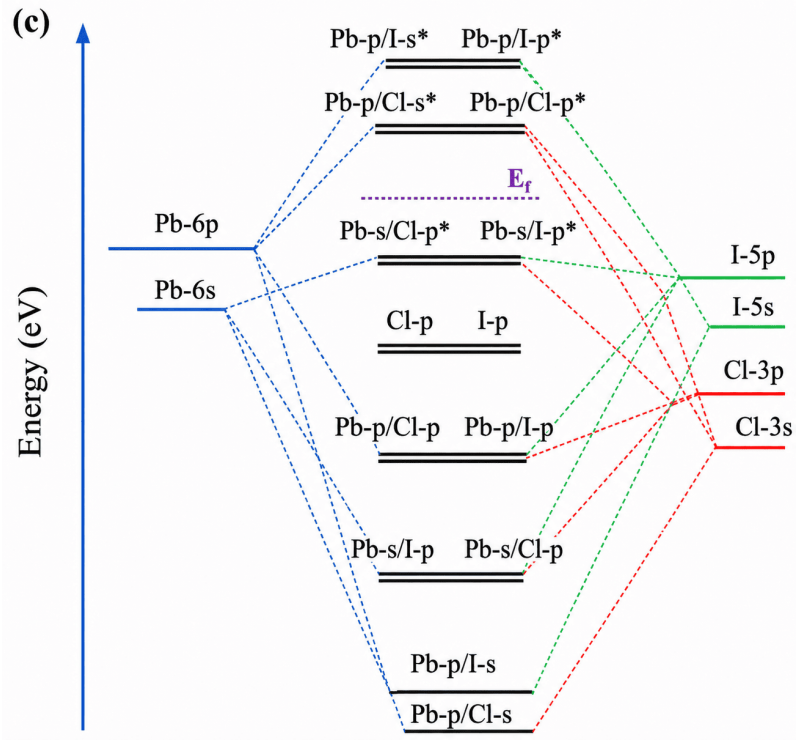

Figure 4.10: Bonding scheme of $Cs_2PbI_2Cl_2$, adapted from Ref. [11].

For the $n > 1$ structures, positional local disorder modifies both Pb–I and Pb–Cl bond lengths and changes both Pb–I–Pb and Pb–Cl–Pb bond angles. To quantify the role of the bond-angle changes, we separated the contributions of the in-plane Pb–Cl–Pb angle and the out-of-plane Pb–I–Pb angle. First, we considered only the Pb–Cl–Pb angle change while keeping the Pb–I–Pb angle fixed at 180°, and then calculated the resulting band gap opening. Next, we considered only the Pb–I–Pb angle change while keeping the Pb–Cl–Pb

angle equal to that of the monomorphous structure. The band gap openings obtained from these isolated cases were then compared with the full band gap opening of the polymorphous structure, as shown in Figure 4.11.

We found that the Pb–I–Pb angle change does not give a noticeable band gap opening, whereas the Pb–Cl–Pb angle change clearly opens the band gap. This result indicates that the in-plane angle distortion plays the dominant role in the band gap opening. This interpretation is consistent with previous studies. Knutson *et al.* [28] investigated a series of idealized $(SnI_4)^{2-}$ perovskites and showed that the in-plane Sn–I–Sn bond angle has the strongest effect on the band gap. In our case, the Pb–Cl–Pb angle is the in-plane angle, while the Pb–I–Pb angle is the out-of-plane angle. Pedesseau *et al.* [10] also reported the dominant role of the in-plane angle in controlling the band gap of 2D perovskites. The Pb–I–Pb angle has only a small effect on the band gap because it mainly perturbs the out-of-plane Pb(6s)–I(p_z) interaction, whereas the band-edge states are more strongly controlled by the in-plane Pb(6s)–Cl($p_{x,y}$) antibonding overlap. Therefore, Pb–Cl–Pb distortion lowers the VBM much more efficiently and dominates the band gap opening.

A clear relationship is observed between the in-plane Pb–Cl–Pb angle change and the band gap opening as shown in Figure 4.11b. Thicker 2D structures have larger in-plane angle changes (see also Fig. 4.7), and these larger angle changes lead to a larger band gap opening. Therefore, the stronger band gap opening in thicker polymorphous structures can be mainly attributed to the larger deviation of the in-plane Pb–Cl–Pb angle.

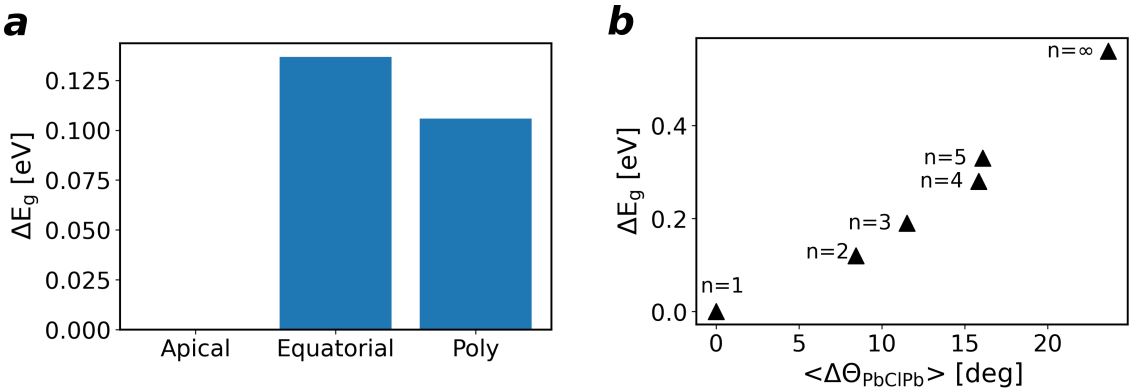

Figure 4.11: Band gap opening due to positional local disorder. **a** Contributions of equatorial (Pb–Cl–Pb) and apical (Pb–I–Pb) angle changes to the band gap opening induced by positional local disorder. **b** Relationship between the band gap opening and the in-plane Pb–Cl–Pb angle change.

4.3.3 Effect of positional local disorder on effective masses

Positional local disorder changes the curvature of the band edges and therefore modifies the carrier effective masses. In particular, disorder flattens the band dispersion near the valence-band maximum (VBM) and conduction-band minimum (CBM), leading to heavier

holes and electrons. In this section, we focus only on the in-plane effective masses, because the bands along the out-of-plane direction are almost flat, as discussed above, and therefore give very large effective masses.

Figure 4.12a shows the in-plane electron and hole effective masses for the monomorphous and polymorphous configurations as a function of the octahedral layer thickness n. In the monomorphous configuration, both carrier effective masses remain relatively small and generally decrease with increasing n. By contrast, in the polymorphous configuration, the electron and hole effective masses increase as the octahedral layer becomes thicker. Thus, positional local disorder reverses the effective-mass trend with respect to the monomorphous model.

This opposite behavior can be understood from the increasing magnitude of the local distortion. As shown in Fig. 4.7a, thicker structures show larger deviations of the B–X–B bond angle from the ideal linear geometry. These distortions reduce the orbital overlap between Pb and halogen atoms. As a result, the band dispersion around the VBM and CBM becomes flatter, and the effective masses increase. Therefore, the stronger increase of effective mass at larger n is directly related to the larger structural distortion in the polymorphous configurations.

For example, in the monomorphous structures, the electron effective mass remains close to ~ 0.20, while the hole effective mass decreases from about 0.32 for $n = 1$ to about 0.20 for $n = 5$. In the polymorphous structures, the electron effective mass increases from about 0.20 for $n = 1$ to about 0.28 for $n = 5$, while the hole effective mass increases from about 0.32 to about 0.45 over the same range. This shows that the effect of positional local disorder becomes stronger for thicker octahedral layers.

To quantify this effect we define an effective-mass enhancement factor $\lambda_{e/h}$ as in Ref. [16]

$$m^{p}_{e/h} = \left(1 + \lambda_{e/h}\right) m^{m}_{e/h}, \tag{4.6}$$

where $m^{p}_{e/h}$ and $m^{m}_{e/h}$ are the electron or hole effective masses in the polymorphous and monomorphous configurations, respectively. The calculated enhancement factors are shown in Fig. 4.12b. Both λ_e and λ_h increase with increasing octahedral layer thickness. From $n = 1$ to $n = 5$, λ_e increases from 0 to about 0.42, while λ_h increases from 0 to about 1.24. For the $n \to \infty$ reference structure, the enhancement factors reach about 0.57 for electrons and 1.30 for holes. This confirms that local disorder has a much stronger effect on the effective masses in thicker structures.

The larger enhancement of the hole effective mass indicates that the VBM is more sensitive to positional local disorder than the CBM. This is consistent with the orbital character of the band edges discussed above. The VBM is mainly formed by antibonding hybridization between Pb(6s) and halogen p orbitals, especially the in-plane Pb(6s)–Cl(3$p_{x,y}$) contribution. Because this antibonding interaction is strongly affected by changes in the Pb–Cl–Pb angle, local disorder strongly modifies the VBM dispersion. The CBM is also affected by disorder, but its dispersion changes less strongly. This explains why λ_h is larger than λ_e.

The increase in effective mass also helps explain the weaker dependence of the band

gap on the octahedral layer thickness in the polymorphous configurations. According to the effective-mass quantum confinement model in Eq. 4.5, the confinement contribution is inversely proportional to the reduced effective mass. Therefore, when positional local disorder increases the effective masses, the confinement term becomes smaller. This reduces the slope of the band-gap trend with increasing n, as observed in Fig. 4.9d. Thus, the effective-mass enhancement provides a consistent explanation for the weaker quantum-confinement trend in the polymorphous structures.

A similar effect of positional local disorder on effective masses was reported by Zacharias *et al.* [16] for 3D halide perovskites. They showed that local disorder enhances the carrier effective masses and that the enhancement factor increases from $CsPbBr_3$ to $CsPbI_3$, where the structural distortion is larger. This supports our interpretation that effective-mass enhancement is closely related to the magnitude of local octahedral distortion. A related trend was also reported by Peksa *et al.* [29], who showed that reducing octahedral distortion in 2D perovskites leads to smaller reduced effective masses.

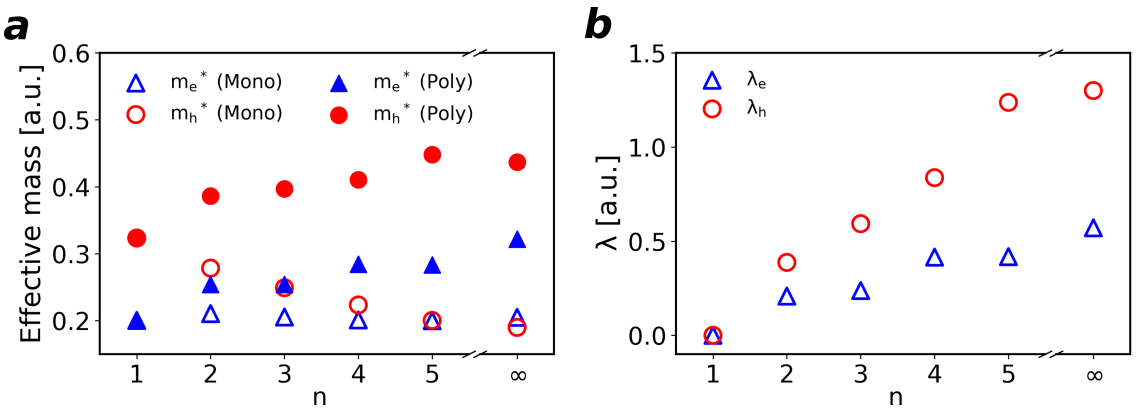

Figure 4.12: Effective masses of 2D perovskites. **a** In-plane electron and hole effective masses calculated for the monomorphous and polymorphous configurations as a function of the octahedral layer thickness n. **b** Enhancement factors λ_e and λ_h for the electron and hole effective masses induced by positional local disorder.

Although experimental effective-mass data are not yet available for different phases of $Cs_{n+1}Pb_nI_{n+1}Cl_{2n}$, useful comparisons can be made with hybrid layered perovskites. Dyksik *et al.* [30] measured the reduced effective mass in the $(\mathrm{PEA})_2(\mathrm{MA})_{n-1}\mathrm{Pb}_n\mathrm{I}_{3n+1}$ family and found that it increases with increasing n. This trend agrees with our polymorphous results. By contrast, Zhang *et al.* [31] reported lighter carriers at larger n in idealized calculations, which is closer to the trend obtained here for the monomorphous configurations. The difference suggests that neglecting positional local disorder can lead to an incomplete description of carrier effective masses in layered halide perovskites.

Overall, these results show that positional local disorder is essential for describing the effective masses of layered perovskites. The monomorphous model gives lighter carriers at larger n, whereas the polymorphous model gives heavier carriers as the octahedral

layer becomes thicker. This trend is consistent with the increase in local distortion and with available experimental observations for related 2D perovskite families.

4.4 Surface Properties of 2D Perovskites

4.4.1 Surface terminations and slab structures

We constructed symmetric slab models of 2D perovskites, with the same termination on both sides of the slab, as shown in Fig. 4.13a,b. This choice avoids artificial dipole–dipole interactions between the two surfaces. Most of the slabs were built with the (001) surface orientation, which is normal to the stacking direction of the 2D perovskite layers. Because previous theoretical [32] and experimental [33] study revealed the most stable orientation of 2D among low index surfaces is (001). For this orientation, three main surface terminations were considered: CsI, double-CsI, and $PbCl_2$ terminations, shown in Fig. 4.13c–e. However, vertically aligned 2D perovskites, which expose lateral surfaces, have also been synthesized [34]. For comparison, we also studied a lateral surface with the (100) orientation, which is perpendicular to the stacking direction. This lateral slab has only one surface termination, as shown in Fig. 4.13f.

The slab thickness and the number of fixed atomic layers were tested for convergence, as discussed in the Appendix. Based on these tests, we used slabs with seven unit cells along the surface-normal direction. During structural relaxation, the atoms in the outer two octahedral layers on both sides of the slab were allowed to relax, while the atoms in the middle region were fixed to preserve the bulk-like structure.

The effect of positional local disorder on surface properties was studied only for the $n = 2$ slabs. Extending this analysis to larger n values would require much larger slab models because the number of atoms increases rapidly with the octahedral layer thickness. For the same reason, the lateral surface was studied only for the $n = 1$ structure.

We analyzed surface relaxation by comparing the average geometry of the relaxed surface region with that of the fixed middle layer. The relaxation mainly affects the outer Pb–halide framework, and its magnitude depends strongly on the surface termination. For the CsI and double-CsI terminations, the average surface Pb–Cl and Pb–I bond lengths remain close to the middle-layer values. However, the Pb–Cl–Pb angle decreases more clearly, especially for thicker slabs. In contrast, the $PbCl_2$ termination shows the strongest reconstruction. At this surface, the Pb–I bond shortens by about 0.11–0.16 Å, the Pb–Cl bond elongates by up to about 0.02 Å, and the Pb–Cl–Pb angle decreases by up to about 13–14°. These changes indicate a stronger inward relaxation and a larger distortion of the surface octahedra.

For the lateral surface of the $n = 1$ slab, Pb–Cl bonds shorten by about 0.033 Å, whereas the Pb–I bonds slightly elongate by about 0.009 Å. The Pb–Cl–Pb angle remains almost unchanged, while the Pb–Pb distance decreases by about 0.051 Å. This behavior suggests a small inward contraction of the surface Pb layer rather than a strong octahedral tilt.

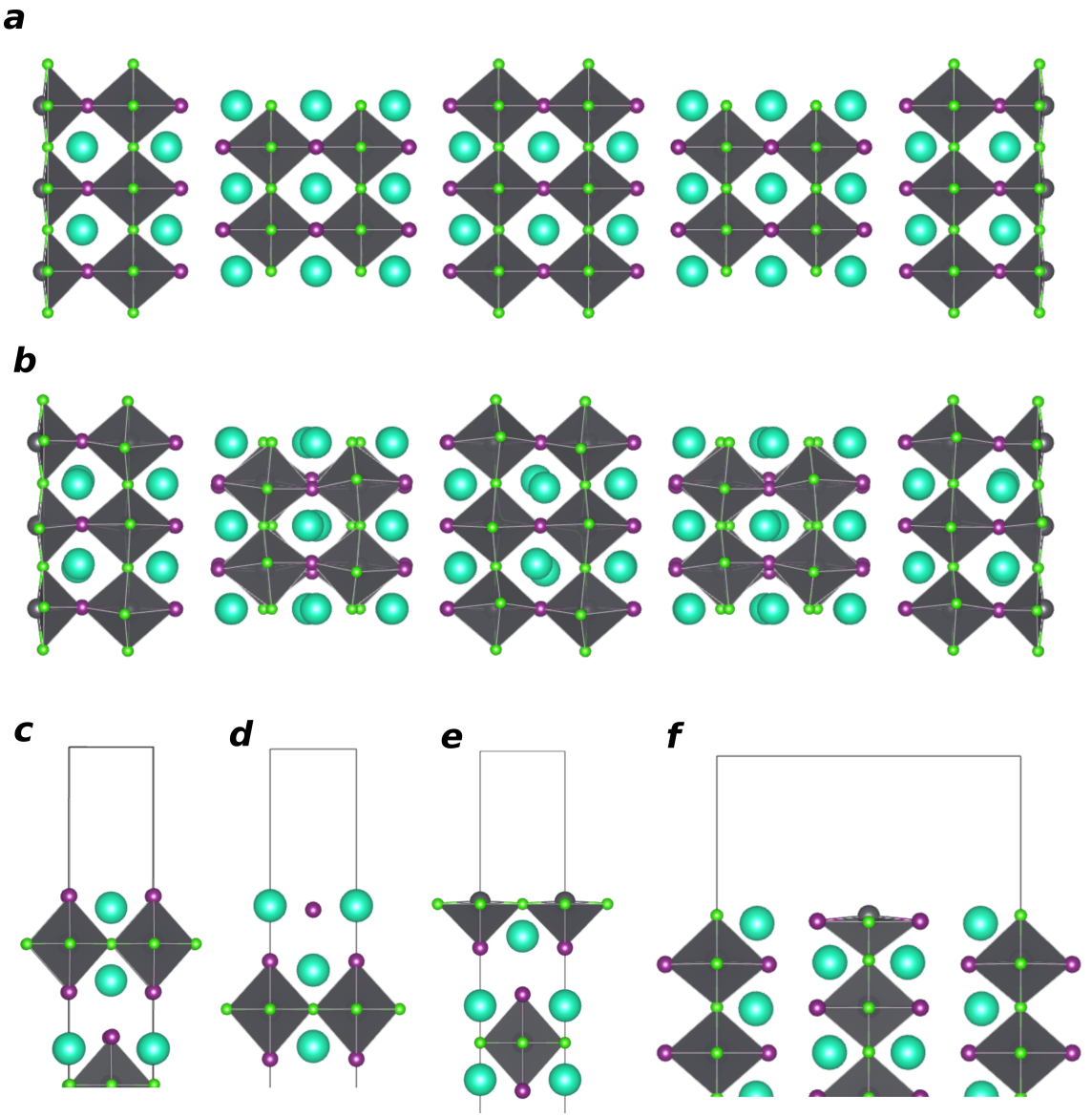

Figure 4.13: Surface slab models of 2D perovskites. **a,b** Symmetric slab models of monomorphous (a) and polymorphous (b) $Cs_3Pb_2I_3Cl_4$ ($n = 2$). **c–e** CsI (c), double-CsI (d), and $PbCl_2$ (e) terminations of $Cs_2PbI_2Cl_2$ ($n = 1$). These slabs have the (001) orientation, normal to the stacking direction of the 2D perovskite. **f** Lateral surface slab with the (100) orientation, perpendicular to the stacking direction.

In the $n = 2$ polymorphous slabs, local disorder changes the magnitude of surface relaxation compared with the monomorphous structures. For the CsI termination, disorder produces an outward expansion of the surface Pb layer: both Pb–Cl and Pb–I bond lengths increase by about 0.016 Å, while the Pb–Cl–Pb angle decreases by 4.27°. For the double-CsI termination, the Pb–Cl bond elongation is larger, about 0.027 Å, and the Pb–Cl–Pb angle decreases by 7.05°, whereas the Pb–Pb distance remains nearly unchanged. In contrast, the $PbCl_2$ termination still shows inward contraction, with a large Pb–I bond shortening of about 0.140 Å and a Pb–Pb distance decrease of 0.096 Å. However, in the polymorphous $PbCl_2$-terminated slab, the Pb–Cl–Pb angle changes only weakly.

4.4.2 Surface energy and phase stability

The stability of the 2D perovskites $Cs_{n+1}Pb_nI_{n+1}Cl_{2n}$ depends on the growth conditions. These conditions can be described using the chemical potentials of the constituent elements. In chemical-potential space, the 2D phase competes with binary compounds, 0D phases, and 3D perovskites as possible secondary phases. Therefore, the 2D perovskite is thermodynamically stable only within the region where its formation energy is lower than that of all competing phases.

Figure 4.14a shows the stability region of the $n = 1$ compound as a function of the Pb, Cl, and I chemical potentials. The stability region extends over a relatively wide range of Pb chemical potential, but it is much narrower in the Cl–I chemical-potential plane. A similar elongated stability region for $Cs_2PbI_2Cl_2$ was also reported by Qu *et al.* [21]. To analyze the stability more clearly, we also show a 2D slice of the phase diagram in the Cl–I chemical-potential plane under Pb-rich conditions, i.e., $\Delta\mu_{\mathrm{Pb}} = 0$ (Fig. 4.14b). In this slice, the stability region of the $n = 1$ phase is small. Three representative growth conditions were selected from the corners of this region: A corresponds to Cl-poor and I-poor conditions, B to Cl-rich and I-rich conditions, and C to Cl-rich and I-poor conditions. The phase diagrams for the other members of the series are provided in the Appendix.

For the surface-energy analysis, we selected the A–C line in the 2D phase diagram (Fig. 4.14b). This line changes the Cl chemical potential at fixed Pb-rich and I-poor conditions and passes through the stability regions of $Cs_2PbI_2Cl_2$, $CsPbCl_3$, and $CsPbI_3$ (see Fig. 4.15). For the $n = 1$ compound, the surface energies of the lateral surface and the CsI-terminated (001) surface do not change with $\Delta\mu_{\mathrm{Cl}}$ because these slab models are stoichiometric. In contrast, d-CsI and $PbCl_2$ terminations are the non-stoichiometric and their surface energies depend on the chemical potential. The surface energy of the d-CsI termination increases with increasing $\Delta\mu_{\mathrm{Cl}}$, whereas the surface energy of the $PbCl_2$ termination decreases as $\Delta\mu_{\mathrm{Cl}}$ increases. A similar dependence on Cl chemical potential is observed for the n = 2 structure (see Fig. 4.15b).

For n=2 structure, we also compared monomorphous and polymorphous surface slabs. For all studied terminations, the polymorphous slabs have lower surface energies than the corresponding monomorphous slabs. This indicates that positional local disorder stabilizes the surface of all inorganic 2D perovskites as we found for 3D halide

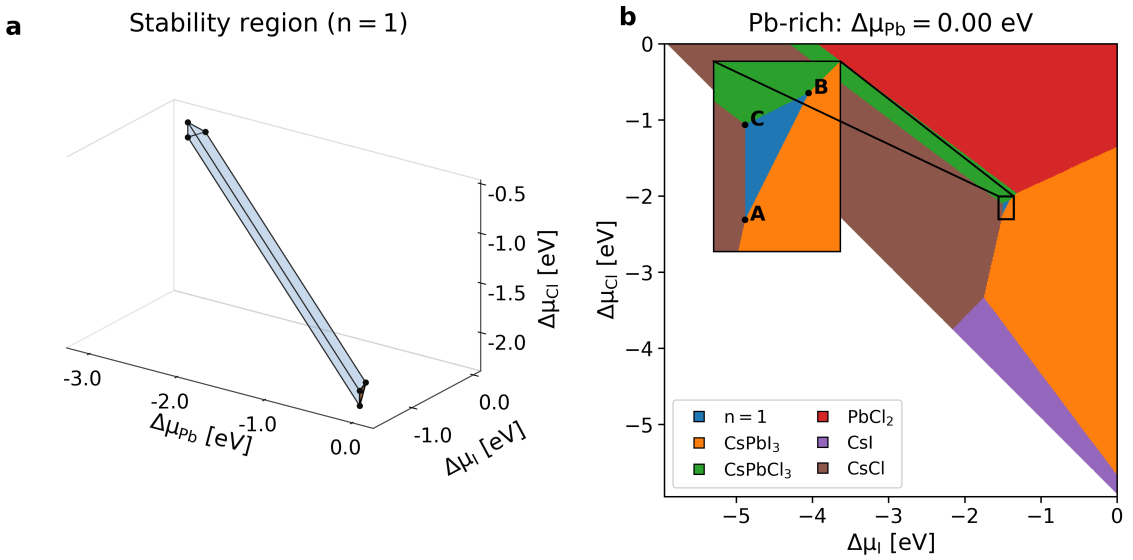

Figure 4.14: Phase diagram of the $n = 1$ 2D perovskite $Cs_2PbI_2Cl_2$. **a** Three-dimensional chemical-potential stability region as a function of $\Delta\mu_{\mathrm{Pb}}$, $\Delta\mu_{\mathrm{Cl}}$, and $\Delta\mu_{\mathrm{I}}$. Only the stability region of the $n = 1$ compound is shown. **b** Two-dimensional slice of the phase diagram under Pb-rich conditions, $\Delta\mu_{\mathrm{Pb}} = 0$, shown as a function of $\Delta\mu_{\mathrm{Cl}}$ and $\Delta\mu_{\mathrm{I}}$. The points A, B, and C mark representative limits of the stability region.

perovskites. For both $n = 1$ and $n = 2$, the CsI termination has the lowest surface energy within the thermodynamic stability window. This trend is also consistent with our previous results for 3D perovskites, where the CsI termination was the most favorable under comparable chemical-potential conditions. The surface-energy trends for the $n > 2$ compounds are given in the Appendix and show the same qualitative dependence on the Cl chemical potential.

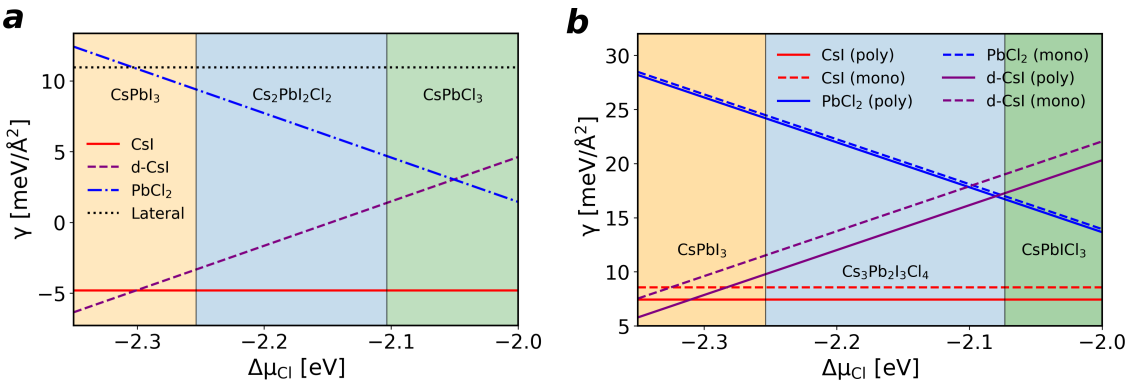

Figure 4.15: Surface energy of the $n = 1$ **(a)** and $n = 2$ **(b)** structures as a function of the Cl chemical potential. The background color maps show the stability regions of the 2D perovskites and the competing 3D phases.

Figure 4.16 summarizes the surface energies as a function of the octahedral layer thickness n. We considered two representative growth conditions, A and C, defined in Fig. 4.14b. For all compounds from $n = 1$ to $n = 5$, the CsI termination has the lowest surface energy. Therefore, CsI is the most favorable termination across the whole series. This result is consistent with the work of Yadav *et al.* [35], who found that the CsCl termination is the most stable surface in Cs_2PbCl_4. It is also in line with the general tendency of layered perovskites to expose spacer-terminated surfaces; for example, Choghaei *et al.* [36] reported organic-cation-terminated surfaces in hybrid 2D Ruddlesden–Popper perovskites.

Among the studied compounds, the $n = 1$ structure has the lowest surface energy for all terminations and under both growth conditions. For $n > 2$, the surface energies change only weakly with increasing octahedral layer thickness. The double-CsI termination becomes less favorable under condition C than under condition A because condition C is more Cl-rich. In contrast, the $PbCl_2$ termination remains the least favorable termination in most cases. This high surface energy can be understood from the bonding geometry: forming a $PbCl_2$-terminated surface cuts through the inorganic octahedral framework and breaks Pb–I bonds. Therefore, this termination requires a larger energy cost than the CsI-terminated surface, which cleaves more naturally between the inorganic layer and the CsI spacer region.

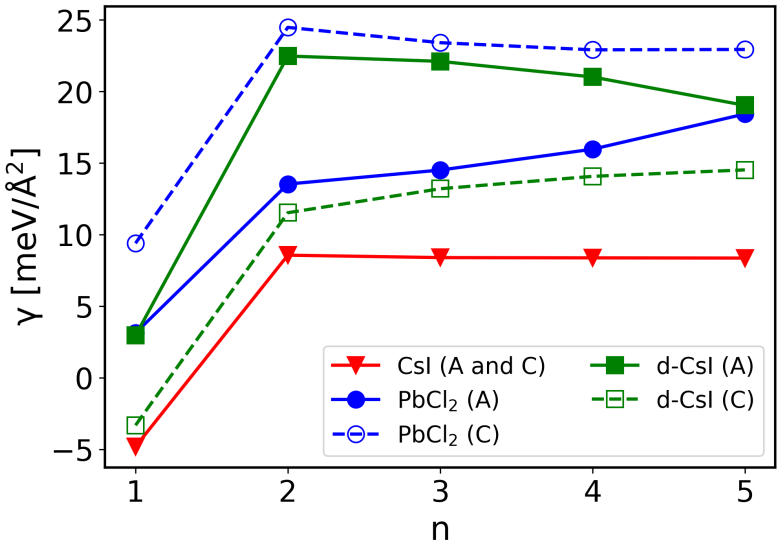

Figure 4.16: Surface energy as a function of octahedral layer thickness n. The points A and C correspond to the Pb-rich growth conditions marked in Fig. 4.14b: A is Cl-poor and I-poor, while C is Cl-rich and I-poor. Because the surface energies of the CsI termination are identical at points A and C, they are represented by a single red curve.

4.4.3 Ionisation potential

Figure 4.17a shows the planar-averaged electrostatic potentials of the most stable, CsI-terminated surface slab and the corresponding bulk 2D perovskite. The electrostatic potential of the slab is shifted downward relative to the bulk reference, which indicates the formation of a surface dipole. Figure 4.17b shows the ionisation potentials of the $n = 1$ slabs with $PbCl_2$, CsI, d-CsI, and lateral terminations. For all terminations, DFT-1/2 gives larger ionisation potentials than GGA. This difference originates from the well-known limitation of GGA, which over delocalises the halogen p states and shifts the valence-band maximum (VBM) artificially upward. As a result, GGA underestimates the ionisation potential. DFT-1/2 partly corrects this problem by stabilising the VBM.

Within DFT-1/2, the $PbCl_2$ termination gives the largest ionisation potential, 7.74 eV, whereas the d-CsI termination gives the smallest value, 6.84 eV. As discussed in the previous chapter, such differences mainly arise from changes in the surface dipole. The effect of surface orientation is smaller than the effect of surface termination. For example, the ionisation potential of the lateral surface is 7.31 eV, which is close to the value of 7.49 eV obtained for the CsI terminated surface.

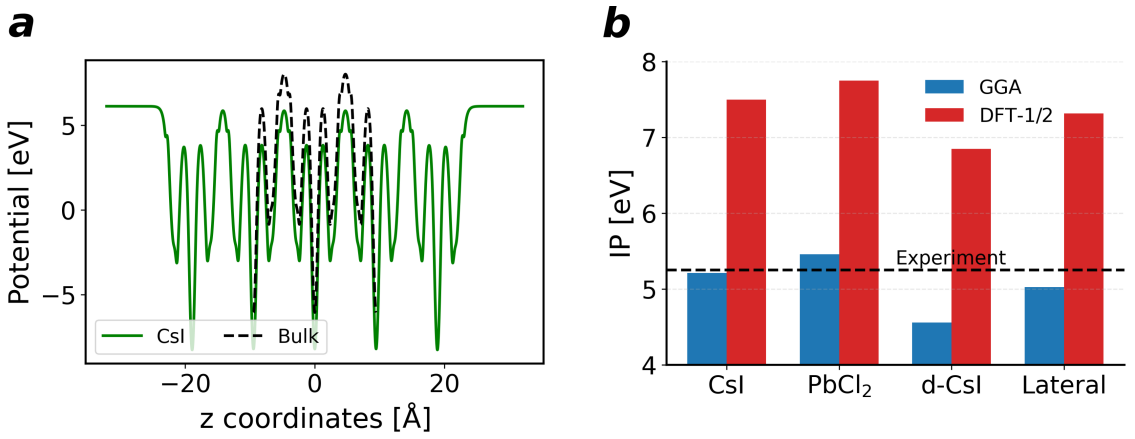

Figure 4.17: **a** Planar-averaged electrostatic potentials of the $n = 1$ d-CsI-terminated surface slab and the bulk reference. **b** Ionisation potentials of the $n = 1$ surface slabs with $PbCl_2$, CsI, d-CsI, and lateral terminations, calculated using GGA and DFT-1/2. The black dashed line shows the experimental value reported by Liu *et al.* [37].

To the best of our knowledge, Liu *et al.* [37] reported the only experimental value of the ionisation potential of $n = 1$ $Cs_2PbI_2Cl_2$. Ultraviolet photoelectron spectroscopy (UPS) measurements on colloidally synthesised $Cs_2PbI_2Cl_2$ nanosheets placed the VBM at 5.25 eV below the vacuum level. This value should, however, be interpreted as the ionisation potential of the as-prepared nanosheet surface rather than that of an ideal, bare crystallographic termination. The nanosheets were synthesised using oleic acid and oleylamine and were therefore capped with oleate and oleylammonium ligands, while their exposed surface termination and surface stoichiometry were not independently established. Consequently, comparisons between this experimental value and calculated

ionisation potentials for ideal surface terminations should be regarded as qualitative. Interestingly, the GGA value for the CsI termination, 5.2 eV, is close to the experimental value. However, this agreement should be treated with caution, since it is most likely caused by error cancellation. In GGA, the upward shift of the VBM caused by the over delocalisation of halogen p states reduces the calculated ionisation potential. In addition, experimental ionisation potentials can strongly depend on surface termination, surface quality, and sample preparation. This sensitivity is also observed for $CsPbI_3$, for which reported experimental ionisation potentials vary from about 5.2 to 6.25 eV [38, 39, 40, 41, 42].

Figure 4.18 shows the dependence of the ionisation potential on the octahedral layer thickness n. In both GGA and DFT-1/2 calculations, the ionisation potential decreases as n increases and gradually approaches the 3D reference value, because the quantum confinement weakens with increasing thickness of the octahedral layer. In other words, for small n, the inorganic layer is strongly confined, which lowers the VBM relative to the vacuum level and gives a larger ionisation potential. As n increases, the 2D perovskite becomes more 3D-like, the band gap decreases, and the VBM shifts upward toward the 3D limit. Consequently, the ionisation potential decreases.

This trend is also reflected in practical 2D/3D perovskite devices, where the $n = 1$ and $n = 2$ phases were found to introduce a barrier to charge extraction. More favourable charge extraction was obtained for the $n = 3$ and $n = 4$ phases [43]. In addition, Zhong *et al.* [44] measured the absolute band positions of $BA_2MA_{n-1}Pb_nI_{3n+1}$ from $n = 1$ to $n = 5$ and observed a decrease in ionisation potential with increasing number of octahedral layers. Other experimental [44, 45, 46, 47] and theoretical [27] studies have also shown that 2D perovskites usually have larger ionisation potentials than their 3D counterparts. Therefore, the higher ionisation potential of the $n = 1$ structure compared with the 3D reference is consistent with the general behaviour of quantum-confined layered perovskites.

The 3D reference used in this work, $CsPbICl_2$, is a mixed-halide perovskite. Direct experimental ionisation potentials for this exact composition are not available. Therefore, we compare our results only qualitatively with available mixed-halide trends. Schröder *et al.* [48] studied mixed-halide hybrid perovskites and showed that the ionisation potential of $CH_3NH_3Pb(I_{1-x}Br_x)_3$ lies between those of the two halide end members and is roughly linear with composition. By this analogy, the ionisation potential of $CsPbICl_2$ may be expected to lie between those of $CsPbI_3$ and $CsPbCl_3$.

Tao *et al.* [42] reported experimental ionisation potentials of 6.25 eV for $CsPbI_3$ and 6.8 eV for $CsPbCl_3$. Since $CsPbICl_2$ contains more Cl than I, its ionisation potential should be closer to that of $CsPbCl_3$. Our DFT-1/2 value for the CsI-terminated 3D reference, 6.72 eV, lies within this expected range, while the $PbCl_2$-terminated value, 6.96 eV, is slightly higher but still close to the $CsPbCl_3$ limit. In contrast, most GGA values are below this experimental range. Since 2D perovskites are generally expected to have larger ionisation potentials than their 3D references, our DFT-1/2 results appear more consistent with the experimental trends than the GGA results. However, further experimental measurements

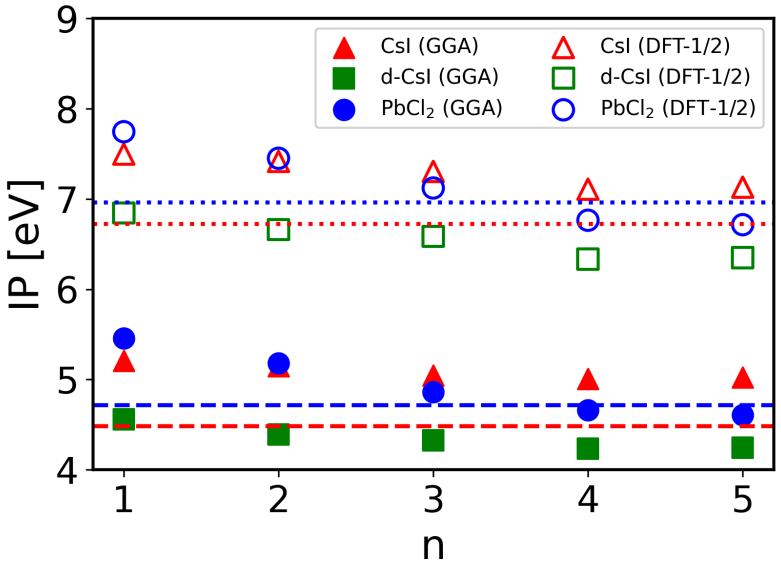

Figure 4.18: Ionisation potentials of the 2D perovskites calculated using GGA and DFT-1/2 as a function of the octahedral layer thickness n. The dashed blue and red lines show the GGA ionisation potentials of the $n \to \infty$ surface slabs with $PbCl_2$ and CsI terminations, respectively. The dotted lines show the corresponding DFT-1/2 results.

on well-defined $Cs_2PbI_2Cl_2$ surfaces are required for a direct comparison.

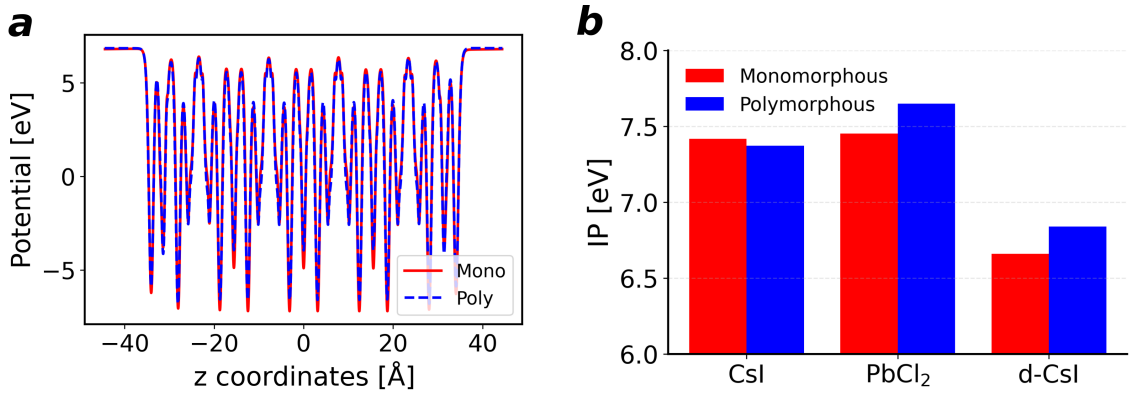

Figure 4.19: **a** Electrostatic potentials of the monomorphous and polymorphous $n = 2$ structures with $PbCl_2$ termination. **b** Ionisation potentials of the monomorphous and polymorphous $n = 2$ structures with $PbCl_2$, CsI, and d-CsI terminations, calculated using DFT-1/2.

Finally, we examined the effect of positional local disorder on the electrostatic potential and ionisation potential of the $n = 2$ structure, as shown in Figure 4.19. The electrostatic potential profiles of the monomorphous and polymorphous structures are very similar, indicating that local disorder does not strongly affect the overall potential profile.

However, it still changes the ionisation potential in a termination-dependent manner. In DFT-1/2, local disorder increases the ionisation potentials of the d-CsI and $PbCl_2$ terminations by about 0.2 eV, whereas it decreases the ionisation potential of the CsI termination by only 0.04 eV.

These changes can be understood from the combined effects of the electrostatic potential shift and the VBM shift. Positional local disorder shifts the electrostatic potential upward by 0.14 eV for the CsI termination, but downward by 0.09 eV for the $PbCl_2$ termination. At the same time, local disorder stabilises the bulk VBM by 0.11 eV. For the CsI termination, the upward shift of the electrostatic potential is slightly larger than the VBM stabilisation, leading to a small decrease in the ionisation potential. For the $PbCl_2$ termination, the downward shift of the electrostatic potential and the stabilisation of the VBM act in the same direction, resulting in an increased ionisation potential. This behaviour is similar to that observed in 3D perovskites, where changes in the electrostatic potential were attributed to changes in the surface dipole. Thus, in 2D perovskites, positional local disorder affects the ionisation potential through both the bulk VBM and the surface dipole.

4.5 2D/3D Perovskite Interfaces

4.5.1 Adhesion energy of different interface terminations

In this section, we discuss the calculated interfaces between the 3D perovskite $CsPbBr_3$ and the 2D perovskite $Cs_2PbI_2Cl_2$. The first term in the interface notation refers to the termination of $CsPbBr_3$, whereas the second term refers to the termination of $Cs_2PbI_2Cl_2$. The $CsPbBr_3$ slab can terminate either with CsBr or $PbBr_2$, while the $Cs_2PbI_2Cl_2$ slab can terminate with CsI, d-CsI, or $PbCl_2$. Therefore, six distinct interface terminations are possible, as shown in Figure 4.20.

The adhesion energies and optimized distances between the 3D and 2D regions are summarized in Table 4.2. The CsBr/$PbCl_2$ and $PbBr_2$/CsI interfaces have the smallest interface distances, 2.99 and 3.19 Å, respectively. These short distances indicate strong structural matching at the interface, where the PbX_6 octahedral framework remains continuous across the 3D/2D junction.

In contrast, the CsBr/CsI, $PbBr_2$/d-CsI, and $PbBr_2$/$PbCl_2$ interfaces show larger optimized separations. This is attributed to a discontinuity of the octahedral network and less favorable atomic matching at the junction. Among these terminations, CsBr/CsI has the largest interface distance, 4.47 Å, suggesting the weakest interfacial contact.

Figure 4.21 shows the relationship between calculated adhesion energies, E_{adh}, and optimized distances. The CsBr/$PbCl_2$ interface has the highest adhesion energy, followed by the $PbBr_2$/CsI interface. These two interfaces are also the ones with the shortest optimized interface distances, indicating that compact interfacial contact and continuous octahedral connectivity strongly enhance the adhesion energy.

The lowest adhesion energies are obtained for CsBr/CsI, $PbBr_2$/d-CsI, and $PbBr_2$/$PbCl_2$.

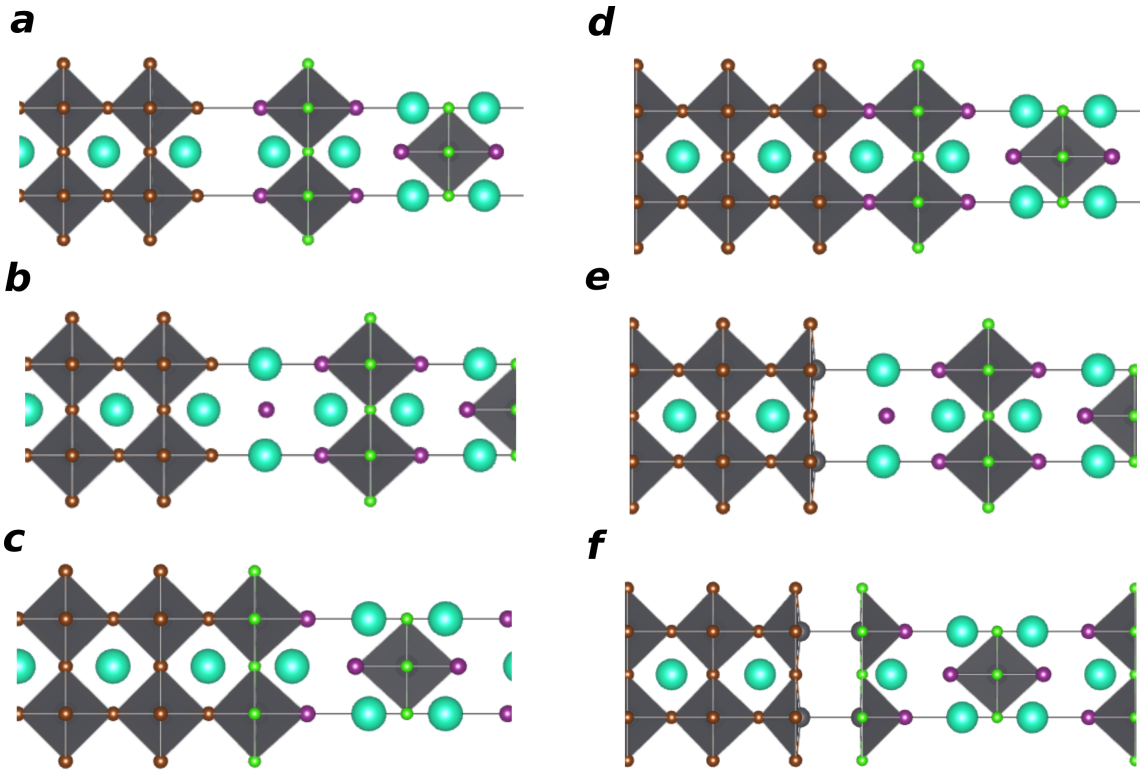

Figure 4.20: $CsPbBr_3/Cs_2PbI_2Cl_2$ interface terminations: a) CsBr/CsI, b) CsBr/d-CsI, c) $CsBr/PbCl_2$, d) $PbBr_2$/CsI, e) $PbBr_2$/d-CsI, and f) $PbBr_2/PbCl_2$.

Table 4.2: Adhesion energy and optimized distance between the 3D $CsPbBr_3$ and 2D $Cs_2PbI_2Cl_2$ regions for different interface terminations.

Interface	**Distance (Å)**	**$E_{adh.}$ (meV/Å^2)**
CsBr/CsI	4.47	5.07
CsBr/d-CsI	3.47	18.06
$CsBr/PbCl_2$	2.99	22.95
$PbBr_2$/CsI	3.19	20.95
$PbBr_2$/d-CsI	4.41	5.85
$PbBr_2/PbCl_2$	4.19	7.27

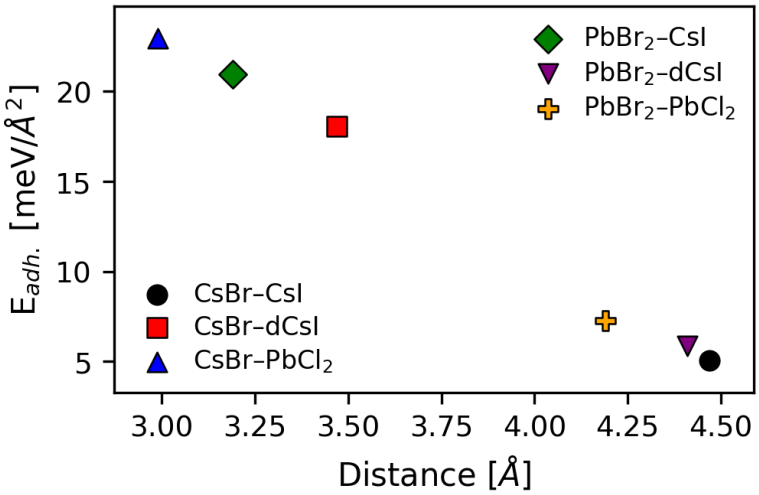

Figure 4.21: The relationship between adhesion energy, E_{adh}, of $CsPbBr_3/Cs_2PbI_2Cl_2$ interfaces with different terminations and optimized interface distance.

These terminations are characterized by larger interface distances and discontinuity of the octahedral framework at the junction. Overall, the adhesion energy increases as the optimized interface distance decreases, as shown in Figure 4.21. The chemical termination and the continuity of the PbX_6 octahedral network determine the optimized interface distance, so they consequently govern the interfacial adhesion and stability.

4.5.2 Band offsets

In this work, the band offsets of the $CsPbBr_3/Cs_2PbI_2Cl_2$ interfaces were calculated using the potential-lineup method proposed by Van de Walle and Martin [49]. Figure 4.22 compares the band offsets of the $CsBr/PbCl_2$ and $PbBr_2/CsI$ interfaces calculated using GGA and DFT-1/2. As discussed in the surface-property analysis, DFT-1/2 provides a better description of the band edges than GGA. GGA usually underestimates the band gap and the ionisation potential. The self-interaction error in GGA mainly affects the bulk VBM positions, while the electrostatic potential are less affected. In our case, the two materials are chemically similar lead-halide perovskites, so part of the error in the bulk VBM positions cancels when the valence band offset (VBO) is calculated. Therefore, the VBOs obtained from GGA and DFT-1/2 differ only by about 0.1 eV.

The lattice mismatch between $Cs_2PbI_2Cl_2$ and $CsPbBr_3$ is 4.3%. This value is relatively large for a fully coherent interface. Therefore, in the interface supercells, the 2D perovskite was strained to match the in-plane lattice constant of the 3D perovskite. The standard potential-lineup method gives the band offset of this strained coherent interface. However, to estimate the natural band offsets, the strain effect must be corrected. Therefore, we applied the absolute deformation potential (ADP) correction [50] and the three-step approach [51].

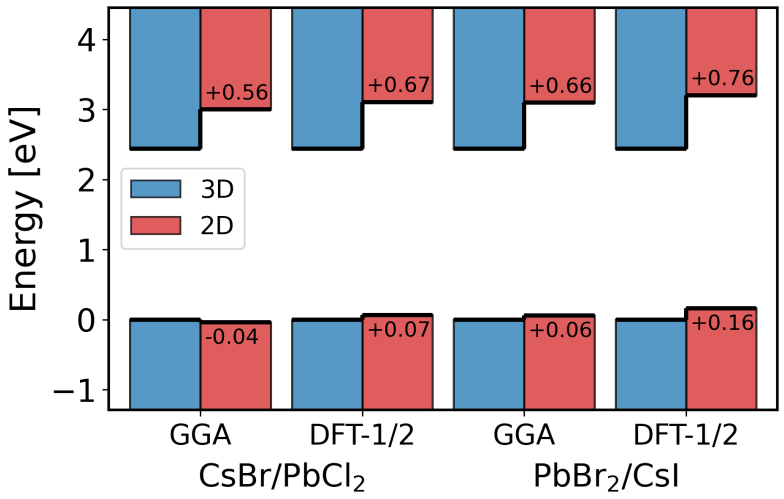

Figure 4.22: Comparison of the band offsets of the $CsBr/PbCl_2$ and $PbBr_2/CsI$ interfaces calculated using GGA and DFT-1/2. The blue bars represent $CsPbBr_3$, and the red bars represent $Cs_2PbI_2Cl_2$.

Figure 4.23 shows the band offsets calculated using DFT-1/2 combined with the three-step strain correction. To the best of our knowledge, the only experimental determination of the band offset for the $CsPbBr_3/Cs_2PbI_2Cl_2$ interface is the one by Huang *et al.* [52], reporting a VBO of 0.74 eV obtained by UPS/IPES measurements. Table 4.3 summarizes the VBOs obtained using the standard Van de Walle method, the ADP correction, and the three-step approach.

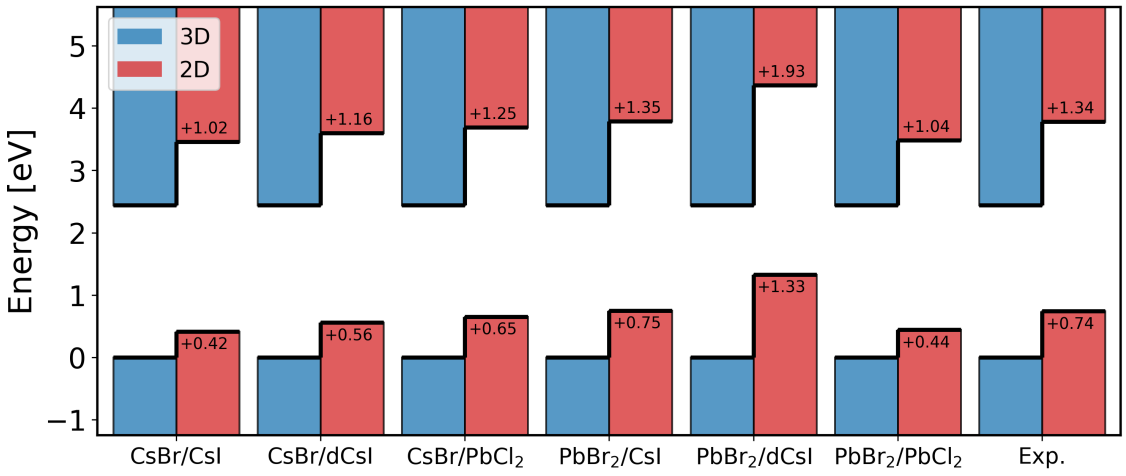

Figure 4.23: Band offsets of the $CsPbBr_3/Cs_2PbI_2Cl_2$ interfaces calculated using DFT-1/2 with the three-step strain correction. The experimental value is taken from Ref. [52].

The strain correction has a strong effect on the absolute VBO values. Compared with the standard method, both the ADP and three-step approaches shift the VBOs upward by

Table 4.3: Calculated valence band offsets for different models of the $CsPbBr_3/Cs_2PbI_2Cl_2$ interface. The experimental value is taken from Ref. [52].

Interface	Valence band offset, eV			
	Standard	ADP	Three-step	Experiment
CsBr/CsI	-0.17	0.47	0.42	0.74
CsBr/d-CsI	-0.03	0.61	0.56	
$CsBr/PbCl_2$	0.07	0.71	0.65	
$PbBr_2$/CsI	0.16	0.80	0.75	
$PbBr_2$/d-CsI	0.74	1.38	1.33	
$PbBr_2/PbCl_2$	-0.14	0.50	0.44	

about 0.6 eV. This shows that strain has a significant influence on the band-edge positions of the 2D perovskite. The ADP correction gives VBOs that are about 0.05–0.06 eV higher than those obtained from the three-step approach. Such a small overestimation of the ADP correction for interfaces with relatively large lattice mismatch is consistent with the trend reported by Lang *et al.* [51].

Among the different terminations, the $PbBr_2$/CsI interface gives a three-step VBO of 0.75 eV, which is very close to the experimental value of 0.74 eV. The $CsBr/PbCl_2$ interface also gives a comparable VBO of 0.65 eV. These two interfaces are also the most stable terminations according to the adhesion-energy calculations discussed in the previous subsection. They have the highest adhesion energies and the shortest interface distances, indicating stronger interfacial contact and better structural matching. Therefore, the agreement between their calculated VBOs and the experimental value is physically meaningful.

In contrast, the standard method gives a VBO of 0.74 eV for the $PbBr_2$/d-CsI interface, which is equal to the experimental value. However, after strain correction, the VBO of this interface increases to 1.33 eV. Moreover, this termination has a relatively low adhesion energy and a large interface distance. Therefore, the agreement obtained from the uncorrected standard method is likely accidental and should not be used to identify $PbBr_2$/d-CsI as the most realistic interface.

According to the three-step results in Figure 4.23, all interface terminations show type-II band alignment. The VBM of $Cs_2PbI_2Cl_2$ is higher than that of $CsPbBr_3$, which favors hole transfer from the 3D perovskite to the 2D perovskite. At the same time, the CBM of $Cs_2PbI_2Cl_2$ is also higher than that of $CsPbBr_3$, creating an energy barrier for electron transfer into the 2D layer. Therefore, electrons are confined mainly in the 3D $CsPbBr_3$ region, while holes can be transferred to the 2D $Cs_2PbI_2Cl_2$ region. This staggered alignment suggests that $Cs_2PbI_2Cl_2$ can act as a hole-selective capping layer between the 3D perovskite absorber and the hole-transport layer, while also blocking electron leakage and reducing interfacial recombination. A similar type-II alignment was also reported by Pan *et al.* [53] for the $Cs_2PbI_2Cl_2/MAPbI_3$ heterostructure.

References

[1] Jiangwei Li, Qin Yu, Yihui He, Constantinos C. Stoumpos, Guangda Niu, Giancarlo G. Trimarchi, Hang Guo, Guifang Dong, Dong Wang, Liduo Wang, and Mercouri G. Kanatzidis. $Cs_2PbI_2Cl_2$, All-Inorganic Two-Dimensional Ruddlesden–Popper Mixed Halide Perovskite with Optoelectronic Response. *Journal of the American Chemical Society*, 140(35):11085–11090, August 2018.

[2] S. N. Ruddlesden and P. Popper. New compounds of the K_2NiF_4 type. *Acta Crystallographica*, 10(8):538–539, August 1957.

[3] Xinting Shuai, Siraj Sidhik, Mingrui Xu, Xiang Zhang, Michael De Siena, Laurent Pedesseau, Hao Zhang, Guanhui Gao, Anand B. Puthirath, Wenbin Li, Ayush Agrawal, Jianan Xu, Jin Hou, Jessica H. Persaud, Jeremy Daum, Anamika Mishra, Yafei Wang, Robert Vajtai, Claudine Katan, Mercouri G. Kanatzidis, Jacky Even, Pulickel M. Ajayan, and Aditya D. Mohite. Vapor Growth of All-Inorganic 2D Ruddlesden–Popper Lead- and Tin-Based Perovskites. *ACS Applied Materials & Interfaces*, 16(35):46560–46569, August 2024.

[4] Atsushi Togo, Kohei Shinohara, and Isao Tanaka. Spglib: a software library for crystal symmetry search. *Sci. Technol. Adv. Mater., Meth.*, 4(1):2384822–2384836, 2024.

[5] Boubacar Traore, Laurent Pedesseau, Linda Assam, Xiaoyang Che, Jean-Christophe Blancon, Hsinhan Tsai, Wanyi Nie, Constantinos C. Stoumpos, Mercouri G. Kanatzidis, Sergei Tretiak, Aditya D. Mohite, Jacky Even, Mikaël Kepenekian, and Claudine Katan. Composite Nature of Layered Hybrid Perovskites: Assessment on Quantum and Dielectric Confinements and Band Alignment. *ACS Nano*, 12(4):3321–3332, February 2018.

[6] Mikaël Kepenekian, Boubacar Traore, Jean-Christophe Blancon, Laurent Pedesseau, Hsinhan Tsai, Wanyi Nie, Constantinos C. Stoumpos, Mercouri G. Kanatzidis, Jacky Even, Aditya D. Mohite, Sergei Tretiak, and Claudine Katan. Concept of Lattice Mismatch and Emergence of Surface States in Two-dimensional Hybrid Perovskite Quantum Wells. *Nano Letters*, 18(9):5603–5609, August 2018.

[7] Aniruddha Ray, Daniela Maggioni, Dmitry Baranov, Zhiya Dang, Mirko Prato, Quinten A. Akkerman, Luca Goldoni, Enrico Caneva, Liberato Manna, and Ahmed L. Abdelhady. Green-Emitting Powders of Zero-Dimensional Cs_4PbBr_6: Delineating the Intricacies of the Synthesis and the Origin of Photoluminescence. *Chemistry of Materials*, 31(18):7761–7769, August 2019.

[8] M. Oluchi Anunobi and Robert F. Berger. Energetic Stability and Band-Edge Orbitals of Layered Inorganic Perovskite Compounds for Solar Energy Applications. *The Journal of Physical Chemistry C*, 127(41):20217–20225, October 2023.

[9] Yu-Qing Zhao, Ying Xu, Dai-Feng Zou, Jun-Nian Wang, Guo-Feng Xie, B Liu, Meng-Qiu Cai, and Shao-Long Jiang. First-principles study on photovoltaic properties of 2D Cs_2PbI_4-black phosphorus heterojunctions. *Journal of Physics: Condensed Matter*, 32(19):195501, February 2020.

[10] Laurent Pedesseau, Daniel Sapori, Boubacar Traore, Roberto Robles, Hong-Hua Fang, Maria Antonietta Loi, Hsinhan Tsai, Wanyi Nie, Jean-Christophe Blancon, Amanda Neukirch, Sergei Tretiak, Aditya D. Mohite, Claudine Katan, Jacky Even, and Mikaël Kepenekian. Advances and Promises of Layered Halide Hybrid Perovskite Semiconductors. *ACS Nano*, 10(11):9776–9786, October 2016.

[11] Zhuo Xu, Ming Chen, and Shengzhong Frank Liu. Layer-Dependent Ultrahigh-Mobility Transport Properties in All-Inorganic Two-Dimensional $Cs_2PbI_2Cl_2$ and $Cs_2SnI_2Cl_2$ Perovskites. *The Journal of Physical Chemistry C*, 123(45):27978–27985, October 2019.

[12] Yan Shao, Wei Gao, Hejin Yan, Runlai Li, Ibrahim Abdelwahab, Xiao Chi, Lukas Rogée, Lyuchao Zhuang, Wei Fu, Shu Ping Lau, Siu Fung Yu, Yongqing Cai, Kian Ping Loh, and Kai Leng. Unlocking surface octahedral tilt in two-dimensional Ruddlesden–Popper perovskites. *Nature Communications*, 13(1), January 2022.

[13] Jonathon S. Bechtel and Anton Van der Ven. Octahedral tilting instabilities in inorganic halide perovskites. *Physical Review Materials*, 2(2), February 2018.

[14] Emily Y. Chen and Bartomeu Monserrat. Lattice Dynamics of Quasi-2D Perovskites from First Principles. *The Journal of Physical Chemistry C*, 128(29):12194–12205, July 2024.

[15] Paribesh Acharyya, Tanmoy Ghosh, Koushik Pal, Kaushik Kundu, Kewal Singh Rana, Juhi Pandey, Ajay Soni, Umesh V. Waghmare, and Kanishka Biswas. Intrinsically Ultralow Thermal Conductivity in Ruddlesden–Popper 2D Perovskite $Cs_2PbI_2Cl_2$: Localized Anharmonic Vibrations and Dynamic Octahedral Distortions. *Journal of the American Chemical Society*, 142(36):15595–15603, August 2020.

[16] Marios Zacharias, George Volonakis, Feliciano Giustino, and Jacky Even. Anharmonic electron-phonon coupling in ultrasoft and locally disordered perovskites. *npj Computational Materials*, 9(1), August 2023.

[17] Jin Hou, Jared Fletcher, Siedah J. Hall, Hao Zhang, Marios Zacharias, George Volonakis, Claire Welton, Stefan Zeiske, Isaiah W. Gilley, Donghoon Shin, Faiz Mandani, Isaac Metcalf, Shuo Sun, Bo Zhang, Yinsheng Guo, Bin Chen, G. N. Manjunatha Reddy, Claudine Katan, Jacky Even, Matthew Y. Sfeir, Mercouri G. Kanatzidis, and Aditya D. Mohite. Exciton diffusion beyond 2 μm enabled by maximum symmetry in two-dimensional perovskites. *Nature Synthesis*, April 2026.

[18] Xin-Gang Zhao, Gustavo M. Dalpian, Zhi Wang, and Alex Zunger. Polymorphous nature of cubic halide perovskites. *Physical Review B*, 101(15), April 2020.

[19] Chan Myae Myae Soe, G. P. Nagabhushana, Radha Shivaramaiah, Hsinhan Tsai, Wanyi Nie, Jean-Christophe Blancon, Ferdinand Melkonyan, Duyen H. Cao, Boubacar Traoré, Laurent Pedesseau, Mikaël Kepenekian, Claudine Katan, Jacky Even, Tobin J. Marks, Alexandra Navrotsky, Aditya D. Mohite, Constantinos C. Stoumpos, and Mercouri G. Kanatzidis. Structural and thermodynamic limits of layer thickness in 2D halide perovskites. *Proceedings of the National Academy of Sciences*, 116(1):58–66, December 2018.

[20] Eugenia S. Vasileiadou, Bin Wang, Ioannis Spanopoulos, Ido Hadar, Alexandra Navrotsky, and Mercouri G. Kanatzidis. Insight on the Stability of Thick Layers in 2D Ruddlesden–Popper and Dion–Jacobson Lead Iodide Perovskites. *Journal of the American Chemical Society*, 143(6):2523–2536, February 2021.

[21] Yating Qu, Xin Xu, Yujia Gao, Ang Li, Xi Huang, Yating Cai, Tengcheng Huang, Zhuxia Wu, Pengyi Liu, Keqiu Chen, Tingting Shi, and Weiguang Xie. Thermodynamic stability and electronic properties of 2D all-inorganic halogen perovskites. *Physica B: Condensed Matter*, 668:415210, November 2023.

[22] Anu Bala, Arpan Krishna Deb, and Vijay Kumar. Atomic and Electronic Structure of Two-Dimensional Inorganic Halide Perovskites $A_{n+1}M_nX_{3n+1}$ (n = 1–6, A = Cs, M = Pb and Sn, and X = Cl, Br, and I) from *ab Initio* Calculations. *The Journal of Physical Chemistry C*, 122(13):7464–7473, March 2018.

[23] Xiaotong Li, Justin Hoffman, Weijun Ke, Michelle Chen, Hsinhan Tsai, Wanyi Nie, Aditya D. Mohite, Mikaël Kepenekian, Claudine Katan, Jacky Even, Michael R. Wasielewski, Constantinos C. Stoumpos, and Mercouri G. Kanatzidis. Two-Dimensional Halide Perovskites Incorporating Straight Chain Symmetric Diammonium Ions, $(NH_3C_mH_{2m}NH_3)(CH_3NH_3)_{n-1}Pb_nI_{3n+1}$ (m = 4–9; n = 1–4). *Journal of the American Chemical Society*, 140(38):12226–12238, August 2018.

[24] Jacky Even, Laurent Pedesseau, and Claudine Katan. Understanding Quantum Confinement of Charge Carriers in Layered 2D Hybrid Perovskites. *ChemPhysChem*, 15(17):3733–3741, September 2014.

[25] J.-C. Blancon, A. V. Stier, H. Tsai, W. Nie, C. C. Stoumpos, B. Traoré, L. Pedesseau, M. Kepenekian, F. Katsutani, G. T. Noe, J. Kono, S. Tretiak, S. A. Crooker, C. Katan, M. G. Kanatzidis, J. J. Crochet, J. Even, and A. D. Mohite. Scaling law for excitons in 2D perovskite quantum wells. *Nature Communications*, 9(1), June 2018.

[26] Claudio Quarti, Claudine Katan, and Jacky Even. Physical properties of bulk, defective, 2D and 0D metal halide perovskite semiconductors from a symmetry perspective. *Journal of Physics: Materials*, 3(4):042001, August 2020.

[27] Boubacar Traore, Jacky Even, Laurent Pedesseau, Mikaël Képénekian, and Claudine Katan. Band gap, effective masses, and energy level alignment of 2D and 3D halide perovskites and heterostructures using DFT-1/2. *Physical Review Materials*, 6(1), January 2022.

[28] Jeremy L. Knutson, James D. Martin, and David B. Mitzi. Tuning the Band Gap in Hybrid Tin Iodide Perovskite Semiconductors Using Structural Templating. *Inorganic Chemistry*, 44(13):4699–4705, May 2005.

[29] Paulina Peksa, Arthur Maufort, Michał Baranowski, Alessandro Surrente, Laurence Lutsen, Paulina Płochocka, Wouter T. M. Van Gompel, and Mateusz Dyksik. Engineering the Effective Mass in 2D Perovskites via Octahedral Distortion. *The Journal of Physical Chemistry C*, 128(42):17984–17989, October 2024.

[30] Mateusz Dyksik, Shuli Wang, Watcharaphol Paritmongkol, Duncan K. Maude, William A. Tisdale, Michal Baranowski, and Paulina Plochocka. Tuning the Excitonic Properties of the 2D $(PEA)_2(MA)_{n-1}Pb_nI_{3n+1}$ Perovskite Family via Quantum Confinement. *The Journal of Physical Chemistry Letters*, 12(6):1638–1643, February 2021.

[31] Lei Zhang and WanZhen Liang. How the Structures and Properties of Two-Dimensional Layered Perovskites $MAPbI_3$ and $CsPbI_3$ Vary with the Number of Layers. *The Journal of Physical Chemistry Letters*, 8(7):1517–1523, March 2017.

[32] Svetozar Najman, Hsin-An Chen, Hsin-Yi Tiffany Chen, and Chun-Wei Pao. Surface structures and equilibrium shapes of layered 2D Ruddlesden–Popper perovskite crystals from density functional theory calculations. *Materials Today Communications*, 26:101745, March 2021.

[33] Jifei Wang, Shiqiang Luo, Yun Lin, Yifu Chen, Yehao Deng, Zhimin Li, Ke Meng, Gang Chen, Tiantian Huang, Si Xiao, Han Huang, Conghua Zhou, Liming Ding, Jun He, Jinsong Huang, and Yongbo Yuan. Templated growth of oriented layered hybrid perovskites on 3D-like perovskites. *Nature Communications*, 11(1), January 2020.

[34] Alexander Z. Chen, Michelle Shiu, Jennifer H. Ma, Matthew R. Alpert, Depei Zhang, Benjamin J. Foley, Detlef-M. Smilgies, Seung-Hun Lee, and Joshua J. Choi. Origin of vertical orientation in two-dimensional metal halide perovskites and its effect on photovoltaic performance. *Nature Communications*, 9(1), April 2018.

[35] Kiran Yadav and Nirat Ray. Surface termination and strain-induced modulation of the structure and electronic properties in 2D perovskites (Cs_2BCl_4 & CsB_2Cl_5, B = Pb, Sn): a first-principles study. *Physical Chemistry Chemical Physics*, 25(47):32330–32335, 2023.

[36] Maryam Choghaei, Maximilian Schiffer, Viren Tyagi, Marcello Righetto, Jiaxing Du, Maximilian Buchmüller, Kai Oliver Brinkmann, Geert Brocks, Patrick Görrn, Laura M. Herz, Shuxia Tao, Thomas Riedl, and Selina Olthof. Odd-even effects in lead-iodide-based Ruddlesden–Popper 2D perovskites. *Journal of Materials Chemistry A*, 13(24):18935–18947, 2025.

[37] Yueli Liu, Xiaolei Zhang, Zifan Yang, Keqiang Chen, and Wen Chen. Passivation of 2D $CsPbI_2Cl_2$ Nanosheets for Efficient and Stable $CsPbI_3$ Quantum Dot Solar Cells. *ACS Applied Materials & Interfaces*, 16(17):22197–22206, April 2024.

[38] Yanqiang Hu, Fan Bai, Xinbang Liu, Qingmin Ji, Xiaoliang Miao, Ting Qiu, and Shufang Zhang. Bismuth Incorporation Stabilized α-$CsPbI_3$ for Fully Inorganic Perovskite Solar Cells. *ACS Energy Letters*, 2(10):2219–2227, September 2017.

[39] Hui Bian, Dongliang Bai, Zhiwen Jin, Kang Wang, Lei Liang, Haoran Wang, Jingru Zhang, Qian Wang, and Shengzhong (Frank) Liu. Graded Bandgap $CsPbI_{2+x}Br_{1-x}$ Perovskite Solar Cells with a Stabilized Efficiency of 14.4%. *Joule*, 2(8):1500–1510, August 2018.

[40] Kang Wang, Qingwen Tian, Guangtao Zhao, Jialun Wen, Jin Huang, Changji Gao, Zhuo Xu, Yucheng Liu, Lei Liang, Lina Meng, Lu Zhang, Zhike Liu, Zhiwen Jin, Selina Olthof, and Shengzhong (Frank) Liu. Beach-Chair-Shaped Energy Band Alignment for High-Performance β-$CsPbI_3$ Solar Cells. *Cell Reports Physical Science*, 1(9):100180, September 2020.

[41] Jianyu Yuan, Xufeng Ling, Di Yang, Fangchao Li, Sijie Zhou, Junwei Shi, Yuli Qian, Jiaxin Hu, Yuansheng Sun, Yingguo Yang, Xingyu Gao, Steffen Duhm, Qiao Zhang, and Wanli Ma. Band-Aligned Polymeric Hole Transport Materials for Extremely Low Energy Loss α-$CsPbI_3$ Perovskite Nanocrystal Solar Cells. *Joule*, 2(11):2450–2463, November 2018.

[42] Shuxia Tao, Ines Schmidt, Geert Brocks, Junke Jiang, Ionut Tranca, Klaus Meerholz, and Selina Olthof. Absolute energy level positions in tin- and lead-based halide perovskites. *Nature Communications*, 10(1), June 2019.

[43] Siraj Sidhik, Yafei Wang, Michael De Siena, Reza Asadpour, Andrew J. Torma, Tanguy Terlier, Kevin Ho, Wenbin Li, Anand B. Puthirath, Xinting Shuai, Ayush Agrawal, Boubacar Traore, Matthew Jones, Rajiv Giridharagopal, Pulickel M. Ajayan, Joseph Strzalka, David S. Ginger, Claudine Katan, Muhammad Ashraful Alam, Jacky Even, Mercouri G. Kanatzidis, and Aditya D. Mohite. Deterministic fabrication of 3D/2D perovskite bilayer stacks for durable and efficient solar cells. *Science*, 377(6613):1425–1430, 2022.

[44] Xinjue Zhong, Xiaojuan Ni, Siraj Sidhik, Hong Li, Aditya D. Mohite, Jean-Luc Brédas, and Antoine Kahn. Direct Characterization of Type-I Band Alignment in 2D Ruddlesden–Popper Perovskites. *Advanced Energy Materials*, 12(45), September 2022.

[45] Dongguen Shin, Fengshuo Zu, Edgar R. Nandayapa, Lennart Frohloff, Emily Albert, Emil J. W. List-Kratochvil, and Norbert Koch. The Electronic Properties of a 2D Ruddlesden–Popper Perovskite and its Energy Level Alignment with a 3D Perovskite Enable Interfacial Energy Transfer. *Advanced Functional Materials*, 33(2), November 2022.

[46] Chenjian Lin, Yuanhao Tang, Wenzhan Xu, Prashant Kumar, and Letian Dou. Charge Transfer in 2D Halide Perovskites and 2D/3D Heterostructures. *ACS Energy Letters*, 9(8):3877–3886, July 2024.

[47] Scott Silver, Jun Yin, Hong Li, Jean-Luc Brédas, and Antoine Kahn. Characterization of the Valence and Conduction Band Levels of n = 1 2D Perovskites: A Combined Experimental and Theoretical Investigation. *Advanced Energy Materials*, 8(16), February 2018.

[48] Vincent R. F. Schröder, Felix Hermerschmidt, Sabrina Helper, Carolin Rehermann, Giovanni Ligorio, Hampus Näsström, Eva L. Unger, and Emil J. W. List-Kratochvil. Using Combinatorial Inkjet Printing for Synthesis and Deposition of Metal Halide Perovskites in Wavelength-Selective Photodetectors. *Advanced Engineering Materials*, 24(4), December 2021.

[49] Chris G. Van de Walle and Richard M. Martin. Theoretical calculations of heterojunction discontinuities in the Si/Ge system. *Physical Review B*, 34(8):5621–5634, October 1986.

[50] Chris G. Van de Walle. Band lineups and deformation potentials in the model-solid theory. *Physical Review B*, 39(3):1871–1883, January 1989.

[51] Li Lang, Yue-Yu Zhang, Peng Xu, Shiyou Chen, H. J. Xiang, and X. G. Gong. Three-step approach for computing band offsets and its application to inorganic ABX_3 halide perovskites. *Phys. Rev. B*, 92:075102, 7, August 2015.

[52] Xing Huang, Kuanxin Lv, Wenqiang Zhu, Zhenzhen Li, and Hang Zhao. Accessible New Non-Quantum Dot $Cs_2PbI_2Cl_2$-Based Photocatalysts for Efficient Hole-Driven Photocatalytic Applications. *Molecules*, 29(14):3249, July 2024.

[53] Ling-Yu Pan, Yu-Feng Ding, Huang-Qing Liu, and Meng-Qiu Cai. High-performance photovoltaic application of the 2D all-inorganic Ruddlesden–Popper perovskite heterostructure $Cs_2PbI_2Cl_2$/$MAPbI_3$. *Physical Chemistry Chemical Physics*, 23(41):23703–23710, 2021.

Chapter 5

Conclusion & Perspectives

This chapter presents the general conclusions of the thesis and outlines perspectives for future work. First, the main findings obtained throughout the thesis are summarized, with particular emphasis on the role of local positional disorder in determining the structural, electronic, surface, and interface properties of all-inorganic halide perovskites. Then, possible directions for future research are discussed, including finite-temperature simulations, the extension of the polymorphous approach to broader chemical compositions, and further applications to layered perovskite compounds.

5.1 General conclusion

In this thesis, we demonstrated that local positional disorder plays a central role in determining the bulk and surface properties of the all-inorganic 2D and 3D halide perovskites studied here. We first focused on improving the calculation of surface properties by including local positional disorder in $CsBX_3$ compounds (B = Sn or Pb and X = I, Br, or Cl). We also examined different levels of theory. Our results show that semilocal GGA fails to reproduce the trend of the ionization potential with halogen substitution in both monomorphous and polymorphous structures, predicting a decrease with increasing halogen electronegativity. In contrast, DFT-1/2 corrects this behavior and yields an increasing trend. Combining the polymorphous approach with DFT-1/2 improves the prediction of band gaps and absolute band positions, demonstrating that local positional disorder is essential for describing the electronic structure of these materials. We found that local positional disorder stabilizes the bulk VBM and modifies the surface dipole, producing an electrostatic-potential shift that lowers the absolute VBM. In addition, polymorphous surface slabs have lower surface energies than ideal and reconstructed monomorphous slabs, indicating that they provide a more realistic description of perovskite surfaces. These results show that high-symmetry monomorphous models are useful as reference structures, but they are not sufficient for a realistic and quantitative description of halide perovskites.

In the second part of the thesis, we focused on layered 2D perovskites of composition $Cs_{n+1}Pb_nI_{n+1}Cl_{2n}$. Lattice-dynamics calculations show that the high-symmetry structure with $n = 1$ is dynamically stable, whereas structures with $n > 1$ are dynamically unstable and relax toward lower-energy locally distorted configurations. The energy gain and the change in the B-X-B bond angle induced by local positional disorder increase with increasing octahedral-layer thickness, n, indicating that the influence of local disorder becomes stronger as the structure approaches the 3D limit. Decomposition-energy calculations show that high-symmetry structures with $n > 4$ are unfavorable, whereas all members of the 2D perovskite series become favorable when local positional disorder is included. In addition, the decomposition energy of the polymorphous configurations saturates toward the $n \to \infty$ limit for $n > 4$. These results provide experimentalists with a more realistic criterion for identifying potentially stable and synthesizable layered perovskite compositions.

Local positional disorder also significantly modifies the electronic-property trends of 2D perovskites. It opens the band gap primarily through changes in the in-plane B-X-B bond angle and decreases the slope of the band-gap trend with increasing n, bringing the calculated trend closer to experiment. It also reverses the effective-mass trend. In monomorphous structures, the effective mass decreases with increasing n. In contrast, in polymorphous structures, the effective mass increases because local positional disorder flattens the band dispersion around the VBM and CBM. Moreover, for both electrons and holes, the disorder-induced effective-mass enhancement factor, λ, increases with n, in agreement with available experimental results in similar materials. This effect is stronger

for the hole effective mass than for the electron effective mass. Therefore, increasing the octahedral-layer thickness may reduce the band gap while simultaneously producing heavier carriers, revealing a trade-off between optical absorption and charge transport in device design.

Surface-energy calculations for 2D perovskites revealed that CsI is the most favorable termination for all studied values of n. The ionization potential decreases with increasing octahedral-layer thickness, n. Because of computational-size limitations, the effect of local positional disorder on surface properties was evaluated only for the $n = 2$ 2D perovskite. As in 3D perovskites, local positional disorder decreases the surface energy of 2D perovskites.

We also studied interfaces between 2D and 3D perovskites. The effect of local positional disorder was not included in the interface calculations, because its inclusion would increase the model size by at least a factor of four and would therefore be computationally prohibitive. The interface study shows that surface termination strongly affects both interface stability and band alignment, indicating that termination control during fabrication can influence interface adhesion and carrier extraction simultaneously. Among the six possible interfaces, the CsI-$PbCl_2$ and $PbBr_2$-CsI interfaces exhibit the largest adhesion energies. The three-step strain-correction method gives improved band offsets compared with the ADP method, and the calculated band offsets for the most favorable interfaces are close to experimental values.

Overall, this thesis shows that local positional disorder must be included to obtain a realistic description of halide perovskites, because it affects structural stability, surface energy, decomposition energy, band gaps, absolute band positions, and effective masses. Since these properties govern light absorption, charge transport, interfacial charge extraction, and material stability, their accurate first-principles description is essential for interpreting experiments and for rationally designing efficient and stable 3D/2D perovskite solar cells.

5.2 Perspectives

In this thesis, we extended the positional local disorder formalism beyond bulk systems by applying it to surfaces and to layered 2D perovskites. This demonstrates that local disorder is not only important for describing 3D bulk perovskites, but also plays a crucial role in surface stability, layered-structure stability, and electronic-property trends.

A natural next step is to investigate how these surface structures and properties evolve at finite temperature. However, realistic surface models are often too large for extensive simulations based only on ab initio methods and the ASDM approach. Molecular dynamics (MD) simulations based on machine-learning interatomic potentials (MLIPs) provide a promising alternative, as they allow much larger systems and longer simulation times to be studied while retaining near-DFT accuracy [1, 2]. MLIPs have already been used to investigate finite-temperature phase transitions [3, 4, 5] and dynamic local structures [6, 7] in halide perovskites. They have also been applied to

more complex systems, including halide-perovskite surfaces [8] and grain boundaries [9]. These developments suggest that MLIP-based MD simulations could be combined with the local-disorder framework developed in this thesis to study the finite-temperature structural and electronic properties of surfaces and interfaces in both 3D and layered halide perovskites.

In bulk 3D perovskites, finite-temperature properties have already been widely investigated [10, 11]. The present study of polymorphous 2D perovskites can therefore serve as a starting point for future finite-temperature calculations of layered perovskites. Such calculations would make it possible to study the temperature evolution of electronic properties and to identify possible phase transitions in 2D perovskites with different octahedral layer thicknesses, including both n = 1 and n > 1 structures.

Another important direction is to extend the present study to a broader chemical space. In this thesis, the effect of positional local disorder was studied only for the $Cs_{n+1}Pb_nI_{n+1}Cl_{2n}$ series. Future work could apply the same methodology to other Sn- and Pb-based layered perovskites, as well as to different mixed-halogen compositions such as Br-Cl and I-Br systems. This would enable a more systematic understanding of local positional disorder in layered all-inorganic perovskites.

Overall, future work could combine polymorphous structural modeling, finite-temperature simulations, and broader compositional screening to build a more complete picture of the stability and electronic properties of layered all-inorganic perovskites.

Declaration of AI Use

During the preparation of this manuscript, ChatGPT (OpenAI; GPT-5.5) was used exclusively to assist with language proofreading and grammatical corrections. Generative AI was not used to formulate original scientific ideas, generate research findings, conduct analyses, develop scientific interpretations, or produce original scientific content. All scientific contributions, critical evaluations, and conclusions presented in this thesis are the author's own.

References

[1] Ryosuke Jinnouchi, Ferenc Karsai, and Georg Kresse. On-the-fly machine learning force field generation: Application to melting points. *Physical Review B*, 100(1), 2019.

[2] John C. Thomas, Jonathon S. Bechtel, Anirudh Raju Natarajan, and Anton Van der Ven. Machine learning the density functional theory potential energy surface for the inorganic halide perovskite $CsPbBr_3$. *Physical Review B*, 100(13), October 2019.

[3] Ryosuke Jinnouchi, Jonathan Lahnsteiner, Ferenc Karsai, Georg Kresse, and Menno Bokdam. Phase Transitions of Hybrid Perovskites Simulated by Machine-Learning Force Fields Trained on the Fly with Bayesian Inference. *Physical Review Letters*, 122(22), 2019.

[4] Tom Braeckevelt, Ruben Goeminne, Sander Vandenhaute, Sander Borgmans, Toon Verstraelen, Julian A. Steele, Maarten B. J. Roeffaers, Johan Hofkens, Sven M. J. Rogge, and Veronique Van Speybroeck. Accurately Determining the Phase Transition Temperature of $CsPbI_3$via Random-Phase Approximation Calculations and Phase-Transferable Machine Learning Potentials. *Chemistry of Materials*, 34(19):8561–8576, 2022.

[5] Xia Liang, Johan Klarbring, and Aron Walsh. Phase Stability and Transformations in Lead Mixed Halide Perovskites from Machine Learning Force Fields. *Chemistry of Materials*, 37(23):9392–9405, 2025.

[6] William J. Baldwin, Xia Liang, Johan Klarbring, Milos Dubajic, David Dell'Angelo, Christopher Sutton, Claudia Caddeo, Samuel D. Stranks, Alessandro Mattoni, Aron Walsh, and Gábor Csányi. Dynamic Local Structure in Caesium Lead Iodide: Spatial Correlation and Transient Domains. *Small*, 20(3), 2023.

[7] Julia Wiktor, Erik Fransson, Dominik Kubicki, and Paul Erhart. Quantifying Dynamic Tilting in Halide Perovskites: Chemical Trends and Local Correlations. *Chemistry of Materials*, 35(17):6737–6744, August 2023.

[8] Frederico P. Delgado, Frederico Simões, Leeor Kronik, Waldemar Kaiser, and David A. Egger. Machine-Learning Force Fields Reveal Shallow Electronic States on Dynamic Halide Perovskite Surfaces. *ACS Energy Letters*, 10(7):3367–3374, 2025.

[9] Yifan Wu, Dongyu Liu, Weibin Chu, Bipeng Wang, Andrey S. Vasenko, and Oleg V. Prezhdo. Fluctuations at metal halide perovskite grain boundaries create transient trap states: machine learning assisted ab initio analysis. *ACS Applied Materials & Interfaces*, 14(50):55753–55761, December 2022.

[10] Marios Zacharias, George Volonakis, Laurent Pedesseau, Claudine Katan, Feliciano Giustino, and Jacky Even. Roadmap for electronic structure, anharmonicity, and electron-phonon calculations in locally disordered inorganic and hybrid halide perovskites. *Physical Review B*, 113(8), February 2026.

[11] Lorenzo Monacelli and Nicola Marzari. First-Principles Thermodynamics of $CsSnI_3$. *Chemistry of Materials*, 35(4):1702–1709, February 2023.

Appendix A

Effect of vdW Correction and XC Functionals on the Electronic Properties

A.1 vdW correction

To account for dispersion interactions during structural relaxation, all equilibrium structures considered in this thesis were optimized using the optB86b-vdW functional. However, because of an implementation limitation in Quantum ESPRESSO, the nonlocal optB86b-vdW functional could not be used together with spin-orbit coupling (SOC) in the electronic-structure calculations. Therefore, SOC-corrected band positions reported in the main text were obtained using optB86b+SOC calculations performed at the fixed geometries previously optimized with optB86b-vdW. In this approach, the explicit electronic contribution from the nonlocal vdW potential is not included in the SOC calculations, while the structural influence of vdW interactions is retained through the optimized geometries.

To evaluate the possible effect of this omission, additional non-SOC calculations were carried out using both optB86b and optB86b-vdW at the same optB86b-vdW relaxed geometries. This comparison separates the electronic effect of the nonlocal vdW term from changes arising from structural relaxation. The results, presented in Table A.1, show that including the nonlocal vdW term shifts the absolute VBM positions downward by about 0.14–0.24 eV and increases the band gaps by roughly 0.08–0.17 eV. These shifts can therefore be regarded as an estimate of the quantitative uncertainty introduced by neglecting the nonlocal vdW contribution in the SOC calculations. Since these differences are smaller than the variations caused by composition and atomic configuration discussed in the main text, the overall qualitative trends in band alignment are expected to be unaffected.

Material	Monomorphous ΔE_{VBM} (eV) CsX	Monomorphous ΔE_{VBM} (eV) BX_2	Monomorphous ΔE_g (eV)	Polymorphous ΔE_{VBM} (eV) CsX	Polymorphous ΔE_{VBM} (eV) BX_2	Polymorphous ΔE_g (eV)
$CsSnI_3$	-0.20	-0.17	0.13	-0.19	-0.16	0.11
$CsSnBr_3$	-0.24	-0.17	0.15	-0.22	-0.16	0.13
$CsSnCl_3$	-0.24	-0.17	0.17	-0.24	-0.17	0.15
$CsPbI_3$	-0.15	-0.15	0.10	-0.16	-0.14	0.08
$CsPbBr_3$	-0.19	-0.17	0.13	-0.18	-0.15	0.10
$CsPbCl_3$	-0.21	-0.16	0.14	-0.20	-0.16	0.12

Table A.1: Difference between optB86b-vdW and optB86b electronic calculations performed without SOC at the same optB86b-vdW optimized geometries. The values quantify the electronic contribution of the nonlocal vdW term, independent of structural relaxation effects. Here, $\Delta E_g = E_g^{\text{optB86b-vdW}} - E_g^{\text{optB86b}}$ and $\Delta E_{\mathrm{VBM}} = E_{\mathrm{VBM}}^{\text{optB86b-vdW}} - E_{\mathrm{VBM}}^{\text{optB86b}}$.

A.2 Exchange–correlation functionals

The sensitivity of the calculated band gaps and absolute VBM positions to the choice of XC functional was examined by comparing optB86b, PBE, and PBEsol. All calculations were performed using the fixed optB86b-vdW optimized geometries with SOC included, so that the comparison isolates the effect of the XC functional on the electronic structure.

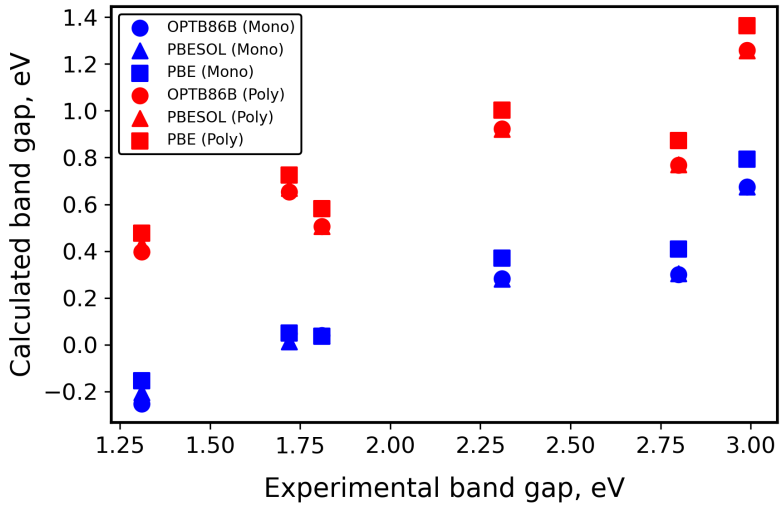

Figure A.1: Calculated band gaps of the monomorphous and polymorphous configurations as a function of experimental band gap. Results are shown for the optB86b, PBE, and PBEsol exchange–correlation functionals. All calculations were performed at the fixed optB86b-vdW optimized geometries with SOC included.

Appendix A. Effect of vdW Correction and XC Functionals on the Electronic Properties

As shown in Fig. A.1, the overall band-gap trends are not changed by the choice of XC functional. For both monomorphous and polymorphous configurations, optB86b and PBEsol give very similar band gaps, whereas PBE gives slightly larger values, typically by about 0.1 eV. Thus, the choice among the tested XC functionals changes the absolute band-gap values only modestly and does not alter the overall trend. Negative or nearly zero calculated gaps, where present, should be interpreted as a consequence of the known band-gap underestimation of semilocal DFT in combination with strong SOC; therefore, the results are used primarily for relative trend analysis rather than as quantitatively predictive band gaps.

A similar conclusion is obtained for the absolute VBM positions, shown in Fig. A.2. For both monomorphous and polymorphous configurations, the relative VBM trends are preserved across the three XC functionals. The functional-induced spread in the VBM values is relatively small, remaining below about 0.12 eV for the monomorphous configurations and below about 0.07 eV for the polymorphous configurations. These variations are much smaller than the changes associated with composition and structural configuration, indicating that the qualitative band-alignment trends discussed in the thesis are robust with respect to the tested XC functionals.

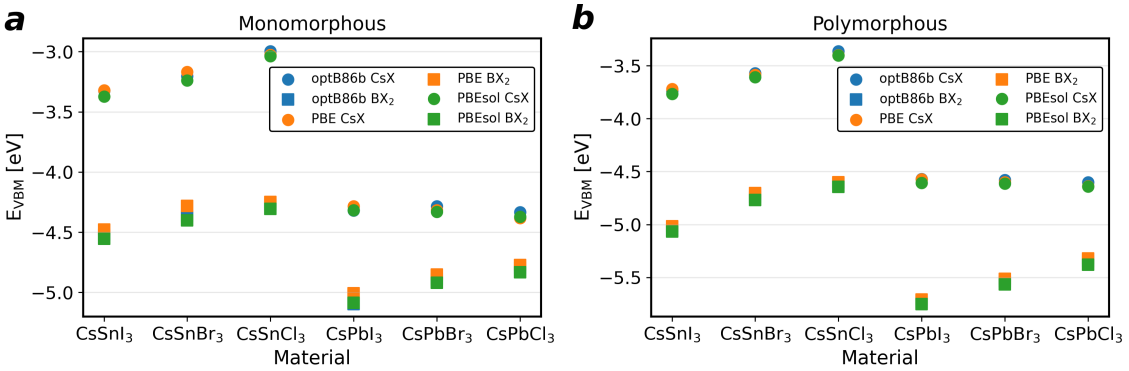

Figure A.2: Absolute VBM positions of the (a) monomorphous and (b) polymorphous configurations calculated using the optB86b, PBE, and PBEsol exchange–correlation functionals. The calculations were performed at the fixed optB86b-vdW optimized geometries with SOC included. The CsX and BX_2 labels denote the two surface terminations or alignment references used in the calculations. Blue points are not always visible because of overlapping with the greeen ones.

Appendix B

Effect of Volume Relaxation on Polymorphous Structures

In the main calculations, the polymorphous structures of the 3D perovskites were relaxed while keeping the lattice constant and cubic cell shape fixed. Here, the effect of allowing volume relaxation is examined. The relative volume change is defined as

$$\frac{\Delta V}{V} = \frac{V_{\text{relaxed}} - V_{\text{fixed}}}{V_{\text{fixed}}} \times 100\%, \tag{B.1}$$

and the additional energy gain due to volume relaxation is defined as

$$\Delta E_{\text{gain}} = E_{\text{gain}}^{\text{relaxed}} - E_{\text{gain}}^{\text{fixed}}. \tag{B.2}$$

Positive values of ΔE_{gain} therefore indicate additional stabilization of the polymorphous structure after the lattice parameters are allowed to relax. Because $E_{\text{gain}}^{\text{fixed}}$ and $E_{\text{gain}}^{\text{relaxed}}$ are magnitude of gained energies.

Volume relaxation lowers the total energy of all polymorphous structures, but the magnitude of the additional stabilization depends strongly on composition. Among the 3D perovskites, $CsPbI_3$ exhibits the largest additional energy gain, 26.35 meV/f.u., together with the largest volume reduction, -4.76%. In contrast, $CsSnCl_3$ shows the smallest additional energy gain, 2.59 meV/f.u., and the smallest volume reduction, -1.25% (Table B.1). The trend in additional energy gain follows the same general trend as the energy gain obtained at fixed lattice constant: compounds with larger polymorphous stabilization also gain more energy upon volume relaxation. The volume reduction is mainly accommodated by changes in the B–X–B bond angle, indicating that the energy gain remains strongly coupled to octahedral tilting and local structural distortion. We also tested full structural relaxation without imposing symmetry constraints, allowing both the atomic positions and the shape of the crystal cell to change. The energy is lowered by 43 meV/f.u. relative to the fixed-volume polymorphous structure [1]. Departure from cubic symmetry after full relaxation and associated sizeable energy gain is probably related to the small size of our polymorphous model and has to be taken with care.

A similar behavior is observed for the 2D perovskite series (Table B.2). Volume relaxation generally reduces the total volume and provides additional stabilization. The $n = 4$ structure shows the largest additional energy gain among the finite-n 2D structures, 16.05 meV/f.u., together with the largest volume reduction, -2.55%. Although the c lattice parameter expands for some members of the series, the overall volume decreases, mainly because of contraction in the in-plane lattice parameter. Therefore, allowing volume relaxation does not change the main correlation between polymorphous energy gain and the average B–X–B bond-angle deviation, as shown in Fig. B.1.

Table B.1: Relative volume change and additional energy gain of 3D perovskites due to volume relaxation.

Compound	$\Delta V/V$ (%)	ΔE_{gain} (meV/f.u.)
$CsPbI_3$	-4.76	26.35
$CsPbBr_3$	-3.81	18.23
$CsPbCl_3$	-3.08	12.77
$CsSnI_3$	-2.62	8.81
$CsSnBr_3$	-1.99	4.71
$CsSnCl_3$	-1.25	2.59

Table B.2: Relative changes in volume, lattice parameters, and additional energy gain of polymorphous $n > 1$ 2D perovskites due to volume relaxation.

n	$\Delta V/V$ (%)	$\Delta a/a$ (%)	$\Delta c/c$ (%)	ΔE_{gain} (meV/f.u.)
2	-0.75	-0.63	$+0.51$	2.79
3	-0.89	-0.86	$+0.83$	3.12
4	-2.55	-2.14	$+1.76$	16.05
5	-1.90	-0.74	-0.43	3.58
∞	-2.48	-0.87	-0.77	8.27

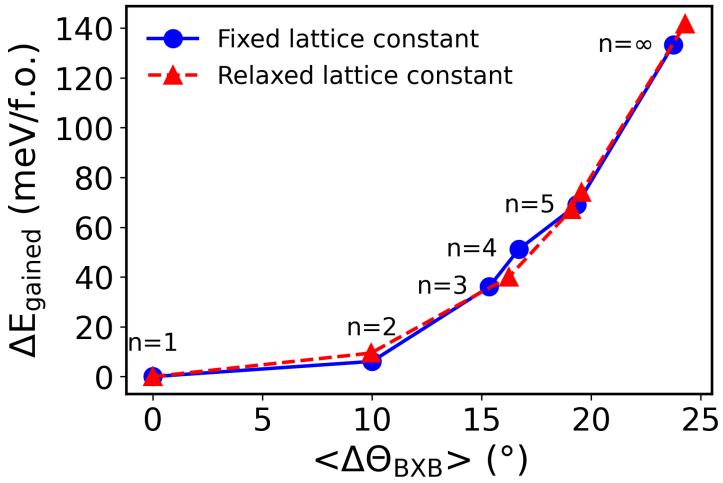

Figure B.1: Relationship between the polymorphous energy gain and the average B–X–B bond-angle deviation, $\langle \Delta\theta_{\mathrm{BXB}} \rangle$, calculated using fixed lattice constants and volume-relaxed lattice constants. The nearly overlapping trends indicate that volume relaxation does not alter the correlation between structural distortion and energy stabilization.

Appendix C

Projected Density of States of 2D Perovskites

For both the $n = 1$ and $n = 2$ 2D perovskites, the upper valence band is dominated by I-$5p$ states, with smaller contributions from Cl-$3p$ and Pb-$6s$ states. The lower conduction band is dominated mainly by Pb-$6p$ states. This orbital character is consistent with the typical electronic structure of lead-halide perovskites, where the VBM originates primarily from antibonding interactions between halide p states and Pb-$6s$ states, whereas the conduction-band minimum (CBM) is mainly derived from Pb-$6p$ states.

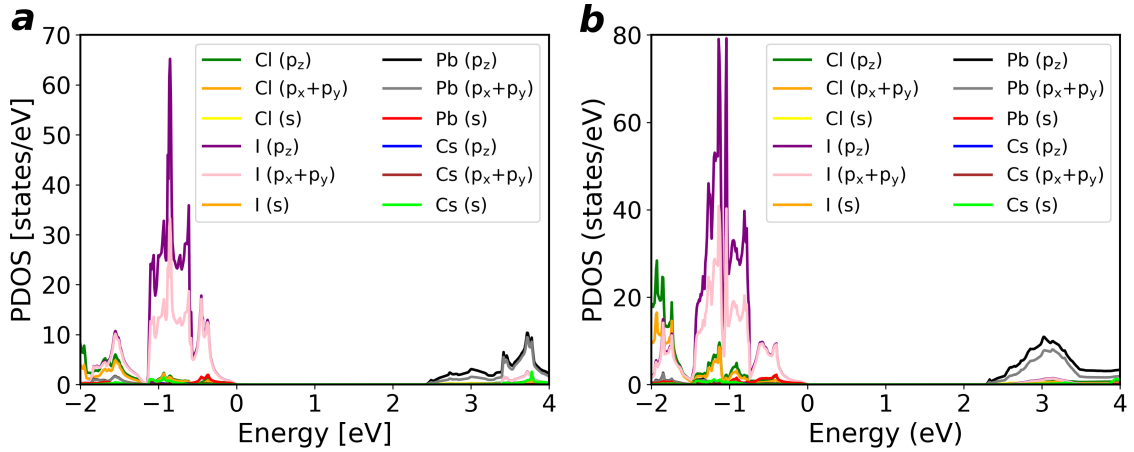

Figure C.1: Projected density of states of the $n = 1$ and $n = 2$ $Cs_{n+1}Pb_nI_{n+1}Cl_{2n}$ 2D perovskites. The zero of energy is set to the VBM. The upper valence band is mainly composed of I-$5p$ states with minor Cl-$3p$ and Pb-$6s$ contributions, while the lower conduction band is dominated by Pb-$6p$ states.

Appendix D

Phonon Dispersion of $CsPbICl_2$

$CsPbICl_2$ is the 3D reference structure, corresponding to the ($n \to \infty$) limit of the 2D perovskite series $Cs_{n+1}Pb_nI_{n+1}Cl_{2n}$. The monomorphous configuration of the 3D reference structure has imaginary phonon modes, indicating the dynamical instability of the high-symmetry structure. This behavior is consistent with the instability commonly observed in ideal cubic 3D halide perovskites. In contrast, the polymorphous configuration stabilizes these imaginary modes, demonstrating that local positional disorder and symmetry breaking provide a dynamically more stable structural description.

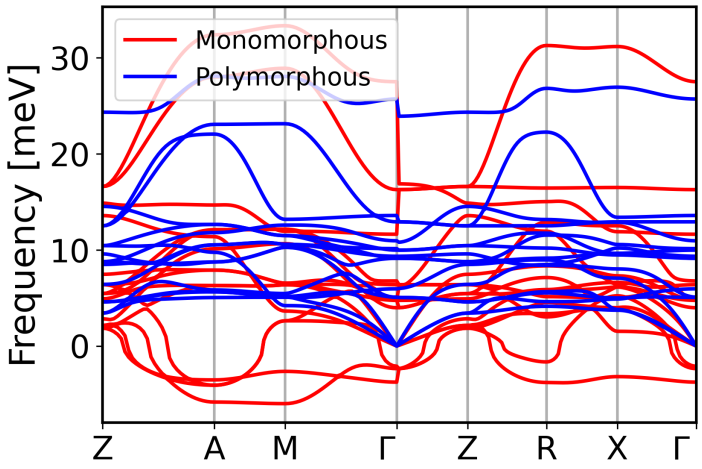

Figure D.1: Phonon dispersion of monomorphous and polymorphous $CsPbICl_2$ ($n \to \infty$). Imaginary phonon modes in the monomorphous structure indicate the dynamical instability of the high-symmetry phase, while their suppression in the polymorphous structure indicates stabilization by local positional disorder.

Appendix E

Effect of biaxial strain on the electronic properties of the 2D perovskite $Cs_2PbI_2Cl_2$

In this thesis, we studied 2D/3D perovskite interfaces. When such an interface is formed, lattice mismatch can generate strain, which is often accommodated mainly by the thinner and softer 2D layer. Since 2D perovskites are commonly used as thin passivation layers on 3D perovskites, it is important to understand how strain affects their electronic properties.

Here, we investigated biaxial strain from -6% to $+6\%$ in $Cs_2PbI_2Cl_2$, where negative and positive values correspond to compressive and tensile strain, respectively. Figure E.1a shows that the strain energy increases with increasing strain magnitude. The response is asymmetric: at -6% compressive strain, the strain energy is approximately 0.21 eV/f.u., whereas at $+6\%$ tensile strain it is about 0.12 eV/f.u..

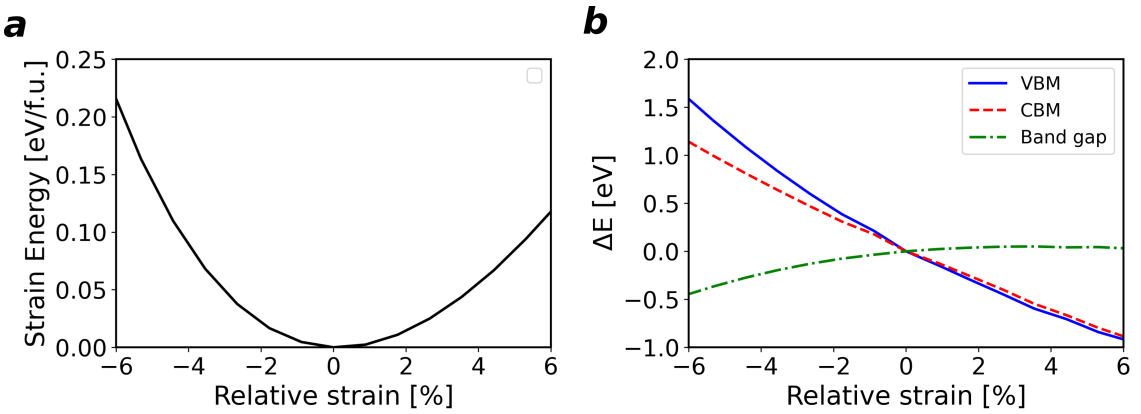

Figure E.1: Effect of biaxial strain on $Cs_2PbI_2Cl_2$. **a** Strain energy relative to the unstrained structure. **b** Strain-induced changes in the bulk VBM, CBM, and band gap relative to the unstrained bulk structure. Negative and positive strain values correspond to compressive and tensile strain, respectively.

Appendix E. Effect of biaxial strain on the electronic properties of the 2D perovskite $Cs_2PbI_2Cl_2$

The applied in-plane strain also changes the out-of-plane c lattice parameter, as shown in Figure E.2. In-plane compression causes expansion along the c direction, whereas tensile strain causes contraction. Even at about 6% tensile strain, the change in the c lattice parameter is only approximately 2.5%, showing that the out-of-plane response is smaller than the applied in-plane deformation.

Figure E.1b shows the strain-induced changes in the bulk VBM, CBM, and band gap. The VBM and CBM correspond to the highest occupied and lowest unoccupied Kohn–Sham states, respectively, and their shifts are given relative to the unstrained bulk structure. Under compressive strain, both the VBM and CBM shift upward, whereas under tensile strain both shift downward.

These changes are related to the strain-induced modification of Pb–halide bonds. The VBM is mainly formed by antibonding interactions between Pb $6s$ and halide p orbitals, while the CBM is mainly associated with Pb $6p$ states. Under compressive strain, the in-plane Pb–Cl bond length decreases and the out-of-plane Pb–I bond length increases. The opposite trend occurs under tensile strain.

To distinguish the roles of in-plane and out-of-plane deformation, we also changed the in-plane and out-of-plane lattice parameters separately. A 5% change in the in-plane lattice parameters shifts the VBM and CBM by about twice as much as a 5% change in the out-of-plane c lattice parameter. This indicates that the strain-induced shifts of the bulk VBM and CBM are mainly controlled by changes in the in-plane Pb–Cl bond lengths.

Under compressive strain, the VBM shifts more strongly than the CBM, leading to a reduction of the band gap. In contrast, under tensile strain, the VBM and CBM shift by similar amounts, and the band gap remains nearly unchanged. Overall, these results show that biaxial strain can strongly modify the bulk band edges of $Cs_2PbI_2Cl_2$, with the dominant contribution coming from changes in the in-plane Pb–Cl bonding.

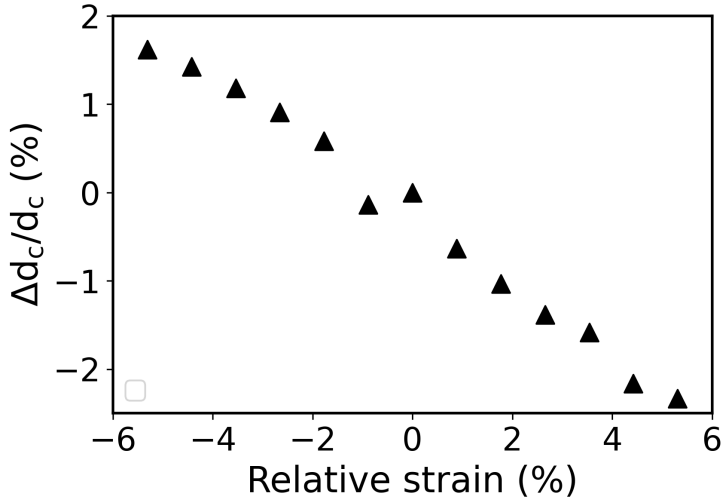

Figure E.2: Relative change in the out-of-plane c lattice parameter as a function of the applied in-plane biaxial strain.

References

[1] Jasurbek Gulomov, Guido Roma, Marios Zacharias, Jacky Even, and Claudine Katan. The role of local disorder in surface properties of inorganic halide perovskites. Manuscript submitted to Physical Review Materials, 2026.